

AD702095

ARL 69-0155
OCTOBER 1969



Aerospace Research Laboratories

RESEARCH ON THE MECHANISM OF THE PHOTOVOLTAIC EFFECT IN HIGH EFFICIENCY CdS THIN-FILM SOLAR CELLS

L. R. SHIOZAWA
F. AUGUSTINE
G. A. SULLIVAN
J. M. SMITH, III
W. R. COOK, JR.
CIEVITE CORPORATION
CLEVELAND, OHIO

Contract No. AF33(615)-5224
Project No. 7885

This document has been approved for public release and sale;
its distribution is unlimited.

D D C
REF ID: A652140
MAR 17 1970
C.

OFFICE OF AEROSPACE RESEARCH United States Air Force

Reproduced by the
CLEARINGHOUSE
for Federal Scientific & Technical
Information Springfield Va. 22151



217

REASON FOR	
REF ID	WHITE SEC FORM
DOC	DATA SECTION <input type="checkbox"/>
UNANNOUNCED	<input type="checkbox"/>
NOTIFICATION	
BY	<input type="checkbox"/>
DISTRIBUTION/AVAILABILITY	
LIST	AVAIL <input type="checkbox"/> NOT TO BE REGARDED

NOTICES

When Government drawings, specifications, or other data are used for any purpose other than in connection with a definitely related Government procurement operation, the United States Government thereby incurs no responsibility nor any obligation whatsoever; and the fact that the Government may have formulated, furnished, or in any way supplied the said drawings, specifications, or other data, is not to be regarded by implication or otherwise as in any manner licensing the holder or any other person or corporation, or conveying any rights or permission to manufacture, use, or sell any patented invention that may in any way be related thereto.

Agencies of the Department of Defense, qualified contractors and other government agencies may obtain copies from the

Defense Documentation Center
Cameron Station
Alexandria, Virginia 22314

This document has been released to the

CLEARINGHOUSE
U.S. Department of Commerce
Springfield, Virginia 22151

for sale to the public.

Copies of ARL Technical Documentary Reports should not be returned to Aerospace Research Laboratories unless return is required by security considerations, contractual obligations or notices on a specified document.

BLANK PAGE

ARL 69-0155

**RESEARCH ON THE MECHANISM OF THE
PHOTOVOLTAIC EFFECT IN HIGH EFFICIENCY
CdS THIN-FILM SOLAR CELLS**

OCTOBER 1969
CLEVITE CORPORATION
ELECTRONIC RESEARCH DIVISION
CLEVELAND, OHIO 44108

By

L. R. SHIOZAWA

F. AUGUSTINE

G. A. SULLIVAN

J. M. SMITH, III

W. R. COOK, JR.

Contract No. AF33(615)-5224
Project No. 7885

This document has been approved for public release and sale;
its distribution is unlimited.

AEROSPACE RESEARCH LABORATORIES
OFFICE OF AEROSPACE RESEARCH
UNITED STATES AIR FORCE
WRIGHT-PATTERSON AIR FORCE BASE, OHIO

FOREWORD

This Final Technical Report was prepared by the Electronic Research Division, Clevite Corporation, Cleveland, Ohio, on Contract AF 33(615)-5224, for the Aerospace Research Laboratories, Office of Aerospace Research, United States Air Force. The research reported herein was accomplished on Project No. 7885 under the technical cognizance of Mr. Donald C. Reynolds of the Aerospace Research Laboratories, ARX.

L. R. Shiozawa, G. A. Sullivan, F. Augustine, J. M. Smith III, and W. R. Cook Jr. of the Electronic Research Division of Clevite Corporation carried out the main research effort and prepared this technical report on research performed in the period 1 June 1966 through 31 May 1969. The contents of the ten quarterly progress reports written during the contract period beginning in June 1966 have been incorporated in this report.

Acknowledgment is made of the contribution of the Solar Battery Section under F. A. Shirland in the supply of solar cells, for the use of solar test facilities, and the sharing of extensive experience with thin film solar cells.

ABSTRACT

A tentative $\text{Cu}_2\text{S}:\text{CdS}$ heterojunction model which involves intrinsic absorption in a thin Cu_2S surface layer and photoconductivity in an adjacent layer of CdS was studied by electrical, optical, and chemical measurements. The proposed barrier height in the dark of ~ 1.2 eV changing to ~ 0.85 eV in sunlight is consistent with the observed differences in the IV characteristics, the measured photoconductive properties of Cu-compensated CdS , the observed maximum low-temperature open-circuit voltage (0.8 V), and published work function data. The photoconductivity of the i - CdS layer which controls the current generated in the Cu_2S layer adequately explains the enhancement and quenching effects of biasing light as well as the transient properties of the cell. The lattice mismatch between the epitaxially formed Cu_2S and the CdS introduces strains and interface states, the latter acting as recombination centers during forward bias. The Cu_2S layer initially formed as chalcocite undergoes transformation to djurleite and other phases during room-temperature exposure to air, and these changes are accelerated at elevated temperatures, giving rise to rapid degradation of current output at 150°C . The measured diffusivity ($\sim 10^{-7} \text{ cm}^2/\text{sec}$) and mobility ($\sim 3 \times 10^{-6} \text{ cm}^2/\text{V-sec}$) of Cu ions in Cu_2S is sufficiently large to account for the observed formation of Cu nodules during open-circuit illumination, the threshold voltage for this process being ~ 0.4 V. The diffusivity of Cu in CdS [$D = 2.1 \times 10^{-3} \exp(0.96/kT) \text{ cm}^2/\text{sec}$] derived from capacitance and low-temperature solubility [$[\text{Cu}] = 6.6 \times 10^{22} \exp(-0.505 \text{ eV}/kT) \text{ cm}^{-3}$] measurements indicates that the i - CdS layer grows to a thickness of $\sim 1 \mu$ during cell processing and that the subsequent thickening at 65°C is slow enough to allow 3 to 5 years of continuous operation. The more rapid degradation in vacuum at higher temperatures is shown to be controllable by donor doping of the CdS . Although the maximum theoretical efficiency is shown to be $\sim 15\%$, realistic constraints limit the achievable efficiency to $\sim 10\%$.

TABLE OF CONTENTS

	<u>Page</u>
FOREWORD	ii
ABSTRACT	iii
LIST OF ILLUSTRATIONS	vii
LIST OF TABLES	xii
1. INTRODUCTION	1
2. SUMMARY OF THE CLEVITE SOLAR CELL MODEL	2
3. EXPERIMENTAL RESULTS AND ANALYSIS	7
3. 1 Brief Review of the Construction and Structure of the CdS Solar Cell	7
3. 2 The Cuprous Sulfide Layer	9
3. 2. 1 Thickness and Topology of the Cu ₂ S Layer	9
3. 2. 2 Formation of Cu ₂ S on CdS Single Crystals	12
3. 2. 3 Electrical Properties of Cu ₂ S	13
3. 2. 4 Optical Properties of Cu ₂ S	14
3. 2. 5 Calculated Quantum Absorption Efficiency in Cu ₂ S	17
3. 2. 6 Stoichiometry of Dip-Formed Cu ₂ S	20
3. 2. 7 X-Ray Crystallography and Epitaxial Orientation of Cu ₂ S	21
3. 2. 7. 1 Studies on Large Crystals; Growth Rate of Cu ₂ S Layer	23
3. 2. 7. 2 Studies on Needle Crystals	33
3. 2. 7. 3 Studies on Copper Sulfide Powders	37
3. 2. 7. 4 Conclusions From the X-Ray Data on Copper Sulfide	37
3. 2. 8 Diffusion and Mobility of Cu Ions in Cu ₂ S	38
3. 3 The Cu-Compensated i-CdS Layer	44
3. 3. 1 Diffusion of Cu in CdS Crystals and Films	44
3. 3. 2 Solubility of Cu in CdS	50
3. 3. 3 Thickness of the i-Layer in Thin Film Cells	53
3. 3. 4 Optical Transmission of Cu-Saturated CdS Crystals	55
3. 3. 5 Growth and Decay of Photoconductivity of Cu-Compensated CdS	57

	<u>Page</u>
3.4 The n-CdS Layer	60
3.4.1 Grain Structure and Crystallographic Orientation of CdS Films	60
3.4.2 The Non-Stoichiometry of Vacuum Deposited CdS	63
3.5 The IV Characteristics of CdS Solar Cells	64
3.5.1 The Light-to-Dark IV-Cross-Over Effect	64
3.5.2 Temperature Dependence of IV Characteristics	66
3.5.3 Light Intensity Dependence of IV Characteristics	69
3.5.4 Cu ₂ S-Thickness Dependence of IV Characteristics	79
3.5.5 The Effects of Series and Shunt Resistances on IV Characteristics	80
3.5.6 Determination of I _o and the Diode A-Factor	81
3.5.7 Maximum Observed Open-Circuit Voltage	88
3.5.8 The IV Characteristics of Related Systems	94
3.5.8.1 The p-Cu ₂ S:i-CdS Junction	94
3.5.8.2 The n-CdS:i-CdS Homojunction	97
3.5.8.3 The p-Si:n-CdS Heterojunction	100
3.6 The Spectral Response of CdS Solar Cells	101
3.6.1 In-Doped Ceramic Cells, with Cu ₂ S-Thickness Dependence	102
3.6.2 Un-doped Ceramic Cells, with Cu ₂ S-Thickness Dependence	110
3.6.3 Single Crystal Cells	121
3.6.4 Thin Film Cells	125
3.6.5 Transient Effects	127
3.6.6 Antimonochromatic Spectral Response	127
3.7 Miscellaneous Studies	139
3.7.1 Reaction of Zn and Ag at Metallized Substrate	139
3.7.2 Synthesis of Cuprous Sulfide	140
3.7.3 Cell Output vs. Angle of Illumination	143
3.8 Calculation of Maximum Efficiency of the CdS Solar Cell	143
3.8.1 Maximum Theoretical Efficiency	143
3.8.2 Maximum Achievable Efficiency	147

	<u>Page</u>
4. CRITICAL DISCUSSION OF THE WORKS OF OTHERS IN RELATION TO THE CLEVITE MODEL	149
4. 1 The Active Role of the Cu ₂ S Layer	149
4. 2 The Existence and Nature of the i-CdS Layer	150
4. 3 Change in Barrier Height and the IV Cross-Over Phenomenon	152
4. 4 Cd and Cl in the Cu ₂ S Layer	158
4. 5 The Stanford Tunnelling Model	160
5. FAILURE MECHANISMS	164
5. 1 High-Temperature Degradation in Vacuum	164
5. 2 Open-Circuit Degradation; Cu-Nodule Formation	165
5. 3 High-Temperature Degradation in Air	171
5. 4 Thermal-Cycling Degradation	175
6. SUMMARY OF NEEDS FOR FUTURE WORK	176
7. ACKNOWLEDGMENTS	177
8. REFERENCES CITED	178
9. APPENDIX: Literature Review of the Cu-S Phase Diagrams by William R. Cook	181

LIST OF ILLUSTRATIONS

Figure	Page
1. Energy Band Diagram for $\text{Cu}_2\text{S}-\text{CdS}$ Solar Cell, According to the Clevite Model.	2
2. True-View Cross-Section of A Standard CdS Solar Cell (500X).	8
3. True-View Cross-Sections of CdS Cells Etched in HCl and Exposed to Standard Cu^+ Solutions for Different Times	12a
4. Absorption Coefficient and Refractive Index of Vacuum Evaporated Cu_2S Thin Films.	15
5. Square Root of Absorption Coefficient of Cu_2S as a Function of Photon Energy.	16
6. Quantum Absorption Efficiency for Cu_2S at Different Wave- Lengths and Cu_2S Thicknesses. Planar (one dimensional) Geometry. Absorption Coefficients From Dip-Formed Films.	18
7. Quantum Absorption Efficiency for Cu_2S at Different Wave- Lengths and Cu_2S -Thicknesses. Planar (one dimensional) Geometry. Absorption Coefficients from Evaporated Thin Films.	19
8. Polished Surface of (0001) Plate of CdS After Being Dipped in CuCl Solution at 90°C for 59 Minutes, Mag. 80X.	26
9. (1010) Plate of CdS After Being Dipped in CuCl Solution at 90°C for 90 Minutes, Mag. 80X. The Top View is of the Polished Surface. The Bottom View is of a (0001) Cleavage Plane Perpendicular to the Main Surface and in the Position Indicated.	27
10. (1120) Plate of CdS After Being Dipped in CuCl Solution at 90°C for 90 Minutes, Mag. 80X. The Top View is of the Polished Surface. The Bottom View is of a (1010) Cleavage Plane Perpendicular to the Main Surface and in the Position Indicated.	28
11. Thickness of Cu_2S Layer vs. Dipping Time for Oriented CdS Plates.	30

<u>Figure</u>	<u>Page</u>
12. (a) CdS Crystal, Rotated Around <u>c</u> Axis. (b) Cu ₂ S Chalcocite) Crystal, Rotated Around <u>c</u> Axis.	34
13. (a) Cu _{1.96} S Crystal Rotated Around <u>c</u> Axis. (b) Cu _x S with 1.96 > x > 1.8 Rotated Around <u>c</u> Axis. (c) Crystal Rotated Around <u>c</u> Axis of Djurleite.	36
14. Transport Number vs. Voltage, Showing Voltage Threshold for Electrolytic Plating of Cu.	41
15. Square of the Effective Parallel Plate Spacing (Proportional to 1/C ²) vs. Time.	46
16. Temperature Dependence of the Time Rate of Increase of the Square of the Effective Capacitor Thickness.	47
17. Effective Diffusion Coefficient for Cu in CdS (Parallel to <u>c</u> -Axis).	48
18. Diffusion Coefficients; Comparison of Present Work with Previous Investigations.	49
19. Square of the Reciprocal Capacitance of a Solar Cell Section as a Function of Time--Beginning of Run.	51
20. Square of the Reciprocal Capacitance of a Solar Cell Section as a Function of Time--End Portion of Run.	52
21. Solubility Data for Cu in CdS.	54
22. Transmission Spectrum of CdS Crystals Saturated with Cu at 250°C.	56
23. Growth of Photoconductivity of CdS Saturated with Cu at 250°C.	58
24. Decay of Photoconductivity of CdS Saturated with Cu at 250°C.	59
25. Grain Boundary Structure of Vacuum Deposited CdS Layer; View Parallel to Film Thickness After Polishing and Light Etching (1600X).	61
26. IV Characteristics as a Function of Temperature.	67
27. Operating Parameters vs. Temperature, No. N110AK4-Standard Process Cell.	68
28. IV Characteristics vs. Illumination Intensity "Typical Standard Process Thin CdS Solar Cell No. H337B7.	70

<u>Figure</u>	<u>Page</u>
29. IV Characteristics vs. Illumination Intensity Ceramic CdS Solar Cell No. 28-10.	71
30. Operating Parameters vs. Illumination Intensity, "Typical" Standard Process Thin Film CdS Solar Cell No. H337B7.	73
31. Operating Parameters vs. Illumination Intensity, Ceramic CdS Solar Cell No. 28-10.	74
32. Effect of External Series Resistance.	82
33. Effect of External Shunt Resistance.	83
34. Effect of External Shunt Between Series Resistances. $R_1 = R_2 = 0.1 \Omega$.	84
35. Effect of External Shunt Between Series Resistances. $R_1 = R_2 = 0.05 \Omega$.	85
36. IV Characteristic Clevite Ceramic Solar Cell No. 30-17.	87
37. Graphical Determination of A-Factor and Series Resistance, R_s , of Clevite Ceramic Solar Cell No. 30-17; Active Area = 1.1 cm^2 .	89
38. Graphical Determination of A-Factor and Maximum Reverse Current, I_o , of Clevite Ceramic Solar Cell No. 30-17; Active Area = 1.1 cm^2 .	90
39. Open-Circuit Voltage as a Function of Illumination for a Ceramic and a Single-Crystal CdS Cell at Liquid Helium and Liquid Nitrogen Temperatures.	92
40. Open Circuit Voltage vs. Temperature, 4.2° to 60°K .	93
41. Electrode Configuration for Measuring IV Characteristics of the $\text{Cu}_2\text{S}:i\text{-CdS}$ Junction.	96
42. Current-Voltage Characteristics of the Systems InAu: $\text{Cu}_2\text{S}:i\text{-CdS:In}$ and In:i-CdS:In in Room Light, 7 mW/cm^2 .	98
43. Current-Voltage Characteristics of the Systems InAu: $\text{Cu}_2\text{S}:i\text{-CdS:In}$ and In:i-CdS:In Under 1 Sun.	99
44. Spectral Response vs. Dip Time. CdS Ceramic Solar Cells. Response Adjusted to Constant Energy Input. CuCl in Dip Solution = 17 g/l .	103

<u>Figure</u>		<u>Page</u>
45.	Spectral Response of Indium Doped CdS Ceramics Solar Cells Enhanced by White Light for Various Dip Times.	104
46.	Enhancement Curves of Indium-Doped CdS Ceramic Solar Cells Formed in 16.7 g/ℓ CuCl Soln.	105
47.	Photoconductive Response vs. Wavelength, CdS Ceramic Solar Cells with Cu₂S Layer Removed.	107
48.	I-V Characteristics of CdS Ceramic Solar Cells with Varying Dip Times.	109
49.	Spectral Response of Undoped CdS Ceramic Solar Cells vs. Dip Time.	111
50.	Spectral Response of Undoped CdS Ceramic Solar Cells Enhanced by White Light for Various Dip Times.	112
51.	Enhancement Curves of Undoped CdS Ceramic Solar Cells Formed in 16.7 g/ℓ CuCl Soln.	113
52.	I-V Characteristics of Undoped CdS Ceramic Solar Cells with Varying Times.	114
53.	Spectral Response of Undoped CdS Ceramic Solar Cells vs. Dip Time.	117
54.	Spectral Response of CdS Ceramic Solar Cells vs. Dip Time.	118
55.	Enhancement Curves of Undoped CdS Ceramic Solar Cells Formed in 1 g/ℓ CuCl Soln.	119
56.	IV Characteristic of Undoped CdS Ceramic Solar Cell with Varying Dip Times.	120
57.	Spectral Response of In-Doped CdS Single Crystal Solar Cell.	122
58.	Effect of One Hour Heat Treatment in Vacuum at 300°C on the Backwall Spectral Response of Cell 4-46.	123
59.	Spectral Response of Thin Film CdS Solar Cell No. B696E8.	126
60.	The Effect of Rate of Sweep (Increase of Wavelength) on the Spectral Response, Cell No. B-810D-5.	128
61.	Short Circuit Current as a Function of Wavelength, Illustrating the Effect of the Direction of Sweep.	129

<u>Figure</u>	<u>Page</u>
62. Photograph of the 1-Sun Antimonochromator.	131
63. Schematic of the One Sun Antimonochromator.	132
64. Antimonochromatic Spectral Response, CdS Thin Film Cell.	134
65. Antimonochromatic Spectral Response, In-Doped CdS Ceramic Cell.	135
66. Antimonochromatic Spectral Response, Undoped CdS Ceramic Cell.	136
67. Antimonochromatic Spectral Response, CdS Single Crystal Cell.	137
68. Proposed Method of Preparing Large Single Crystals of Cuprous Sulfide.	142
69. Comparison of Short Circuit Current vs. Angle of Incidence (~1 Sun White Radiation) and Sine Curve, Normalized so that the Maxima Coincide.	144
70. Room Temp. Properties of In-Doped Ceramic Solar Cells vs. Exposure Time at 150°C in Argon Atmosphere and Ambient Light.	166
71. High-Temperature Degradation of CdS Solar Cells Heated in Air, Exposure Temperature = 143°C.	172

Appendix Figures

1. Cu-S Phase Diagram.	185
2. Cu-S Phase Diagram in the Vicinity of Chalcocite and Digenite.	186
3. Cu ₂ S-Cu _{1.8} S Roughly According to Djurle, ⁽¹⁾ with Modifications from Ruhl and Saur. ⁽⁷⁾	188
4. Cu ₂ S-Cu _{1.8} S Roughly According to Rau. ⁽²³⁾	188
5. Cu ₂ S-Cu _{1.8} S Roughly According to Kullerud ⁽¹⁵⁾ (Cu _{2-x} S Solid Solutions Djurle ⁽¹⁾ and Rau ⁽²³⁾).	189

LIST OF TABLES

<u>Table</u>		<u>Page</u>
I.	Thickness of the Cu ₂ S Layer Determined by Chemical Analysis of Cu After Stripping with KCN, Bathocuproine Colorimetric Method.	11
II.	Principle Lines of Copper Sulfide Patterns.	22
III.	Lattice Constants of Phases Present in CdS Plates After Successive Dips in CuCl At 90°C.	24
IV.	Formation of Copper Nodules at Different Applied Voltages.	39
V.	Quantum Intensity of Solar Radiation.	146

1. INTRODUCTION

Three years of research on the operating mechanisms of the CdS thin-film solar cell are described in this report. The essential information contained in all reports previously issued under this contract has been reassembled in this report together with new results obtained during the past few months. Past interpretations of results have been reworded in some cases so as to be consistent with our latest thinking. The results of this program up to November, 1968 were summarized at the Seventh Photovoltaic Specialists Conference at Pasadena. It became evident at that time that the Clevite model for the CdS solar cell had gained considerable acceptance in most of its essential features. Some objections have been raised about specific parts of the model and alternate schemes have been advanced. These are discussed in detail at appropriate places in the report. In order to accomodate one particular objection, the Clevite model has been modified to include interface states at the $\text{Cu}_2\text{S:CdS}$ junction which act as recombination centers when the cells are forward biased. New information, not previously reported include data on the antimonochromatic spectral response of different types of cells, measurements of the threshold voltage for electrolytic deposition of copper from Cu_2S , observations on the formation of copper whiskers on Cu_2S by heating, X-ray crystallographic data on low-temperature phase transformations of cuprous sulfide, measurements of optical transmission of Cu-saturated CdS single crystals, data on the photo-conductive rise and decay times of Cu-compensated CdS, discussion of the beneficial role of oxygen in promoting the photovoltaic effect during cell fabrication, and the subsequent degrading effects of oxygen during high temperature exposure.

2. SUMMARY OF THE CLEVITE SOLAR CELL MODEL

The Clevite model of the CdS solar cell is shown in Fig. 1 in the usual form of a simplified energy-band diagram. Since the two active components of the cell, Cu_2S and CdS, have different work functions, it is necessary to know where their band edges are located with respect to a common reference level. The "vacuum level" shown in Fig. 1 serves as such a reference level. Because of the absence of direct work-function data for Cu_2S , the positions of the band edges relative to the vacuum level were chosen so as to be most compatible, in our opinion, with the observed properties of the cell. The band diagram is shown for a cell under strong illumination and with the terminals of the cell

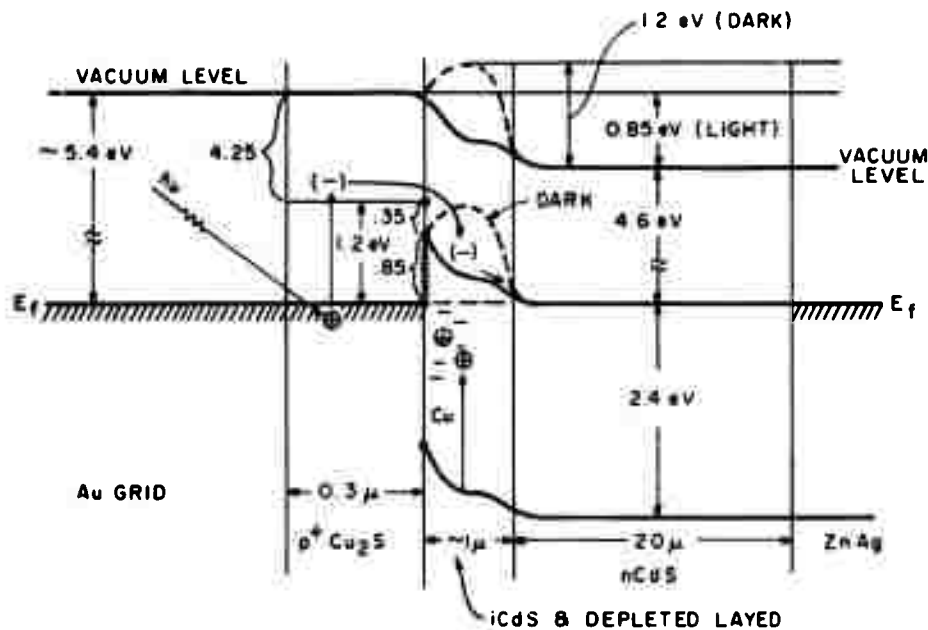


FIG. 1. ENERGY BAND DIAGRAM FOR $\text{Cu}_2\text{S}-\text{CdS}$ SOLAR CELL, ACCORDING TO THE CLEVITE MODEL.

shorted. The band diagram for the case of no illumination is quite different, as shown by the dotted lines in Fig. 1. The pertinent features of the model, which has been modified twice during the course of this study (see Section 4.3), can be summarized as follows:

1. Gold makes an ohmic contact to p- Cu_2S .
2. The ZnAg substrate electrode makes an ohmic contact to n-CdS.
3. Almost all of the light absorption occurs in a thin layer of p- Cu_2S , the highly non-planar topology of which greatly aids the absorption. The spectral response of the cell corresponds to the intrinsic absorption spectrum of Cu_2S modified by the photoconductive properties of the i-CdS layer. Cu_2S has an indirect band gap of ~ 1.2 eV.
4. The Cu-compensated i-CdS layer results from Cu diffusion during cell fabrication. The layer is insulating in the dark but becomes appreciably conducting when it is illuminated through the Cu_2S by sunlight. The quasi-Fermi level for electrons moves upward close to the conduction band during illumination, making it act like weakly n-type CdS. The layer possesses the typical photoconductive properties of Cu-compensated CdS.
5. When the cell is illuminated with sunlight, the principal photo voltaic junction occurs between the Cu_2S and the i-CdS, the space charge being located almost entirely on the i-CdS side. The electrostatic barrier height is ~ 0.85 eV.
6. In the dark, the principal junction occurs between the i-CdS and the n-CdS. The electrostatic barrier height is ~ 1.2 eV. A small junction of reversed polarity occurs between the p- Cu_2S and i-CdS layers. The barrier height is ~ 0.35 eV. This barrier disappears when the cell is illuminated.
7. Under forward bias, recombination occurs principally at interface states at the p- Cu_2S :i-CdS junction, although recombination also occurs in the bulk and on the illuminated surface of the Cu_2S layer.
8. Cu_2S at room temperature has a small but significant ionic mobility, which increases with increasing temperature.

9. The stoichiometry and crystal structure of the Cu_2S layer as well as its electrical and optical properties are affected by exposure to air, especially at high temperature due to reaction with oxygen.

The validity of most of these points will be discussed in detail later. For purposes of orientation a qualitative description of what happens in the cell when it is exposed to sunlight will be presented first.

All photons with energy less than 1.2 eV pass through the Cu_2S layer without appreciable absorption. These photons likewise pass through the i-CdS and the n-CdS and are reflected or absorbed in the metallic ZnAg electrode. The indirect band gap of the Cu_2S requires the absorption coefficient of photons with energy greater than 1.2 eV to rise rather slowly with increasing photon energy (similar in this respect and in band gap to Si). This property and the small thickness of this layer ($\sim 0.3 \mu$) allows a small but appreciable number of photons having energies between 1.2 eV and ~ 2.4 eV to pass into the i-CdS layer such that the absorption of some of these induces a substantial photoconductivity in the i-CdS layer making it behave like weakly n-type CdS. The majority of the photons in this energy band, however, are absorbed in the Cu_2S layer, as are the photons having greater energy.

The majority of the hole-electron pairs are thus generated in the Cu_2S layer, the more energetic photons being absorbed closer to the illuminated surface. The electrons are the minority carriers in the $\text{p}^+\text{Cu}_2\text{S}$ and these must diffuse to the Cu_2S -i-CdS interface--the indirect band structure of Cu_2S and its crystallized state apparently allowing a relatively large minority-carrier lifetime (again similar to Si). The electrons entering the i-CdS are collected by the electric field in this region, which in turn is dependent on the loading condition of the cell. The minority electrons are thus collected into the "friendly" n-type layer and pass eventually into the ohmic ZnAg electrode.

As each photogenerated electron leaves the Cu_2S layer into the i-CdS layer, a corresponding photogenerated hole is annihilated at the ohmic gold electrode by an incoming electron. The lateral collection of holes over the relatively large distances between the gold grids is easily accomplished since the holes are the majority carriers in $\text{p}^+\text{Cu}_2\text{S}$.

Recombination occurs in the bulk and at two surfaces of the Cu_2S

That the recombination losses are amazingly low under short circuit conditions is inferred by nearly unity quantum efficiency observed for high output cells in the band 0.5 to 0.9 μ . Under forward bias, the decrease of the external current arises from a corresponding increase in the recombination rate at the $\text{Cu}_2\text{S}:\text{CdS}$ interface, the interface states acting as fast recombination centers.

The diminished response at photon energies beyond 2.4 eV occurs (again, as in Si cells) because the higher absorption coefficients for these photons require the generation of hole-electron pairs to occur increasingly closer to the illuminated Cu_2S surface--and consequently the recombination rate is higher due to (1) higher density of free carriers in excess of equilibrium values, and (2) their increased proximity to surface recombination centers.

The Clevite model for the CdS solar cell* is compatible with the following experimental observations:

1. The low-energy threshold of photovoltaic response occurs at 1.2 eV (the band gap of Cu_2S).
2. With increasing Cu_2S thickness, the short circuit current increases to a maximum and then decreases to low values, the "blue" response reaching a maximum before the "red" response (a steady rise in absorption is offset by a steady increase in recombination losses in the Cu_2S layer, and the absorption coefficient of red light is lower than that of blue light).
3. The enhancement of "red" response by "green" light bias (activation of photoconductivity in the i-CdS layer).
4. The decrease of "green" response by infrared light bias (quenching of photoconductivity).
5. Transient effects in spectral response measurements with time constants of the order of seconds (rise and decay of photoconductivity).

*While the cell is now known to be a $\text{Cu}_2\text{S}:\text{CdS}$ solar cell, we retain the name "CdS solar cell" for simplicity and for historical reasons.

6. The appearance of effects (3), (4) and (5) only after heating of the cell (formation of i-CdS layer by Cu diffusion).
7. Capacitance of cells decreases by additional heat treatment (further growth of the i-layer).
8. The dark IV curve crosses the light IV curve in such a way that the barrier in the dark appears to be about 0.35 eV larger than that in the light (barrier height changing from 1.2 eV in the dark to 0.85 eV in the light).
9. Indium doping of the n-CdS layer causes the enhancement spectrum to shift towards longer wavelengths (Cu-compensated In-doped CdS has photoconductive response that extends to much longer wavelengths).
10. Slow shifts of points on the IV curve during constant-current or constant voltage measurements (migration of Cu in the Cu₂S layer, deposition of Cu in some cases).
11. Formation of Cu nodules during open-circuit operation of the cell (electrodeposition of Cu from the Cu₂S onto metallic shorts).
12. High resistance of uncovered cells to electron and proton irradiation damage, and high damage recovery rate at 150°C (annealing of damage in the Cu₂S layer due to high Cu mobility).
13. Improvement in short-circuit current by etching of CdS layer before forming Cu₂S layer (formation of Cu₂S in grain boundaries--improving light absorption).
14. Improvement in squareness of IV curves upon heat treatment (loss of abrupt pCu₂S:n-CdS junction by growth of i-layer with consequent loss of tunnelling, shunting paths).
15. Strong irreversible decrease in short-circuit current when cell is heated at 150°C in air (oxidation of Cu₂S causing increase in recombination rate and/or changes in stoichiometry resulting in decreased optical absorption).
16. Slow, irreversible increase in series resistance of cells heated in vacuum or inert gas at > 150°C (growth of i-layer by Cu diffusion).

17. Drastic reduction of effect (16) by donor doping of the CdS layer (greater diffusion of Cu needed to compensate n-CdS, and greatly improved photoconductive sensitivity of i-layer at longer wavelengths).
18. The highest measured open-circuit voltage of high efficiency cells at 4°K and ~ 5 sun illumination is ~ 0.8 volts (under these conditions, internal barrier of 0.85 eV is approached).

These correlations, we believe, establish a strong base of plausibility for the Clevite model. Some objections to the model and some non-conforming results have been raised by workers at other laboratories. These are discussed in considerable detail in Section 4. We believe that most of the objections and inconsistencies have been satisfactorily overcome.

In the following sections, experimental data taken over the past three years on specific aspects of the CdS solar cell are presented. The essential results of these studies have been summarized above. A more detailed presentation of the properties of the cell and its components now follows. We begin with a short review of the construction and micro-structure of the cell.

3. EXPERIMENTAL RESULTS AND ANALYSIS

3.1 Brief Review of the Construction and Structure of the CdS Cell

A cross-section of a typical thin-film solar cell is shown in Fig. 2. The substrate consists of 1 mil Kapton coated with a thin layer of powdered Ag dispersed in Pyre-ML (partially polymerized Kapton). After curing the Ag:Pyre-ML layer, a thin layer of Zn is electroplated onto the Ag layer. During cell processing, the Zn and Ag react to form a ZnAg phase (see Section 3.7.1). The darkness of this layer seen in Fig. 2 resulted from atmospheric corrosion of the Ag. For fresh cross-sections this layer is very bright.

The n-CdS layer is vacuum deposited to a thickness of about 1 mil and is composed of individual crystallites ~ 1 - 3 μ in diameter. The crystallites are elongated the full thickness of the film and the crystallites are highly oriented with the c-axis perpendicular to the substrate (see Section 3.4). Etching of the cell in aqueous HCl removes some of the surface and exaggerates the unevenness of the surface by preferential etching at the grain boundaries. The cells are then dipped in a Cu⁺ ion solution which converts a thin layer of

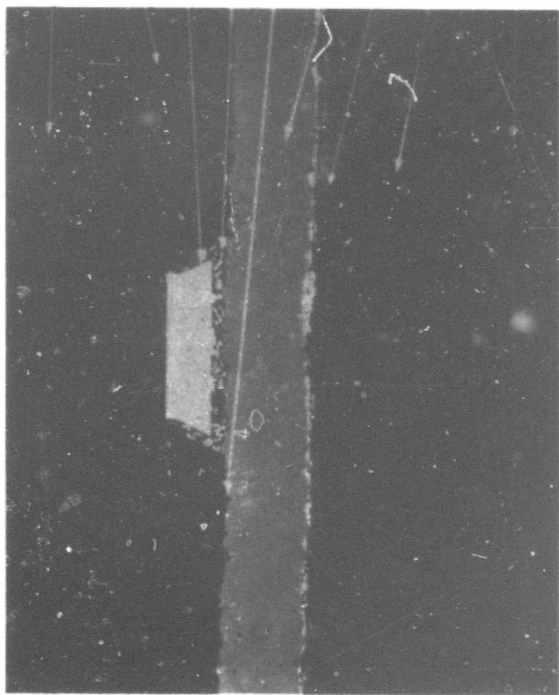
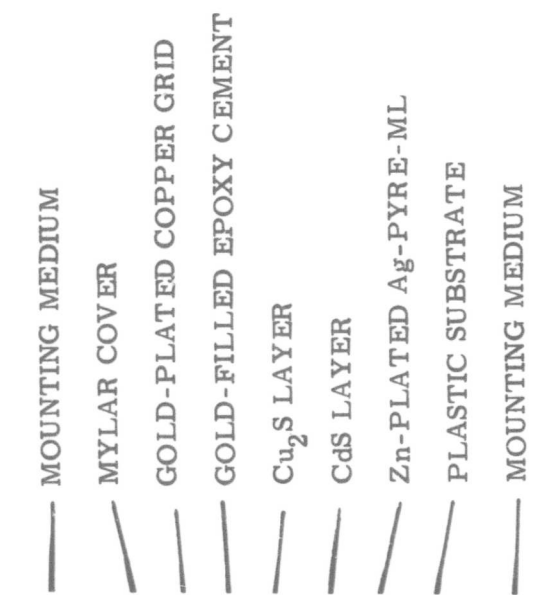


FIGURE 2. TRUE-VIEW CROSS-SECTION OF A STANDARD CdS SOLAR CELL (500X).

the exposed CdS surface to Cu_2S . This layer can be seen in Fig. 2, as a thin white line on the surface of the CdS and partially penetrating the grain boundaries. After the Cu_2S layer is formed the cell is heated in air for about 2 min. at 250°C. The conductivity of the Cu_2S layer is increased by this treatment (see Section 5.3). The Cu_2S layer is then contacted with a gold-plated copper grid (0.5 mils thick) using a gold-filled epoxy cement. A single grid section is shown in the photograph. There are 60 such grid lines per inch perpendicular to the terminal tabs of the cell and 10 grid lines per inch parallel to the terminal tabs.

After curing of the grid cement, a 1 mil cover plastic of Kapton or Mylar is laminated over the grid using a 0.5 mil layer of β -stage epoxy precoated on the cover plastic. The gridding, laminating, and curing processes expose typical cells to a total of ~ 2 hrs. at $\sim 200^\circ\text{C}$ and about 30 hrs. at $\sim 130^\circ\text{C}$, all in vacuum environments. These treatments and the 2 min. exposure in air at 250°C cause the formation of the i-CdS layer.

Additional details about the fabrication, structure, and performance of the CdS solar cell can be found in an article by Shirland.⁽¹⁾

3.2 The Cuprous Sulfide Layer

Since the Cu_2S layer plays such an important role in the operation of the cell, a considerable effort has been expended in studying the properties of this compound. The epitaxial formation of chalcocite on CdS was recognized fairly early in the study. Very recently, however, we have discovered that chalcocite, even at room temperature, undergoes transformation to djurleite, and at higher temperatures to other, often confusing, structures. Thus, it is not at all clear at this point what form of cuprous sulfide actually exists in normal CdS solar cells. Therefore, in most of this report, the formula Cu_2S is used generically, and unless the composition or structure is specifically under discussion, it is to be interpreted as an unspecified form of cuprous sulfide.

3.2.1 Thickness and Topology of the Cu_2S Layer

The thickness of the Cu_2S layer on typical thin-film cells was obtained by dissolving off all of the Cu_2S on known areas with dilute KCN and analyzing the solutions colorimetrically⁽²⁾ for copper. Control experiments indicated an absolute accuracy of about 1% for the quantities of Cu

involved. The average thickness was found to be $0.35 \pm .1$ microns for typical cells. True variations in the average thickness of Cu_2S among nominally identical cells and also among different parts of 3" x 3" cells amounted to $\sim 0.1 \mu$. A somewhat wider spread ($0.38 \pm 0.15 \mu$) was found for cells produced in different evaporators on different substrates and at different times, as shown in Table I. Although recent cells have not been measured, the lower spread in I_{sc} indicates that the Cu_2S thickness is now more uniform than those of earlier cells. The average thickness was computed using the nominal cell area (usually 1.00 cm^2) that was stripped of Cu_2S . Since the actual surface is very non-planar, the true Cu_2S area is about 3 times the cell area, and the local thickness of Cu_2S is correspondingly thinner than the average thickness computed for planar geometry. The average thickness nevertheless is the more relevant quantity since almost all of the Cu_2S participates in light absorption, including the Cu_2S that partially penetrates the grain boundaries of the CdS layer. The light not only enters the Cu_2S obliquely, which corresponds to a larger absorption length, but much of the light that penetrates the Cu_2S layer is directed by strong refraction at the initial surface to laterally situated "walls" of Cu_2S in the grain boundaries and has second and third chances of being absorbed. We note that the Cu_2S layer is electrically continuous so that this secondary absorption still contributes to the collected current. The important point here is that while the absorption thickness is much greater than the actual thickness, the distance that the minority carriers must diffuse is no larger than the actual Cu_2S thickness, the collecting junction being equally non-planar and parallel to the Cu_2S layer. This mechanism helps to explain a peculiar observation of long standing about single-crystal solar cells: The current output is qualitatively proportional to the degree of coarseness of abrasion of the crystal surface. Very smooth surfaces yield the lowest currents and very coarsely sanded surfaces (always followed by an HCl etch) yield the highest currents. The HCl etch itself makes a major contribution to the "roughness" of CdS film cells, a result independently confirmed by Palz, et al.⁽³⁾ The high short-circuit currents obtained with ceramic solar cells (Section 3.6) is likewise attributed to the tortuous convolutions of their surfaces which is even greater than that in the thin-film cells.

Table I. Thickness of the Cu_2S Layer Determined by Chemical Analysis of Cu After Stripping With KCN, Bathocuproine Colorimetric Method.

<u>Cell No.</u>	<u>Date of Preparation</u>	<u>$\mu\text{g Cu/cm}^2$</u>	<u>Cu_2S Thickness (μ)</u>
D 358C	7/ 6/66	189	0.41
D 594F	5/23/67	237	0.51
A 891C	1/12/67	245	0.53
A 951A	6/ 7/67	126	0.27
N 5A5	3/16/67	106	<u>0.23</u>
			0.38 ± 0.15

Notes:

1. D 358C and D 594F: NRC vertical evaporator, Ag Pyre ML on Kapton substrate, Zn interlayer.
2. A 891C: Veeco vertical evaporator, copper substrate, Zn interlayer.
3. A 951A: Veeco vertical evaporator, brass substrate, Al interlayer.
4. N 5A5: NRC horizontal evaporator, Ag Pyre ML on Kapton substrate, Zn interlayer.

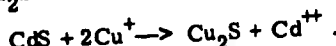
All cells pre-etched in 3:2 (conc. $\text{HCl:H}_2\text{O}$) and 5 sec in standard Cu^+ solution at 90°C.

True view cross-sectional photomicrographs of thin film cells dipped for 0, 5, 10, and 20 seconds in a Cu^+ solution at 90°C are shown in Fig. 3. The more reflective Cu_2S layer, a few tenths of a micron in thickness, is clearly seen on the surface of the CdS on the three cells that were exposed to the Cu^+ solution, but only a very faint hint of something similar can be detected on the undipped cell. We notice that the HCl etch which is used prior to dipping in the Cu^+ solution causes a preferential attack of grain boundaries. Considerable variation of the severity of this attack can be seen among the cells. However, the most significant thing shown in these photographs is the formation of the Cu_2S not only on the exposed CdS surface but within the grain boundaries. The cell dipped for 20 seconds, in particular, shows a deep penetration of the Cu_2S . The branching structure suggests a delineation of grain boundaries. Local penetration of the Cu_2S to the metallic substrate is the probable cause of shorting in cells dipped for too long a time. This effect puts a limitation on the minimum thickness of CdS that can be employed. The uneven thickness of the Ag-Pyre ML layer seen in Fig. 3 has been substantially improved in cells of more recent vintage.

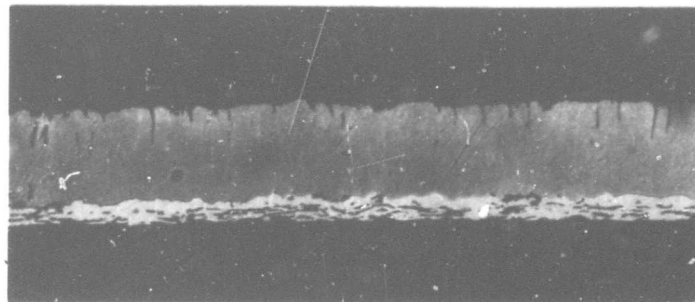
An earlier measurement⁽⁴⁾ of the Cu_2S thickness (0.59 μ) obtained on a graded-thickness specimen of CdS that had been partially converted to Cu_2S is now known to be too large because the effects of grain-boundary penetration were not properly taken into account. Further discussion of the thickness of the Cu_2S layer is given in Section 4.1.

3.2.2 Formation of Cu_2S on CdS Single Crystals

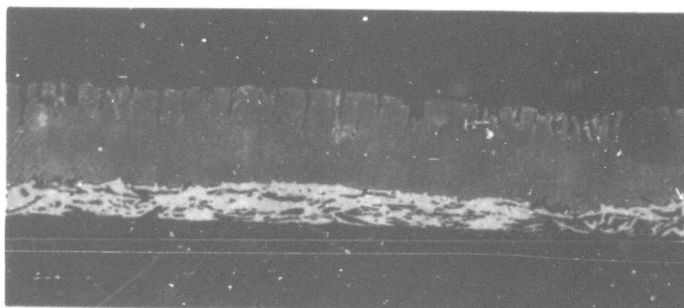
When a CdS single crystal is exposed to a Cu^+ solution at 90°C, a surface film of Cu_2S develops. On chemically polished CdS surfaces, the film forms immediately and appears under 25X magnification to be continuous after a few seconds in the solution. The sides of the hexagonal etch pits on the (0001) surface of deeply etched CdS, however, are not immediately coated with Cu_2S but rather require several minutes before they are covered by lateral extension of the adjoining Cu_2S film. In either case, after the surface is covered, the Cu_2S film thickens with time according to the reaction:



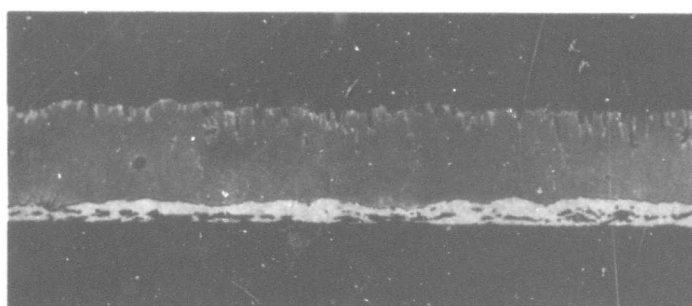
The molar volume of Cu_2S being ~ 9% less than that of the CdS places the Cu_2S



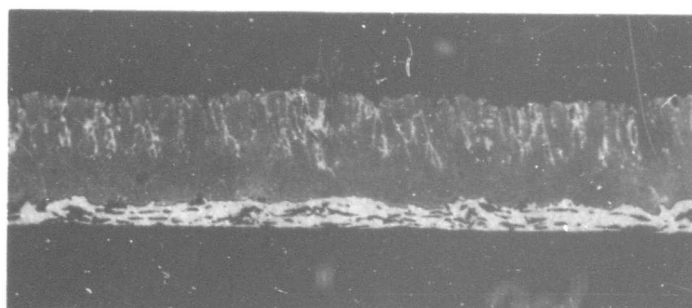
0 SEC.



5 SEC.



10 SEC.



20 SEC.

FIGURE 3. TRUE-VIEW CROSS-SECTIONS OF CdS CELLS ETCHED IN HCl AND EXPOSED TO STANDARD Cu^+ SOLUTIONS FOR DIFFERENT TIMES.

BLANK PAGE

film in tension (a thin platelet of CdS exposed to the solution in one side only develops a tight curl with the Cu_2S layer on the concave side). The severe stresses eventually cause the formation of a multitude of fine cracks to develop in the Cu_2S film (Figs. 8-10). The adhesion between the Cu_2S and the CdS substrate remains strong at all times. Before cracking occurs, the reaction must proceed by diffusion of Cu^+ and Cd^{++} ions through the solid Cu_2S film. The Cu^+ ions react with $\text{S}^=$ at the $\text{Cu}_2\text{S}:\text{CdS}$ interface while the displaced Cd^{++} ions diffuse back to the solution preserving overall as well as microscopic electroneutrality. Cracking of the Cu_2S film allows the solution to flow into the cracks and accelerates the reaction at these points, at least temporarily. As the Cu_2S film thickens on all surfaces, the stress in the underlying CdS also increases in a complex manner such that cracks also develop in it. When the volume of Cu_2S approaches and then exceeds the volume of the remaining CdS, the macroscopic stress distribution reverses and the CdS goes into tension, and hence easily cleaves. Crystals of CdS 1 cm^2 in area and 1 mm thick have been completely converted to pseudo single crystal Cu_2S . The resulting Cu_2S usually remains intact despite the fact that it is riddled with fine cracks. Occasionally, macroscopic cleavage of a CdS crystal causes complete parting of the specimen during the conversion process. In regard to the thin Cu_2S layers on solar cells, it cannot be decided at this time whether cracking occurs. See Section 3.7.2.1 for more information on conversion of CdS to Cu_2S .

3.2.3 Electrical Properties of Cu_2S

The thermoelectric potential of Cu_2S at 25°C was measured with a simple apparatus consisting of a differential thermocouple and a Keithly 150B micro-voltmeter. A thin plate of Cu_2S was glued between two brass blocks, one being the heat source and the other the sink. Indium wires were soldered to two points on the Cu_2S plate. The two junctions of the differential thermocouple were electrically insulated with a thin plastic coating and were spring-loaded against the specimen at the indium connections. Good thermal contact was obtained by putting a drop of silicone grease over each thermocouple junction and indium connection.

With this apparatus, the thermoelectric potential of a crystalline specimen of Cu_2S (fully converted from CdS as described in the

previous section) was found to be $76.5 \mu\text{V}/\text{C}^\circ$. The sign of the thermoelectric power (cold junction positive) showed that the Cu_2S was p-type, as expected from earlier references. The electrical resistivity, by 4-probe measurement, was $2 \times 10^{-2} \Omega \text{ cm}$.

The specimen was then heated to 250°C in air for 2 minutes. After heat-treatment, the average thermoelectric potential was $49.4 \mu\text{V}/\text{C}^\circ$ at 27°C and $\sim 84 \mu\text{V}/\text{IC}$ at 38°C . The electrical resistivity decreased, measuring $9.0 \times 10^{-3} \Omega$ after heat-treatment. This change indicates a reaction in air (probably with oxygen) and it is likely that this reaction is partially responsible for the development of photovoltaic response in the thin-film cells following the standard "heat shot" at 250°C for 2 minutes. This treatment at least lowers the series-resistance contribution of the Cu_2S layer. Detrimental effects of over-heating in air are discussed in Section 5.3. Resistivity measurements on other Cu_2S crystals gave similar results. The lowest resistivity measured was $3 \times 10^{-3} \Omega \text{ cm}$. Other workers have reported Cu_2S as a degenerate p-type semiconductor having hole concentrations⁽⁵⁾ of 10^{19} to 10^{20} cm^{-3} and hole mobilities^(5, 6) of 10 to $25 \text{ cm}^2/\text{V sec}$, which correspond well to the range of resistivities quoted above.

3.2.4 Optical Properties of Cu_2S

Optical transmission measurements were carried out on thin Cu_2S films vacuum deposited on Pyrex substrates and on thin layers of Cu_2S formed on polished CdS crystals. The original data and the methods of analysis by which the absorption coefficients and the refractive indices were obtained are given in Ref. 4. Film thicknesses were determined interferometrically and by direct chemical analysis for copper. The data were corrected for reflection losses and, in the case of the converted layers, for light scattering at the Cu_2S -CdS interface. The results are summarized in Figs. 4 and 5, the latter containing earlier published results. The absorption coefficients derived from Sorokin et al's⁽⁷⁾ transmission measurements are about an order of magnitude too low, resulting perhaps from an error in film thickness or a strong deviation in film stoichiometry. Our results on vacuum deposited film, likewise, are noticeably low, probably due to a deviation in film stoichiometry and, perhaps, to the presence of very small pinholes in the film. The detailed results of Marshall and Mitra,⁽⁸⁾ shown highly

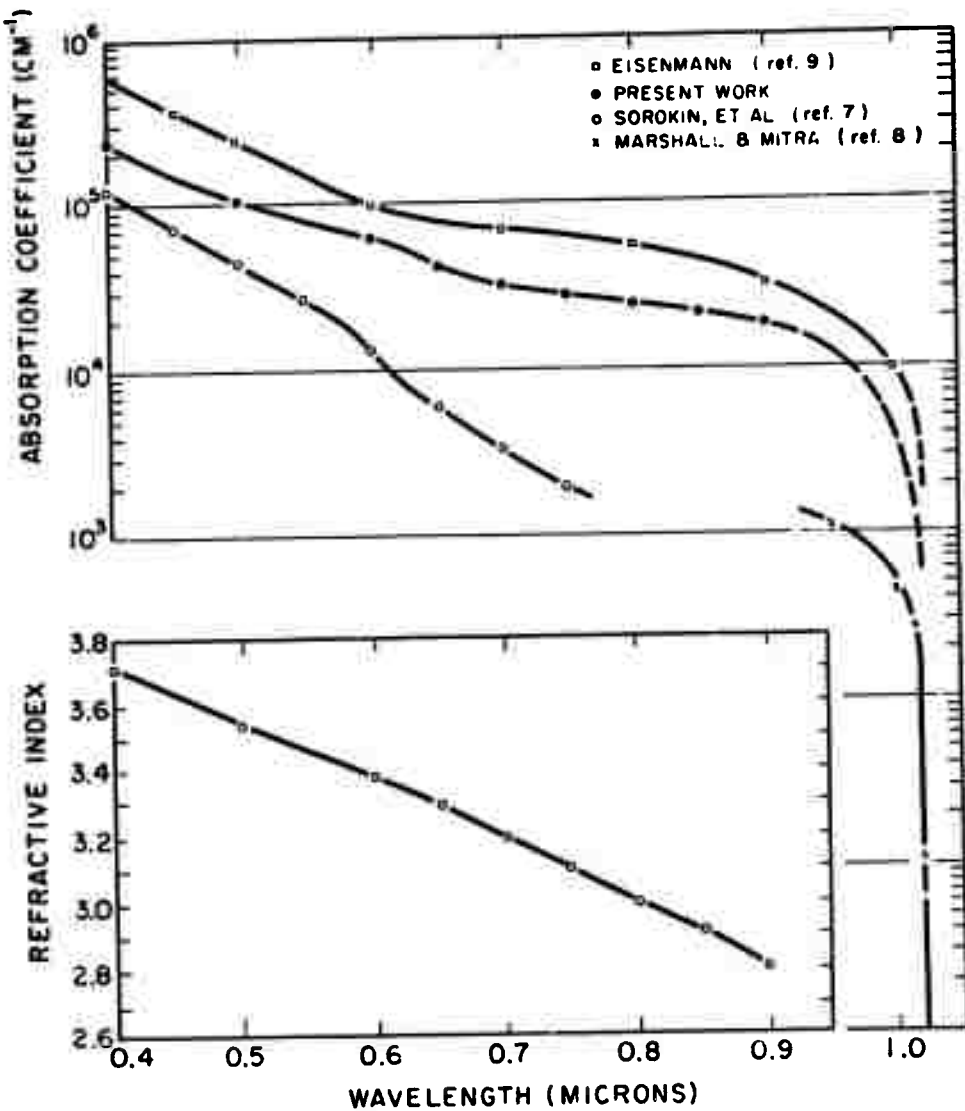


FIG. 4. ABSORPTION COEFFICIENT AND REFRACTIVE INDEX OF VACUUM EVAPORATED Cu_2S THIN FILMS.

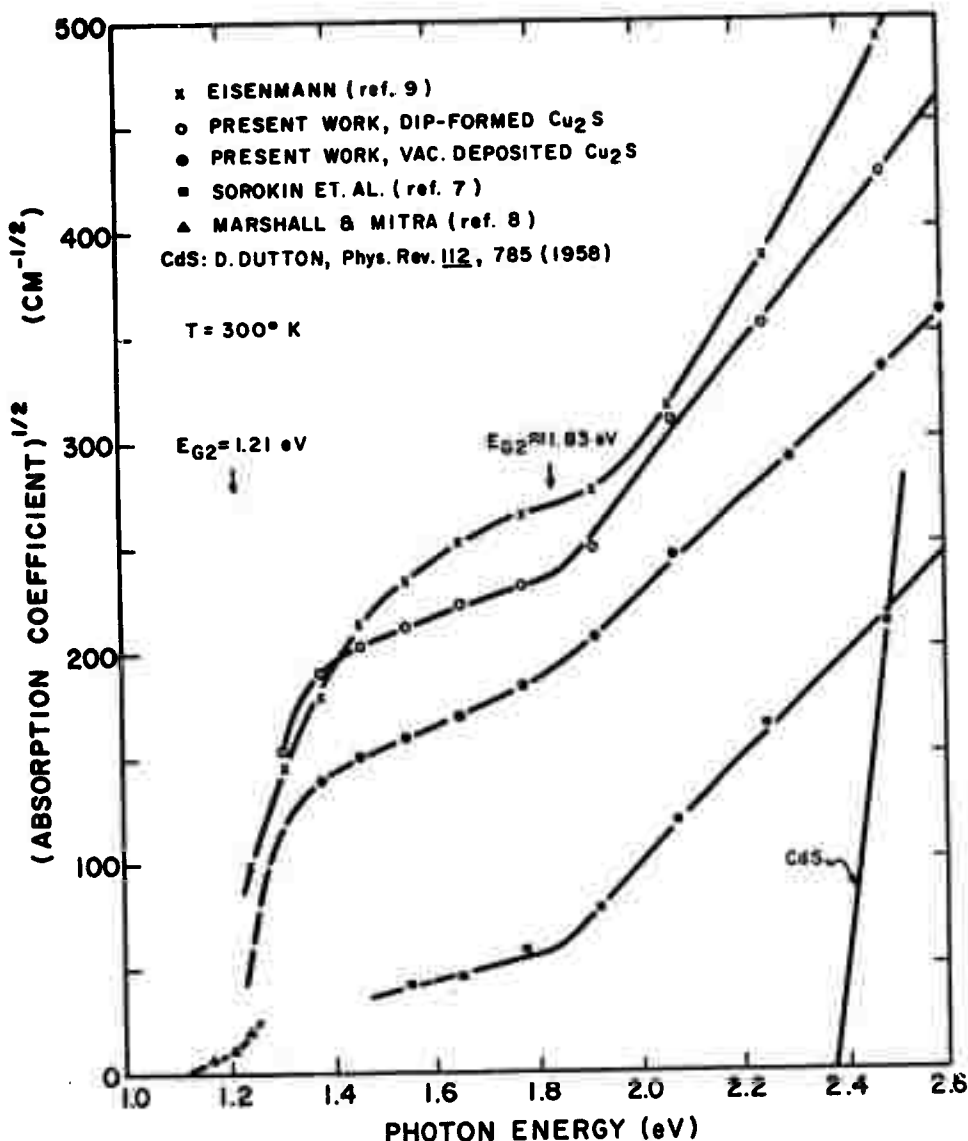


FIG. 5. SQUARE ROOT OF ABSORPTION COEFFICIENT OF Cu_2S AS A FUNCTION OF PHOTON ENERGY.

compressed in Fig. 5, clearly indicate an indirect band gap at ~ 1.2 eV. Our results also indicate a band edge at this energy. In addition, all of the curves indicate a second band edge at ~ 1.8 eV which probably represents the threshold for direct optical transitions.

The refractive index data shown in Fig. 4 were derived by an indirect and rather inaccurate method and are therefore only approximations. An accuracy between ± 5 and $\pm 10\%$ is estimated.

3.2.5 Calculated Quantum Absorption Efficiency in Cu_2S

The optical absorption coefficients obtained from the transmission measurements on dip-formed Cu_2S on single crystal CdS substrates were then used to calculate the quantum absorption efficiency at different wavelengths and Cu_2S thicknesses. The results are shown in Fig. 6. Similar curves using the absorption coefficients obtained from the transmission measurements on vacuum deposited layers of Cu_2S on Pyrex substrates are shown in Fig. 7. For comparison, one curve for $\text{Si}^{(10)}$ (thickness = 2×10^{-4} cm and minority carrier diffusion lengths = 8×10^{-4} cm) is presented together with a normalized solar photon spectrum. It is evident that the absorption is much stronger in Cu_2S than in Si; and hence a much thinner layer of Cu_2S is sufficient to absorb the same fraction of solar radiation. The fractional change of absorption with wavelength, on the other hand, is similar for Cu_2S and Si. For the thickness of Cu_2S shown, the absorption efficiencies are seen to be very high, in agreement with the high quantum efficiencies calculated from observed short-circuit currents. The drop-off at the longer wavelengths can be reduced only by using thicker layers of Cu_2S , but this, in turn, increases the recombination losses. A compromise must be made between these two effects and also with the effect of Cu_2S thickness on the amount of light that can reach and induce photoconductivity in the i-CdS layer.

The absorption efficiencies were calculated on the basis of planar geometry. It is apparent from the earlier discussion that the average or effective thickness of the Cu_2S layer is the appropriate value to use in planar calculations even though the actual, local, thickness is substantially smaller. The thicknesses shown in the figures encompass the average thicknesses measured on typical high-output cells.

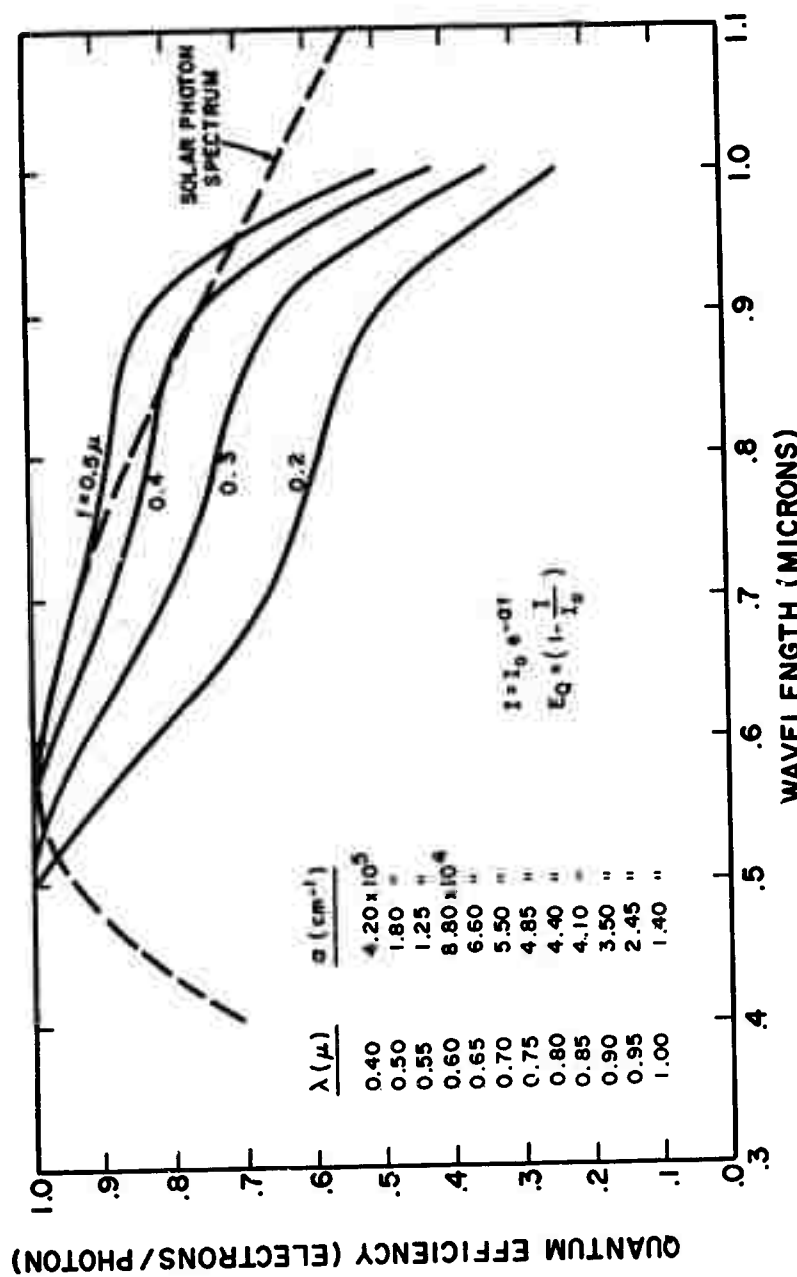


FIG. 6. QUANTUM ABSORPTION EFFICIENCY FOR Cu_2S AT DIFFERENT WAVELENGTHS AND Cu_2S THICKNESSES. PLANAR (ONE DIMENSIONAL) GEOMETRY. ABSORPTION COEFFICIENTS FROM DIP-FORMED FILMS.

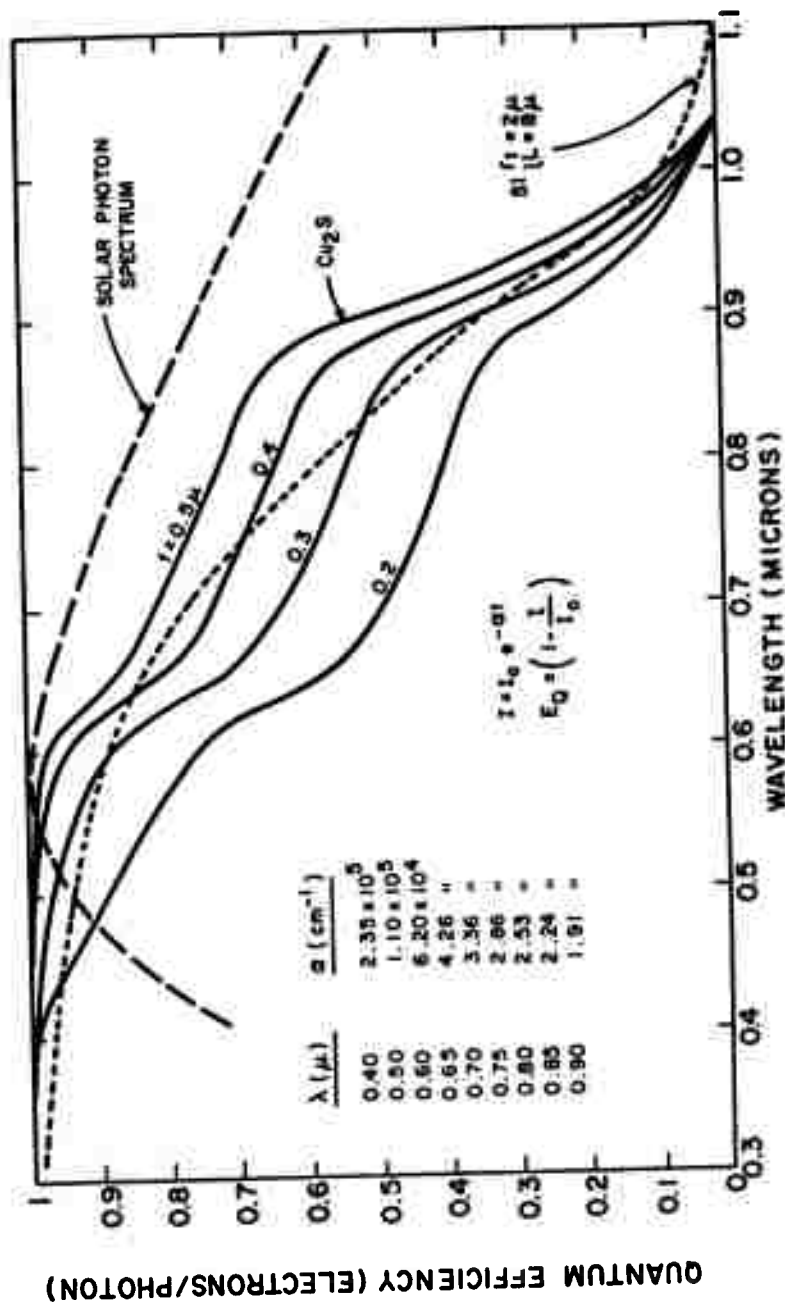


FIG. 7. QUANTUM ABSORPTION EFFICIENCY FOR Cu_2S AT DIFFERENT WAVELENGTHS AND Cu_2S -THICKNESSES, PLANAR (ONE DIMENSIONAL) GEOMETRY. ABSORPTION COEFFICIENTS FROM EVAPORATED THIN FILMS.

The best cells have efficiencies of ~ 7% (including single-crystal backwall cells). This efficiency applies to sunlight (air mass = 1) at 25°C and is calculated as the ratio of maximum electrical power output to total incident radiant power input. The incident power includes that falling on grids and includes all wavelengths of the solar spectrum. We would like to know the efficiency of present cells with regard to only those wavelengths to which the cell responds and with respect to the radiant power (in this bandwidth) that actually enters the cell. One sun = 0.1 W/cm², but (from Table V) only 62% of this power lies in the wavelength band, 0.45 to 0.97 μ , to which the cells respond strongly. Since 10% of the light is lost on the grid and ~ 15% is lost by reflections from the Cu₂S-plastic + air-plastic interfaces, the internal power efficiency in the responsive band is

$$\text{Eff}_{(\text{power})} = 7 \times \frac{1}{0.62} \times \frac{1}{0.90} \times \frac{1}{0.85} = 14.8\% .$$

Since the average photon energy in this wavelength band is ~ 1.90 eV, and electrons are delivered from the cell at ~ 0.37 V (max. power point), the internal quantum efficiency is:

$$\text{Eff}_{(\text{quantum})} = \frac{1.90}{0.37} \times \text{Eff}_{(\text{power})} \approx 76\% .$$

Since some wavelengths, e. g., ~ 0.52 μ , are more efficient than that averaged over the whole band, the internal quantum efficiency at these wavelengths must be very close to 100%. This tells us that the present efficiency is limited principally by the lack of response at the long and short wavelength parts of the solar spectrum. The power efficiency is much lower than the quantum efficiency due to the large (4 to 1) mismatch between the energy of the effective photons and the potential at which the free carriers are delivered from the cell.

3.2.6 Stoichiometry of Dip-Formed Cu₂S

During the conversion of large amounts of CdS to Cu₂S in the Cu⁺ dipping process, a considerable amount of excess, undissolved CuCl must be present in order to insure that complete conversion takes place. During the course of the reaction the decrease in the amount of this excess CuCl can be clearly followed. By starting with a solution just

saturated with CuCl at 90°C and then adding a calculated amount of excess CuCl that is chemically equivalent to the amount of CdS that is to be converted, the progress of the reaction can be followed quantitatively by measuring the amount of CuCl remaining at any given time. However, we have used this technique merely as a qualitative guide. Nevertheless, in two experiments, data were obtained on the initial and final weights of CdS and Cu₂S from which the deviation in the stoichiometry of the Cu₂S could be estimated. In the first experiment, five single crystal plates of CdS having thicknesses slightly less than 1 mm and having a total weight of 2.0480 g were completely converted to Cu₂S by a 10-day exposure to the Cu⁺ solution at 90°C. About 3 mg of CuCl in excess of the theoretical amount needed was used and a residue of about this amount was present during the last three days of exposure, indicating that the reaction was complete after 7 days. After thorough rinsing in continuously deionized water and drying at 83°C, the Cu₂S was found to weigh 2.2582 g. The calculated theoretical weight of stoichiometric Cu₂S is 2.2559 g or 0.0023 g less than that measured. Expressed another way, the formula derived from this experiment corresponds to Cu_{2.0025}S. In the duplicate run, the derived formula was Cu_{2.0073}S. Possible reasons for this apparently high Cu content are incomplete rinsing of the crystals and the presence of a small concentration of Cd⁺⁺ in the Cu₂S. Additional discussion of changes in stoichiometry during prolonged exposure to air at room temperature and during heating in air or vacuum will be found in the following section and in Section 5.3.

3.2.7 X-Ray Crystallography and Epitaxial Orientation of Cu₂S

Over the past two years a number of experiments have been performed on copper sulfide which has been converted from CdS in order to elucidate the structural relationships involved in the solar cells. Experiments fall into three classes: those done on large single crystals, those done on small needle-like crystals, and those done on powders.

The first thing that is needed is a well-identified pattern of the various phases with proper intensities. X-ray patterns are available for most of the known materials, but they are not indexed in all cases (which helps check that they are single phase) and in other cases the relative intensities are unreasonable. In Table II are given powder patterns of all the

TABLE 8. PRINCIPAL LINES OF COPPER SULFIDE PATTERNS

presently known phases, with Miller indices and intensities. The patterns are aligned to put similar spacings near each other. Very weak lines, of which there are a tremendous number, are left out. The data are taken from the ASTM powder data file, with intensities, d-spacings, and Miller indices modified to conform with our own experience as well as other powder patterns in the literature such as for djurleite⁽¹¹⁾ and Cu_{1.92}S⁽¹²⁾. The Cu_xS pattern was from a rotation pattern and must therefore be regarded as incomplete; some of the strong lines may be missing. Lattice constants and other data on the copper sulfide phases are given in the Appendix.

3.2.7.1 Studies on Large Crystals; Growth Rate of Cu₂S Layer

Three large crystal plates ($> 1 \text{ cm}^2$ area) of CdS were cut and chemically polished with the (0001), (1010), and (1120) axes respectively perpendicular to the surface. Two of the three plates were initially oriented within 10° of the crystal plane and the orientation of the third one, (1120), was within 30°. The lattice constants were determined by plotting the lattice constant calculated from various orders of the reflection versus the Nelson-Riley function.⁽¹³⁾ The plates were then dipped for successively longer times in CuCl solution at 90°C and the CdS and Cu₂S lattice constants were determined. While it appears that the Cu₂S lattice constants may shift slightly with increasing dip times (Table III), it is also possible that this is merely an instrumental factor due to the changed depth of Cu₂S contributing to the x-ray pattern. The lattice constants of the Cu₂S resulting from dipping are thus $a = 11.848 \pm .002\text{A}$, $b = 27.330 \pm .005\text{A}$, and $c = 13.497 \pm .003\text{A}$, which results in a density of $5.803 \pm .003 \text{ g/cm}^3$. The molar volume of stoichiometric Cu₂S is $27.424 \pm .016 \text{ cm}^3/\text{mole}$, whereas for CdS it is $29.980 \pm .005 \text{ cm}^3/\text{mole}$, which differs by about 8.9%.

It should be noted that each Cu₂S axis is equivalent to only one CdS direction. This is in contradiction to Singer and Faeth⁽¹⁴⁾ who found that although $a_{\text{Cu}_2\text{S}}$ usually corresponded to a_{CdS} , a lesser amount of $b_{\text{Cu}_2\text{S}}$ was also observed. Over an area of at least 0.5 cm^2 only one Cu₂S orientation was observed for each of the plates in our crystals. The misfit along the c axis was small, with the Cu₂S lattice constant exceeding twice the c lattice constant of CdS by 0.40%. The misfit along a is 4.5%, with a_{CdS} larger than $\frac{a}{3}$ for Cu₂S. The misfit along b is 4.8%, with $(10\bar{1}0)_{\text{CdS}}$ larger than

Table III. Lattice Constants of Phases Present in CdS Plates
After Successive Dips in CuCl At 90°C.

Phases	(0001) CdS Plate			(1010) CdS Plate			(1120) CdS Plate		
	Total Dip Time (min.)	Lattice Constants (A)		Total Dip Time (min.)	Lattice Constants (A)		Total Dip Time (min.)	Lattice Constants (A)	
CdS	0	c = 6.7179 + 0.0006		0	a = 4.1378 ± 0.0003		0	*	
CdS	10.6	c = 6.7177 ± 0.0006		15	a = 4.1370 ± 0.0007		15	*	
Cu ₂ S	10.6	c = 13.4900 ± 0.0015		15	b = 27.31 ± 0.03		15	a = 11.84 ± 0.01	
CdS	15.8	c = 6.7183 ± 0.0006		45	a = 4.1360 ± 0.0005		45	a = 4.1377 ± 0.0005	
Cu ₂ S	15.8	c = 13.4944 ± 0.0015		45	b = 27.333 ± 0.002		45	a = 11.875 ± 0.015	
CdS	21.8	c = 6.7170 ± 0.0007					90	a = 4.1371 ± 0.0005	
Cu ₂ S	21.8	c = 13.496 ± 0.002		90	b = 27.327 ± 0.005		90	a = 11.848 ± 0.003	
CdS	33.8	c = 6.7185 ± 0.0007					153	a = 4.1370 ± .0007	
Cu ₂ S	33.8	c = 13.497 ± 0.002						a = 11.848 ± 0.002	
Cu ₂ S	58.8	c = 13.5000 + 0.0016							
heat treated ~ 90°									
Cu ₂ S	5280	c = 13.497 ± 0.010							

*(1120) data were combined with (1010) data in determining lattice constant.

$\frac{b}{8}$ for Cu_2S . The 4 to 5% misfit of the lattice causes severe strains and cracking of the crystal surface. This may be seen in Figs. 8-10 which show the surface after dipping for the three CdS plates discussed above. In each case the original surface was polished and was free of flaws. The (1120) plate was considerably more cracked than in Fig. 10 after having been dipped for 153 minutes.

The small change of length and the conversion to Cu_2S in a single crystal orientation strongly suggest that the same basic sulfur network is found in both structures, with only the placement of the metal atom differing. (This is also true of the other copper sulfides which have been obtained in single crystal form from Cu_2S and which are discussed later.)

The orientation of the CdS and Cu_2S axes is parallel within $10'$, since when a well-oriented plate was rotated around its axis in the sample holder, the unevenness of intensity of a line was the same, whether it was a CdS line or a Cu_2S line. This is a very sensitive test and would have shown up differences if the misorientation was as little as $10'$. It is possible, of course, that individual small regions could be misoriented by larger amounts of random sign, so that they averaged to a zero net misorientation.

It is seen in Table III from the dipping times necessary to eliminate the CdS pattern that the effective diffusion rate in the three directions tested is different, with the (1120) direction being much slower than the other two. A rough measurement of the rate of thickening of the Cu_2S layer can be obtained from intensity measurements of the CdS pattern after successive dips, since the Cu_2S layer will absorb increasing amounts of the diffraction from the CdS. The average thickness can be calculated from the relation⁽¹⁵⁾

$$X = - \frac{u}{\rho}^{-1} \frac{\sin\theta}{2\rho} \ln \frac{I}{I_0}$$

where $\frac{u}{\rho}$ is the mass absorption coefficient of Cu_2S (60.5), ρ is the density of Cu_2S (5.80 g/cm^3), X is the thickness of the layer in centimeters, I is the diffracted intensity from a particular set of CdS planes, I_0 is the corresponding intensity in the absence of the Cu_2S layer, and θ is the Bragg angle. The term $\frac{\sin\theta}{2}$ enters because the x-ray beam is penetrating the layer at the angle θ , and

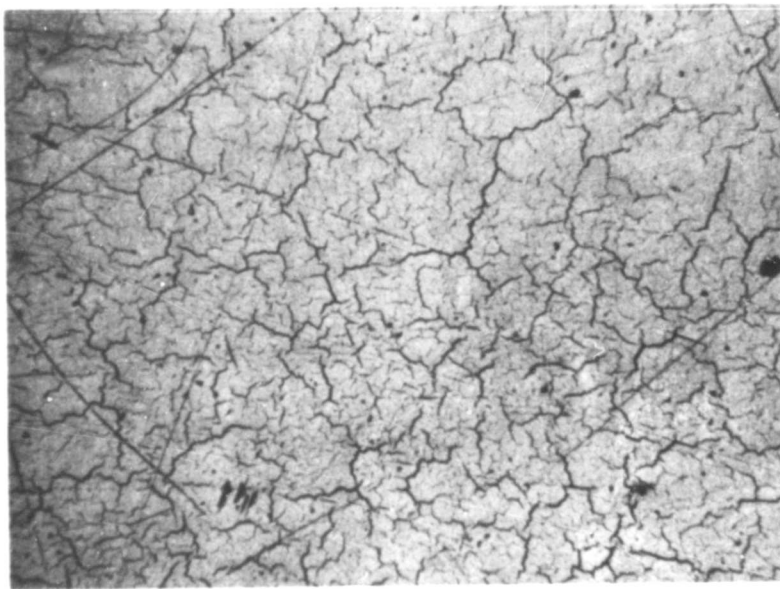


Fig. 8. Polished surface of (0001) plate of CdS after being dipped in CuCl solution at 90°C for 59 minutes, mag. 80X.

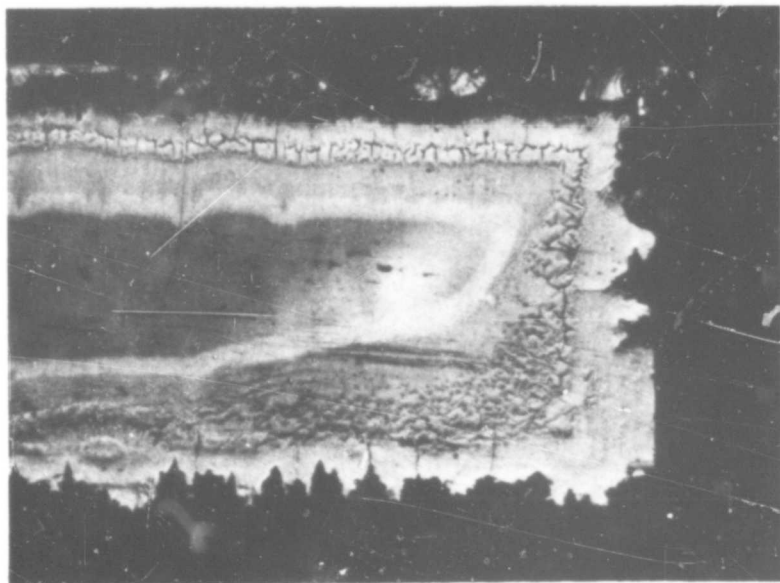
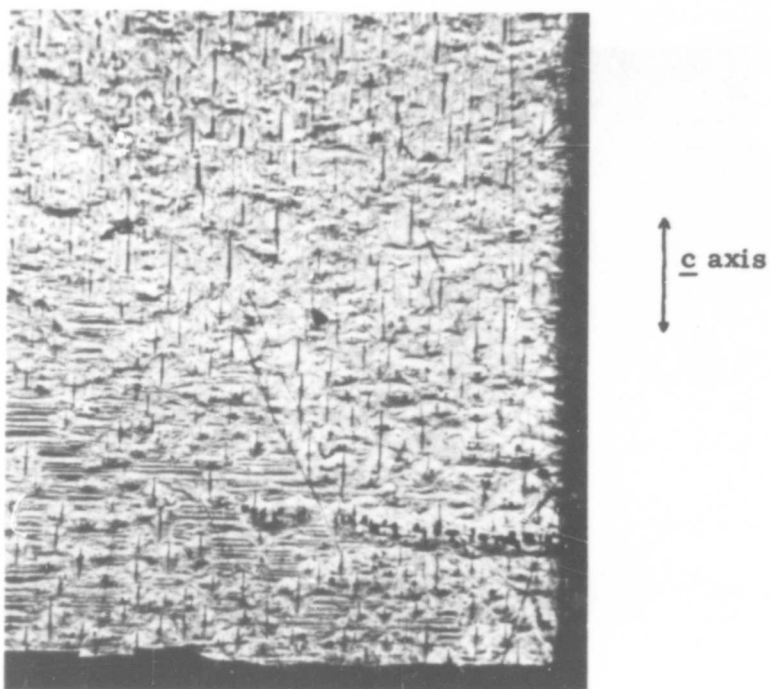


Fig. 9. (1010) plate of CdS after being dipped in CuCl solution at 90°C for 90 minutes, mag. 80X. The top view is of the polished surface. The bottom view is of a (0001) cleavage plane perpendicular to the main surface and in the position indicated.

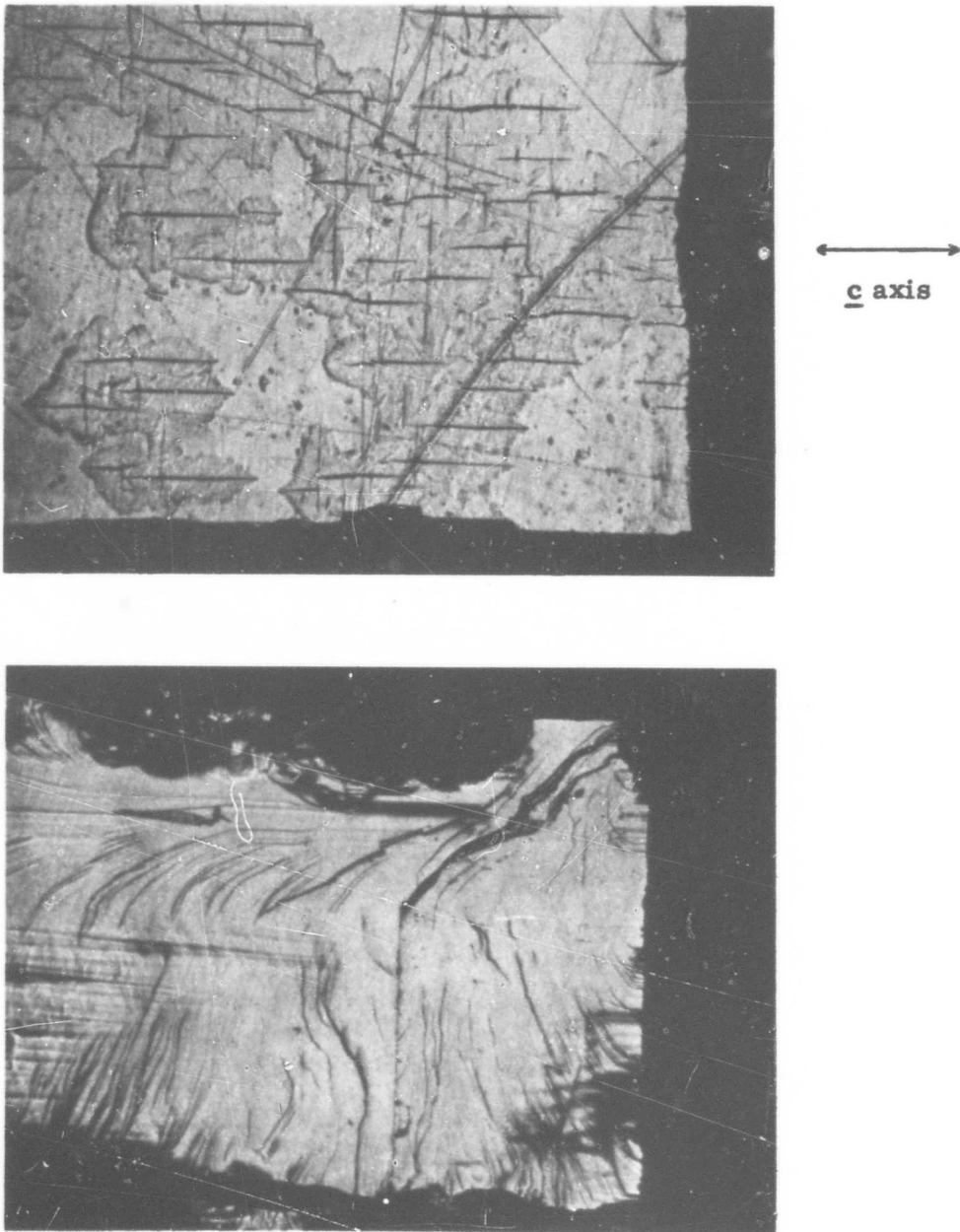


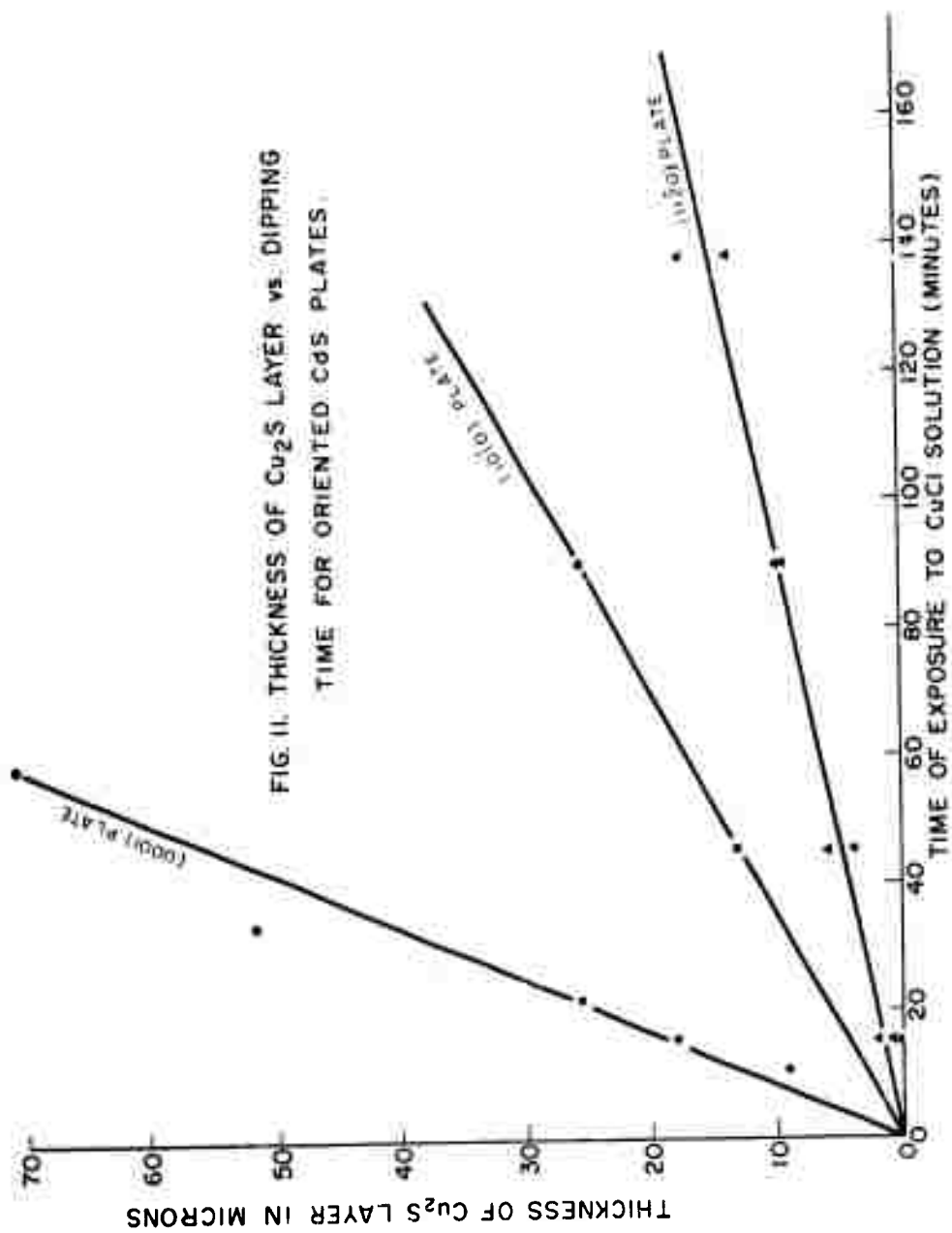
Fig. 10. $(11\bar{2}0)$ plate of CdS after being dipped in CuCl solution at 90°C for 90 minutes, mag. 80X. The top view is of the polished surface. The bottom view is of a $(10\bar{1}0)$ cleavage plane perpendicular to the main surface and in the position indicated.

the beam must traverse the layer twice before it reaches the detector.

The variation of thickness with time is approximately linear as shown in Fig. 11. Figure 11 does not tell the whole story. In the (0001) and (1010) directions microcracks occurred in the plate surface rather quickly and diffusion occurred primarily through the solution which penetrated the cracks. This meant that the slow "one-half-power" diffusion acted only over short distances and the overall apparent diffusion is linear. It should be noted in Fig. 11 that the thickness calculated from the absorption was below the line for the first time period for both the (0001) and (1010) plates. While this may be experimental error, it more likely is due to the slower one-half-power diffusion prior to cracking of the plate. The appearance of the plates is shown in Figs. 8 and 9. The zoning in the cross section of the (1010) plate is due to etching by the solution. Evidently the plate had partly cleaved before it was removed from the CuCl solution.

The appearance of the (1120) plate was different. In this case some areas quickly cracked and diffusion was rapid via the cracks. In other areas it did not crack and diffusion was slow, being only that occurring in the solid. This is shown in Fig. 10, where both a top and a side view are shown of the same area of the plate.

For the (1120) plate the minimum thickness of the diffused layer measured along the cross section is about nine microns, the same as that measured by X-ray absorption. For the (1010) plate the minimum thickness of the layer in Fig. 9 is ~ 60 microns, whereas the X-ray absorption measurement yielded only 25 microns. The explanation of this difference is that when the layer cracks, the diffusion along the cracks leaves behind islands of CdS which are only slowly converted, and the piece naturally breaks along these initial cracks. Thus the thickness of the layer as measured by X-ray absorption is too little, because the intensity of the CdS pattern from these "islands" is too strong, and the thickness measured on the cleaved side is too great. In the case of the (1120) plate, the thickness is approximately correct because large areas have not yet cracked, and much of the CdS is therefore at the correct level. Thus the thicknesses measured for the (1120) plate are closer to those determined by diffusion alone.



Let us consider the type of strain present in each plate surface. In the (0001) plate, the two directions at right angles are $[11\bar{2}0]$ with a 4.5% contraction and $[10\bar{1}0]$ with a 4.8% contraction. Thus the Cu_2S layer is in severe tension in all directions and cracks quickly and irregularly. This probably accounts in part for the rapid rate of thickening of the layer on the (0001) plate. The $(10\bar{1}0)$ plate contains the $[0001]$ direction with a 0.4% expansion and the $[11\bar{2}0]$ direction with a 4.5% contraction. The $(11\bar{2}0)$ plate contains the $[0001]$ direction with a 0.4% expansion and the $[0\bar{1}0]$ direction with a 4.8% contraction. The crack patterns shown in Figs. 8 to 10 are consistent with this since the (0001) plate shows a two-dimensional crack pattern, whereas in both the $(10\bar{1}0)$ and $(11\bar{2}0)$ plates the cracks run perpendicular to the direction of large contraction. The only question is why areas survived uncracked in the $(11\bar{2}0)$ plate and apparently did not in the $(10\bar{1}0)$ plate. The strains in the surface are quite similar in both cases. The answer may lie in the relative amount of extra phases in the two cases, discussed below.

There are three CdS \underline{a} axes in the plane perpendicular to \underline{c} and thus three possible Cu_2S orientations. For the alignment of a CdS plate as used here two of the possible orientations are symmetrical with respect to the plate direction and will therefore give rise to only one additional Cu_2S orientation. For the $11\bar{2}0$ plane of CdS which becomes the (100) plane of Cu_2S , the Cu_2S twin orientation is (140) . For the $10\bar{1}0$ plane of CdS which is (010) for Cu_2S , the twin orientation is (340) . The (0001) plane of CdS has only one possible orientation in Cu_2S : (001) . It will be shown later that Cu_2S (chalcocite) also converts to a single crystal of djurleite ($\text{Cu}_{1.96}\text{S}$). The original and twin directions for djurleite which are equivalent to CdS are respectively: for $(11\bar{2}0)$ CdS , (100) and (230) ; for $(10\bar{1}0)$ CdS , (010) and (210) ; for (0001) CdS , only (001) . The chalcocite twin orientation was not observed for any of the three plates. However, this was not necessarily true for djurleite as discussed later.

In two of the three plates, there were indications of an extra phase present besides the single Cu_2S orientation. No extra lines were found in the $11\bar{2}0$ plate, but this may be because conversion to Cu_2S was not complete. However, upon re-X-raying the plate after almost two years a weak line was observed with d-spacing 2.400 Å, which is probably the (350)

line of djurleite. If this identification is correct one should also expect to see diffraction from the (230) line of djurleite. The (460) line is a strong line, but is masked by the (600) line of Cu_2S . The (8.12.0) line does appear and is fairly strong, but was not present when the plate was originally examined. Thus the twin orientation of djurleite appears to be present.

One extra line of significant strength was obtained for the (0001) plate, with a d-spacing of $2.685 \pm .001\text{\AA}$. This is not a permitted line for Cu_2S (since the (005) of Cu_2S is extinct and, in addition, the d-spacing of (005) should be approximately 2.692\AA). However, it could be the (0.0.10) line for djurleite, and the spacing is correct within the presently known accuracy of the lattice constants. Results on needle crystals discussed later also suggest that it should be a line of djurleite. Heat treating the plate for 88 hours at $\sim 90^\circ\text{C}$ in argon strengthened the peak. The (0001) plate was run again almost two years later and the pattern was similar to the pattern after heat treating.

Two extra lines were obtained on the (1010) plate besides the 0k0 Cu_2S lines; the d-spacings were 2.300\AA and 1.150\AA . The 2.300\AA line was the strongest line of the pattern, and was distinct from the (0.12.0) line of chalcocite (2.274\AA). If the crystal twinned in converting from CdS to Cu_2S (each of the CdS a axes becoming the Cu_2S a axis in different parts of the crystal) the alternate Cu_2S plane would be (340) with $d = 3.426\text{\AA}$. There is no multiple of this leading to a d-spacing of 2.300\AA . In fact, there is no possible plane of chalcocite with a d-spacing of 2.300\AA . Thus the line is due to a different copper sulfide. Possible materials which have a diffraction line in the correct place and of the correct orientation are djurleite (either (060) or its twin equivalent (630), both of which are slightly too small at 2.260 and 2.266\AA respectively; high temperature $\text{Cu}_{1.96}\text{S}$ with the line (104) at 2.302\AA ; and $\text{Cu}_{1.92}\text{S}$ with line (402) at 2.308\AA). Conversion of crystals of chalcocite and djurleite to high temperature $\text{Cu}_{1.96}\text{S}$ show that the (104) line occurs in the correct zone (the $h\bar{k}0$ zone of chalcocite). It is probable that the line belongs to the high temperature $\text{Cu}_{1.96}\text{S}$ phase, indicating that the 1010 plate was heated hot enough to form that phase. Why there is no trace of the phase in the other two plates is not understood. It could be that this plate was slightly hotter than the other two during dipping; more likely, the lattice strain at the interface was such that the high temperature form was preferred.

3.2.7.2 Studies on Needle Crystals

Small crystals of CdS elongated along c were completely converted to copper sulfide by dipping in CuCl solution at 90°C for 20 to 60 minutes. All the crystals were initially converted to chalcocite (Cu_2S). Subsequent heating produced a variety of phases. Typical rotation patterns of CdS and Cu_2S , rotated around their c axes, are shown in Fig. 12. It may be seen that the diffraction spots of Cu_2S are much less sharp than those of CdS, and this has proven to be true of all the copper sulfides. The CdS pattern shows split lines over about 60% of the pattern due to the fact that the CuK α wavelength is actually a close doublet. The doublet does not resolve at all for the Cu_2S . This could be due to several factors: vast quantities of defects in the Cu_2S crystal, very small individual crystals not quite perfectly aligned, strains in the crystals, or a compositional gradient. It is assumed that the replacement of cadmium by copper is complete and that the transition from CdS to chalcocite is spatially very abrupt. Microprobe studies show that this is essentially correct.⁽¹⁶⁾ Neither room temperature aging nor annealing at 90° or 250° sharpened the Cu_2S patterns; this opposes either a small composition gradient of Cd or lattice strain as the cause of the diffuseness of the X-ray pattern. The phase diagrams of Cu-S (Figs. 1 and 2 in Appendix) show that if appreciable nonstoichiometry exists a new copper sulfide phase forms. The high mobility of Cu ions also argues against a stoichiometry gradient. Therefore, the lack of sharpness is probably due to defects or slightly misaligned microcrystals.

One of the converted Cu_2S crystals was heat treated for 88 hours at $\sim 90^\circ\text{C}$ in argon. This crystal proved to be a mixture of orthorhombic djurleite and chalcocite. The reason for the partial conversion to djurleite is not yet understood, but may be due to (1) establishment of equilibrium in a crystal that was converted to a nonstoichiometric copper sulfide but which formed metastably as chalcocite or (2) oxidation of copper on the surface by traces of oxygen left in the argon-filled enclosure which effectively changed the stoichiometry of the crystal.

Recently, almost 2 years after the initial conversion, several crystals were re-examined in preparation for some high

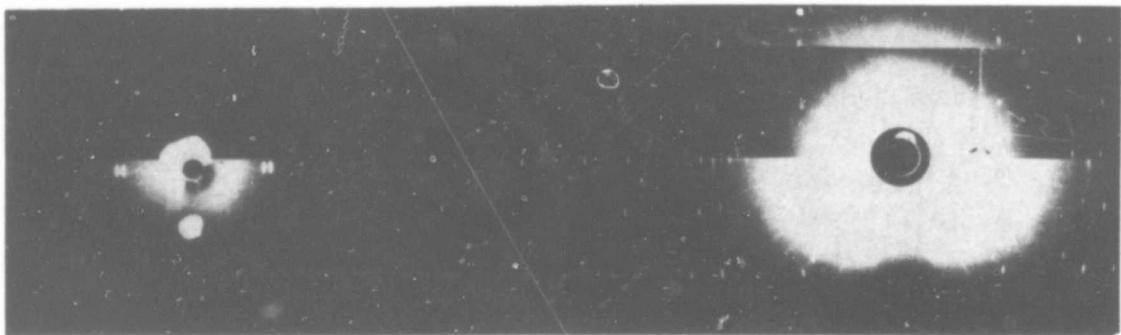


Fig. 12a. CdS crystal, rotated around c axis. The crystal had been dipped 6 min. in CuCl solution at 90°C, but the Cu₂S does not yet show on the film. CuK α radiation, camera diameter 10 cm.

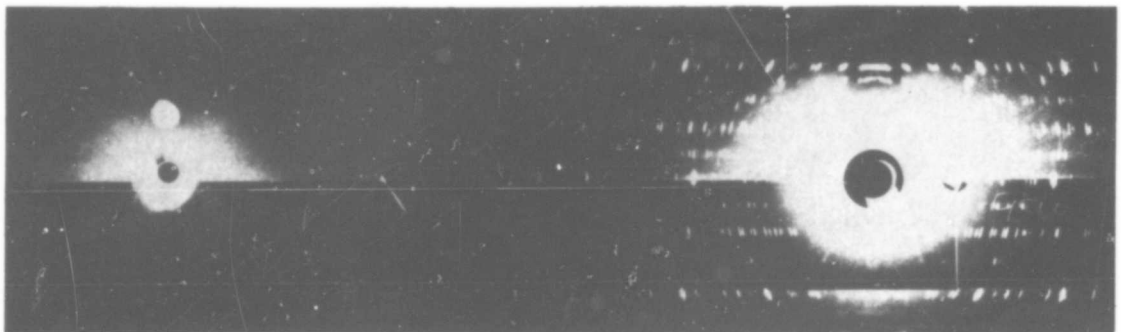


Fig. 12b. Cu₂S (chalcocite) crystal rotated around c axis. The crystal was originally CdS, which was dipped for 61 min. in CuCl solution at 90°C, and was fully converted. The darker strip on each film represents an area covered by Ni foil to eliminate the CuK β radiation.

temperature studies, and it was found that their crystal structure had changed! Those crystals which were originally chalcocite (i. e., converted to copper sulfide, but with no subsequent heat treatment) were now pure djurleite (Fig. 13a). The crystals treated at 90°C in argon (and which were mixed chalcocite and djurleite) were now a new phase! The new phase has a c lattice constant similar to chalcocite ($13.36 \pm .02$ Å for the new phase versus 13.491 Å⁽¹⁷⁾ for chalcocite), but has an entirely different pattern (Fig. 13b). This phase has not been described before in the literature. (It is tempting to assume that it is the same phase as $\text{Cu}_{1.92}\text{S}$ reported by the Russians,⁽¹²⁾ but the patterns are not very similar.) The occurrence of these changes in copper sulfide crystals at room temperature (in air) indicates that copper has appreciable mobility even at room temperature (see Section 3.2.8).

Two crystals that were completely converted to djurleite were heated to 250°C for successive periods of time, one in air and one in argon. Both of these gave qualitatively identical results. There was an increasing conversion to tetragonal $\text{Cu}_{1.96}\text{S}$ with time. Heating for ten minutes caused significant conversion, while heating for one hour was not sufficient to cause complete conversion. The X-ray diffraction pattern (Fig. 13c) indicated that the crystal was probably transforming as a single crystal. Difficulty has been experienced in attempting to establish the orientation of the tetragonal $\text{Cu}_{1.96}\text{S}$ in comparison with the djurleite; one explanation of this may be that its structure is not described correctly. It appears to have been indexed solely from powder patterns.

A second deduction that may be drawn from the relatively sluggish transition of the low to high $\text{Cu}_{1.96}\text{S}$ is that they are not the same composition. The single-crystal or almost single-crystal conversion shows that they have a very similar sulfur network; copper has been shown to be mobile at room temperature and should be very mobile at 250°C. Thus it seems likely that the limited conversion is due to the need for increasing or decreasing the copper content of the crystal. It should also be noted that two X-ray patterns a week apart on the same crystal after heating were unchanged, indicating that conversion back to the room temperature phase was very slow.

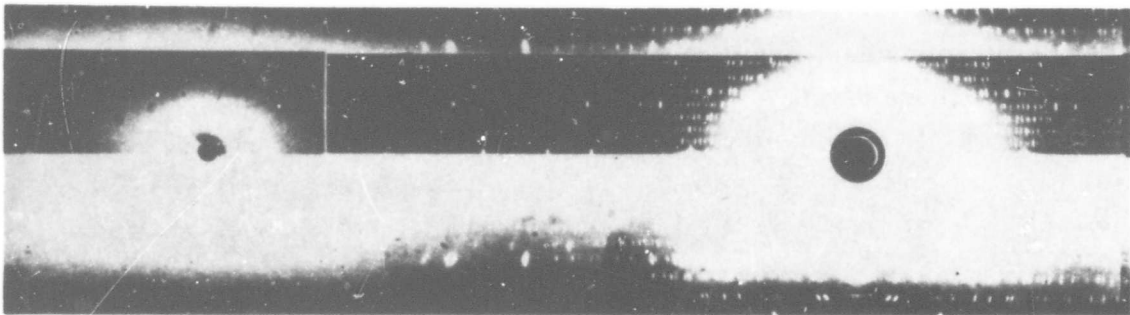


Fig. 13a. $\text{Cu}_{1.96}\text{S}$ crystal, rotated around \underline{c} axis. The crystal had converted from Cu_2S (Fig. 12b) after sitting at room temperature in air for two years.

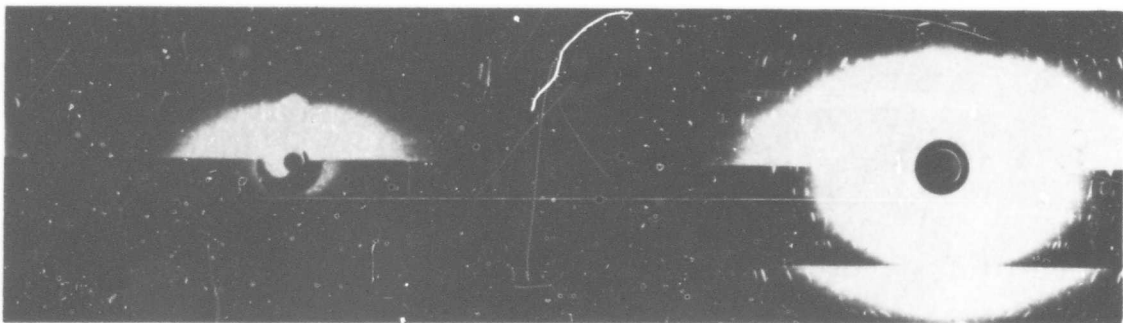


Fig. 13b. Cu_xS , with $1.96 > x > 1.8$, rotated around \underline{c} axis. The crystal had converted from a mixture of chalcocite and tetragonal $\text{Cu}_{1.96}\text{S}$ after sitting at room temperature in air for two years.

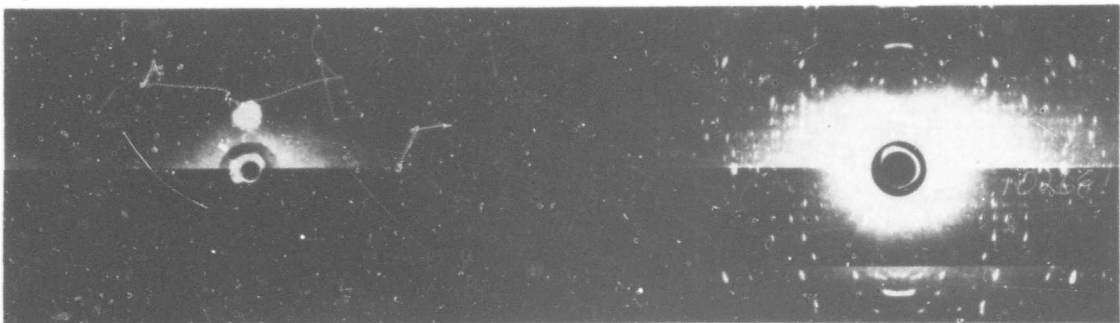


Fig. 13c. Crystal partly converted from djurleite to tetragonal $\text{Cu}_{1.96}\text{S}$ after heating at 250°C in air for ten minutes. Crystal rotated around \underline{c} axis of djurleite.

A third observation is that the high temperature phase of $\text{Cu}_{1.96}\text{S}$ is evidently stable as high as 250°C, in opposition to the literature (see Appendix) which reports that it decomposes above 154°C.

3.2.7.3 Studies on Copper Sulfide Powders

A CdS crystal that had been completely converted to Cu_2S was ground to a powder and then an X-ray diffraction pattern obtained. The material was a mixture of djurleite and chalcocite. The powder was then heated to 250°C in air for nine minutes. After stabilizing in air for 3 to 5 hours the 1 g sample had increased in weight by 0.1 mg, which is the limit of weighing precision. An X-ray pattern of the powder after heating showed a mixture of high temperature $\text{Cu}_{1.96}\text{S}$ and Cu_2S . Thus the only apparent change was the conversion of low temperature $\text{Cu}_{1.96}\text{S}$ to the high temperature form. The stability of the high temperature $\text{Cu}_{1.96}\text{S}$ 100° above its supposed decomposition point was again demonstrated.

3.2.7.4 Conclusions From the X-ray Data on Copper Sulfide

a. The transformation from CdS to chalcocite (Cu_2S), djurleite (orthorhombic $\text{Cu}_{1.96}\text{S}$), Cu_xS (new phase), and probably also tetragonal $\text{Cu}_{1.96}\text{S}$ occurs in such a way that the single crystal nature is maintained. This suggests that they all have the same sulfur arrangement.

b. Copper sulfides tend to change in time from higher to lower copper content: $\text{Cu}_2\text{S} \rightarrow \text{Cu}_{1.96}\text{S} \rightarrow \text{Cu}_x\text{S}$ (with $1.96 > x > 1.8$). A chemical reaction of some sort is required to account for such changes. Although H_2S was occasionally present in the atmosphere, as a source of sulfur, a more likely reaction is with atmospheric oxygen. This would result in a thin surface layer of copper oxide that would not be detectable by X-rays because of the small quantities involved (see Section 5.3).

c. The perfection of the copper sulfides is poor, as shown by the fact that line sharpness is very much reduced in comparison with CdS.

d. The existence of at least one unreported phase of similar composition has been demonstrated.

e. The literature description of the symmetry of djurleite is confirmed; the description of tetragonal $\text{Cu}_{1.96}\text{S}$ may be incorrect.

f. Tetragonal $\text{Cu}_{1.96}\text{S}$ is stable at least as high as 250°C.

g. The rate of growth of the Cu_2S layer is dependent upon crystal orientation, and indirectly upon the lattice fit between Cu_2S and CdS .

3.2.8 Diffusion and Mobility of Cu Ions in Cu_2S

The rapid formation of Cu_2S at 90°C when CdS is exposed to a Cu^+ ion solution requires a large diffusivity of Cu and Cd ions in solid Cu_2S . But because the cracking that occurs reduces the diffusion distance to small and unknown values, a quantitative value of the diffusivity cannot be extracted from the observed growth rate of the Cu_2S layer. However, recent coulometric measurements that were initiated to learn more about the nature of Cu-nodule formation (see Section 5.2) have allowed a quantitative estimate of the room-temperature diffusivity of Cu in Cu_2S .

A pseudo-single crystal of Cu_2S , formed by long exposure of a CdS crystal to a Cu^+ ion solution, was electrolyzed at room temperature using copper foil as an anode and a copper-wire point contact as a cathode. A current of 0.1 ampere was passed through the crystal and the voltage drop across the cell was ~ 0.5 volts. The experiment took place in dim ambient light except for short periods when the cell was examined under the microscope. After one day, very small nodules of copper were observed under the tip of the cathode. After another day the cathode tip was prominently lifted above the surface of the Cu_2S by the growth of the Cu nodules. Several nodules formed under the tip. They were irregularly cone-shaped with their bases attached to the Cu_2S . Cu plating on the underside of the nodules continuously lifts the nodules upward. Plating on the periphery of the contact causes the base to widen with time and imparts the conical or barnacle-like shape to the growing nodules.

This experiment was repeated on a separate Cu_2S crystal using somewhat different electrode geometry and very similar results were obtained. In these experiments, rough measurements were made on the rate of growth of the copper nodules. After four days at a nearly constant current of 100 mA, a total volume of nodules of $\sim (0.1 \text{ mm})^3 = 10^{-6} \text{ cm}^3$ was estimated under the microscope using a calibrated eye-piece reticle. Daily observations

during the experiment indicated that the copper was being plated out at a uniform rate. The measured volume of Cu corresponds to $\sim 1.2 \times 10^{-7}$ moles of Cu which requires 1.2×10^{-2} coulombs of charge to effect the reaction: $\text{Cu}^+(\text{Cu}_2\text{S}) + \text{e}^- \rightarrow \text{Cu}^0$. The measured current of 100 mA passing for four days corresponds to the passage of a total charge of 3.5×10^4 coulombs. Clearly, the vast majority of this charge is carried electronically by holes. The ratio of ionic to electronic charge transport is $1.2 \times 10^{-2}/3.5 \times 10^4 \approx 3 \times 10^{-7}$. If the ionic transport occurs by drift of Cu vacancies, the effective concentration of the ionic carriers is $[\text{V}^-\text{Cu}]$. Also, since the holes arise from the ionization of the Cu vacancies $\text{V}^0\text{Cu} \rightarrow \text{V}^-\text{Cu} + \text{h}$, the free-hole and free-ion concentrations are equal. Therefore, the ion-to-hole mobility ratio is equal to the ion-to-hole current ratio (the applied voltage and geometry being the same for both currents). Since the mobility of the holes is $\sim 10 \text{ cm}^2/\text{V-sec}$, the mobility of the Cu^+ ions is $\sim 3 \times 10^{-6} \text{ cm}^2/\text{V-sec}$; and since the electronic resistivity of Cu_2S is $\sim 3 \times 10^{-3} \Omega \text{ cm}$, the ionic resistivity is $\approx 10^4 \Omega \text{ cm}$. The mobility of the Cu^+ ions then yields through the Einstein relation, a room-temperature diffusivity of $\sim 8 \times 10^{-8} \text{ cm}^2/\text{sec}$. This is $\approx 10^7$ times larger than the diffusivity of Cu^+ in CdS at 150°C , which itself is known to be unusually large.

In order to see if there was a voltage threshold for Cu plating, the above experiment was repeated at four other voltages. The results are summarized in Table IV.

Table IV. Formation of Copper Nodules at Different Applied Voltages

V Volts	I_{ave} ma	Q_T 10^4 Coul	Time Days	Cu Nodule Vol. cm^{-3}	Transport No. σ_i/σ_e
0.30	5.0	0.46	10.6	none	~ 0
0.357	7.2	0.81	13	none	~ 0
0.409	18.3	1.90	12	6.4×10^{-8}	3.6×10^{-8}
0.431	45.4	1.85	4.7	2.4×10^{-7}	1.3×10^{-7}
0.50	100	3.6	4	1×10^{-6}	3×10^{-7}

The transport number, shown in the last column, is the ratio of ionic conductivity to total conductivity, the latter being closely approximated by the hole conductivity. The transport number is plotted against voltage in Fig. 14. A voltage threshold near 0.4 volts is clearly indicated. The relevance of this threshold to the degradation of solar cells operated at open circuit is discussed in Section 5.2. Additional data of this kind and especially the dependence on temperature would be highly desirable.

Plating of Cu was found to occur on all metallic electrodes tested: Cu, Ag, Au, Pt, In, brass, and bronze. In one test at 0.5 volts, no Cu was observed to form when 1 Ω cm CdS was used as the cathode despite the fact that a comparable amount of charge was passed through the contact.

That a voltage threshold might exist in the present system was surmised through analogy to similar phenomena that commonly occur in aqueous electrolytic systems. The situation in solid Cu_2S is presumed to be as follows: When current is forced through the solid, Cu^+ ions drift toward the negative cathode (or the equivalent, negatively charged Cu vacancies drift away from the cathode). The decrease in the concentration of Cu vacancies near the cathode corresponds to a decrease in x in the formula Cu_{2-x}S , i. e., the solid near the cathode becomes richer in Cu. The concentration gradient produced by this drift produces a reverse flow of vacancies due to normal diffusion in a concentration gradient. Below threshold voltage, a steady state is reached in which the drift and diffusion currents are equal. The activity of the Cu in the Cu_2S next to the cathode has a value less than one, i. e., less than that of pure Cu. As the voltage is increased, the steady state concentration gradient increases and the activity of the Cu in the Cu_2S next to the cathode increases. The threshold voltage is then that voltage which forces the activity of Cu in the Cu_2S to reach unity, i. e., to reach the Cu-rich limit of solid stability. The concentration gradient cannot thereafter be increased by further increases in voltage since the solid then will spontaneously eject any additional Cu arriving at the surface, just as Cu whiskers can be extruded when the Cu-rich limit is forced to be exceeded by increasing temperature (to be discussed later). The reverse diffusion of Cu due to the concentration gradient therefore remains constant for all voltages that exceed the threshold. The

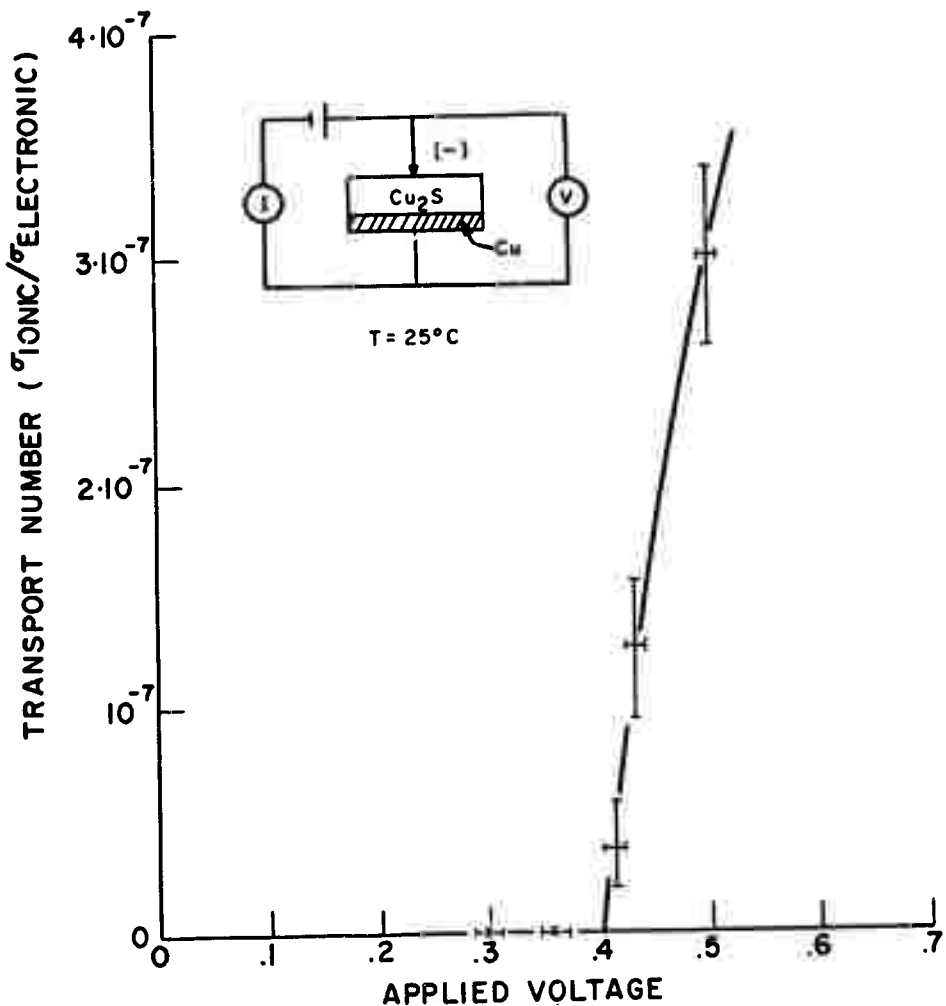


FIG. 14. TRANSPORT NUMBER vs. VOLTAGE, SHOWING VOLTAGE THRESHOLD FOR ELECTROLYTIC PLATING OF Cu.

two ionic currents can no longer balance and the rate of Cu plating becomes proportional to the electronic current in excess of that which was flowing at the threshold voltage. This model predicts that the threshold voltage will be decreased by an increase in temperature since we will shortly see that the limit of Cu-richness of Cu_2S decreases with increasing temperature. The model also predicts that the threshold will be independent of electrode material. The absence of Cu plating when CdS was used as the cathode would then have to be an artifact. The most likely explanation is that a significant part of the 0.5 applied voltage in that particular experiment was developed across the anode contact and reduced the cathode voltage below the threshold value.

The large ionic conductivity of Cu_2S between 150°C and 500°C was reported much earlier by Hirahara. (6)(18) Appreciable ionic conductivity starting at $\sim 130^\circ\text{C}$ was shown to rise rapidly to a large maximum near 400°C and then to fall to small values above 500°C. The high ionic conductivity range was associated with the existence range of " β - Cu_2S ," $\sim 110^\circ\text{C}$ to 470°C . A sharp hundredfold drop in electronic conductivity within the same temperature interval was also reported. In addition, and most significantly to our present discussion, a substantial flow of Cu in a thermal gradient was established, the Cu moving away from the high-temperature zone.

We have observed closely related effects in ungridded and uncovered (but otherwise typical) thin-film solar cells. When such a cell is heated for 2 to 8 hours in vacuum or inert gas at a temperature $\approx 350^\circ\text{C}$, fine metallic "whiskers" of Cu are found protruding from the Cu_2S layer. The whiskers remain after the cell is cooled to room temperature. A similar effect was observed when a large polycrystalline boule of Cu_2S produced from a stoichiometric ratio of Cu and S was cooled from the synthesis temperature of 800°C (see Section 3.7.2). Many fine Cu whiskers extending ~ 1 mm above the surface of the boule were observed when the fused-quartz reaction tube was withdrawn from the furnace. Significantly, as the boule cooled, the whiskers retracted and were completely gone after a few minutes (temperature $\approx 300^\circ\text{C}$). The formation and re-absorption of the whiskers was found to be reversible, as demonstrated by over 20 cycles of heating and cooling.

Clearly, the Cu_2S becomes increasingly deficient in copper as the temperature is increased. Expressed another way, the Cu-rich boundary of the solid-stability field of " Cu_2S " in the Cu-S phase diagram tilts away from the Cu axis. Judging from the amount of rejected Cu relative to the amount of Cu_2S , the boundary is only slightly tilted, and may not even be noticeable in a normal (unexpanded) phase diagram.

The rejection of Cu at elevated temperatures is consistent with the picture of thermal generation of Cu vacancies. Cu_2S evidently has a low solubility for interstitial Cu since Cu was rejected and the Cu_2S became more p-type. The various phase-transformation temperatures that have been reported for Cu_2S are undoubtedly confused by such changes in composition. It is also likely that the many phases observed for Cu-poor compositions represent various states of ordering of the Cu vacancies, all phases maintaining a common sulfur sub-lattice.

The easy motion of Cu in Cu_2S at high temperatures was also demonstrated by heating a dense 3" rod of polycrystalline Cu_2S in a temperature gradient. One end was maintained at 800°C and the other end was at $\sim 700^\circ\text{C}$. After an overnight exposure, large whiskers of Cu were found at the hot end of the rod. About a third of the mass of these whiskers was re-absorbed into the bar as it was cooled to room temperature. The excess copper from the entire rod had, evidently, been driven to the hotter end. The long distance of diffusion in this case did not allow the complete re-absorption of the excess Cu during the short (few minutes) cooling time. This observation appears to be contradictory to Hirahara's results. He heated a horizontal stack of individual Cu_2S specimens for 30-40 hrs in a temperature gradient (180° to 380°C, end-to-end) and found that the specimens on the hot end lost weight and that those at the cold end gained weight (with intermediate results for intermediate specimens). The process was shown to be reversible. He thereby concluded that Cu moved from the hot side to the cold side. Yet we found an accumulation of elemental Cu at the hot side indicating that Cu moved to the hot side. The most likely explanation for these seemingly contradictory results is that Hirahara's specimens were deficient in copper under all temperature conditions whereas our specimen was at the Cu-rich limit of composition near room temperature. All parts of our specimen exceeded the

Cu-rich limit when it was heated, and Cu whiskers initially formed all over the rod although more were formed at the hot end. The hot end having a larger Cu vacancy concentration caused diffusion of Cu vacancies toward the cold end which corresponds to a flow of Cu to the hot end. The whiskers at the cold end were thereby consumed and transferred to the hot end. At the moment the whiskers disappeared the composition of the Cu_2S started to move away from the Cu-rich limit by an increase in concentration of Cu vacancies (different for each temperature). This change then counteracts the further influx of Cu vacancies and a steady state condition was achieved. In Hirahara's experiment the Cu-rich boundary was never reached by any of his specimens (according to our hypothesis) and so the increase in Cu vacancy concentration at the hot end was accommodated by a decrease in vacancy concentration at the cold end, which corresponds to a flow of Cu to the colder end. The steady state is reached by the increase in the activity of the Cu at the colder end which eventually restricts the thermal influx of Cu to this end.

It was previously noted that Hirahara had reported a very large decrease of ionic conductivity between 400°C and 500°C. We have no data to indicate that this is not so; however, the tremendously large diffusivities observed in the vicinity of 800°C demonstrate that if Hirahara's results are correct, then the ionic diffusivity and conductivity must increase very rapidly above 500°C.

3.3 The Cu-Compensated i-CdS Layer

3.3.1 Diffusion of Cu in CdS Crystals and Films

It was recognized early in the study that at least some Cu had to diffuse into the CdS layer during the various heat treatments that the cells were subjected to during fabrication. The published data of Clarke⁽¹⁹⁾ and of Szeto and Somarjai⁽²⁰⁾ extrapolated to typical cell processing temperatures indicated that a substantial diffusion of Cu should take place. Furthermore, the magnitude of the diffusion constant extrapolated to the expected operating temperature in earth orbit (~ 65°C) indicated that the cells would degrade rapidly by continued diffusion of Cu and hence that the cells would not be suitable for such applications. A detailed study of the diffusion of Cu in CdS was thus initiated and a rather extensive body of results has been obtained. A full report of this investigation has been submitted to the Physical

Review and will be published shortly; hence, only a summary of the methods and results will be presented here.

Most of the experiments were carried out using as-grown, non-intentionally doped, 1Ω cm, n-type CdS, single-crystals grown in our laboratory by a sublimation method that does not make use of transport agents. Both sides of an oriented plate were coated with Cu or Cu_2S (no differences were found) and the progress of diffusion at each temperature was followed by dark capacitance measurements. The two growing insulating layers were treated as two identical capacitors in series. Analysis shows that a very deep acceptor diffusing with a normal diffusion profile in a uniformly n-type material produces at the depth where $N_D = N_A$ a very abrupt change in resistivity ($> 10^6 \Omega$ cm in a distance $< 1 \mu$). The thickness of the capacitors is thus well defined. In almost all cases, the diffusion proceeded in a well behaved manner consistent with simple diffusion theory: the $1/C^2$ vs. time plots were very linear, as were the $d(1/C^2)/dt$ vs. temperature plots. Typical examples of such plots are shown in Figs. 15 and 16. Many diffusion experiments at different temperatures were performed serially on each crystal specimen, but always in the direction of increasing temperature and always allowing sufficient time at the new temperature so that the diffusion profile characteristic of the lower temperature was "over-powered" and replaced by the profile characteristic of the new temperature.

In order to obtain explicit values of the diffusion constant from such data, the surface concentration of Cu in CdS at each temperature had to be known. The solubility measurements described in the next section provided these data. The temperature dependence of the diffusion constant computed from these data is shown in Fig. 17. We note that the data extend over four decades in D, and that the values obtained from three independent specimens are nearly identical. These results are compared with the results of previous investigations in Fig. 18. In the low temperature region our results are seen to be two to three orders of magnitude lower than the earlier values, although only one order of magnitude lower at higher temperatures. The reasons for these differences are unknown. It is known, however, that thin film cells have withstood degradation at moderately high temperatures for times that are far in excess of that predicted from Clarke's extrapolated

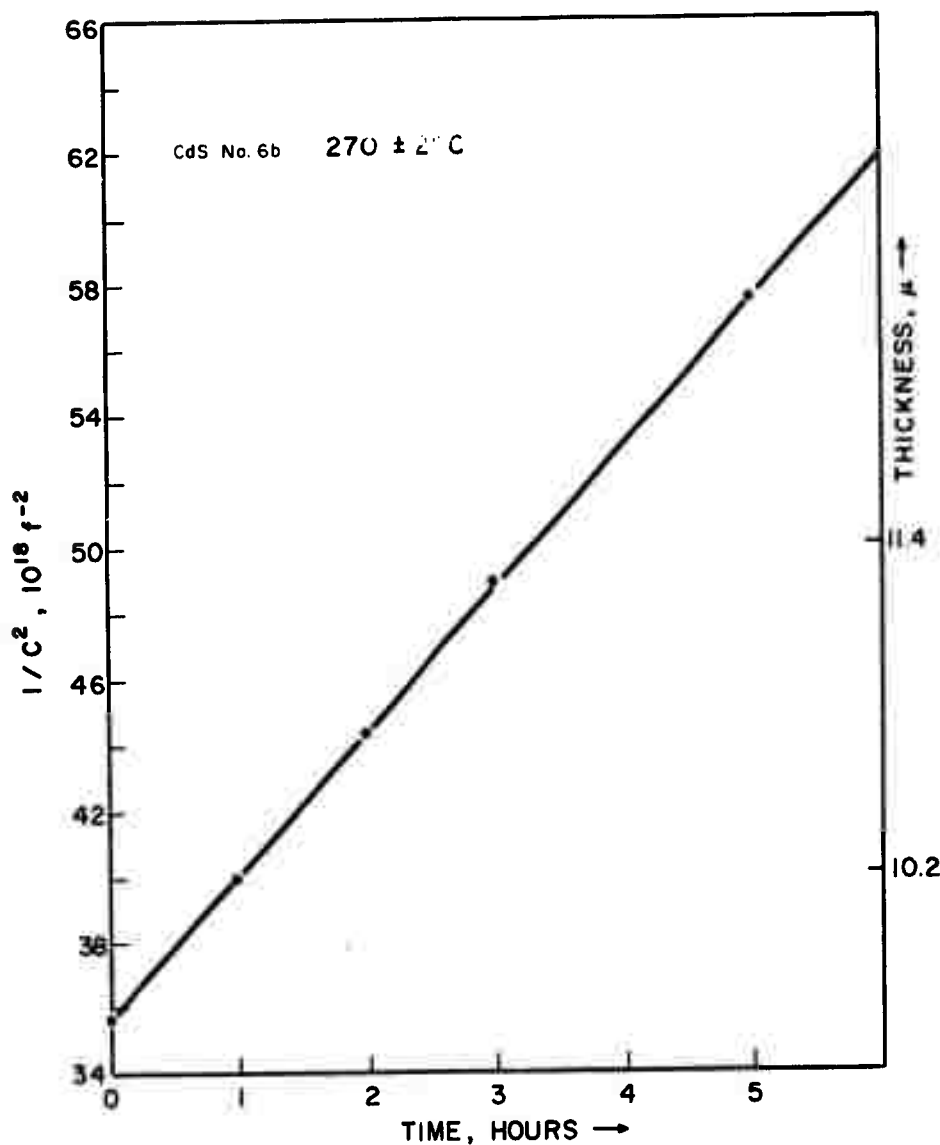
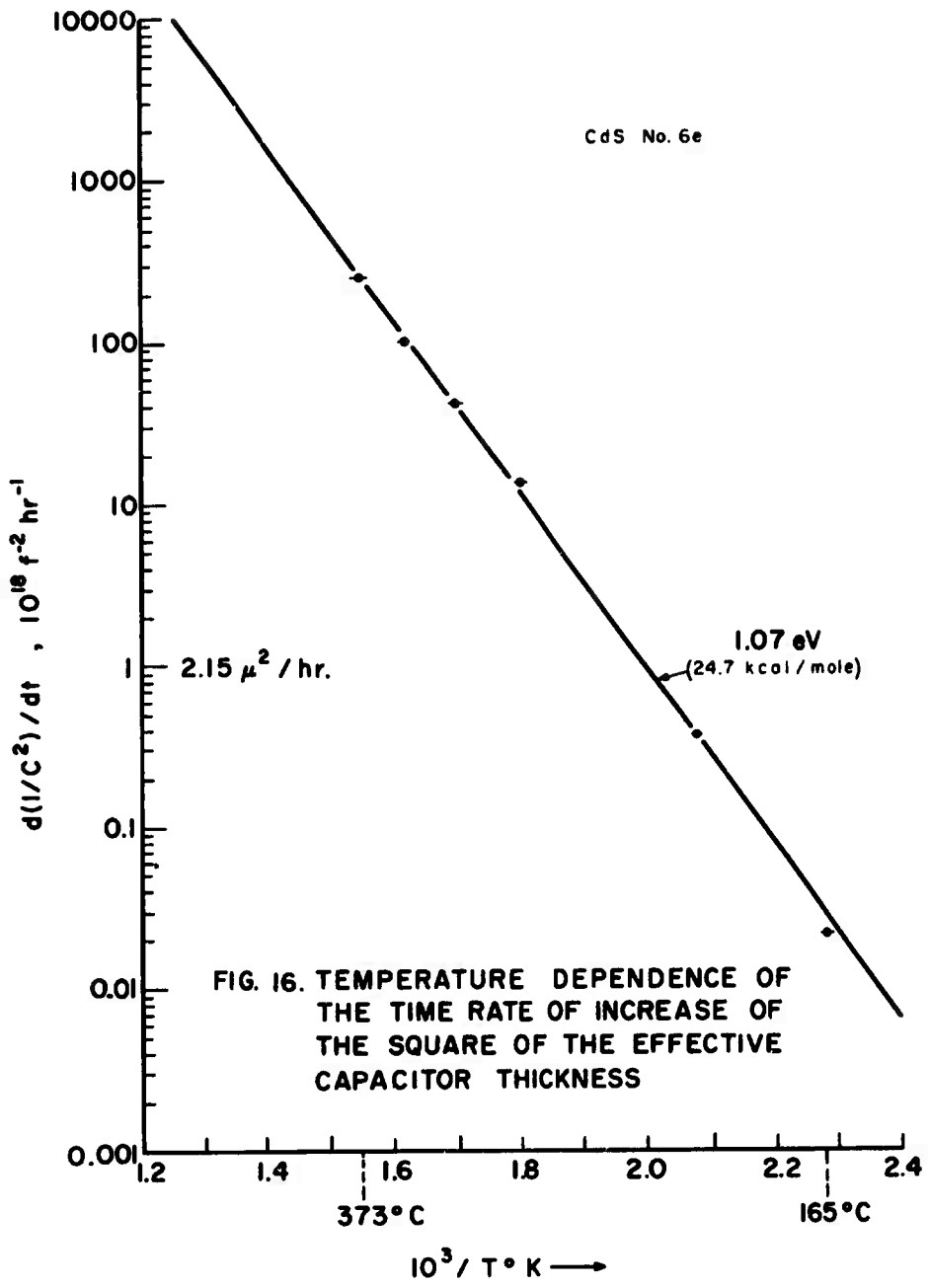
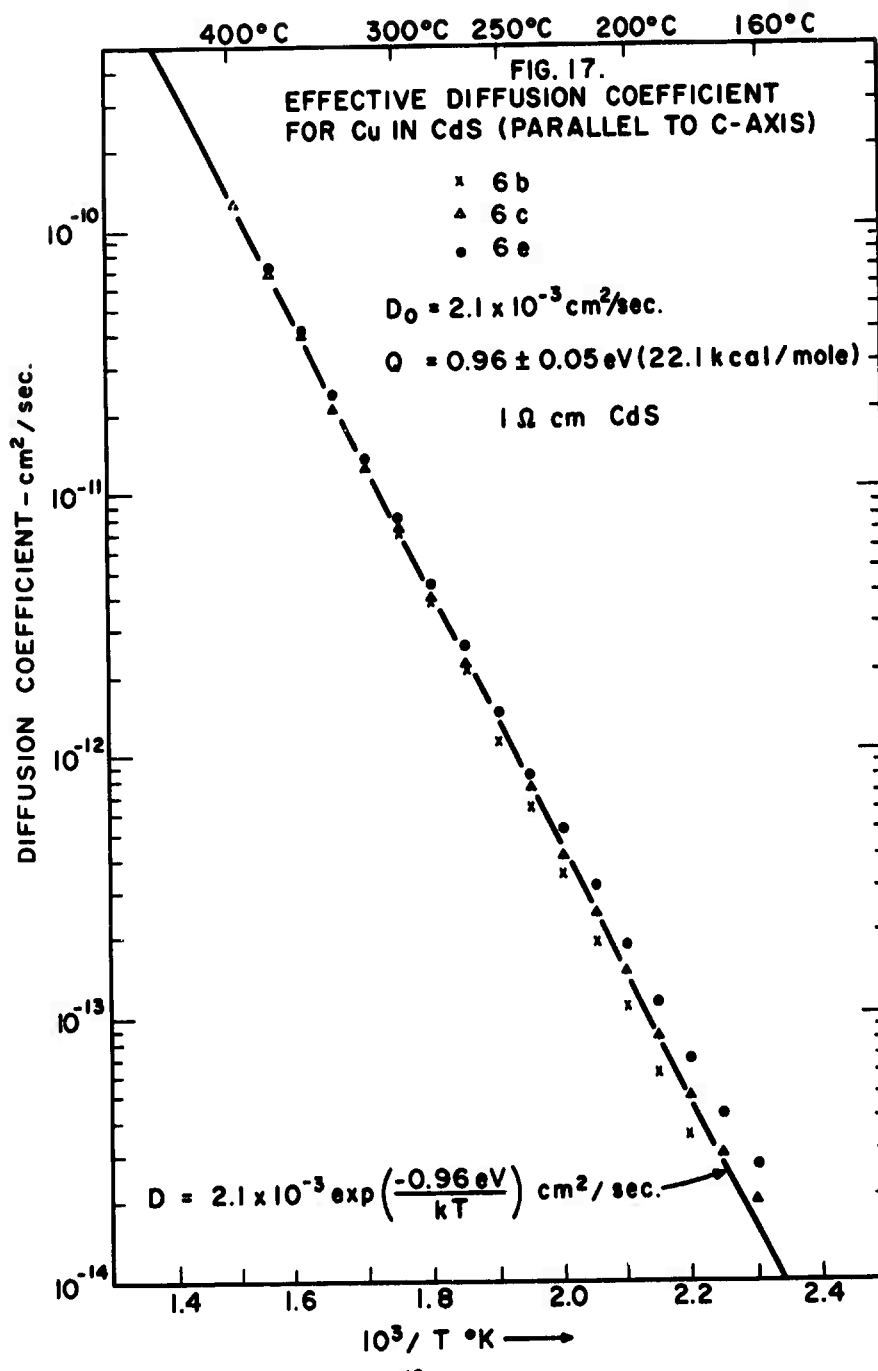


FIG. 15. SQUARE OF THE EFFECTIVE PARALLEL PLATE SPACING (PROPORTIONAL TO $1/C^2$) vs. TIME.





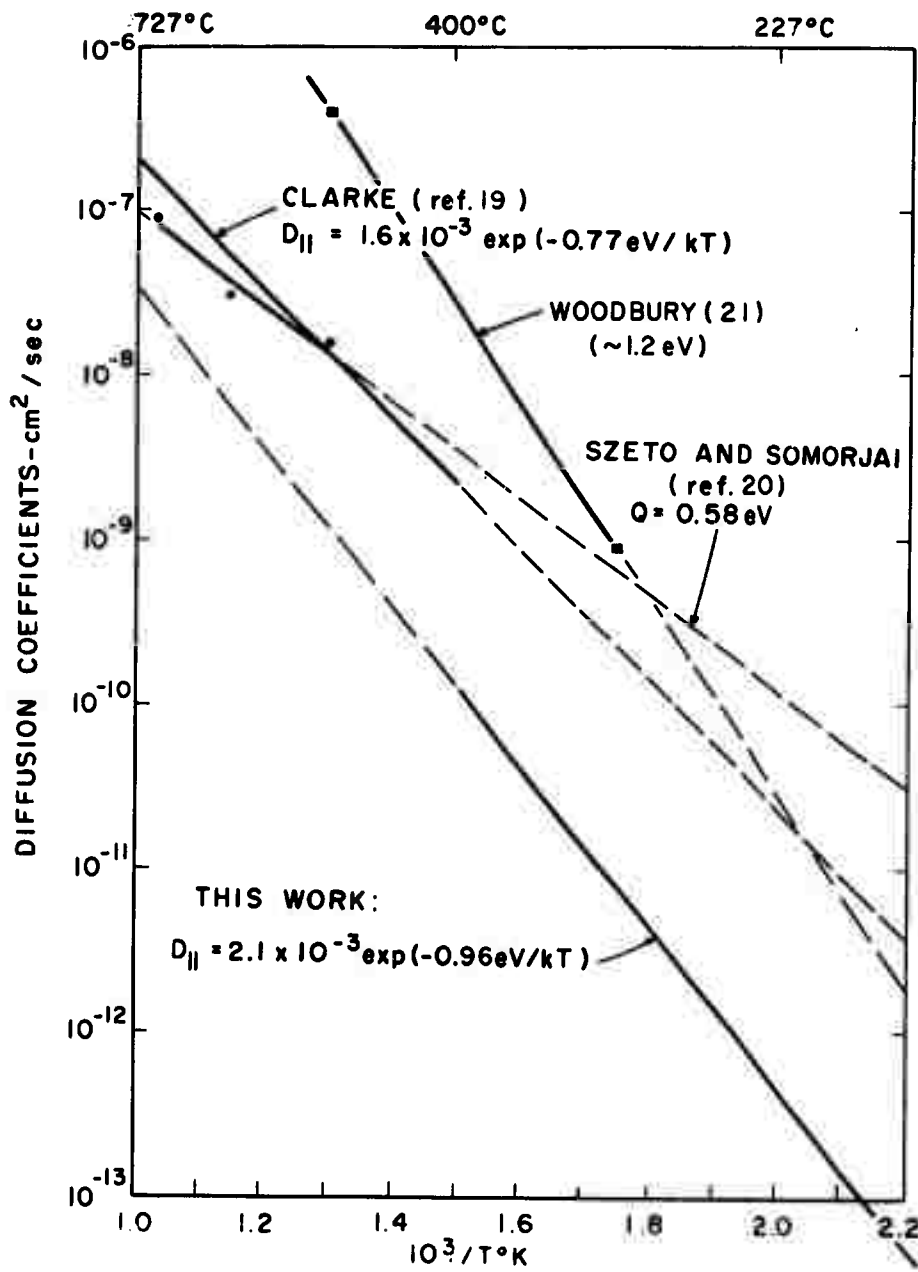


FIG. 18. DIFFUSION COEFFICIENTS; COMPARISON OF PRESENT WORK WITH PREVIOUS INVESTIGATIONS.

data, but which are compatible with our results. This type of degradation is discussed in Section 5.1.

Diffusion perpendicular to the c-axis of CdS was unexpectedly found to be about 30 times faster than that parallel to C. This anisotropy (which was highly variable among crystals) has been tentatively attributed to a larger density of dislocations oriented \perp C than \parallel C. For example, crystals plastically deformed so as to produce many edge dislocations \parallel C yielded diffusion rates in this direction about 10 times greater than that measured before deformation. This anisotropy of diffusion is one probable cause of the difficulty in interpreting diffusion measurements on thin film solar cells. Other complicating effects are the complex topology of the Cu_2S layer and the changing effective area of the i-layer as diffusion proceeds in the thickness direction as well as laterally from the Cu_2S in the grain boundaries. Nevertheless, growth of the i-layer in solar cells has been definitely established as seen, for example, in Fig. 19. The data refer to the early period of diffusion where the complicating effects have not yet developed strongly. The behavior near the end of a series of runs at increasingly higher temperatures is shown in Fig. 20. The "saturation" of $1/C^2$ is attributed to the above effects and to the fact that some parts of the i-layer have by now penetrated to the substrate. A more detailed description of the saturation effect has been given earlier. (22)

3.3.2 Solubility of Cu in CdS

The solubility of Cu in CdS in the temperature range 250 - 500°C was determined by colorimetric and spectrographic analyses of granular crystals of CdS that had been diffusion-saturated with Cu at various temperatures. Single crystals of $\sim 1 \Omega \text{ cm}$, n-type CdS were crushed and sieved and the fraction collected between 20 and 30 mesh sieves were coated with Cu_2S by the dip process. Small samples sealed in evacuated Pyrex ampoules were diffused at temperatures between 250 and 500°C for times over 2000 hrs at the lowest temperature and ~ 100 hrs at the highest temperature. Samples in each lot heated for about 1/3 the maximum times used at each temperature yielded comparable Cu concentrations, showing that the times used were sufficient to establish uniform saturation. The analyses were carried out after removing the Cu_2S surface source by repeated exposure to dilute KCN followed by thorough rinsing and drying. The results are shown in

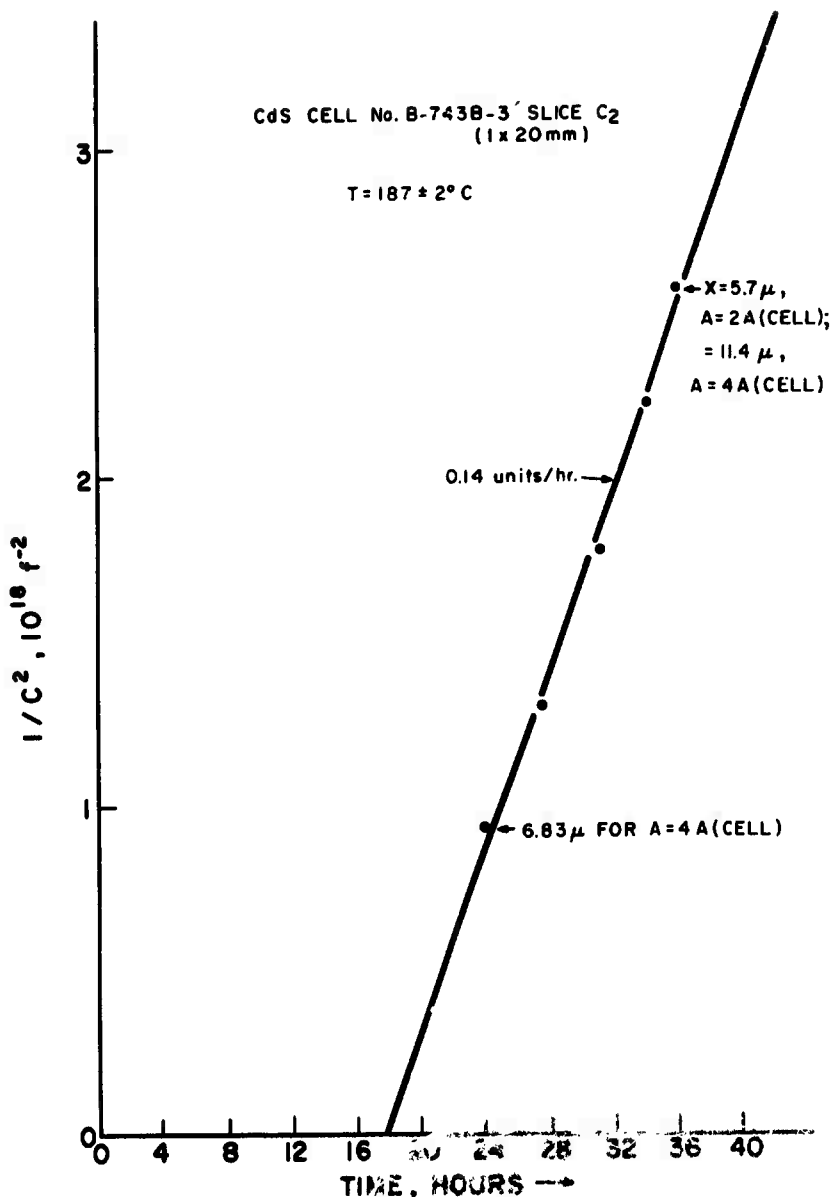


FIG. 19. SQUARE OF THE RECIPROCAL CAPACITANCE OF A SOLAR CELL SECTION AS A FUNCTION OF TIME — BEGINNING OF RUN.

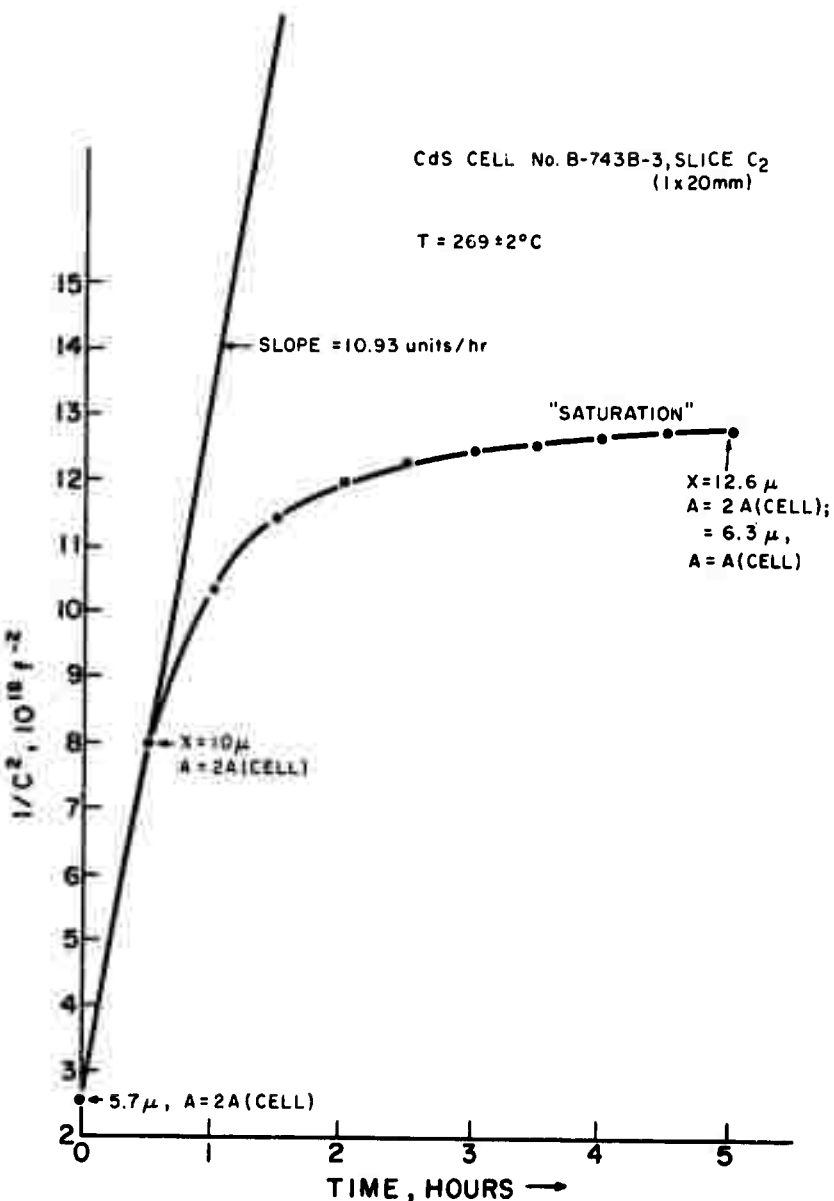


FIG.20: SQUARE OF THE RECIPROCAL CAPACITANCE OF A SOLAR CELL SECTION AS A FUNCTION OF TIME
— END PORTION OF RUN.

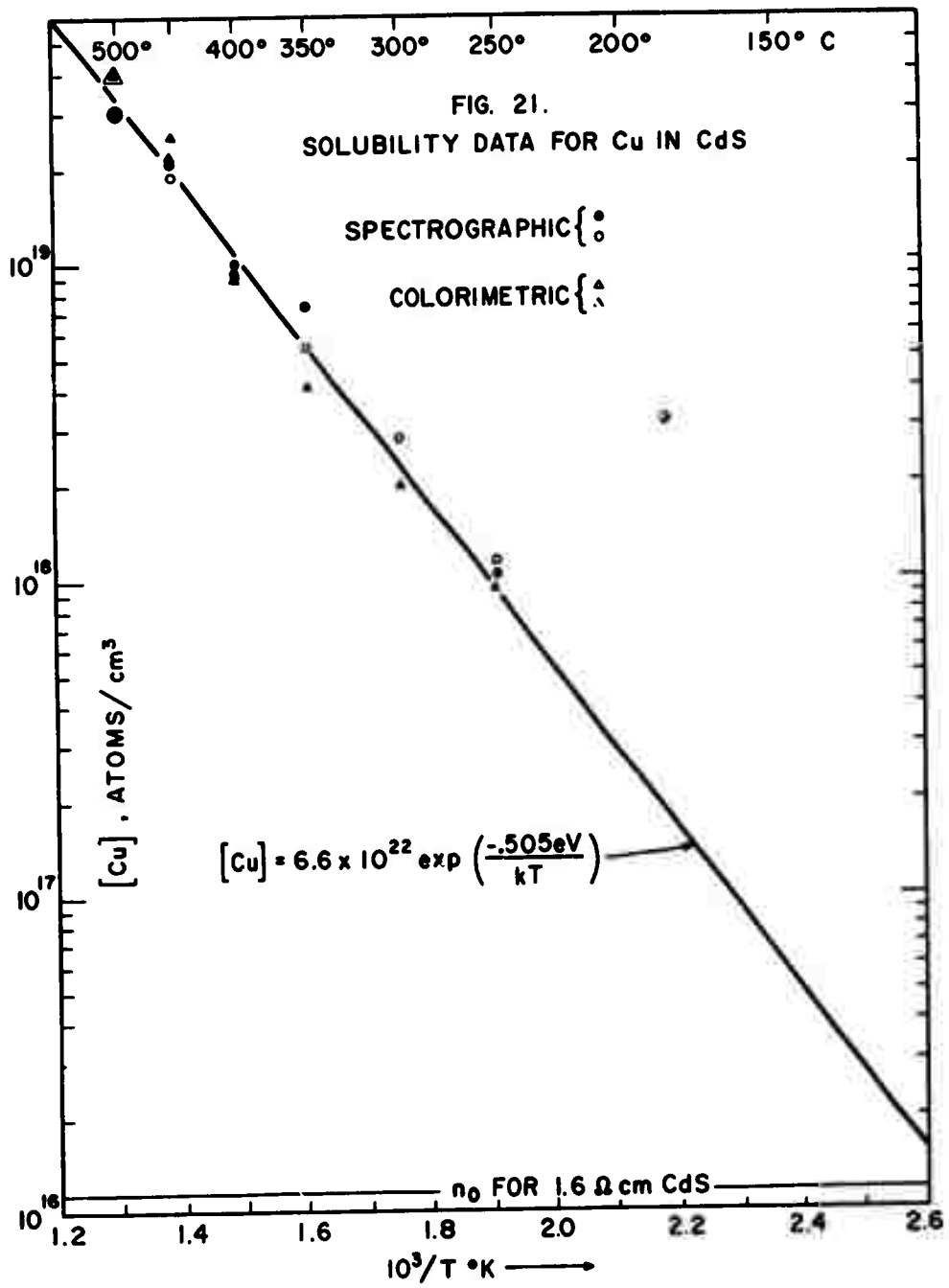
Fig. 21. It can be seen that the solubility of Cu in these crystals at 250°C (the maximum temperature that cells are exposed to during fabrication) is about 10^{18} Cu/cm³. This represents the approximate concentration of Cu in the i-CdS layer immediately adjacent to the Cu₂S layer.

In a few exploratory experiments, the solubility of Cu in CdS was found to be substantially higher for In-doped CdS. The solubility is expected to increase approximately proportional to donor doping due to the effect of compensation. The rate of growth of the i-CdS by Cu diffusion was likewise considerably decreased by increasing the donor concentration in the n-CdS due to the larger concentration of Cu needed to compensate the donors.

3.3.3 Thickness of the i-Layer in Thin-Film Cells

The thickness of the i-layer computed from the integrated time and temperature that typical cells are exposed to during fabrication (using the diffusion data for single crystals) is $\sim 0.55 \mu$. Because of the different doping in thin films and the unknown effects of grain-boundaries and stress in the CdS films, it is not clear that the 0.55μ value can be applied to the thin-film cells. Nevertheless, this value should represent a rough approximation of the true value. In attempting to obtain more direct results by capacitance measurements, it was found necessary to resort to very small cell areas because the available equipment could not reliably measure large capacitances in the presence of large dissipation (low shunt resistances). Therefore, 2 small specimens (4 mm^2 and 2 mm^2) were prepared from larger cells by carefully cutting with a razor blade. The 4 mm^2 cell had a capacitance of $286 \mu\text{uf}$ (after correction for a dissipation factor of 54%). This would imply a parallel plate spacing (presumably the thickness of the i-CdS layer) of 1.24μ . The 2 mm^2 cell had a capacitance of $171 \mu\text{uf}$ (after correction for a 14% dissipation), indicating an i-layer thickness of 1.04μ . These values were obtained taking the nominal area of the cell as the area of the parallel plate capacitor; due to the numerous folds and convolutions of the surface, one might well expect an increase of a factor of 2 or 3 in the actual area. This would then double or triple the estimates of the i-layer thickness to 2.5 and 2.1μ or 3.7 and 3.1μ .

The dark capacitance measurements of Brandhorst⁽²³⁾ indicate an i-layer thickness of $\sim 0.8 \mu$ based on an area-correction factor



of 3. Likewise, the capacitance measurements of Gill, et al⁽²⁴⁾ on crystal cells heated for 1 minute at 250°C indicates a zero bias depletion width of 0.63μ . A 2 minute treatment, as received by Clevite cells, would then have yielded a value $\sqrt{2} \times 0.63 = 0.89 \mu$. The other heat treatments normally encountered by Clevite cells would have increased this to about 1.0μ . In addition, even for single-crystal cells, an area correction of 2 might reasonably be expected since the $\text{Cu}_2\text{S:CdS}$ interface is hardly planar. A projected "depletion" width of 2μ is then obtained.

Thus, there is some disagreement about the actual thickness of the i-layer but a value near 1 or 2μ seems to be indicated. Some have questioned whether such a layer even exists as a distinct entity beyond that of a normal depletion layer. This point is discussed further in Section 4.2. We can only say here that a layer possessing the properties of a normal photoconductor and having a thickness in the range of 1μ explains the observed properties of the cell, and that such a layer treated as a normal depletion layer cannot account for the observations, especially the spectral response measurements discussed in Section 3.6. The results given in Section 3.5.8.1 clearly show that moderately strong photovoltaic response can be obtained from crystal cells when all of the CdS is in the compensated state; i.e., when no n-type CdS is present and the i-layer is $> 500 \mu$ thick.

3.3.4 Optical Transmission of Cu-Saturated CdS Crystals

Several early models^(25, 26, 27) have invoked absorption at impurity centers of impurity bands in the CdS layer to explain the long-wavelength response of the CdS cells. Our long familiarity with the appearance of Cu-doped single crystals indicated that such could not be the case the crystals being too light in appearance to account for appreciable extrinsic absorption. In order to demonstrate this point, two thin single crystals (0.185 and 0.250 mm thick) were diffusion-saturated with Cu from a Cu_2S surface source by heating for 2472 hours at 250°C. After removing the Cu_2S with a KCN solution, the crystals were polished and transmission measurements were made with a Bausch and Lomb grating monochrometer. The results, uncorrected for reflection losses, are shown in Fig. 22. After heat treatment, one of the crystals was noticeably darker than the other, perhaps due to a slight difference in impurity content or precipitation of Cu_2S .

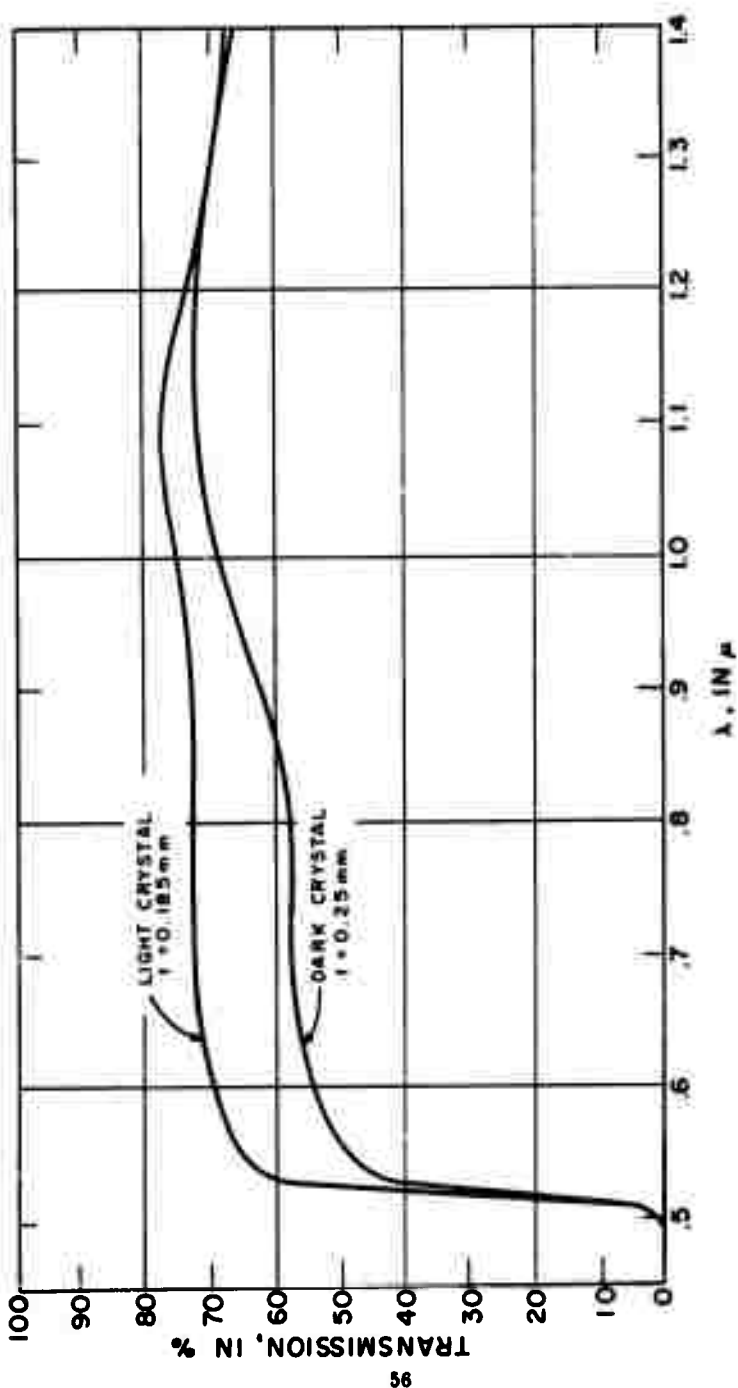


FIG. 22. TRANSMISSION SPECTRUM OF CdS CRYSTALS SATURATED WITH Cu AT 250°C.

In both cases, however, the extrinsic absorption is seen to be far too small to account for the current delivered by the cells, remembering that the Cu-compensated layer in the real cells is about two hundred times thinner than these crystals. The transmission curve of the light colored crystal is in fact almost identical to un-doped CdS. The $\sim 70\%$ transmission in the extrinsic range is completely accounted for by the $\sim 30\%$ reflection losses computed from the known refractive indices of CdS.

It should be noted, however, that extrinsic absorption in double-doped CdS e.g., In + Cu, is substantially larger than that in Cu-doped crystals, the degree depending on the concentration of In. This fact correlates with the much broader spectral response of photoconductivity of double-doped crystals and the larger solubility of Cu in such crystals. However, the absorption in double-doped crystals is still far too small to account for the observed current delivered by the solar cells.

3.3.5 Growth and Decay of Photoconductivity in Cu-Compensated CdS

The spectral response of the two crystals described above consists of a single, narrow, 150 \AA , peak at the band edge of CdS, $\sim 5150\text{ \AA}$. This response is nearly identical to the spectral response of S-compensated CdS crystals. The growth and decay of photoconductivity of the darker of the two crystals are shown in Figs. 23 and 24. The slow rise time of this rather insensitive crystal is due mainly to the low intensity of the exciting light. The decay curve shows several distinct segments having different power-law dependence. The initial slow decay is anomalous and may be an artifact due to the limited response speed of the X-Y recorder.

These curves show a typical property of photoconductors at low light intensities: although substantial changes in light-to-dark resistance ratios are obtained, the time necessary to achieve these ratios is exceedingly long. The rise time is slow because of the low density of hole traps and/or small capture cross-sections. The decay is slow because the depth of the hole traps requires long thermal emptying times. The time constants change during decay because traps of varying depth are present, the shallow traps emptying first. The slow rise and decay of photoconductivity gives rise to the transient photovoltaic effects discussed in Section 3.6.5. The detailed

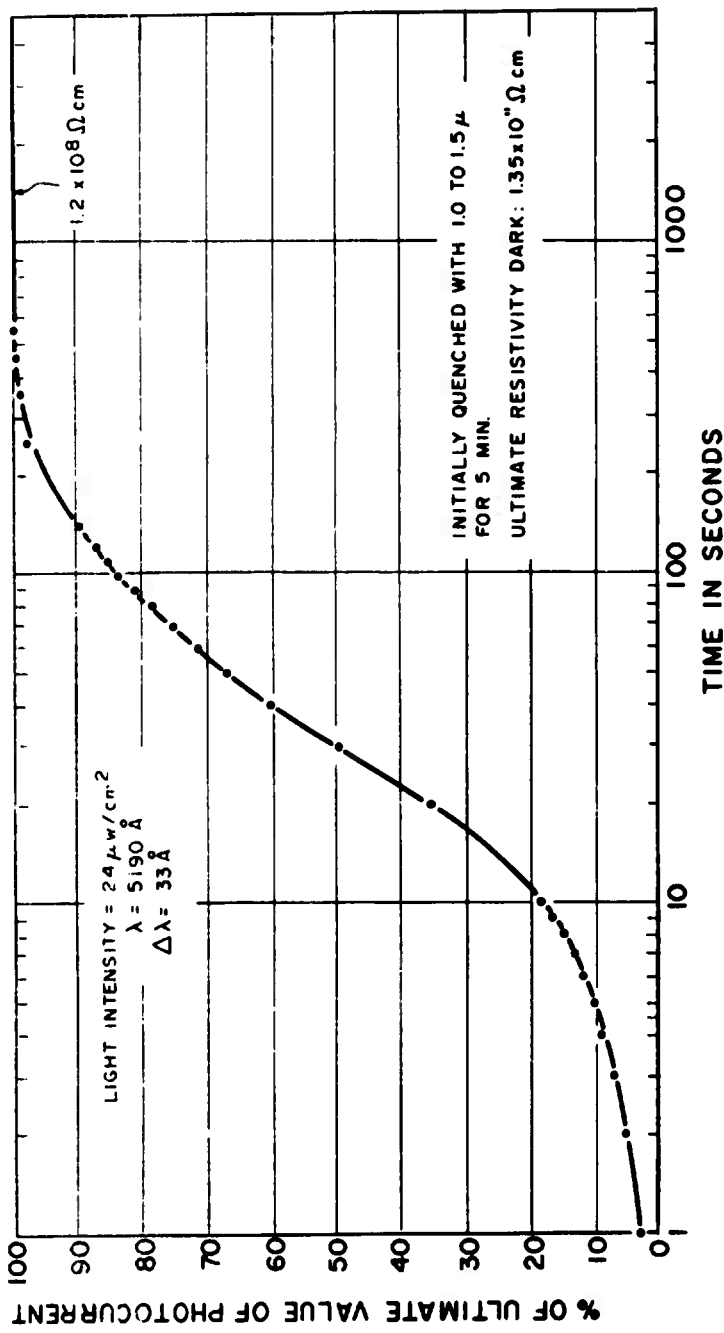


FIG. 23. GROWTH OF PHOTOCOCONDUCTIVITY OF CdS SATURATED WITH Cu AT 250°C

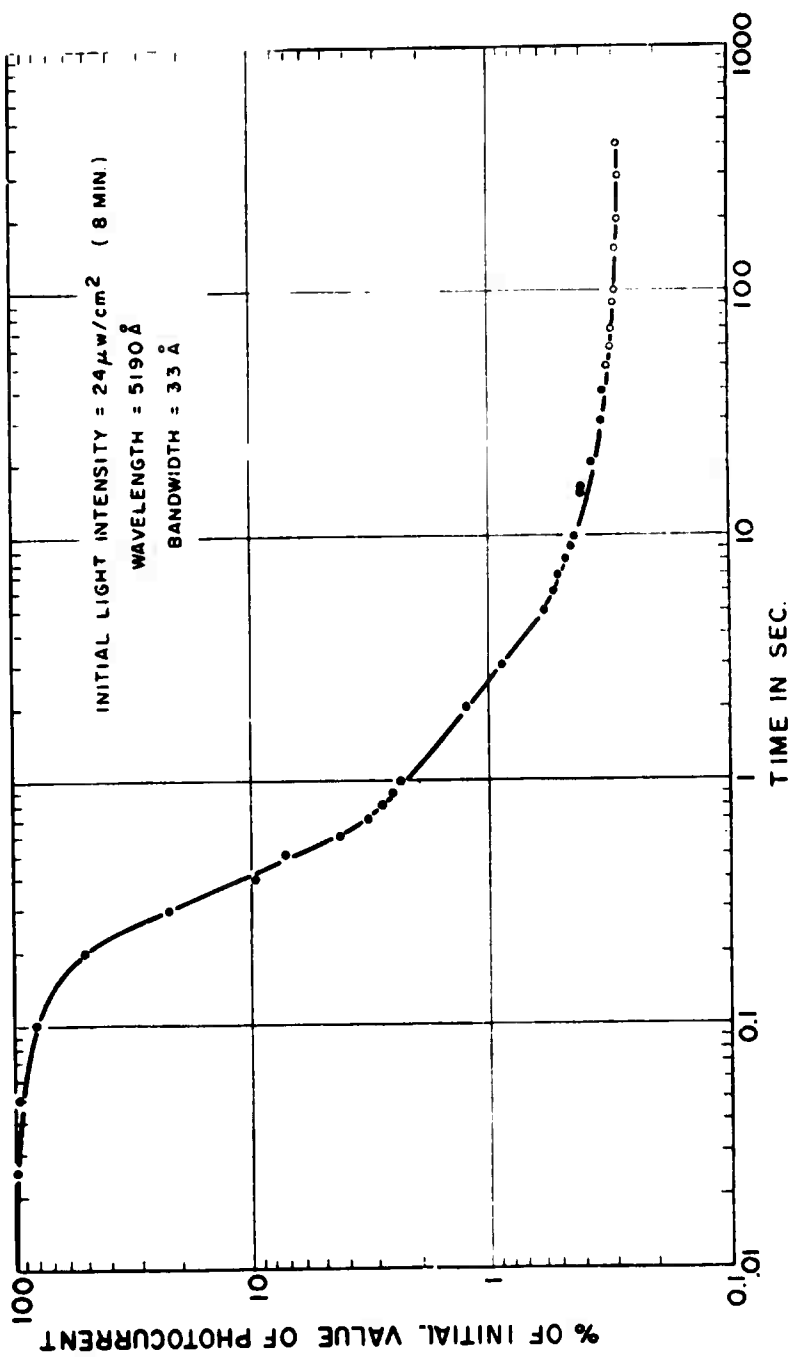


FIG. 24. DECAY OF PHOTOCONDUCTIVITY OF CdS SATURATED WITH Cu AT 250°C

effect of changes in the photoconductive excitation spectrum that results from donor doping of the CdS is discussed in Section 3.6.

3.4 The n-CdS Layer

3.4.1 Grain Structure and Crystallographic Orientation of CdS Films

CdS cells without covers or grids have been beveled by low-angle lapping and polishing techniques in an effort to magnify the cross-section, in particular the region of the Cu_2S layer and directly beneath it where the i-CdS layer is expected to lie. It was thought that once this sectioning technique was perfected, it would then be possible to locate the insulating CdS by electroplating copper to the rest of the surface (conducting), or perhaps by etching techniques.

At first, curved cells were polished on flat surfaces (or else flat cells were polished on cylindrical surfaces of known radius) with the idea that the angle of bevel might be easily calculated by simple geometry. However, the irregular "wavy" behavior of the surfaces of cells has made this approach impracticable; polishing of nominally flat cells on flat surfaces gave comparable results. Thus far no direct measurements of the thickness of the i-CdS layer have been made; but several other structural features have been clearly delineated. Most important, the grain-boundary structure of the evaporated CdS layer viewed parallel to the film thickness (the direction of film growth) has been unambiguously revealed. Figure 25 is a photograph of a polished surface which clearly shows the individual grains (crystals) of CdS. The circumstance that controls the visibility of the boundaries is this: As the high points of the film are polished away, a level is reached at which the surface is smooth and nearly continuous but which is not yet polished deep enough to have removed the Cu_2S that surrounds each grain close to the initial surface. Partial removal of the Cu_2S within the grain boundaries by a short exposure to a dilute KCN solution improves the visibility of the grains. The photograph was taken by reflected light with a Leitz Ortholux microscope on Polaroid film at 1600X magnification using an oil immersion objective. The grain boundary structure can also be seen on fully polished surfaces without etching if phase contrast microscopy is employed at 500 or 1000X. Slight difference in the polishing rates of differently oriented grains is believed to be responsible for the contrast obtained by the latter technique.

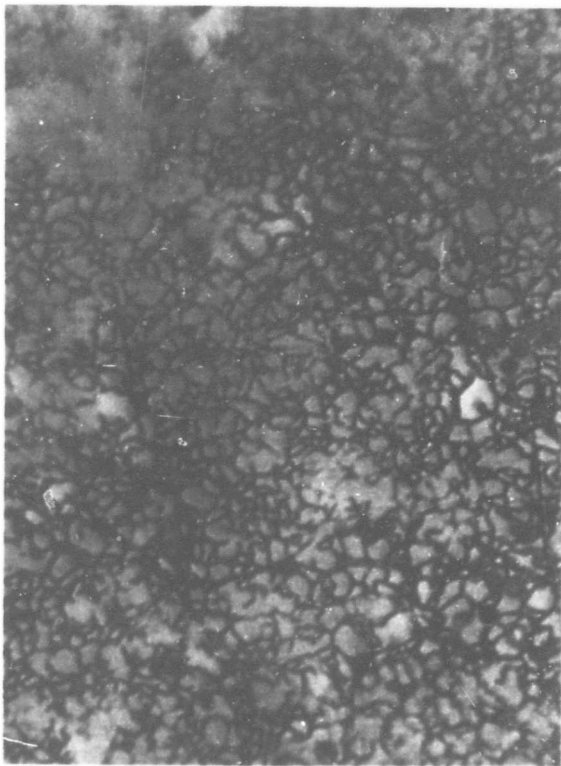


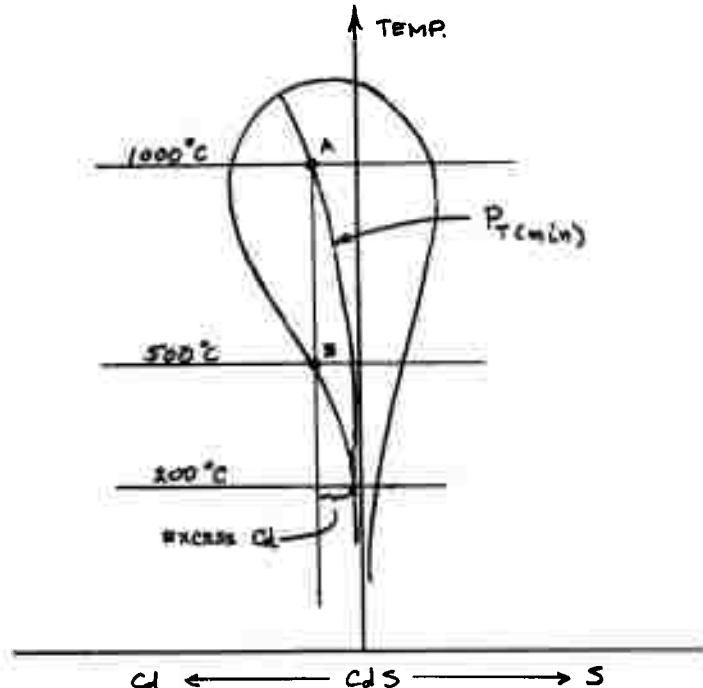
FIGURE 25. GRAIN BOUNDARY STRUCTURE OF VACUUM DEPOSITED CdS LAYER; VIEW PARALLEL TO FILM THICKNESS AFTER POLISHING AND LIGHT ETCHING (1600X).

The grain size in Cell No. H-71B5, a small portion of which is shown in Fig. 25, is approximately two microns but many grains are smaller and some are as large as $5\text{ }\mu$. These can be compared to the typical film thickness of $20\text{ }\mu$. Among cells, 2:1 variations have been found in mean grain size and also differences in size distribution about the mean. The lateral cross-sections shown in Fig. 3 (especially the 20 second dipped specimen) illustrates the penetration of Cu_2S in the grain boundaries. The grain size and distribution in that figure correlates approximately with those in Fig. 25. The grain-boundary structure in the lateral cross-section have also been revealed by careful etching with aqueous HCl of cross-sections such as that shown in Fig. 2. The vertical columnar structure is clearly revealed after such etching, especially when viewed in phase contrast. The region next to the substrate is composed of many more crystals than the region further up. The growth rate of the CdS crystallites is apparently substantially greater in the + c direction than in any other direction. Only those nuclei which have their + c axis disposed perpendicular to the substrate survive the competition for space as growth proceeds, the inclined crystals all running into their neighbors terminating their growth. The grains grow laterally only to the extent of filling the available space. For example, the shapes of the grains in Fig. 25 do not conform with those expected for films that had undergone further grain growth. The characteristic circular arcs and the 120° three-rayed inter-sections are almost wholly absent. Appreciable grain-growth would not, of course, be expected at the low film forming temperature of 220°C .

That the c-axes of the CdS grains are substantially oriented, and that the sense of the c-axis is also substantially the same for all grains, can be inferred from the strong piezoelectric activity of such films when they are compensated. A one-year exposure of $3'' \times 3''$ cells at 150°C in vacuum resulted in all of the n-CdS being compensated. Because of the preferred orientation of the grains, these cells were strongly piezoelectrically active--sounding much like a "tweeter" for example when connected to the output of a hi-fi set.

3.4.2 The Non-Stoichiometry of Vacuum Deposited CdS

It is a general observation that darkly colored, highly conducting films of CdS are produced when CdS is vacuum sublimed and deposited on substrates at temperatures less than $\sim 150^\circ\text{C}$. Even when the substrate temperature is raised to $\sim 200^\circ\text{C}$, where acceptable films are produced, the resulting films have a free electron concentration about ten times greater than that of single crystals grown from the same source of CdS under near-equilibrium conditions. Recent studies⁽²⁸⁾ of precipitation phenomena in CdS single crystals have established the qualitative shape of the solid stability field of the Cd:S system, and these results provide an explanation of the results described above. The solid stability field is shown in the following drawing:



When CdS is freely sublimed in an open crucible at some high temperature, such as 1000°C, the composition of the CdS tends to approach point A on the minimum-total-pressure line independent of the initial starting composition. The CdS at this point is slightly rich in Cd (in the form of S vacancies). This particular composition yields, upon sublimation, vapor of an identical composition; i. e., this solid sublimes congruently. The composition of this vapor lies outside of the single-phase stability field at temperatures below ~ 500°C (point B in the above drawing). Consequently, if deposition is attempted on substrates held below this temperature, the excess Cd must be either rejected from the film or incorporated in the film as a second phase. At temperatures above ~ 200°C most of the excess Cd either does not "stick" to the film or else is re-evaporated from the surface. At lower temperatures larger fractions of the excess Cd are incorporated in the film as elemental Cd or as quenched-in interstitial Cd. We note that as the rate of deposition is decreased, less and less excess Cd is incorporated in the film--the excess Cd having increasing opportunities to escape. Likewise, the simultaneous evaporation of S from a separate source allows the formation of yellow, single-phase films even when the substrate is near room temperature. With a sufficient rate of impingement of excess sulfur, insulating films result; i. e., the composition of the film can be shifted to the S-rich side of the stoichiometric composition.

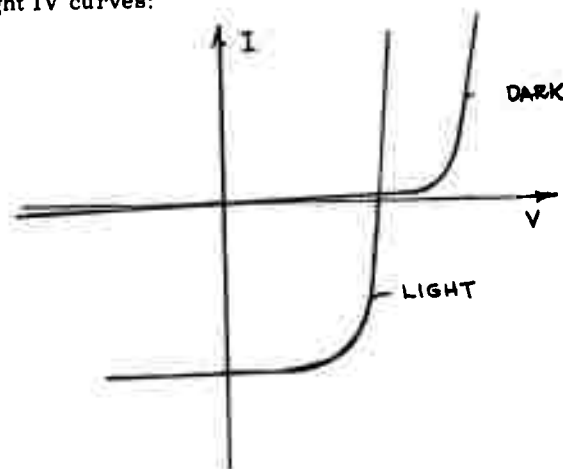
This analysis indicates that CdS films for solar cells could be produced at low substrate temperatures if a small amount of sulfur were simultaneously evaporated with properly doped CdS. Potential benefits of a lower substrate temperature include: (1) reduced curling of the films because of lower differential thermal contraction, (2) less cracking in the CdS films which should reduce the subsequent formation of Cu_2S shunting paths to the metallized substrate and thereby improve cell voltage and low-light-level response, and (3) smaller CdS grain size which should increase light absorption without an increase in Cu_2S layer thickness; and hence result in an improvement in current output and efficiency.

3.5 The IV Characteristics of CdS Solar Cells

3.5.1 The Light-to-Dark IV Cross-Over Effect

One of the earliest phenomena observed for CdS solar cells which distinguished this type of cell from conventional Si solar cells and which

thereby forms one of the key tests of all proposed models is the crossing of the dark and light IV curves:



All cells that have received heat treatments show this effect. Gill, et al., (24) have shown that this effect does not exist for unheat-treated cells. One thereby concludes that the cross-over effect is connected with the presence of the i-CdS layer. The Clevite model says that this effect is due to changes brought about by the photoconductive properties of the i-layer: (1) the resistance of the i-layer is substantially reduced by light, (2) the quasi-Fermi level is thereby raised close to the bottom of the conduction band of CdS, and (3) the barrier height is thereby reduced from 1.2 eV to 0.85 eV. An objection to the last point raised by the group at Stanford is discussed in detail in Section 4.3, hence the main discussion of this effect is deferred to that section.

One particularly significant observation which strongly supports the Clevite model is the transient properties of the cross-over effect: If a cell is strongly illuminated, and an IV curve is traced immediately after the light is turned off, the dark curve is almost the same as the light curve displaced upwards by I_{sc} . Successive curves traced immediately after gradually move over to the static dark curve, the displacement being fast at first (< 1 sec) and very slow as the limiting curve is approached (10-100 sec). We associate this with the decay of photoconductivity in the i-layer, the time constants for both effects being much alike.

3.5.2 Temperature Dependence of IV Characteristics

The IV characteristics at 10°C intervals from 25°C to 100°C both in air and under vacuum have been measured on selected 3" x 3" thin-film solar cells. The particular cells used in this test include a "typical" standard process cell and several cells which had been exposed to temperature environments known to degrade power output. The test included a small single-cell environmental chamber with a cell heater to allow temperature control, an illuminator yielding light equivalent to air-mass-one sunlight, a Spectrolab electronic load, and an X Y recorder. A test cell was connected to insulated leads that passed through the walls of the environmental chamber and was lightly fastened to the area heater with a thin layer of silicone grease. A thermocouple was spring-loaded against the cover plastic at the center of the cell, and the thermocouple bead was embedded in silicone grease to improve the thermal contact to the cell. The environment chamber was then placed below the illuminator and connected to the peripheral instrumentation. With the cell held at 25°C, the illumination intensity was adjusted to yield a short-circuit current that agreed with the measurement previously made on the cell in the standard test block at 25°C; this compensated for the light-loss in the chamber cover plate. A family of IV characteristics were then recorded, alternately under one atmosphere of air and under vacuum, at each temperature as the temperature was incrementally increased. At the end of each series, the 25°C curves were retraced in order to detect any irreversible changes. No differences were found.

The family of IV characteristics for cell No. N110AK4 are shown in Fig. 26, and a reduced form of the data is shown in Fig. 27. This Kapton covered standard process cell had typical 25°C output characteristics. It may be seen that the short-circuit current remained essentially constant from 25°C to 80°C, and then decreased slowly with increasing temperature. Only minor differences were found for measurements in air and in vacuum.

The open-circuit voltage decreased slowly at first, then at an increasing rate as the temperature increased. The efficiency decreased slightly faster than the open-circuit voltage from 25°C to 80°C, due to a small

CELL No. NI10AK4

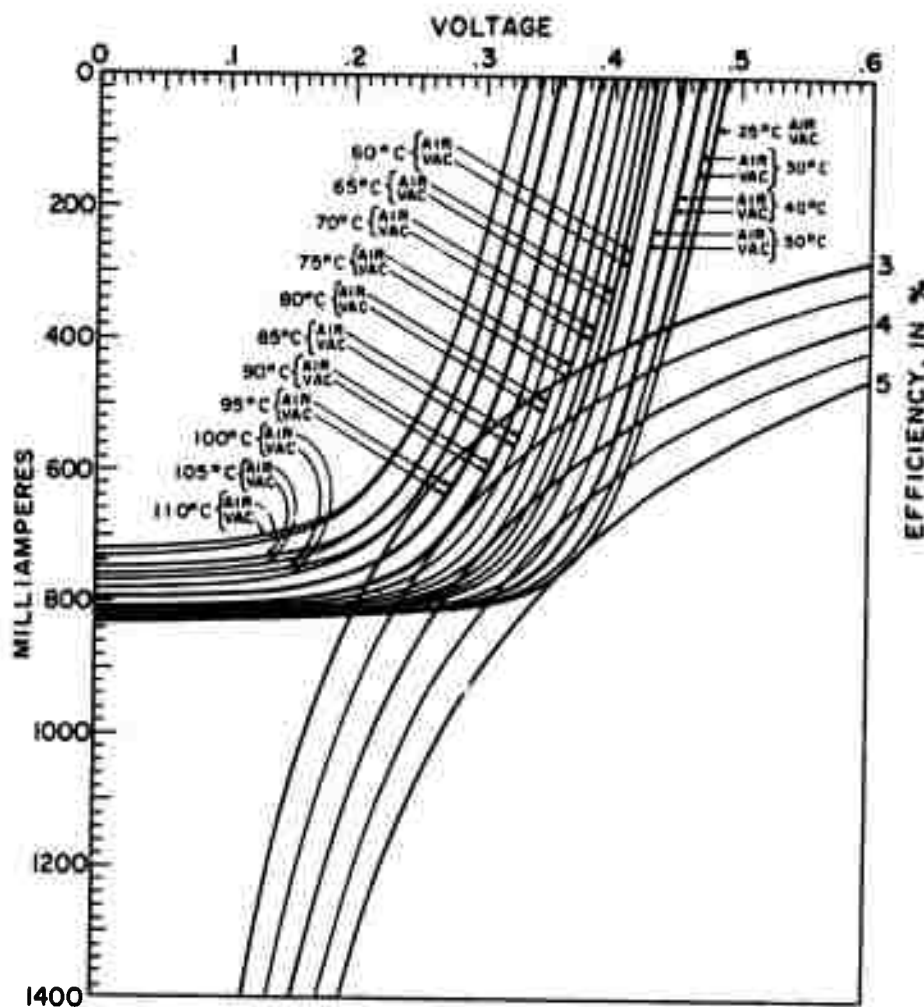


FIG. 26. IV CHARACTERISTICS AS A FUNCTION OF TEMPERATURE.

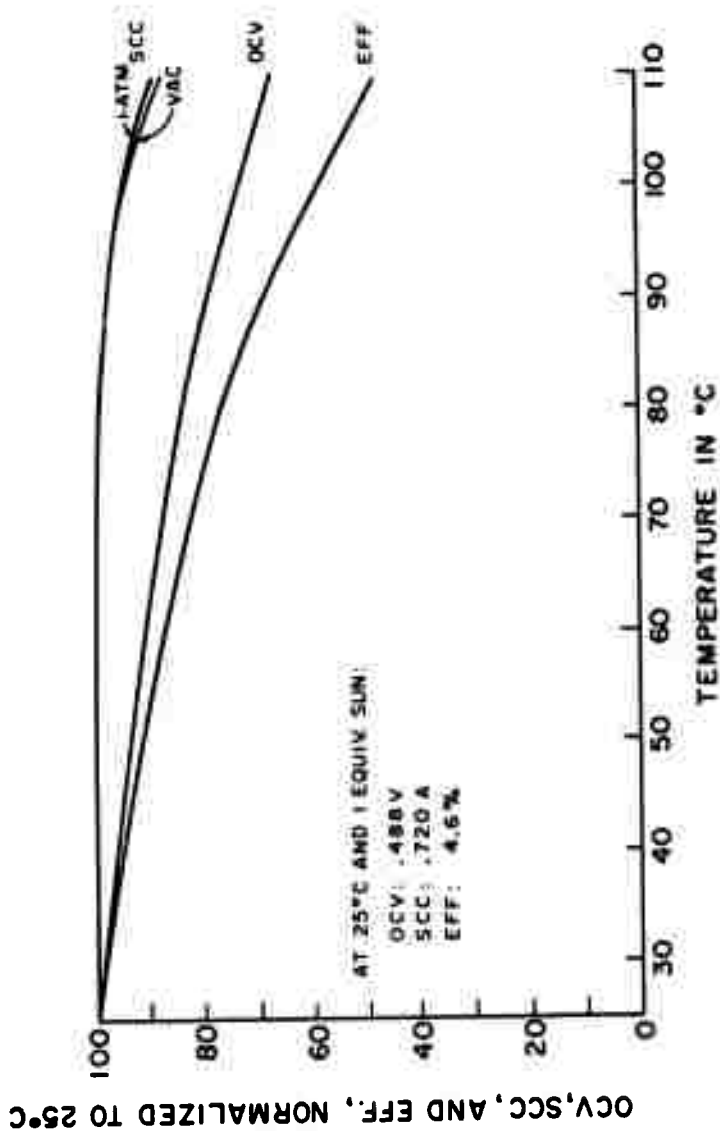


FIG. 27. OPERATING PARAMETERS vs. TEMPERATURE
 No. NI0AK4 - STD. PROCESS CELL

loss of squareness, and then degraded faster at higher temperatures because of the loss of short circuit current as well as voltage. The relatively small loss of squareness apparent in the family of IV characteristics over the entire temperature range coupled with the loss of short circuit current above $\sim 30^{\circ}\text{C}$, indicates that the power loss above this temperature is due to (1) a loss of effective cell area, (2) a decrease in light absorption in the Cu_2S layer, or (3) an increase in recombination rate in or on the surface of the Cu_2S layer.

The loss of I_{sc} at high temperatures indicates that chemical or mechanical changes are occurring in the cell as the cell temperature is changed. The reversibility of the effect indicates that mechanical changes or changes in the recombination rate in the Cu_2S layer are responsible, the latter being somewhat more probable since no obvious mechanical loosening was detected.

Although the data are not shown, similar experiments were carried out on a thermally cycled (and degraded) cell. The significant difference for this cell was that the loss of I_{sc} without loss of squareness began as soon as the cell was heated above room temperature.

3.5.3 Light Intensity Dependence of IV Characteristics

The IV characteristics of several solar cells were measured at half-decade increments of illumination intensity from 30 mV/cm^2 to $3 \mu\text{W/cm}^2$. The light intensity was varied by changing the distance between the cell and a 500-watt tungsten-iodine lamp and was measured with an Epply Normal-Incidence Pyroheliometer. The IV characteristics were generated by the customary technique of bucking the cell output against the output of an artificial load while recording the current drawn by the load and the voltage appearing across the cell terminals.

The IV characteristics as a function of illumination intensity of a typical $3'' \times 3''$ thin-film solar cell and a 1 cm^2 ceramic solar cell measured by this method are shown in Figs. 28 and 29. Because four orders of magnitude of current were measured, necessitating a semi-log plot, the curves are distorted to the extent that apparent squareness is maintained even on those curves which would be straight lines in the usual linear display. To compensate for the exaggerated squareness, the locus of maximum

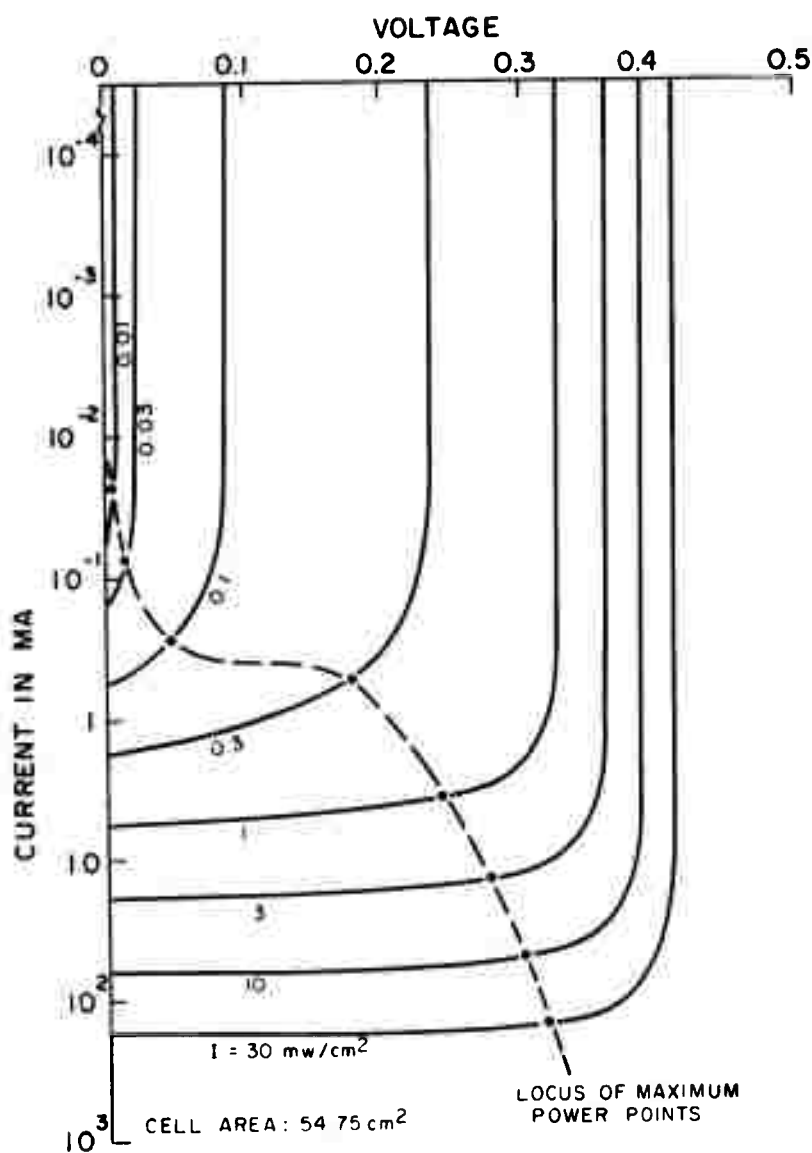


FIG. 28. IV CHARACTERISTICS vs. ILLUMINATION INTENSITY
 "TYPICAL" STANDARD PROCESS THIN CdS
 SOLAR CELL No. H337B7.

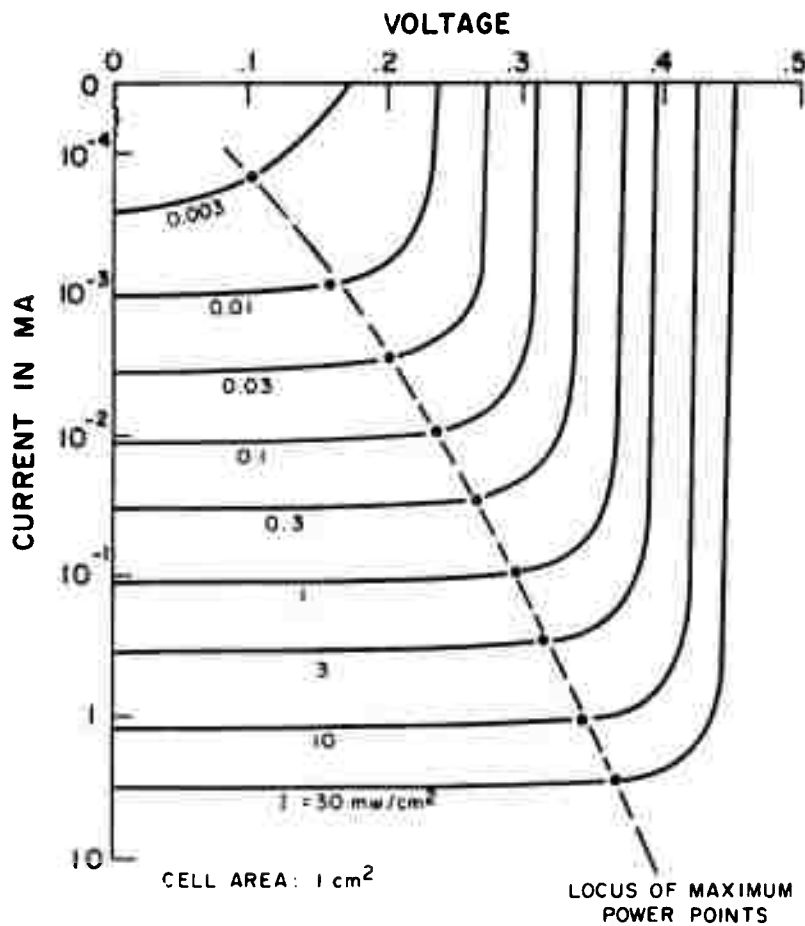


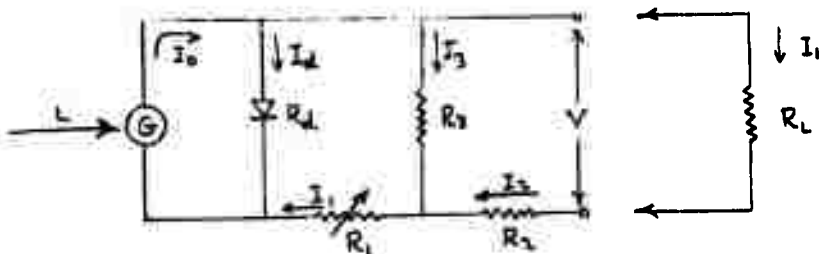
FIG. 29. IV CHARACTERISTICS vs. ILLUMINATION INTENSITY
CERAMIC CdS SOLAR CELL No. 28-10.

power points is also shown. The open circuit voltage, short circuit current, efficiency, power, and output resistance as a function of illumination intensity for each cell are shown in Figs. 30 and 31.

The behavior of thin-film cell, No. H337B7, shown in Fig. 30, was representative of the thin-film solar cells measured to date. The short-circuit current is a straight line at approximately 45° , which on the log-log plot indicates a linear dependence on intensity over the entire range covered. The open circuit voltage at the higher illumination intensity levels is approaching a consistent limiting value, but with decreasing intensity reaches a break-point where it rolls off to a nearly linear dependence. The voltage and current at the maximum power point essentially parallel the open circuit voltage and the short circuit current respectively, and are not shown. The power at the maximum power point at the higher intensities is approaching a linear dependence on intensity, but at lower intensities, passes a break-point and becomes approximately proportional to the square of the intensity. The efficiency, approximately paralleling the open circuit voltage, drops from a nearly constant value at higher intensities to a linear relationship at lower intensities.

Analysis of Results

An equivalent circuit that describes most of the characteristics of the CdS cell is shown below.



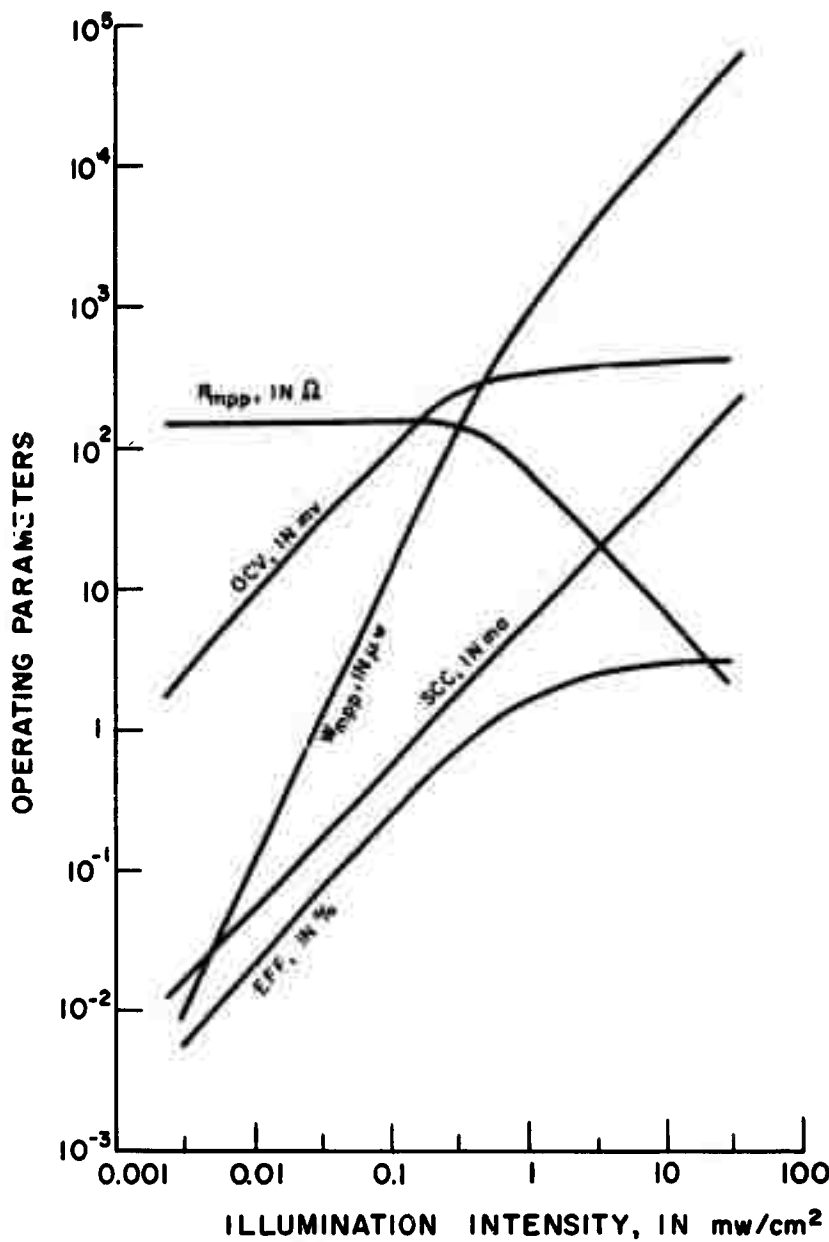


FIG. 30. OPERATING PARAMETERS vs. ILLUMINATION INTENSITY
 "TYPICAL" STANDARD PROCESS THIN FILM CdS
 SOLAR CELL No. H337B7.

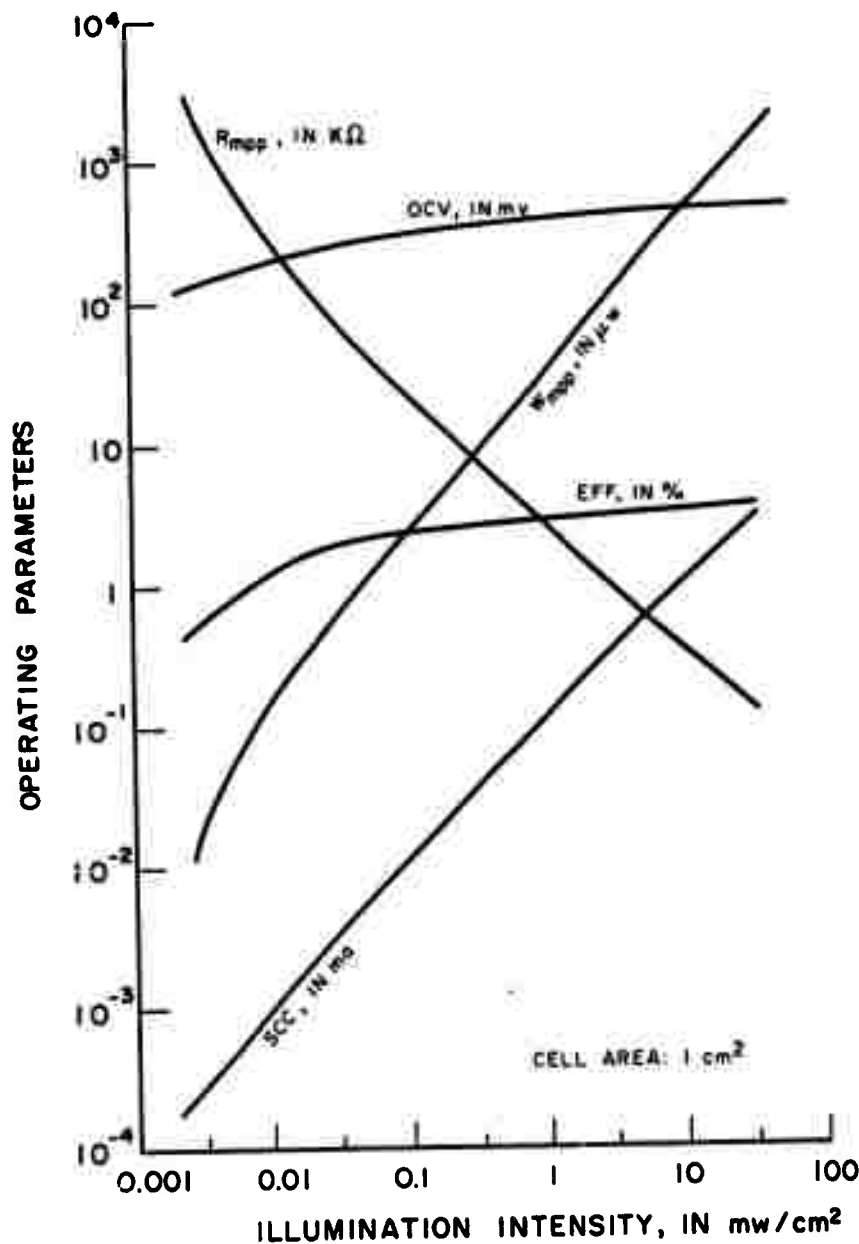


FIG. 31. OPERATING PARAMETERS vs. ILLUMINATION INTENSITY
CERAMIC CdS SOLAR CELL No. 28-10

The constant current generator represents the optical generation of hole-electron pairs in the Cu_2S layer. The current passing through the shunting diode represents that part of the generated current that is lost due to recombination in the Cu_2S layer and at interface states. R_d is the effective resistance of the diode and is strongly and non-linearly dependent on the voltage that appears across it. It is the inverse of the differential slope of the true IV curve of the $\text{Cu}_2\text{S}:i\text{-CdS}$ junction. This curve is the one that would prevail in the dark if all of the other resistive elements were absent and the barrier height remained the same. It is superficially the same as the IV photovoltaic curve measured at high light intensities (with the current origin displaced to I_{sc}). The diode alone would have a higher shunt resistance and a lower series resistance than that indicated by the high intensity curve. R_1 is the resistance of the $i\text{-CdS}$ layer and is approximately inversely proportional to light intensity, L . R_2 is a lumped resistance which corresponds to the series resistance introduced by the grid, the Cu_2S layer, the $n\text{-CdS}$ layer, the metallized substrate, and their contacts. In most cells, R_2 is very small and can be neglected. R_3 is the lumped shunt resistance of the distributed shorting paths that occur between the grid and the $n\text{-CdS}$ layer, between the Cu_2S layer and the metallized substrate, and occasionally between the grid and the substrate. R_2 and R_3 are constants for a given cell and are independent of L (the photoconductive shunt, which has been observed on rare occasions, is ignored in this analysis). Because R_d depends on voltage which in turn depends on L , R_d is indirectly dependent on L . R_L is, of course, the external load resistance.

It will be helpful to list typical values and ranges for these circuit elements. For standard 3" x 3" cells:

$$R_1 = 0.01 \Omega @ 1 \text{ sun, } \alpha CL^{-1}$$

$$R_2 = 0.01 \Omega (0.01-0.02)$$

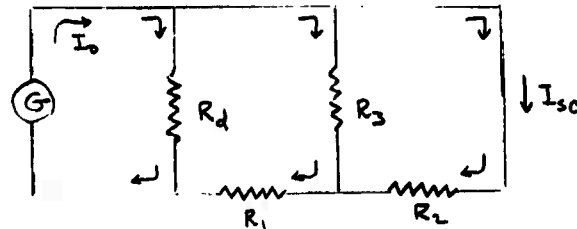
$$R_3 = 100 \Omega (10-1000)$$

$$R_d = > 10^5 \Omega @ < 0.2 \text{ volt; } 0.05 \Omega @ 0.45 \text{ volts}$$

The experimental results will now be compared to the results expected from the equivalent circuit, first under short-circuit conditions, then under open-circuit conditions, and finally under variable-load-conditions--and in particular under optimum-load conditions.

Short-Circuit Conditions

With $R_L = 0$, the equivalent circuit takes the form:



It is easily shown that the short-circuit current is given by

$$I_{sc} = I_o \left[\frac{R_d R_3}{R_d (R_2 + R_3) + R_2 R_3 + R_1 (R_2 + R_3)} \right].$$

For most cells, $R_2 \ll R_3$; and the general expression reduces to:

$$I_{sc} = I_o \left(\frac{R_d}{R_d + R_2 + R_1} \right).$$

This shows that if $(R_2 + R_1) \ll R_d$, $I_{sc} = I_o$; and since I_o is proportional to light intensity (at constant spectral distribution), the observed linear dependence of I_{sc} on L would then be compatible with the equivalent circuit. This condition is clearly fulfilled since R_2 is very small and $R_1 = 0.01 \Omega$ at $L = 100 \text{ mW/cm}^2$ increases at most linearly with decreasing L . Therefore, at the lowest intensities tested ($L = 3 \times 10^{-3} \text{ mW/cm}^2$), $R_1 \approx 0.01 (10^2 / 3 \times 10^{-3}) \approx 300 \Omega$ -- which is much less than $R_d (> 10^5 \Omega)$ at this value of L . At higher values of L , R_1 and R_d both decrease but R_d never becomes as low as R_1 -- although it approaches it at $L = 100 \text{ mW/cm}^2$.

It is relevant to consider whether the values of R_1 used in this analysis are reasonable. The resistance of the i-CdS layer under 1 sun illumination was taken as $R_1 = 0.01 \Omega$. Using this value, the resistivity can be estimated from the thickness of the i-layer, $\sim 10^{-4} \text{ cm}$ (obtained from capacitance measurements), and its area, 10^2 cm^2 , which is about twice the cell because of the convolution at the surface of the cell:

$$\rho = R_1 A / t = 10^{-2} \cdot 10^2 / 10^{-4} = 10^4 \Omega \text{ cm.}$$

This is a reasonable value because compensated single crystals have typical resistivities of $\sim 10^3 \Omega \text{ cm}$ under one sun illumination and the absorption in the Cu_2S layer reduces the intensity of the light reaching the i-CdS layer by a factor of about 10 ($\alpha \approx 10^5 \text{ cm}^{-1}$ and $t(\text{Cu}_2\text{S}) = 0.3 \mu$). The resistivity at the lowest light level used is $\sim 10^9 \Omega \text{ cm}$, which is also reasonable since the dark value of compensated crystals is typically $\sim 10^{10} \Omega \text{ cm}$.

Open-Circuit Conditions

From the equivalent circuit under open-circuit conditions ($R_L = \infty$, $I_2 = 0$), the expression for the open-circuit voltage is derived to be:

$$V_{oc} = I_o R_3 \left[1 - \frac{R_1 + R_3}{R_d + R_1 + R_3} \right]$$

At very low light levels, the diode is forward biased to only a small voltage and its effective resistance under these conditions is $> 10^5 \Omega$. Therefore, $R_d \gg (R_1 + R_3)$; and the second term in the bracket is $\ll 1$. This reduces the general expression to: $V_{oc} = I_o R_3$. Since I_o is proportional to L , and R_3 is a constant, V_{oc} should vary linearly with L at low light levels. This is seen to be closely approximated for the standard cell shown in Fig. 30. It was also found to be true for several other standard cells whose behavior was very similar to the one shown except that R_3 was somewhat different for each cell. A linear variation of V_{oc} with L was not observed for the ceramic cell, shown in Fig. 31, because in this case the lumped shunt resistance R_3 was extremely large (a characteristic of ceramic cells which we associate with the large thickness of the CdS) and the condition $R_d \gg (R_3 + R_1)$ was not fulfilled even at the lowest intensities. The non-linear behavior of R_{mp} at very low light intensities is probably due to the limited input impedance of the measurement circuit. The observed drop off of V_{oc} , W_{mp} , and Eff. at low light levels is also attributed, at least in part, to this effect.

Returning to the behavior of the standard cell (Fig. 30), we note that as L increased beyond $\sim 0.3 \text{ mW/cm}^2$, the forward bias on the diode increased and moved into the "knee" of the IV curve. R_d decreases rapidly with increasing L in this region, and beyond the knee assumes the low values characteristic of the forward region. As R_d approaches $(R_1 + R_3)$, the second term in the bracket becomes appreciably and increasingly less

than unity, and V_{oc} , therefore, does not increase as rapidly as I_o . Since R_d decreases very rapidly in this region the deviation from linearity occurs rather suddenly, as seen in Fig. 30. The "break-point" corresponds roughly to the condition $R_d = R_3$. Above the break-point, the series photo-conductive resistance, R_1 , decreases to negligible values compared to R_3 and also compared to R_d , and the V_{oc} expression is reduced to:

$$V_{oc} = I_o R_3 \left[1 - \frac{R_3}{R_c + R_3} \right]$$

As R_d decreases further with increasing L , R_d becomes increasingly less than R_3 , and the quantity in brackets approaches an increasingly small value. There is, however, a limiting value of R_d and hence a limiting value of V_{oc} . We can estimate the limiting value of R_d in the following way: if we extrapolate the linear dependence of V_{oc} on L at low levels to $L = 30 \text{ mW/cm}^2$, we obtain $V_{oc} \approx 32 \text{ volts}$. But since the observed value is 0.42 volts, the attenuating factor in the brackets must equal $0.42/32 = 0.013$. Then taking $R_3 = 150 \Omega$ and noting that $R_1 \approx 0.02 \Omega$ we obtain $R_d = 2 \Omega$. If the IV curve of the diode alone was available, this problem could be reversed and V_{oc} could be obtained as a function of L .

Optimum-Load Conditions

Turning now to the dependence of the optimum load resistance on light intensity, we see in Fig. 30 that the break in the R_{mp} -vs.- L curve occurs at the same value of L where the break in the linearity of the V_{oc} -vs.- L curve occurs. R_{mp} is constant at light levels below 0.3 mW/cm^2 . This constant value of R_{mp} is associated with the shunt resistance R_3 of the equivalent circuit.

The equivalent resistance, R_e , that the load "sees" can be derived from the equivalent circuit. Noting that the constant-current generator appears as an open circuit (infinite differential resistance), the following expression was derived:

$$R_e = R_3 \left[1 + \frac{R_3}{R_1 + R_3 + R_d} \right] + R_2 .$$

As before, R_2 can be neglected since it is almost always much smaller than R_3 . R_1 and R_d are, of course, dependent on light intensity.

At low light levels, the forward voltage on the diode remains small over the entire IV curve; and hence R_d is large and the current through the diode is very small. $R_d > 10^5 \Omega$ while $R_3 \approx 150 \Omega$. The above expression for R_e shows that when $R_d \gg R_3$, $R_e \approx R_3$, and the load thus faces a purely resistive element. The IV "curve" is therefore a straight line passing through V_{oc} and I_{sc} , and has an inverse slope: $V_{oc}/I_{sc} = R_{mp} = R_e = R_3$. Since both V_{oc} (at low intensities) and I_{sc} vary linearly with light intensity, their ratio, R_{mp} , remains constant; i. e., a set of parallel IV lines is obtained for a set of low intensity measurements. Also, because the IV lines are straight, I_{mp} and V_{mp} must be exactly half of I_{sc} and V_{oc} , respectively. This, of course, applies only to the range in L where R_{mp} is constant. The observed constant value of R_{mp} at low intensities is thus explained, and its value is shown to be equal to R_3 .

The linear decrease of R_{mp} with increasing L at the higher intensities follows from the fact that the fill factor is large in this region and I_{mp} is approximately proportional to I_o . Since V_{mp} varies only by 0.33 while I_o varies by ~ 300 (and is proportional to L), $R_{mp} = V_{mp}/I_{mp}$ is approximately proportional to I_o^{-1} .

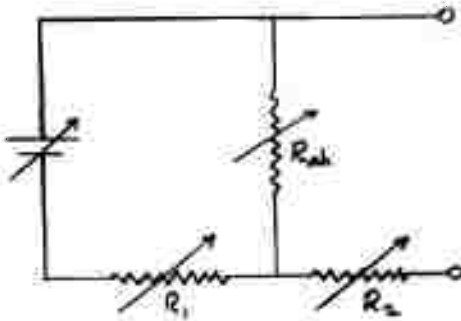
The above analysis suffers somewhat from the uncertainty of changes in barrier height at low light intensities. Apparently, even at the lowest light intensities used in these experiments, the photoconductivity generated in the i-layer was sufficient to prevent a significant increase in barrier height.

3.5.4 Cu_2S Thickness Dependence of IV Characteristics

Variations of the thickness of the Cu_2S layer have a strong effect on the IV characteristics of CdS solar cells. As the thickness increases the light absorption increases. At the same time, the recombination losses in this layer also increase. In addition, the light reaching the i-layer decreases and hence influences the photoconductivity of the i-layer. Furthermore, these changes occur at different rates for different wavelengths, leading to very complex overall behavior. For this reason the effect of Cu_2S thickness is best discussed in terms of the changes it affects on the spectral response. The discussion is therefore deferred to Section 3.6.

3.5.5 The Effects of Series and Shunt Resistances on IV Characteristics

In order to show the effects of internal series and shunt resistances on the IV characteristics of solar cells, a series of curves simulating changes in internal resistances was generated by connecting an external network of resistances to a standard cell and recording the resulting IV characteristics as a function of stepwise variations of each of the three component resistances.



A T-network or a π -network of three suitably chosen resistances can be shown to be electrically equivalent to a two-terminal "black-box" containing a constant current generator and any network of resistive elements. The T-network was chosen because this arrangement of the circuit elements can be more easily visualized in terms of the structural elements of the solar cell. In this measurement, the cell was connected by low resistance leads to a T-network of decade resistance boxes; the output end of the network was then connected to the artificial load and recorded in the usual manner.

The four families of curves shown in Figs. 32, 33, 34, and 35 are the IV characteristics corresponding to variations in series and shunt resistances alone and in combination. The particular cell tested had a rather low efficiency, but this does not influence the effects that are discussed here excepting that for higher efficiency cells the fill factor (squareness) will be somewhat more sensitive to series and shunt resistances. Fig. 32, which gives the effect of series resistance alone, shows that the open-circuit voltage is unaffected by series resistance. The squareness is rapidly lost at resistances above 0.1Ω and a progressive loss of I_{sc} is also evident at the higher values of R_s . Figure 33 for shunt resistance alone (the 0.02Ω shown in the figure being the minimum achievable contact and lead resistance), shows that the short-circuit current is unaffected but that the open-circuit voltage and squareness deteriorate rapidly as lower shunt resistances are applied. A highly shunted condition is frequently seen in "zero output" cells and can sometimes be pinpointed as shorts between the grid and the n-CdS or between the grid and Ag-Pyre ML layer at local flaws in the CdS layer. Shunt resistance in the standard process cells has varied from 10 to 1000 ohms over the past few years. Cells processed during the past few months have tended to fall in the range 200 to 1000 Ω . At one sun intensity, the optimum load resistance of $3'' \times 3''$ cells is $\sim 0.5 \Omega$; therefore, a 10Ω shunt degrades the efficiency by only a few tenths of a percent while a 100Ω shunt introduces practically no loss at all, but at low illumination levels the effects of shunting by approximately 100Ω can be quite pronounced as shown in Section 3.5.3.

Figures 34 and 35 show the effect of shunt resistance between two series resistances. These IV curves are very similar to those of some rejected standard process cells. With the loss of 5 to 10% of the open-circuit voltage and short-circuit current, the squareness of the curve sags to an unsatisfactorily low figure. The common intersection point of the IV curves is displaced into the third quadrant by the amount of the voltage drop across resistance R_2 at the short-circuit current, as would be required to make the voltage drop across the shunt resistance zero, eliminating any current flow through the shunt and making its effect on the circuit zero at the intersection point.

3.5.6 Determination of I_o and the Diode A-Factor

The Clevite ceramic CdS cell is very similar to the thin-film cell in construction and in photovoltaic properties. The principal difference is

CELL No. A993C

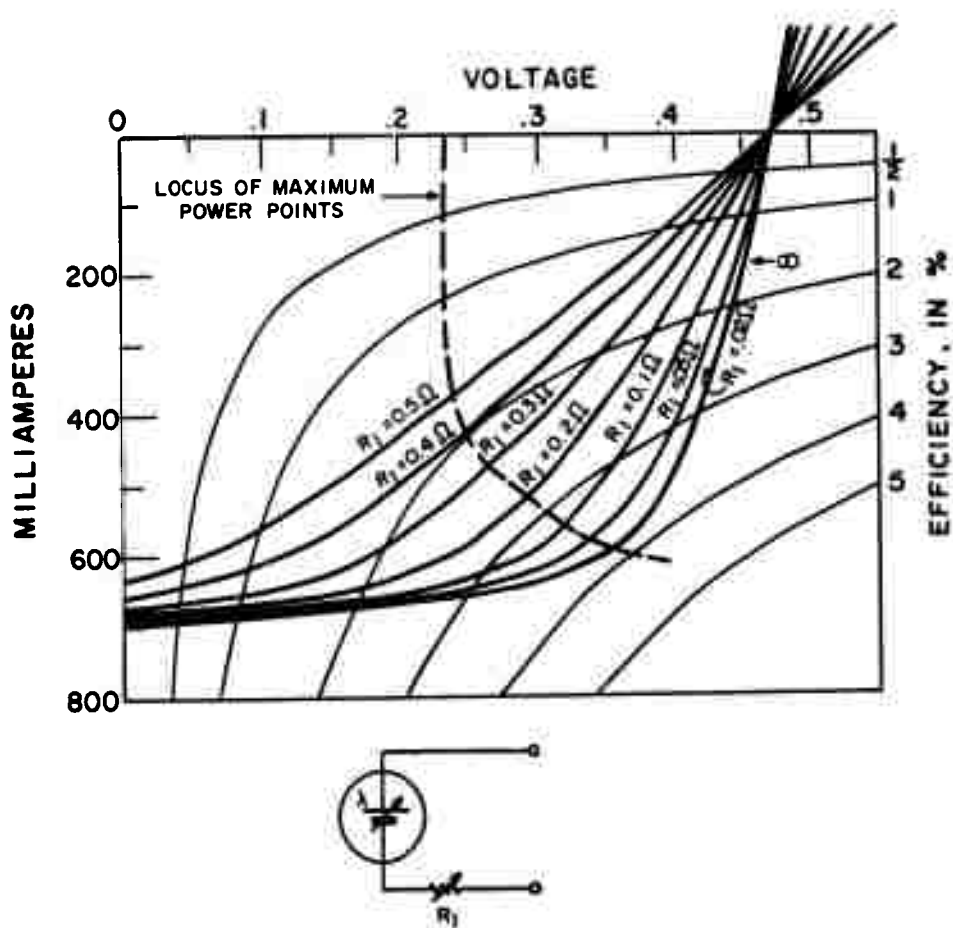


FIG. 32. EFFECT OF EXTERNAL SERIES RESISTANCE.

CELL No. A993C

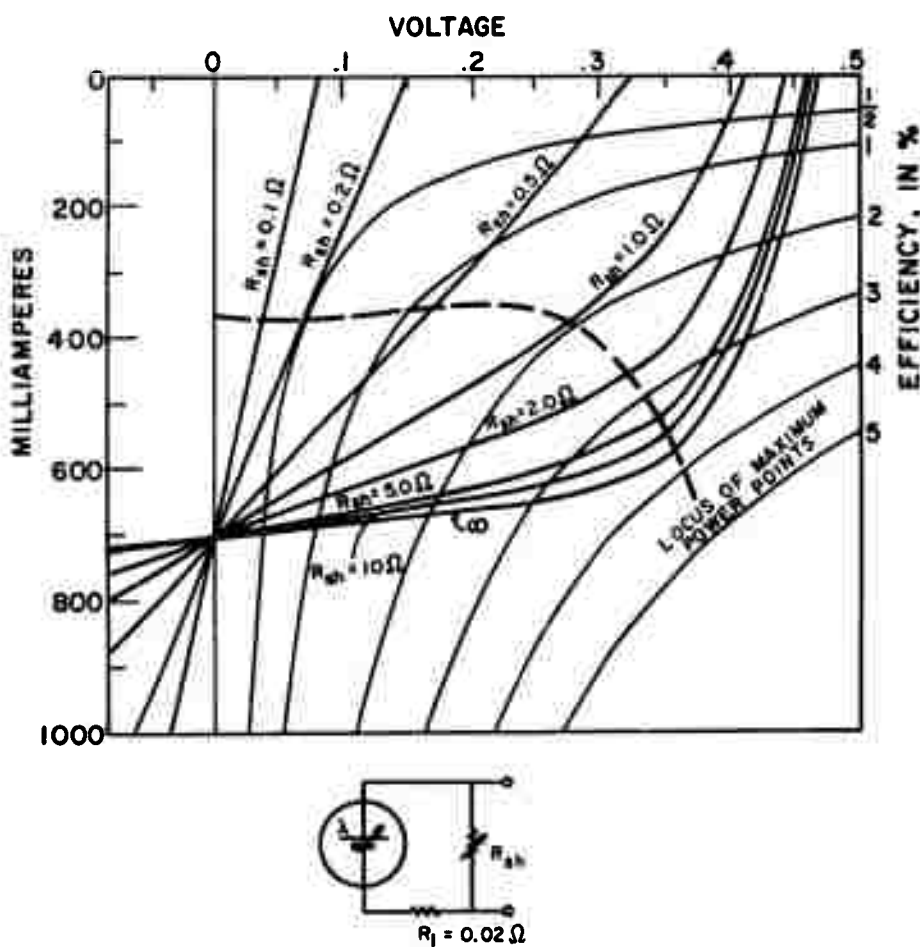


FIG. 33. EFFECT OF EXTERNAL SHUNT RESISTANCE.

CELL No. A993C

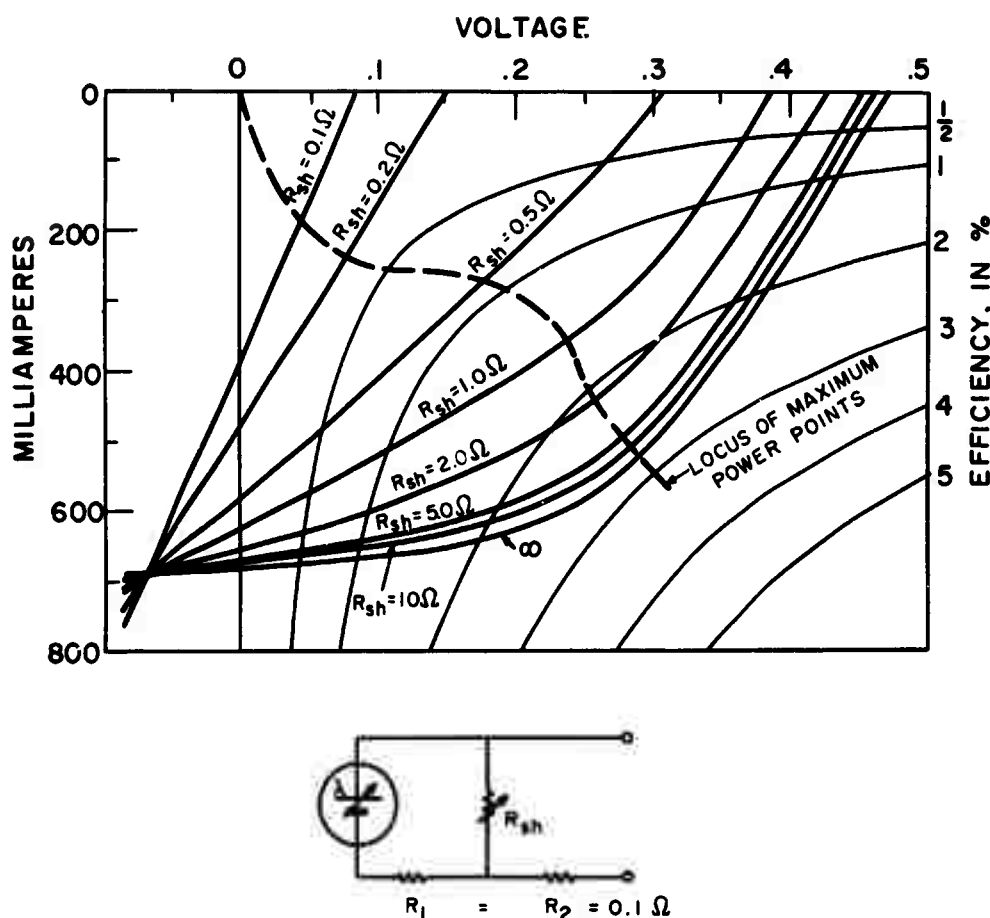


FIG. 34. EFFECT OF EXTERNAL SHUNT BETWEEN SERIES RESISTANCES.

CELL. No. A993C

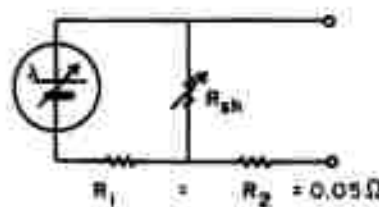
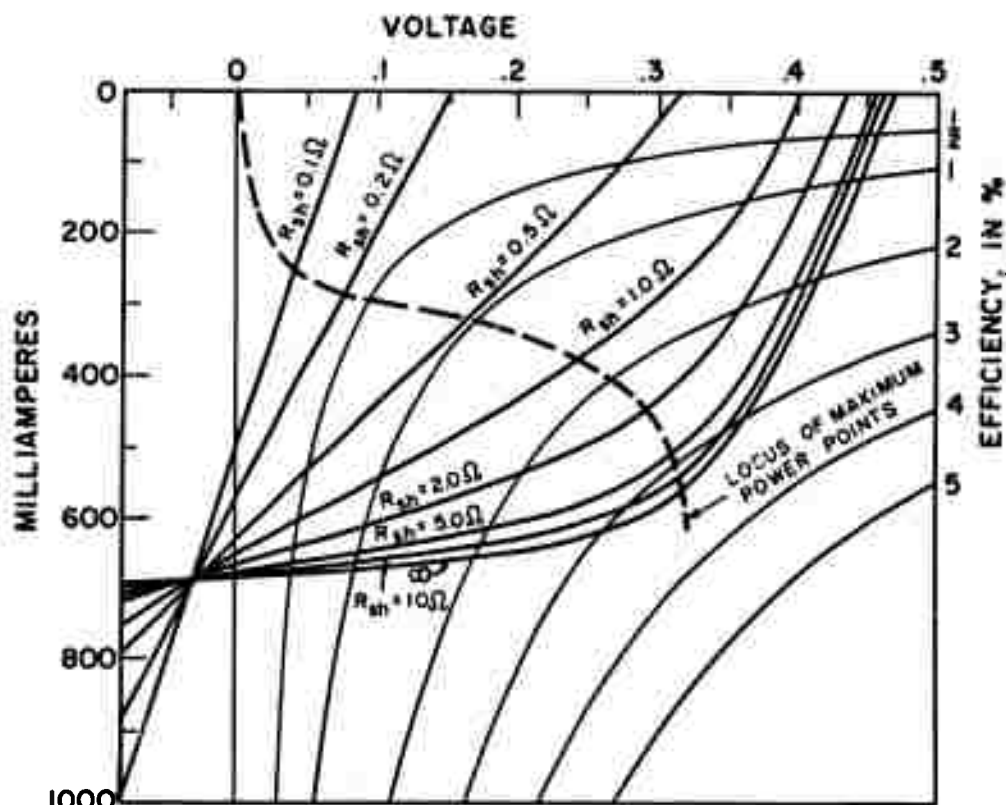


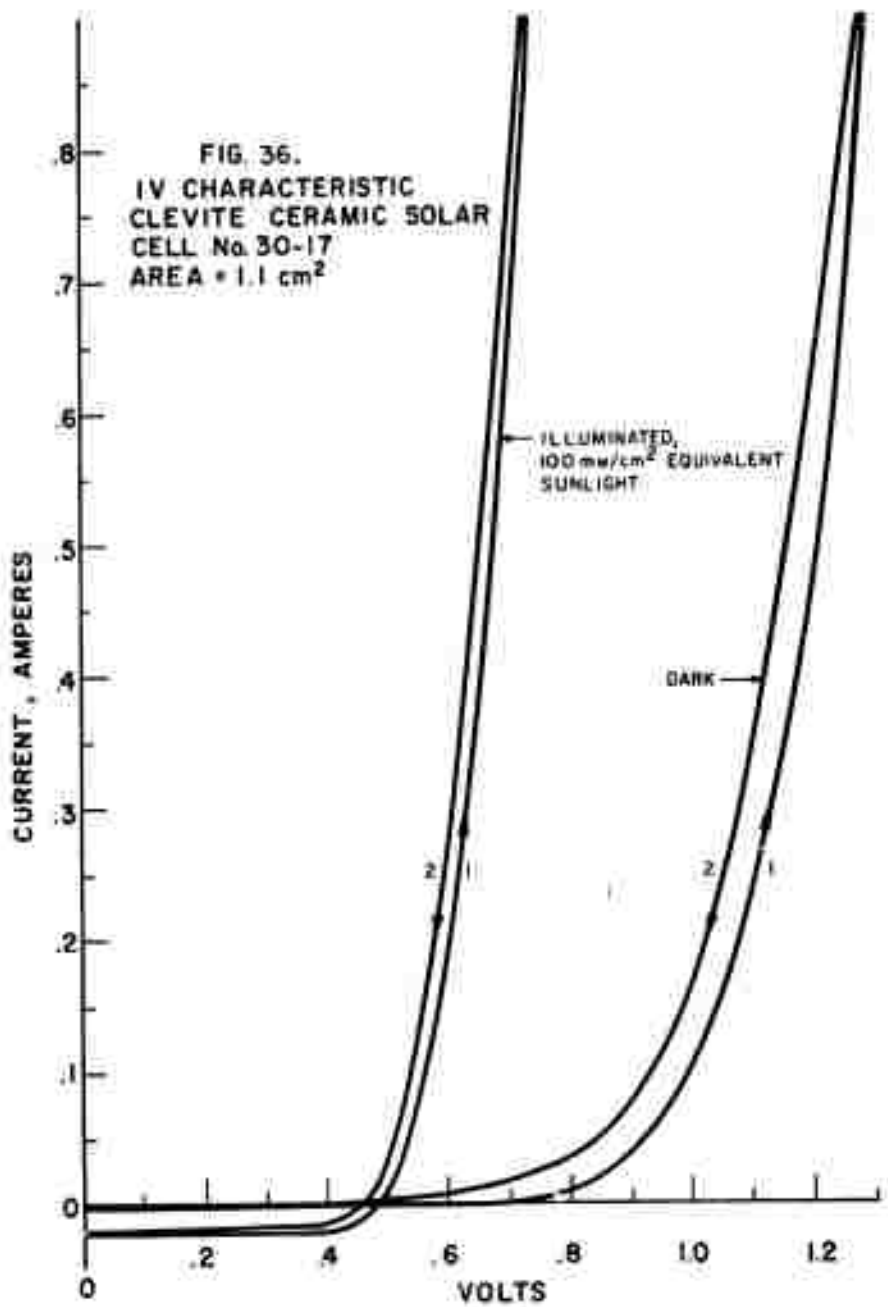
FIG. 35. EFFECT OF EXTERNAL SHUNT BETWEEN SERIES RESISTANCES.

the thickness of the n-CdS base layer (1.0 vs. 0.02 mm), which is the probable reason for the much larger shunt resistance of the ceramic cell ($> 10^5 \Omega$ vs. $\sim 10^3 \Omega$ for 1 cm² area). The large shunt resistance means that the experimental IV curves of the ceramic cell are close approximations of the true diode characteristics of the photovoltaic junction. The series resistance of both types of cells is generally small, and the distortion of the IV curves from this can be easily corrected. We believe that the IV characteristics of the ceramic cell are actually more representative of the internal diode characteristics of the thin-film cell than are the IV curves of the thin-film cells.

Figure 36 shows the room-temperature IV characteristics of a typical Mylar covered ceramic cell in equivalent sunlight and in the dark. It will be noted the curves extend to high voltages where the current densities become very large ($\sim 1 \text{ amp/cm}^2$). The arrows on the curves indicate the direction in which the curves were traced and the adjoining numbers indicate the order in which the traces were taken. Each of the 4 curves shown was traced in about 4 seconds. Many other IV traces (not shown) were taken with the same cell over expanded current ranges in order to facilitate the measurement of current and differential slopes over a wide range.

The hysteresis shown in Fig. 36 is clearly associated with temperature changes. The power dissipation increased as the curves marked 1 were traced, about 1 watt being dissipated at the maximum current point in the dark and about 0.6 watts in the light. The return traces, marked 2, therefore apply to a higher average cell temperature. The voltage hysteresis at each current level is larger for the cell in the dark, in agreement with the larger power dissipation in this case. The first traces are thus more representative of the behavior at 25°C. Even in these curves, the temperature rise during the time of the tracing caused a voltage degradation so that the curves at the highest currents are steeper than they would have been had the temperature remained constant.

In order to determine the diode A factors, the voltages at high currents had to be corrected for series resistance since the voltage across the diode was less than the applied voltage by the drop across the internal series resistance. In the forward region where $I_0 \ll I$, the diode



equation containing the series resistance correction,

$$I = I_o \left[e^{\frac{q(V-IR_s)}{AkT}} - 1 \right]$$

can be solved for V, and differentiated with respect to current to give:

$$\frac{dV}{dI} = \frac{AkT}{q} \frac{1}{I} + R_s$$

Where the 1 in the bracket is neglected. A plot of dV/dI , the inverse differential slope of the IV curve, against $1/I$ should yield a straight line with a slope equal to AkT/q and an intercept of R_s . The results are shown in Fig. 37. The effective series resistance in the dark and in the light are respectively 0.3 and $\sim 0.05 \Omega$, which represent only small corrections. The corresponding diode A factors determined from the slopes over this limited current range are respectively 2.4 and 1.5.

A composite plot of the corrected data from many IV curves is shown in Fig. 38. Linear behavior over ~ 6 decades in the dark and ~ 3 decades in the light is evident. The increasing deviations of the points at the highest currents of the dark curve are due to heating. Similar deviations (not shown) were also noted in the light at somewhat higher currents than those shown. More heating (at a given current) was encountered in the dark due to the larger cell resistance and the longer time needed to trace the curves. The diode A factors in the dark and in the light are 2.4 ± 0.1 and 1.6 ± 0.1 respectively, in agreement with the previous results. The extrapolated values of I_o in the dark and in the light are shown in Fig. 38. The difference of the A factor in the dark and in the light is indicative of the difference in band configurations under these conditions, the dark insulating i-CdS layer introducing an additional energy hump of ~ 0.35 eV which is erased in the light due to photoconductivity. It is interesting to note that the experimental points taken in the dark are displaced from the points taken in the light by approximately 0.35 volts. This is what one would expect since the potential barrier facing the electrons in the n-CdS is ~ 0.35 volts greater in the dark, as shown in Fig. 1.

3.5.7 Maximum Observed Open-Circuit Voltage

Liquid-helium temperature measurements of open-circuit voltage have been carried out with the aid of the NASA-Lewis cryogenic facility.

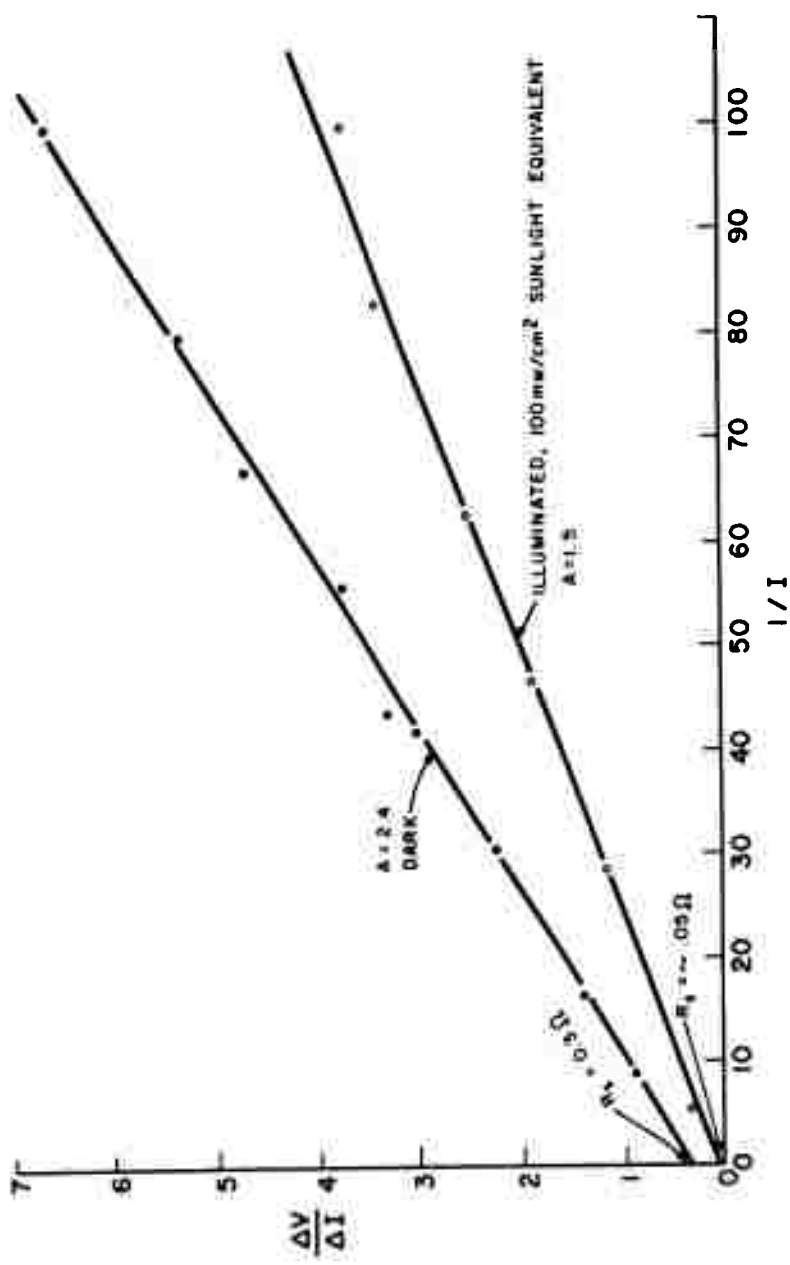
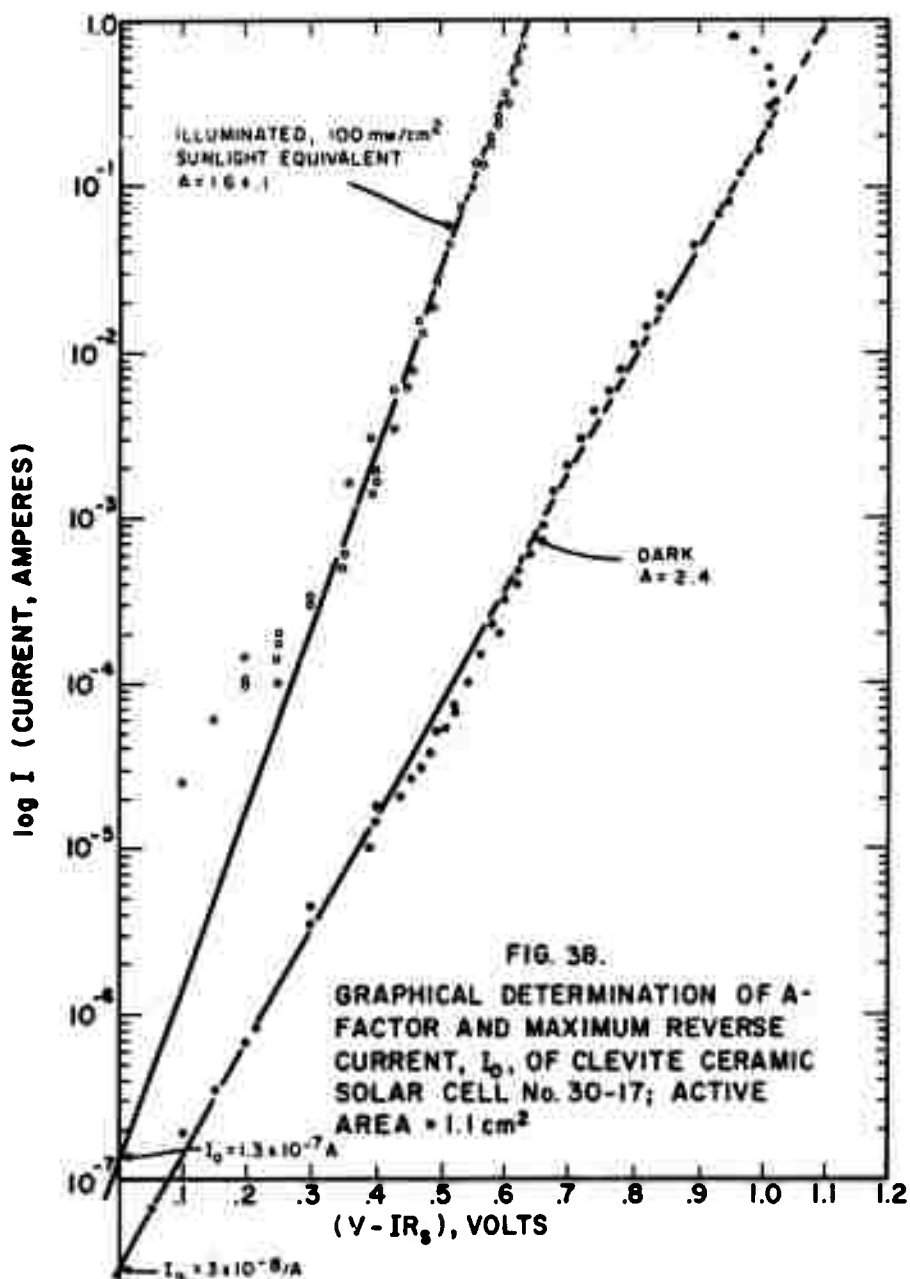


FIG. 37. GRAPHICAL DETERMINATION OF A-FACTOR AND SERIES RESISTANCE, R_s , OF CLEVITE CERAMIC SOLAR CELL No. 30-17; ACTIVE AREA = 1.1 cm².



The method which operated with reasonable success was to immerse a 20" long hollow (15 mm I. D., 17 mm O. D.) evacuated quartz "light-pipe" into a dewar containing approximately 1 ℓ of liquid He. The helium dewar was itself contained in a much larger liquid nitrogen dewar. The light pipe had a flattened bottom onto which a 1 cm^2 solar cell could be taped; the upper end had an open receptacle into which an inverted quartz-iodine 500 W lamp could be inserted. The intensity of light reaching the cell was determined later in this laboratory by first comparing the short-circuit current output of our ceramic cell (#32-9) with that of a standard Si cell under a ~ 1 -sun solar simulator at room temperature, and then to run through a measurement of the short-circuit current of the ceramic cell at the end of the light pipe, as a function of voltage input to the quartz-iodine lamp, with optical conditions as nearly equal as possible to those of the liquid helium runs. To insure equal optical conditions, the cell was immersed in liquid nitrogen and the outside of the light pipe (and insides of the dewar walls) were intentionally frosted up. The intensity of usable light ($E > 1.2$ eV) was found to range from 0.007 to 2.72 suns and it was assumed that this range of intensities prevailed during the liquid helium experiment. A copper-constantan thermocouple fixed to the bottom of the cell indicated that the temperature of the cell (at least for very brief light bursts) remained close to 4.2°K.

Liquid-helium measurements were carried out on two 1 cm^2 cells: ceramic cell #32-9, and single crystal cell #A-27 (containing several grain boundaries). The results are shown in Fig. 39, where open-circuit voltage is plotted against an inverse logarithm function of illumination to facilitate extrapolation to infinite intensity. Extrapolation leads to 0.78 V for cell A-27 and 0.84 V for cell 32-9 as limiting values. Due to charge carrier freeze-out in the n-CdS at 4.2°K, the cell impedances approach that of the Fairchild #7050 digital voltmeter at low light levels. This freeze-out effect is illustrated in Fig. 40 where the V_{oc} of cell #32-9 appears to go through a maximum V_{oc} at ~ 20 °K, and that of cell #A-27 at 10°K. (The base CdS of both cells was indium-doped in the range $10^{17} - 10^{18} \text{ cm}^{-3}$.) These freeze-out measurements were performed by evaporating off the liquid helium and then allowing the cell temperatures to rise to ~ 78 °K, while the open-circuit voltage and thermocouple output were monitored simultaneously by digital voltmeters.

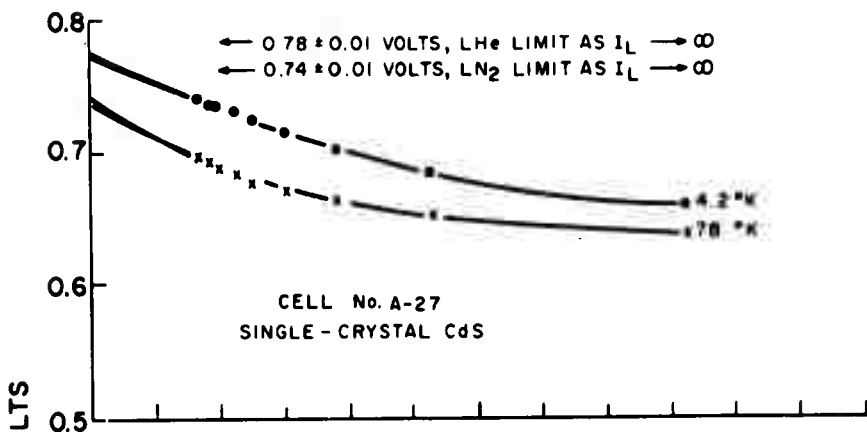
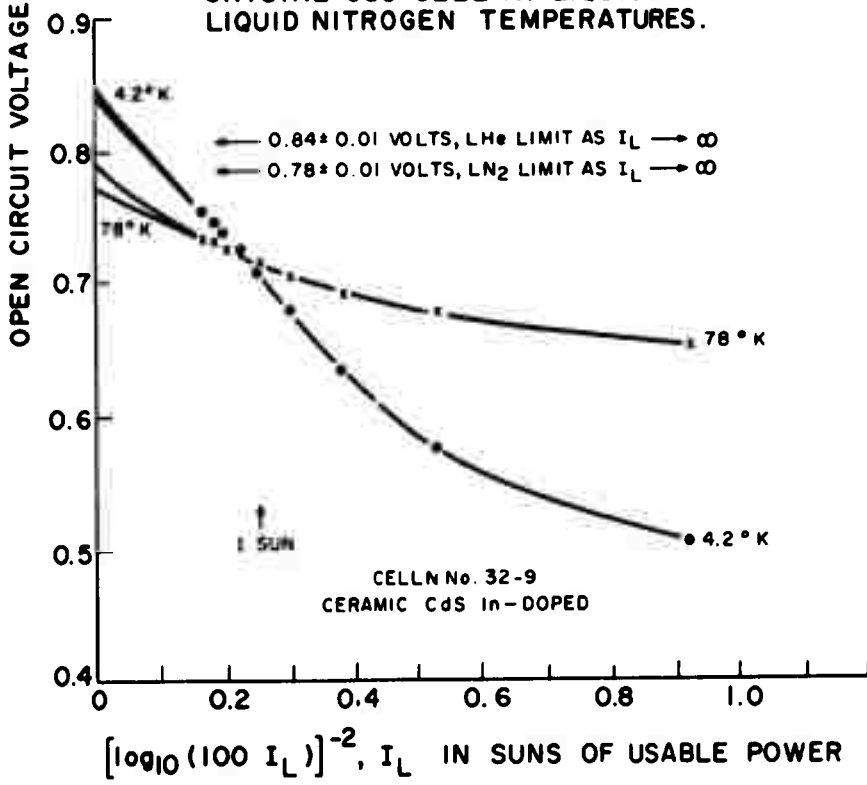
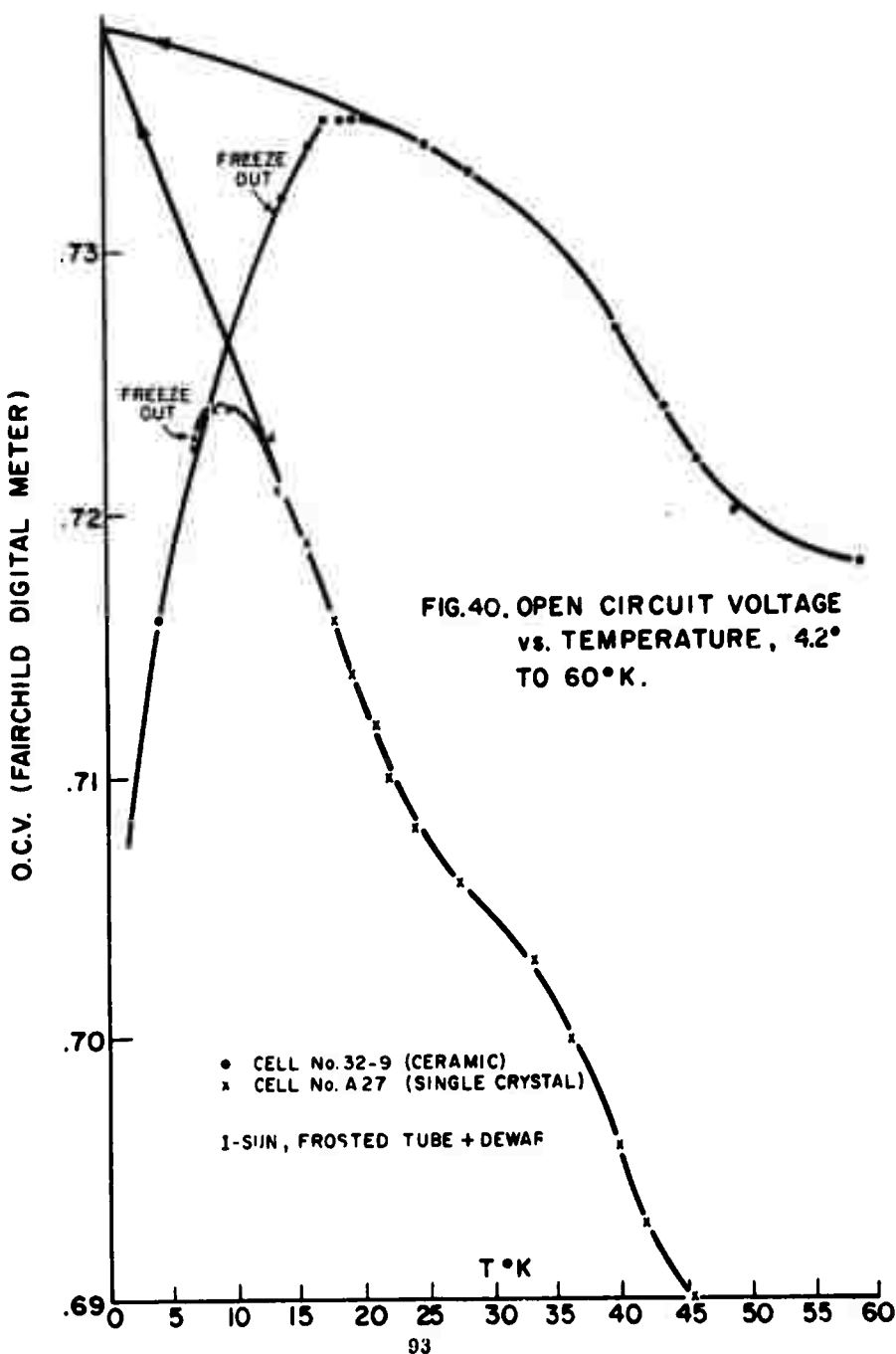


FIG. 39. OPEN-CIRCUIT VOLTAGE AS A FUNCTION OF ILLUMINATION FOR A CERAMIC AND A SINGLE-CRYSTAL CdS CELL AT LIQUID HELIUM AND LIQUID NITROGEN TEMPERATURES.





Even though the present data are complicated by freeze-out effects and uncertainties in light levels due to frosting, they nevertheless substantiate the idea of a maximum open circuit voltage, or barrier height, of ~ 0.8 to 0.85 eV, the latter being more probable since this measurement tends to yield a lower limit.

3.5.8 The IV Characteristics of Related Systems

3.5.8.1 The p-Cu₂S:i-CdS Junction

Our original model (40) presumed that the i-n CdS homojunction gave rise to the photovoltaic effect and that the p+Cu₂S:i-CdS heterojunction was inactive. This assumption was based on the idea that the Fermi level must be ~ 1.2 eV farther below the conduction band edge in i-CdS than in n-CdS due to the presence of Cu acceptor at this level. However, theoretical and experimental evidence indicate that under strong illumination this is not the case. Since in our model electrons are the dominant charge carrier, the proper consideration in determining the band configuration should be the electron quasi-Fermi level (E_{fn}), which in i-CdS under illumination floats toward the conduction band. The distance between E_{fn} and the conduction band edge is given approximately by⁽²⁹⁾

$$\theta = kT \ln\left(\frac{N_c}{n}\right)$$

where N_c = effective density of states in the conduction band $\approx 3 \times 10^{18} \text{ cm}^{-3}$, and n = free electron concentration in the i-CdS under 1-sun illumination $\approx 3 \times 10^{12} \text{ cm}^{-3}$. At room temperature

$$\theta_n = (1/40) \ln\left(\frac{3 \times 10^{18}}{3 \times 10^{12}}\right) = 1/40 (2.3 \times 6) = 0.35 \text{ eV}.$$

The energy band diagram for the CdS solar cell should therefore look like that shown in Fig. 1. The i-n CdS homojunction is nearly gone, and the dominant barrier for electrons is now the ~ 0.85 eV electrostatic potential barrier at the heterojunction. Additional evidence for this alteration is presented below.

Measurements of IV characteristic curves have been carried out for single crystals of Cu-saturated i-CdS, which have been partially converted to Cu₂S in order to form the heterojunction. Ohmic contacts

of indium-mercury amalgam to the i-CdS and In-Au-Hg amalgam to the Cu_2S were used. That these contacts were low resistance and of linear IV characteristics was verified by examining the curves for (In-Au-Hg): Cu_2S : (In-Au-Hg) and (In-Hg):iCdS:(In-Hg) systems.

Indium is known to make an ohmic contact to n-CdS: the initial Fermi Levels of the two materials are nearly the same as measured from the vacuum level. (30, 31, 32) The question then arises as to what happens when In is joined to i-CdS, which initially has an E_f 1.2 to 1.4 eV farther below the vacuum level.

A large barrier is found to be present in the dark. Under strong illumination the barrier is practically gone, and the junction is nearly ohmic. In the dark, and at very low light intensities, the IV curve resembles the reverse breakdown behavior of two rectifiers back-to-back. The reverse breakdown current (at several volts) was limited by the high series resistance of the i-CdS. Under 1-sun, however, (and even in room light), no non-linear characteristics could be detected in the In:i-CdS:In system; the traces of current vs. voltage were nearly straight lines. This is a very strong argument in favor of treating the i-CdS (under illumination) like n-CdS, and of making the principal photovoltaic junction the Cu_2S :i-CdS heterojunction.

We have also carried out measurements on the system (Au-In-Hg): Cu_2S :(Au-In-Hg), in an effort to form ohmic contact to the Cu_2S . The two electrodes shown in Fig. 41 (labeled InAu) on the Cu_2S film were used. In all cases the IV curves were linear, and indicated a low resistance ($\sim 10 \Omega$). Also, Cu_2S is degenerate so that the width of the depletion region should be $< 10 \text{ \AA}$, or \sim tunneling distance for electrons and holes; contact with any metal should therefore be ohmic. On this basis one would expect the Au- Cu_2S contact, which is used in the CdS solar cell, to be ohmic also, as observed.

A diagram of the electrode configuration used for measuring the IV characteristics of the InAu: Cu_2S :i-CdS:In, In:i-CdS:In, and InAu: Cu_2S :InAu systems is shown in Fig. 41. The i-CdS had been diffusion-saturated with Cu atoms at 250°C for 2472 hours; the Cu_2S film was formed on this insulating CdS crystal by exposure to a CuCl solution.

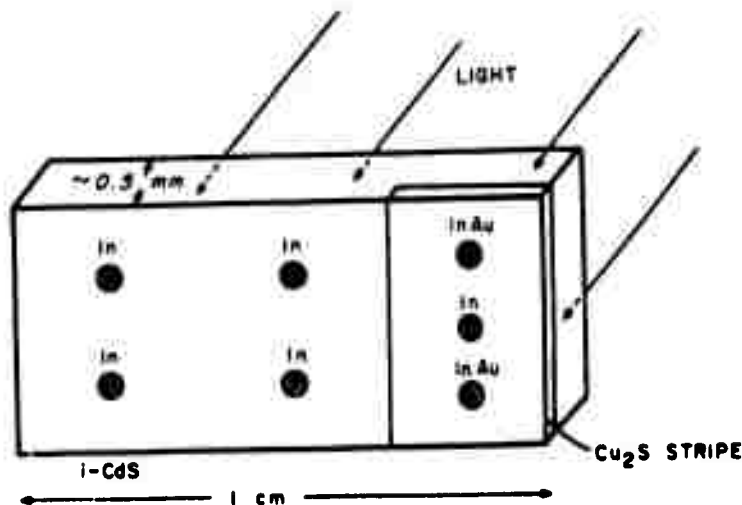


FIG. 41. ELECTRODE CONFIGURATION FOR MEASURING IV CHARACTERISTICS OF THE $\text{Cu}_2\text{S}:1\text{-CdS}$ JUNCTION.

Although this geometry is not ideal for accurately determining the area of the heterojunction, exact knowledge of the area is not critical to this discussion.

The IV characteristics of the In:i-CdS:In and the InAu:Cu₂S:i-CdS:In systems in room light and under 1-sun are shown in Figs. 42 and 43. The In:i-CdS:In system is seen to be very ohmic under both lighting conditions. The InAu:Cu₂S:i-CdS:In system shows definite photovoltaic response under both conditions. The response under 1-sun is moderately strong with $V_{oc} = 0.25$ volts, and $I_{sc} \approx 0.4$ ma/cm². The polarity of the cell is the same as that in normal thin film cells. The unfavorable electrode geometry required the collected electrons to travel as much as 0.5 cm through the i-layer. The junction was therefore non-uniformly forward biased by the IR drop through the i-layer, and the short-circuit current was thereby reduced. The low open circuit voltage is not understood. V_{oc} increased substantially between room light and 1-sun, but not nearly as much as expected. The cell behaved as though the light intensity was much lower than 1 sun. This could be explained by a large recombination rate in the Cu₂S layer or at the Cu₂S-CdS interface. Additional experiments of this kind, with more favorable geometry, appear to be in order. The present results, however, show that a moderately strong photovoltaic response is present in the p-Cu₂S:i-CdS cell, and hence that a finite thickness of a distinct i-layer in thin-film cells is entirely possible.

3.5.8.2 The n-CdS:i-CdS Homojunction

IV characteristic curves were run for a CdS crystal which was n-type, but which had a circular Cu-diffused region on one side a few microns thick. (The specimen was similar to those used in the copper diffusion experiment.) The Cu and Cu₂S had been removed from the surface of the i-CdS by FeCl₃ and KCN solutions, respectively. Indium electrodes were applied to both the i-CdS (shown to be ohmic in the light) and the n-CdS (known to be ohmic in light and dark).

The behavior of this system in the dark and in room light (~ 7 mW/cm²) was that of a rectifying diode, but one which did not "turn on" in the forward region until the applied voltage exceeded ~ 4 V; the slope for $V > 6$ volts corresponded to a low resistance ($\sim 9 \Omega$). No rectification

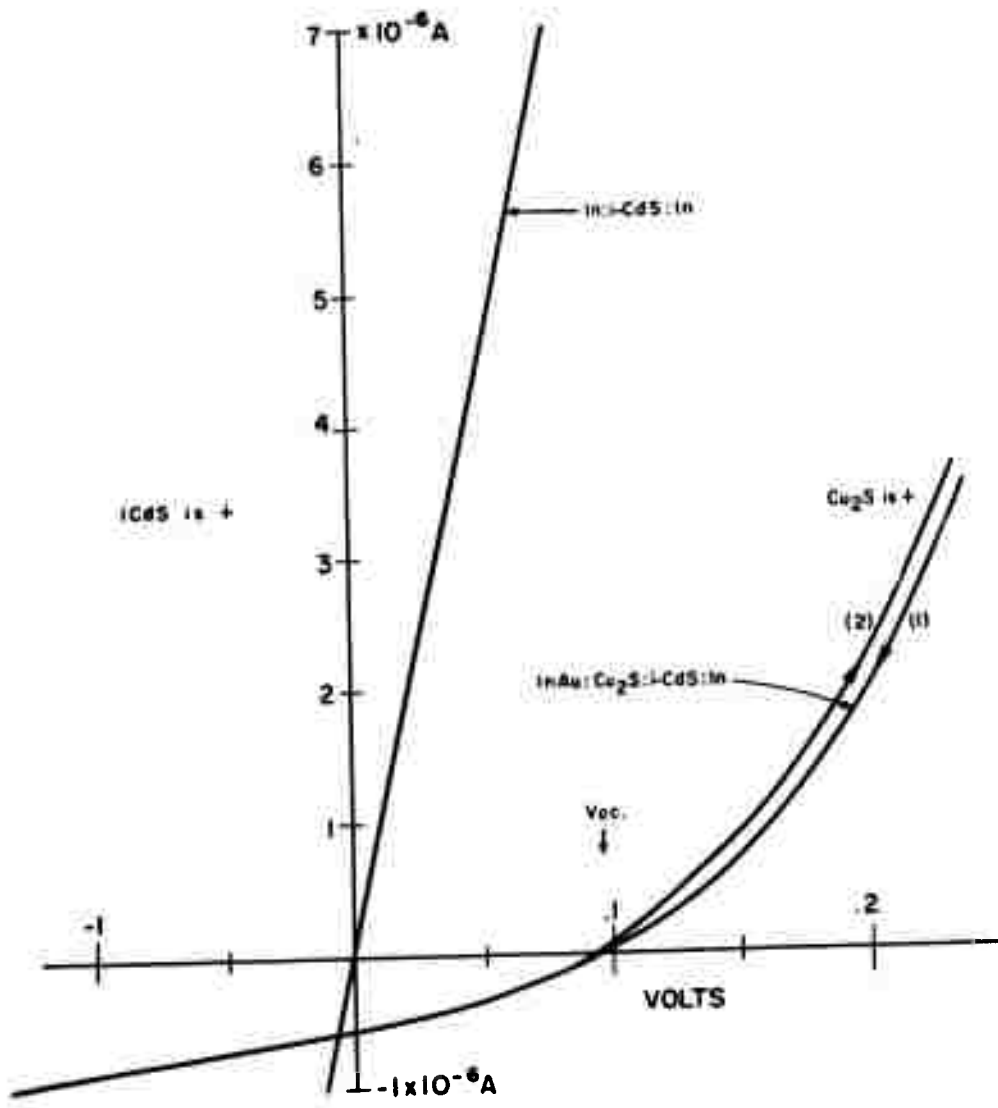


FIG. 42. CURRENT-VOLTAGE CHARACTERISTICS OF THE SYSTEMS $\text{InAu}:\text{Cu}_2\text{S}:\text{i-CdS:In}$ AND $\text{In:}\text{i-CdS:In}$ IN ROOM LIGHT, 7mW/cm^2 .

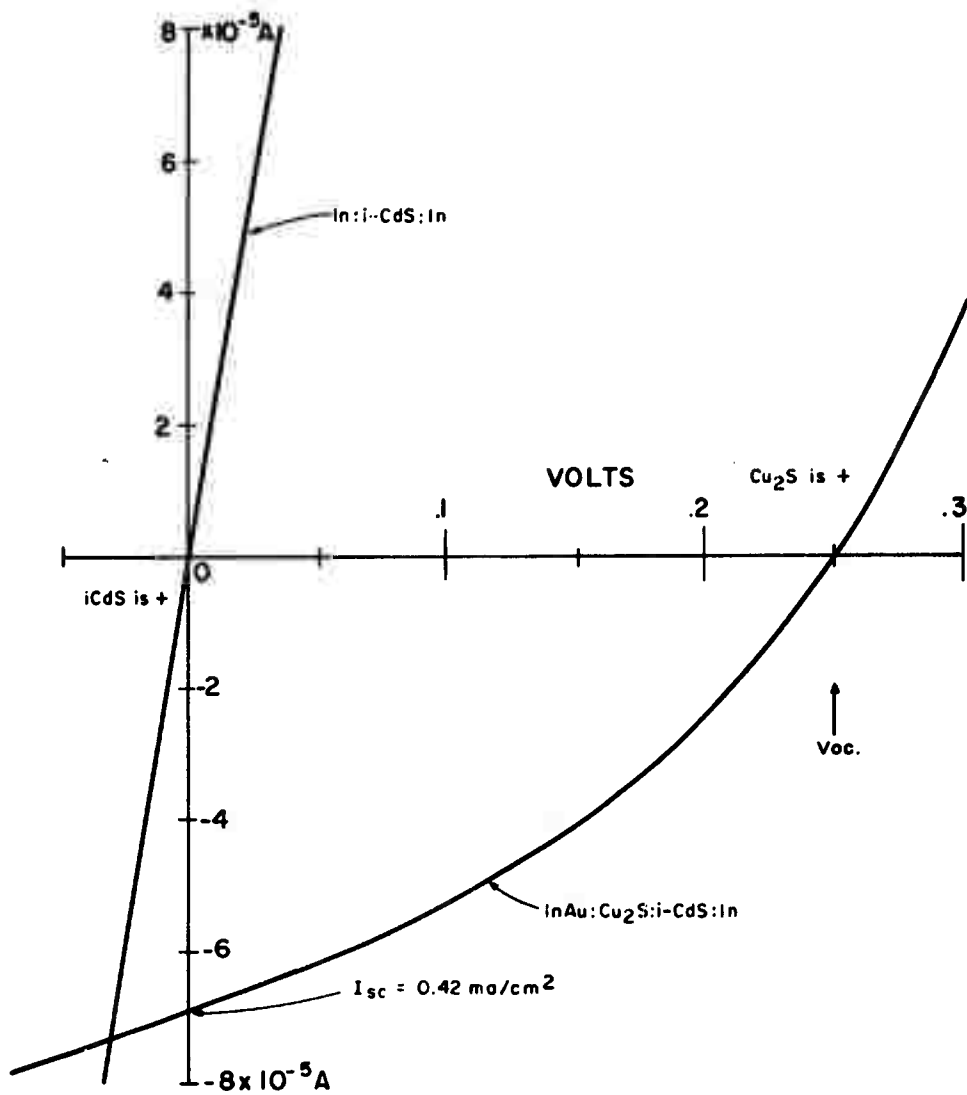


FIG. 43. CURRENT-VOLTAGE CHARACTERISTICS OF THE SYSTEMS $\text{InAu:Cu}_2\text{S:i-CdS:In}$ AND In:i-CdS:In UNDER 1-SUN.

could be found on the more sensitive current scales for $|\pm V| < 4$ volts. In fact, the system had the characteristics of breakdown across the i-CdS when the field there exceeded $\sim 10^4$ V/cm. The possibility of space-charge limited currents is not excluded. No sharp breakdown point was found in the reverse direction, but the specimen suffered irreversible heat damage when the current and voltage were increased too far.

When the 4 to 7.5 volt forward region was analyzed for diode characteristics, an "A" factor of 13 was found. However, the plot of $\ln I$ versus $(V - IR_g)$ was not especially linear; this fact and the breakdown type of behavior makes the meaning of the "A" factor very doubtful. Under 1-sun illumination, the resistance for $|\pm V| < 4$ volts decreases a great deal, due to photoconductivity in the i-CdS, and the IV curves lost their diode appearance, with the current becoming nearly as great in the reverse as in the forward directions. No open-circuit voltage or light-generated photo current was detected.

These results demonstrate that the i-n CdS homojunction is strongly rectifying in the dark and is non-rectifying in the light, in qualitative agreement with the Clevite model.

3.5.8.3 The p-Si:n-CdS Heterojunction

A recent publication by Okimura, et al. (33) shows the IV characteristics of a p-Si:n-CdS heterojunction (n-CdS vapor deposited on p-Si wafers). The open-circuit voltage of these cells is ~ 0.50 volts, nearly the same as that for the Cu₂S:CdS cell. Comparing this to the open-circuit voltage of Si solar cells, 0.55 volts, the barrier height in both types of heterojunctions is implied to be somewhat less than the 1.0 to 1.1 eV barrier at the Si junction. Since p-Si yields nearly the same voltage as p-Cu₂S when they are in contact with n-CdS, p-Si and P-Cu₂S must have very nearly the same work functions. Since the work functions of p-Si⁽³⁴⁾ and n-CdS^(30, 31, 32) have been published, this information together with the above approximate correlation with p-Cu₂S can be used to construct an energy band diagram for the p-Cu₂S:n-CdS heterojunction. The diagram shown in Fig. 1 results from such a construction. The rather loose arguments used to form this band configuration are by themselves not very convincing. But the close quantitative correlation of this construction with the maximum observed open-circuit voltage at low temperatures and the voltage displacement of the dark and light forward currents makes the construction much more plausible.

3.6 The Spectral Response of CdS Solar Cells

Although many spectral response measurements have been made in the past in many laboratories, they were usually made on isolated cells, and since the spectral response depends in a rather complicated way on several cell parameters, it has been difficult to draw general conclusions from such measurements. Therefore, new spectral response measurements on three special sets of ceramic solar cells were completed and analyzed. The thickness of the Cu_2S layer was used as a variable, and both undoped and In-doped CdS wafers were employed.

The use of Ceramic cells in these studies led to reproducible and consistent results, a situation that has been very difficult to achieve with thin-film or single-crystal cells. The reasons for this difference are clear: The properties of the thin film cells are often dominated by the properties of highly localized areas that are associated with various flaws in the cells. Reproducibility thus suffers and the variation of properties that are unintentionally encountered tends to conceal the effects of intentional variations in cell construction. The single-crystal cells are likewise difficult to study because the properties of the cells depend rather strongly on the doping level in the crystals, and uniform doping in large CdS crystals has been difficult to achieve. The ceramic cell which does not suffer from these limitations has thus become a powerful tool for investigating the effects of variations in cell parameters such as the thickness of the Cu_2S layer or the doping in the CdS. The results should be directly applicable to thin-film cells. To make CdS ceramic solar cells, raw CdS powder doped or undoped is pressed into wafers and sintered in a furnace at temperatures from 800 to 1200°C. This results in wafers that are mechanically strong and dense, that can be cut, lapped, etched, dipped in processing solutions and otherwise handled similarly to single crystal wafers of CdS.

The spectral response measurements were made with a Bausch and Lomb 33-86-45, 600 lines/mm grating monochromator using a tungsten filament light source at a color temperature of 2750°K (corrected for emissivity). Light intensity was measured with an Eastman Kodak 2 x 2 mm² N-1 PbS detector in a bridge circuit employing a matched cell of PbS in the dark for ambient temperature compensation. The PbS cell and the output of the monochromator was calibrated against an Epply MK-2 normal-incidence pyroheliometer.

The bandwidth was constant at 100 Å, yielding a light intensity of 430 $\mu\text{W/cm}^2$ at 8000 Å. All of the final results were normalized to this intensity unless otherwise noted. The photovoltaic current was measured by the voltage developed across a 10 Ω load, which gave an adequately close approximation to the short-circuit current. The current-wavelength curves were traced with an Electro-Instruments Model #500 X-Y recorder using the calibrated output of a potentiometer attached to the wavelength drum of the monochromator. Wavelength was varied at 500 Å/minute.

The results on the indium-doped ceramic cells will be discussed first, to be followed by the results on the undoped ceramic cells. Then, in order to show that the effects are quite general, similar results on two single-crystal cells and a thin film cell will be presented.

3.6.1 In-Doped Ceramic Cells, with Cu_2S -Thickness Dependence

The monochromatic spectral response, normalized to constant energy, is shown in Fig. 44. The six curves correspond to six separate cells that were identical except that they were dipped for different periods of time (1 to 40 sec.) in the Cu^+ ion solution ($\text{CuCl} = 17 \text{ g/l}$, 90°C). The response of the same cells measured in the presence of a constant white light bias is shown in Fig. 45. In this figure, the response due to the white light alone was subtracted from the combined response. The integrated intensity of the white light was adjusted to a constant intensity of 430 $\mu\text{W/cm}^2$, equal to the normalized intensity of the monochromatic light. The difference in the response with and without white-light bias represents the "enhancement effect," i.e., the output at some wavelength is greater than the sum of the individual outputs using monochromatic and white lights separately. The "difference curves" (the spectral dependence of the enhancement effect) are shown in Fig. 46.

The enhancement effect has a short-wavelength threshold between 0.6 and 0.7 μ and the enhancement rises steeply at longer wavelengths, reaching a maximum at 0.92 μ (1.35 eV) and then falling steeply at still longer wavelengths, to reach the long-wavelength threshold characteristic of the photovoltaic threshold of all CdS solar cells (the band edge of Cu_2S).

The simplest explanation of the enhancement effect is that the flow of electrons generated in the Cu_2S layer is limited by the conductivity

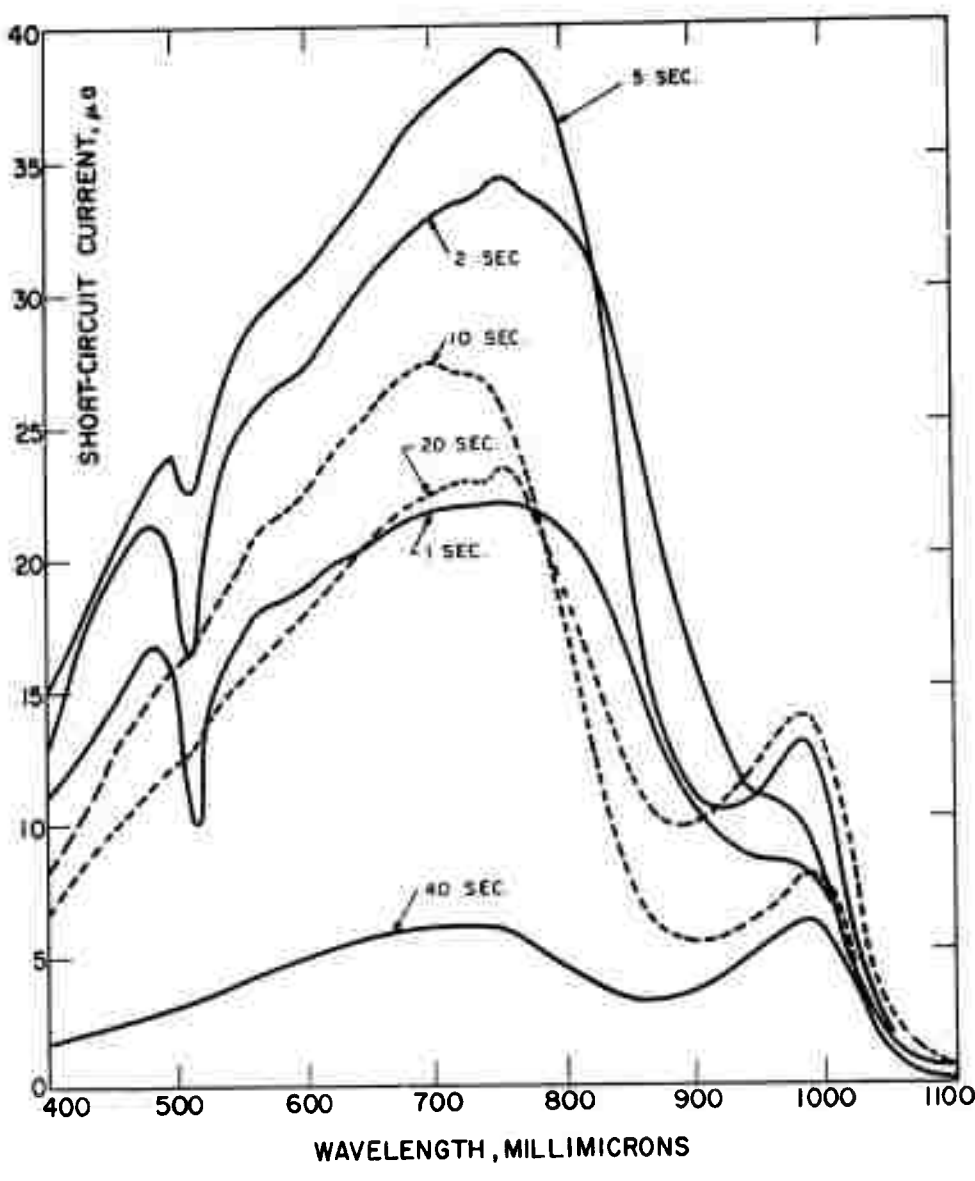
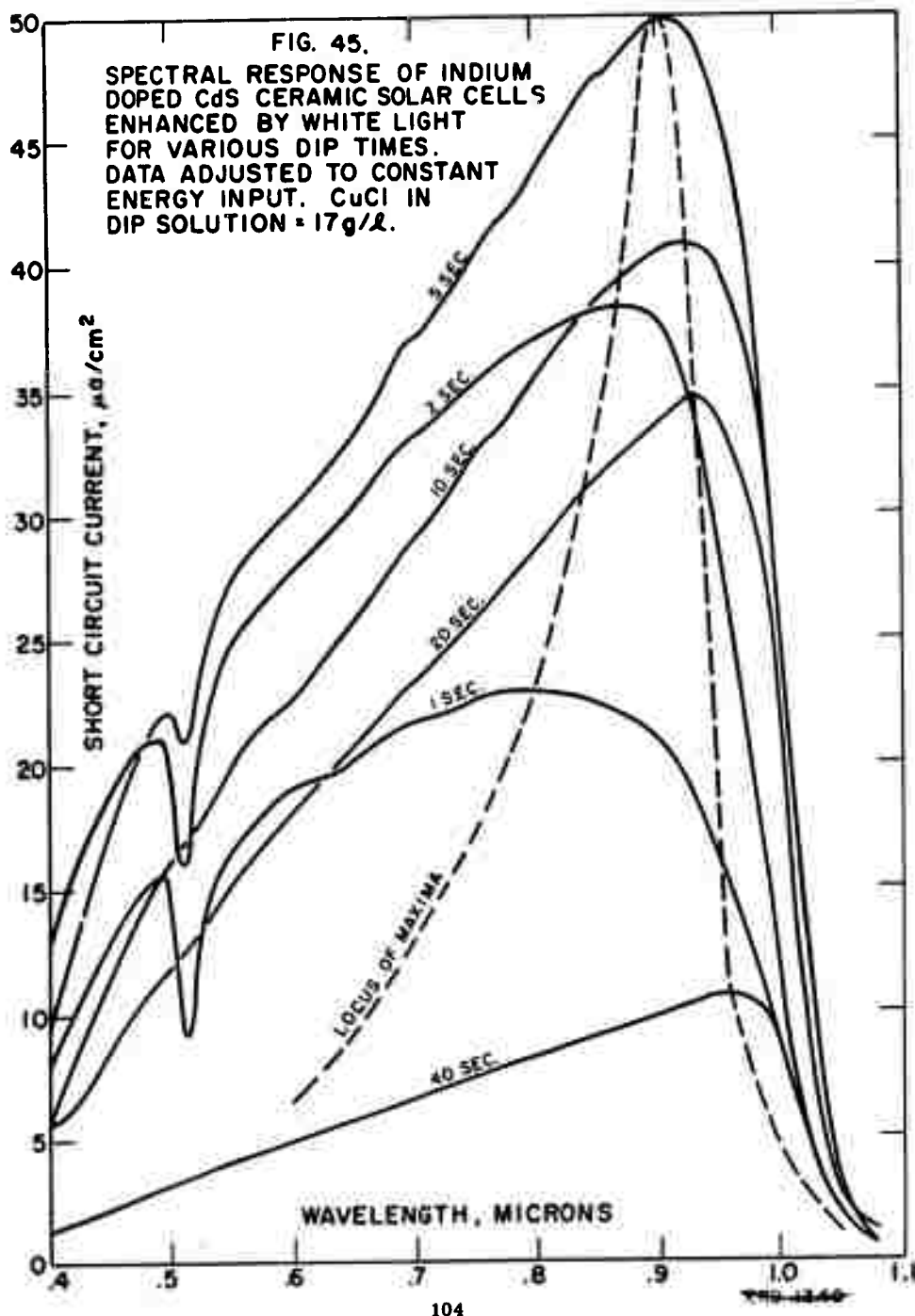


FIG. 44. SPECTRAL RESPONSE vs. DIP TIME. CdS CERAMIC SOLAR CELLS. RESPONSE ADJUSTED TO CONSTANT ENERGY INPUT. CuCl IN DIP SOLUTION = 17 g/l.



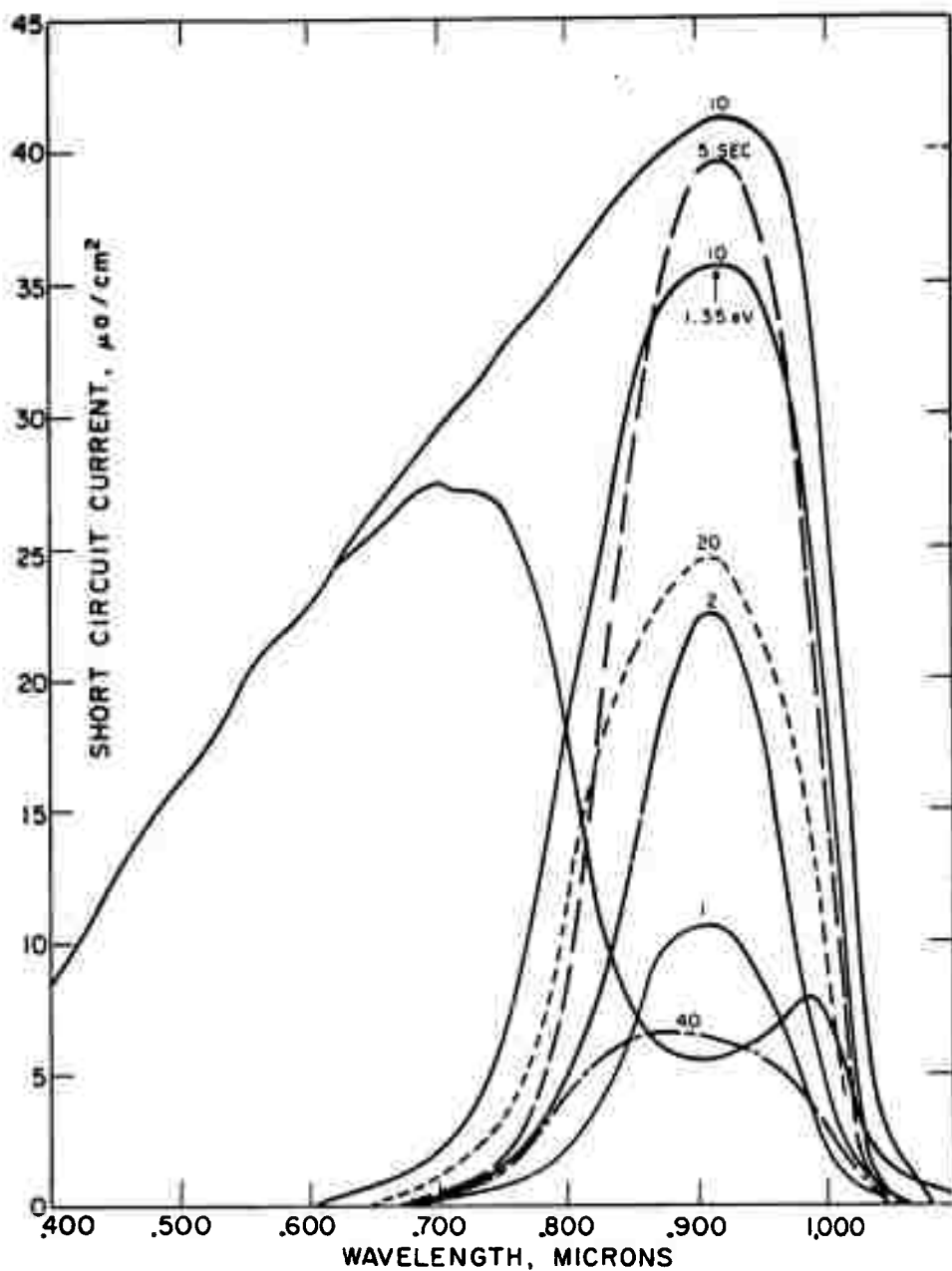


FIG. 46. ENHANCEMENT CURVES OF INDIUM-DOPED CdS CERAMIC SOLAR CELLS FORMED IN 16.7 g/l CuCl SOLN

of the i-CdS layer. The rate of generation of electrons in the Cu_2S layer is controlled by the thickness of the Cu_2S layer and the conductivity of the i-CdS layer is controlled almost entirely by the photoconductivity induced in this layer by the residual light that penetrates the Cu_2S layer. The spectral response of the photoconductivity of Cu-compensated In-doped ceramic CdS is shown as curve A in Fig. 47. The photoconductivity reaches a maximum at $\sim 0.63 \mu$ and then rapidly decreases at longer wavelengths (we temporarily ignore the behavior at the shorter wavelengths). The short-wavelength threshold of the enhancement curve clearly coincides with the start of the fall-off of the photoconductivity in the i-CdS layer, and the rise of the enhancement closely matches the fall of the photoconductivity to about 0.9μ . Since the absorption of light in the Cu_2S layer is fairly uniform in this wavelength range, the current generated in the Cu_2S is also nearly constant for a given cell. The fraction of this generated current that appears in the external circuit depends on the photoconductivity of the series-connected i-CdS layer which acts as a "gate" for the current. For monochromatic excitation in the range 0.6 to 0.9μ , the short-circuit current decreases in direct proportion to the decrease of photoconductivity in the i-CdS layer. On the other hand, the presence of constant white-light bias maintains a substantial photoconductivity in the i-layer so that almost all of the current generated by the monochromatic light is collected. (The steady, nearly linear increase in current with increase in wavelength from 0.55 to 0.9μ seen in Fig. 45 is due largely to the use of a constant-energy normalization. On a constant-photon-flux basis, the current for the cells having intermediate thicknesses of Cu_2S would be nearly constant in this region... more about this in Section 3.6.3.

The absorption edge of Cu_2S at $\sim 1.03 \mu$ causes the enhancement curves of Fig. 46 to drop sharply as this edge is approached. This causes the enhancement curves to peak at $\sim 1.35 \text{ eV}$ (0.92μ). By coincidence this peak occurs at the same energy as one of the two characteristic peaks in the infrared photoconductive quenching spectrum of sensitive CdS crystals. As emphasized by Bube,⁽²⁹⁾ this peak results from a play-off between the simultaneous excitation and quenching roles of radiation in this wavelength region. We believe that the minima near 0.9μ seen in the

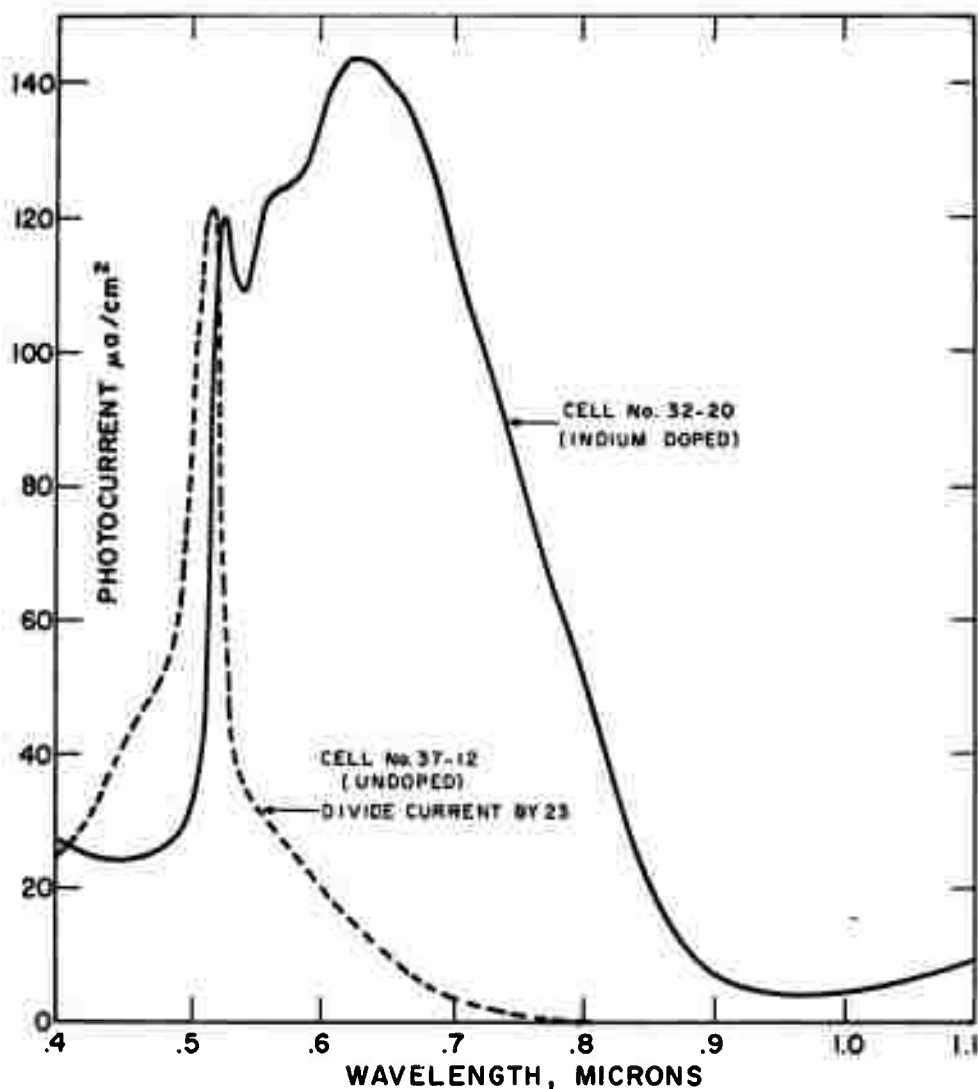


FIG. 47. PHOTOCONDUCTIVE RESPONSE vs. WAVELENGTH, Cds CERAMIC SOLAR CELLS WITH Cu_2S LAYER REMOVED. RESPONSE ADJUSTED TO EQUAL ENERGY ($430\mu\text{w}/\text{cm}^2$ AT 8000\AA IN ORIGINAL SPECTRUM) AT ALL WAVELENGTHS. 9.1 VOLTS ACROSS CELLS. CELL HEATED 30 MIN. AT 500°C BEFORE REMOVING Cu_2S LAYER.

monochromatic response curves of Fig. 44 are a manifestation of partial photoconductive quenching superimposed over the changing photoconductive excitation and further modified by the changing rate of generation of current with wavelength in the Cu_2S layer. The maxima at $\sim 0.98 \mu$ in the monochromatic curves result from the absorption edge of Cu_2S . The detailed differences in the curves due to differences in Cu_2S thickness are too difficult to analyze quantitatively. As the thickness of the Cu_2S layer is increased the current generation rate at first increases and then decreases as the thickness exceeds the diffusion length of the minority electrons in the Cu_2S . At the same time, the amount of light reaching the i-CdS layer decreases monotonically at all effective wavelengths, but the rate of decrease is different for each wavelength. Furthermore, the residual light that reaches the i-layer can cause both excitation and quenching of photoconductivity, and these properties are strongly dependent on wavelength and on intensity. The net effect, however, appears to be dominated by the degree of light absorption in the Cu_2S layer. As seen in Fig. 46, the peaks of the enhancement curves rise steeply with increasing Cu_2S thickness (dip time), reach a maximum near 3.0×10^{-5} cm (5 sec dip), and then fall more slowly as the thickness increases further. The general trend can also be seen in the IV characteristics shown in Fig. 48.

Turning next to the behavior at shorter wavelengths, less than 0.7μ , the only interesting structure seen is the sharp minimum at 0.51μ . The minima are pronounced only for the cells having thin Cu_2S layers. Since no enhancement was observed in this region, the current output was apparently not limited by series resistance in the i-CdS layer. The minima were unaffected by the white-light bias which should be particularly effective in inducing photoconductivity in these cells since they had thin Cu_2S layers. No definite explanation for these minima has come forth. The fact that they are seen only in cells having thin Cu_2S layers and the fact that they occur at the band edge of CdS indicates that they arise from light absorption in the CdS layer. The absorption coefficient of Cu_2S changes smoothly across this region, hence absorption in this layer should not give rise to such structure. The effect may be due to a high concentration of recombination centers at the Cu_2S :i-CdS interface. For very thin Cu_2S layers, an appreciable fraction of the incident light will be transmitted through the Cu_2S . As the band

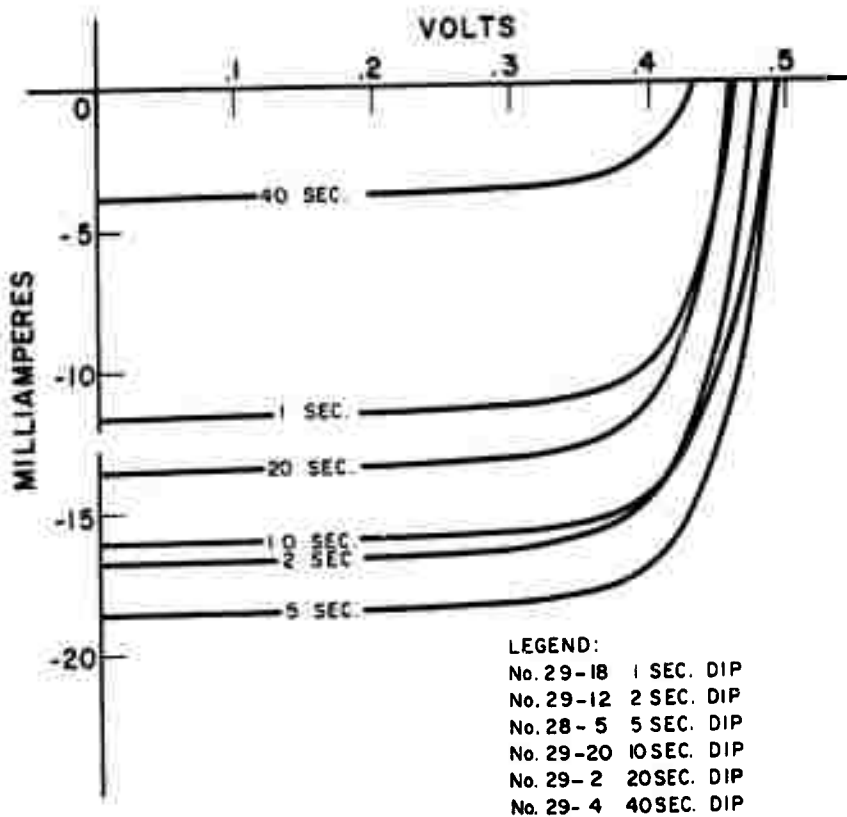


FIG. 48. I-V CHARACTERISTICS OF CdS CERAMIC SOLAR CELLS WITH VARYING DIP TIMES. MEASURED AT 100 mw/cm^2 SIMULATED SUNLIGHT (AM1)

edge of CdS is approached from the long wavelength side, the transmitted light would suddenly become strongly absorbed in the CdS layer adjacent to the interface. A maximum rate of generation of free carriers would then occur at the position where maximum recombination could take place, and a minimum in current output would then occur. However, the recovery of current at still shorter wavelengths would be expected to occur more gradually than that observed since the absorption in the Cu_2S does not rise so rapidly with decreasing wavelength. Recombination at interface states will be inferred again through other considerations, as discussed in Section 4.3.

In concluding this section, we emphasize that, although there are unexplained details, the large enhancement effect observed in these experiments is clearly explained by the photoconductive properties of the i-CdS layer, and that for the particular case of Cu-compensated In-doped cells, the enhancement effect has a threshold at $\sim 0.7 \mu$, the wavelength where the photoconductive response of the i-layer starts to decrease.

3.6.2 Undoped Ceramic Cells, with Cu_2S -Thickness Dependence

It has been known for many years that moderate donor doping of CdS single crystals results in optimum photovoltaic cells, but the reason why this should be so has only recently come to light. The answer, part of which was given in the last section, will become clearer as we discuss the enhancement experiments on undoped CdS ceramic cells. These cells were fabricated for the purpose of further demonstrating the controlling influence of the i-layer.

Five cells dipped for different periods of time in the usual CuCl solution (17 g/l, 90°C), were measured in the same way that the In-doped cells were measured. The spectral response in monochromatic light alone is shown in Fig. 49. The response with white-light bias is shown in Fig. 50, and the enhancement curves are shown in Fig. 51. The photoconductive response of Cu-compensated, undoped ceramic CdS cells was shown earlier as curve B in Fig. 47 (the 23X attenuating factor resulted from the fact that one of the electrodes was on the unilluminated side of the cell). The IV characteristics are shown in Fig. 52.

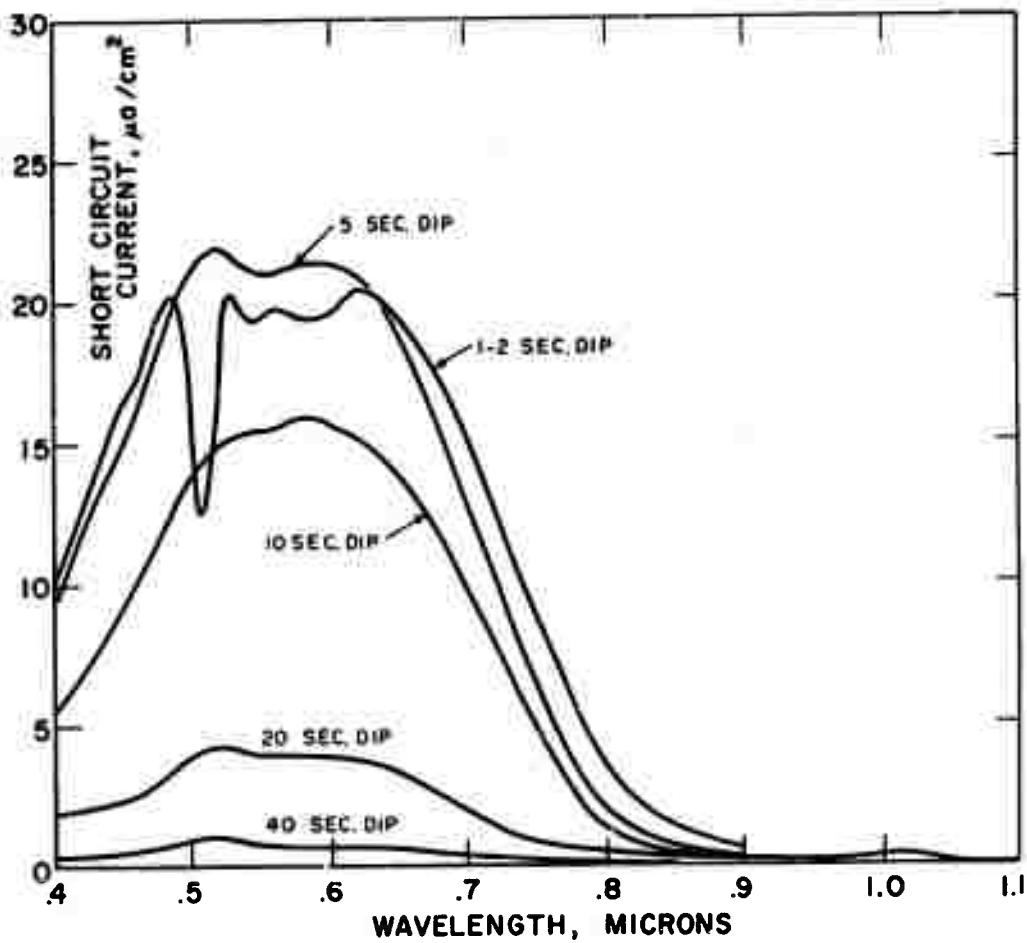


FIG. 49: SPECTRAL RESPONSE OF UNDOPED CdS CERAMIC SOLAR CELLS vs. DIP TIME. RESPONSE ADJUSTED TO CONSTANT ENERGY INPUT. CuCl IN DIP SOLUTION = 17 g/l.

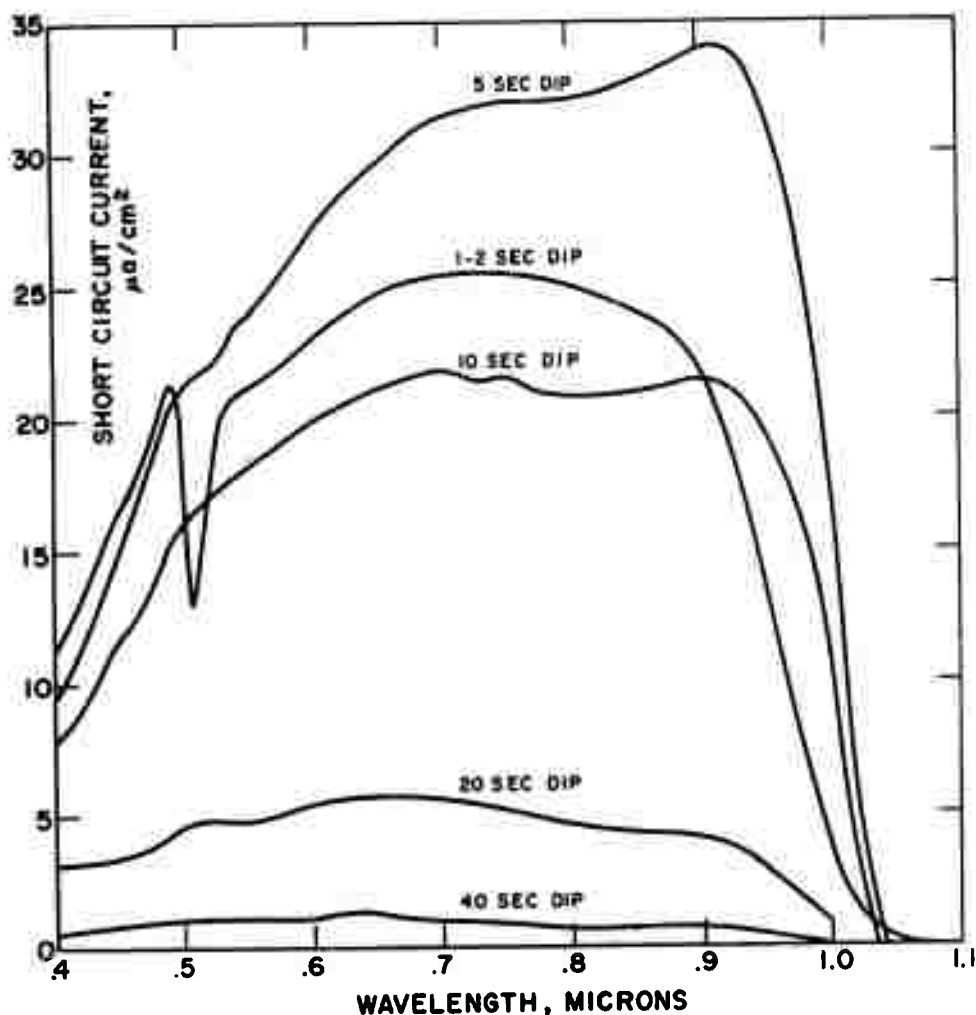


FIG. 50. SPECTRAL RESPONSE OF UNDOPED CdS CERAMIC SOLAR CELLS ENHANCED BY WHITE LIGHT FOR VARIOUS DIP TIMES. DATA ADJUSTED TO CONSTANT ENERGY INPUT. CuCl IN DIP SOLUTION = 17g/l .

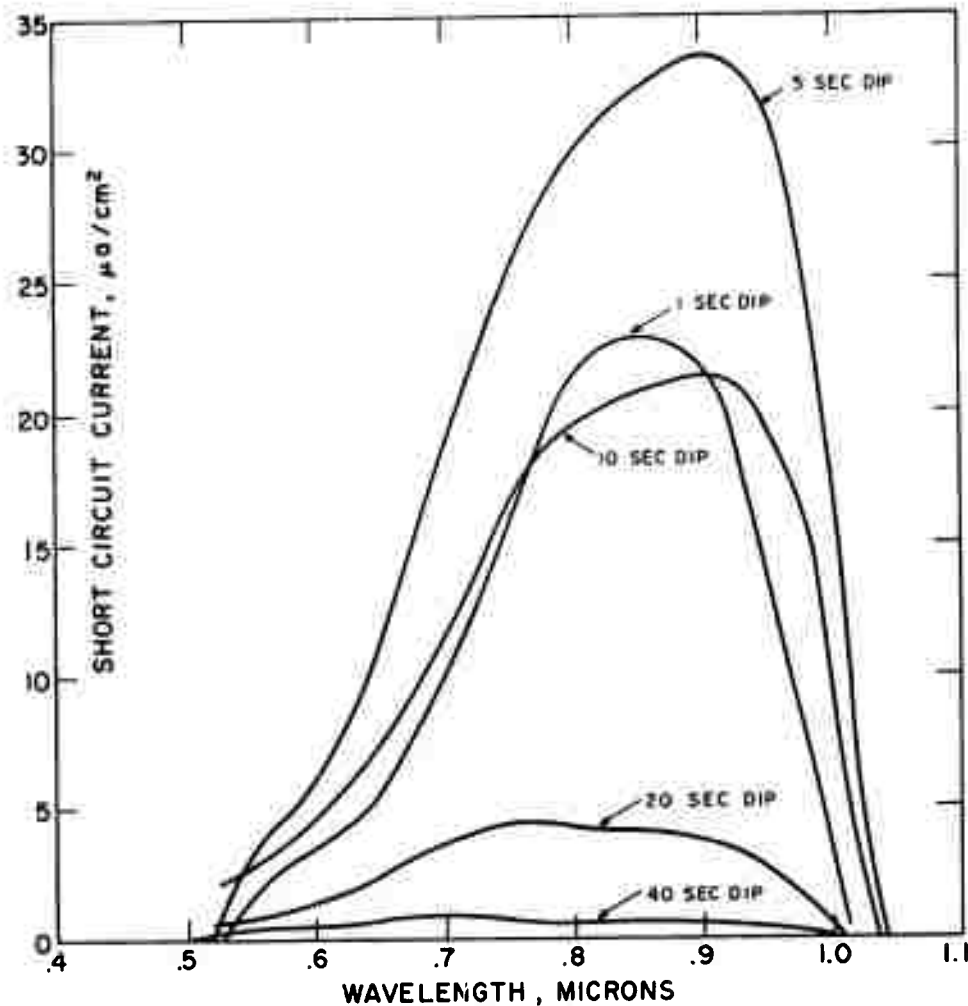


FIG. 51. ENHANCEMENT CURVES OF UNDOPED CdS CERAMIC SOLAR CELLS FORMED IN 16.7 g/l CuCl SOLN.

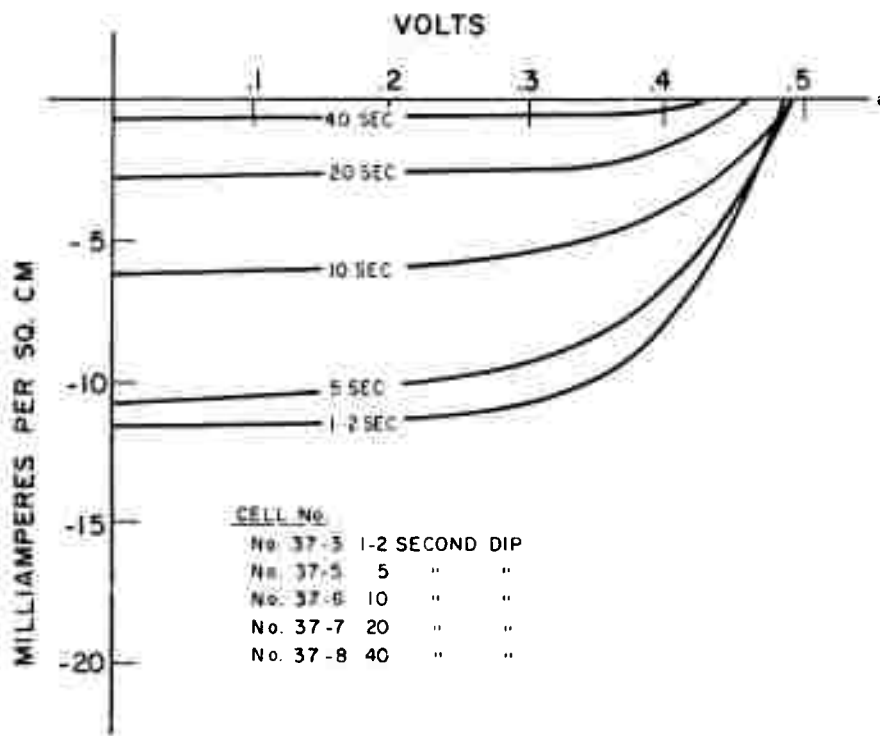


FIG. 52. I-V CHARACTERISTICS OF UNDOPED CdS CERAMIC SOLAR CELLS WITH VARYING TIMES. MEASURED AT 100 mw/cm² SIMULATED SUNLIGHT (AM1). CuCl IN DIP SOLUTION = 17 g/l.

It is immediately evident that the short-circuit current response is weaker for these cells and that the enhancement curves have a threshold at $\sim 0.51 \mu$, the precise wavelength where the photoconductive response (Fig. 47) starts to decrease. The decrease of photoconductivity with increasing wavelength does not follow the rise of enhancement as closely as it did for the In-doped cells but the general trend is unmistakable. A correspondence is seen in the range 0.55 to 0.65 μ where the change in slope of the photoconductivity curve is matched by the small shoulder on the enhancement curves.

The difference in the photovoltaic spectral response of the undoped and In-doped cells is obviously due to the difference in the photoconductive spectral response in the two types of cells. The magnitude of the photovoltaic response is also affected by the photoconductive properties of the i-layer. Because of the weak photoconductive response of the undoped cells, especially at the longer wavelengths, the cells are limited by the series resistance of the i-layer. If one attempts to increase the photoconductivity in this layer by making the Cu_2S layer thinner (shorter dip time), the absorption of light, and hence the short-circuit current, is reduced. At the same time, the sheet resistance of the Cu_2S layer increases and adds to the series resistance of the cell. Conversely, if the sheet resistance of the Cu_2S layer is reduced by making the layer thicker, the light reaching the i-layer is reduced and the series resistance of the latter is increased. Under these circumstances, the series resistance of undoped ceramic cells is always larger than that of In-doped cells. The optimum thickness of Cu_2S for undoped cells corresponds to a 1-2 second dip in the Cu^+ solution. The optimum thickness for In-doped cells corresponds to a ~ 5 second dip in the Cu^+ solution. Furthermore, the short-circuit current of a 1-second dip In-doped cell is almost the same as that of the optimum (1-2 sec) undoped cells. Since the series resistance of the optimum undoped cells does not seriously affect the short-circuit current, the thickness of the Cu_2S layer is probably nearly the same in the optimum cell and in the 1-second In-doped cell. This thickness is estimated as 0.10μ . As the dip time is increased in both types of cells the Cu_2S layer gets thicker, but the increase in series resistance of the undoped cells more than offsets the increase in light absorption and

hence the optimum thickness is thinner for the undoped cell (Fig. 9). For the In-doped cells (Fig. 5), the red and infrared photoconductive response maintains the conductance of the i-layer so that as the Cu_2S layer is increased in thickness, the short-circuit current continues to increase until recombination losses in the Cu_2S layer cause the current to decrease with further increase in thickness. The optimum thickness for the In-doped cells is $\sim 0.3 \mu$ (~ 5 second dip). As shown in Fig. 48, the fill factor of the In-doped cells remains high even for a 40-second dip time, indicating that the series resistance of the i-layer is still quite low. In contrast, for the undoped cells, the fill-factor decreases and the series resistance increases with Cu_2S thickness, as shown in Fig. 52. A large part of the loss in short-circuit current for the undoped cells having thick Cu_2S layers is due to recombination in the Cu_2S layer, just as it is for the In-doped cells.

In an attempt to study the behavior of undoped cells having very thin Cu_2S layers, another group of four undoped cells were dipped in a much weaker Cu^+ solution (1 g CuCl/l , 90°C). The results for these cells are shown in Figs. 53, 54, 55, and 56. It is evident that the optimum dip time is about 10 seconds for this solution, hence only the cell dipped for 5 seconds in this solution has a Cu_2S layer that is thinner than that of the undoped cell dipped for 1-2 seconds in the standard 17 g/l solution. The general trend of the results is essentially the same as those for the undoped cells treated in the standard solution.

The behavior of the open circuit voltage with increase in Cu_2S thickness can be seen in Figs. 48, 52, and 56. As the Cu_2S thickness is increased from zero, the V_{oc} increases very rapidly to a maximum and then decreases rather slowly with further increase in thickness. Concurrently, the short-circuit current also goes through a maximum. For both undoped and In-doped cells, the maximum occurs slightly before or about at the same time that the maximum in V_{oc} is reached. The decrease of V_{oc} beyond the maximum is probably caused by increasing recombination in the Cu_2S layer. The loss of electrons by recombination diminishes the photovoltaic current crossing the junction. Under open circuit-conditions, this current causes the junction to be forward biased. A hypothetical diode current resulting from this bias flows

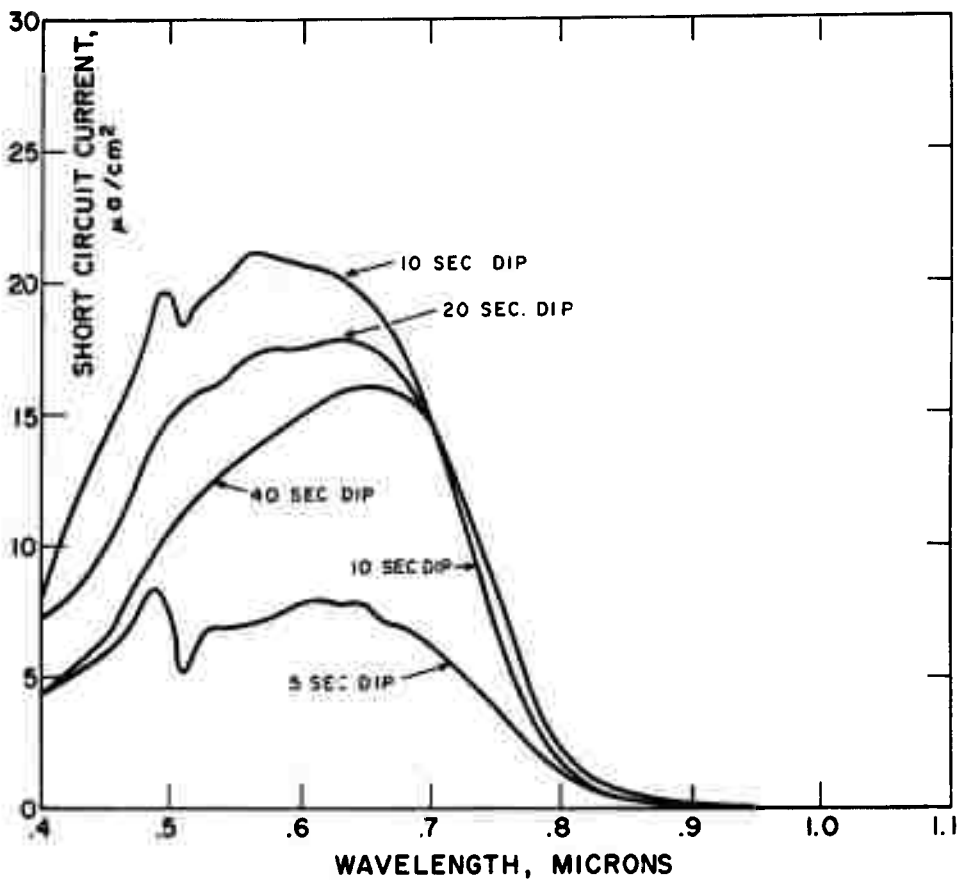


FIG. 53. SPECTRAL RESPONSE OF UNDOPED CdS CERAMIC SOLAR CELLS vs. DIP TIME, MONOCHROMATIC LIGHT. DATA ADJUSTED TO CONSTANT ENERGY INPUT. CuCl IN DIP SOLUTION = 1 g/l.

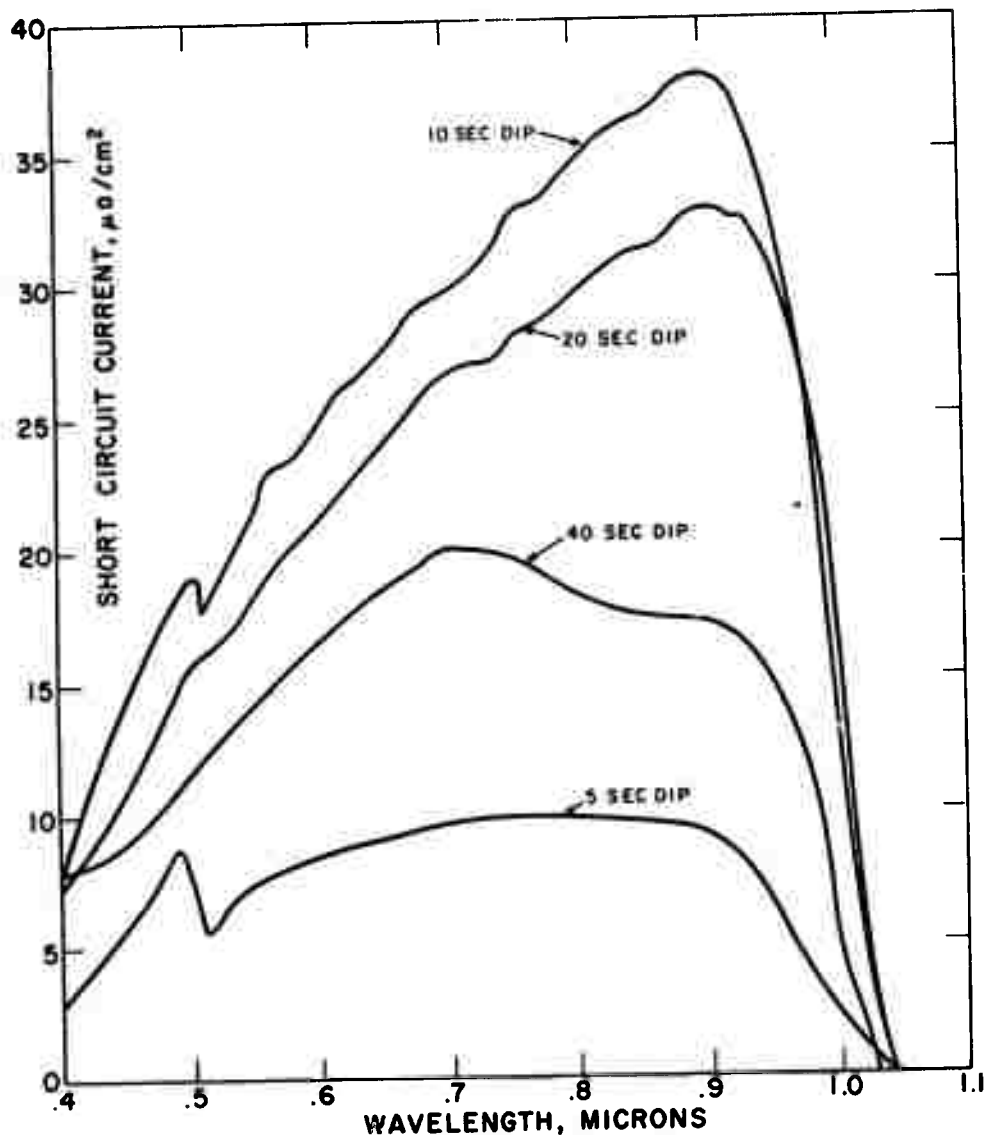


FIG. 54: SPECTRAL RESPONSE OF CdS CERAMIC SOLAR CELLS
vs. DIP TIME. CELLS DIPPED IN 1 g/l CuCl SOLUTION.
WHITE LIGHT ADDED. RESPONSE ADJUSTED TO
CONSTANT ENERGY INPUT.

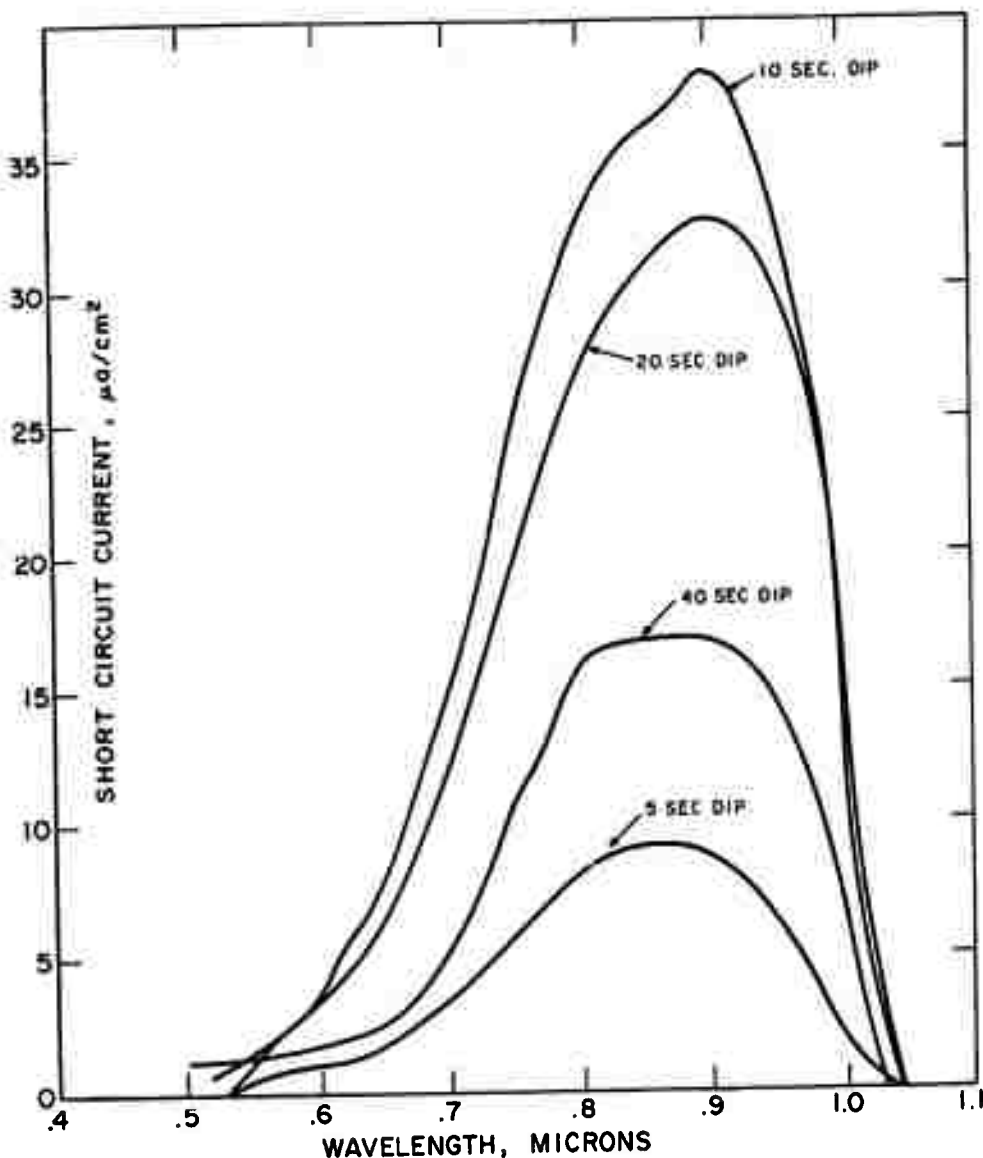


FIG. 55. ENHANCEMENT CURVES OF UNDOPED CdS CERAMIC SOLAR CELLS FORMED IN 1 g/l CuCl SOLN.

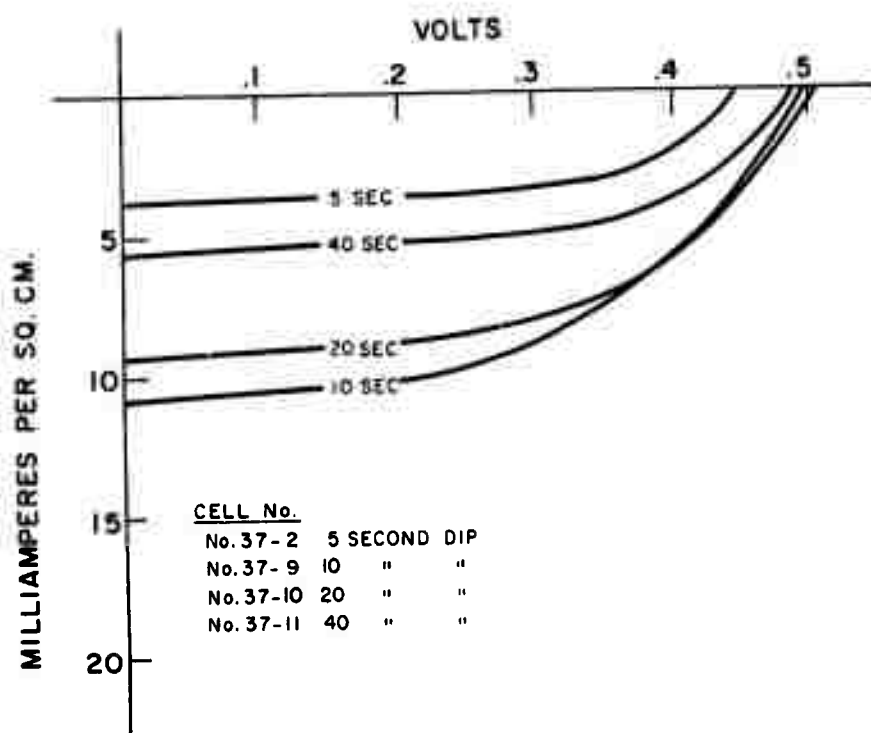


FIG. 56. I-V CHARACTERISTIC OF UNDOPED CdS CERAMIC SOLAR CELL WITH VARYING DIP TIMES. MEASURED AT 100 mw/cm^2 SIMULATED SUNLIGHT (AM1) CuCl IN DIP SOLUTION 1g/l .

in opposition to the photovoltaic current. The steady state condition is reached when these two currents are equal. Since recombination diminishes the photovoltaic current, the forward-bias diode current is also diminished, and the steady-state condition is fulfilled at a lower diode voltage, i. e., at a lower V_{oc} .

The rise of V_{oc} to the maximum value can also be explained on the same basis. As the Cu_2S thickness increases from zero, the light absorption increases very rapidly, hence the photovoltaic current, the balancing forward diode current, and the diode voltage increase with thickness. The V_{oc} thus increases until the photovoltaic current starts to diminish due to recombination in the Cu_2S layer.

The fact that short-circuit current and the open-circuit voltage reached maximum values at nearly the same time (as the Cu_2S thickness was increased) is understandable on this basis. The increase in V_{oc} with "junction current" is highly non-linear, following as it does the usual diode IV relationship. The rise of V_{oc} with increasing light intensity is also a direct result of this relationship. At low light intensities (and in the absence of degrading shunts), V_{oc} rises rapidly with light intensity. At high light intensities, V_{oc} increases only slightly with increasing intensity because now the diode is biased in the strongly forward region where the operating voltage is relatively insensitive to current.

3.6.3 Single Crystal Cells

In order to show that the above effects are not peculiar to ceramic cells, the results on an In-doped single-crystal cell are shown in Fig. 57. The results are seen to be very similar to those of In-doped ceramic cells dipped for 2 to 5 seconds. This single-crystal cell had an efficiency of 4.9% in AMI sunlight. The rather low quantum yield of 12% and the minimum at 0.52μ indicate that the Cu_2S layer was a little too thin for optimum efficiency. The enhancement threshold at $\sim 0.7 \mu$ is a characteristic of In-doped cells, as discussed earlier.

Bube, Gill, and Linquist⁽³⁵⁾ have recently presented back-wall spectral-response measurements on a small single-crystal cell before and after heat-treatment at $300^\circ C$. Their results are reproduced in Fig. 58. The change in response upon heat treatment is surely associated with the

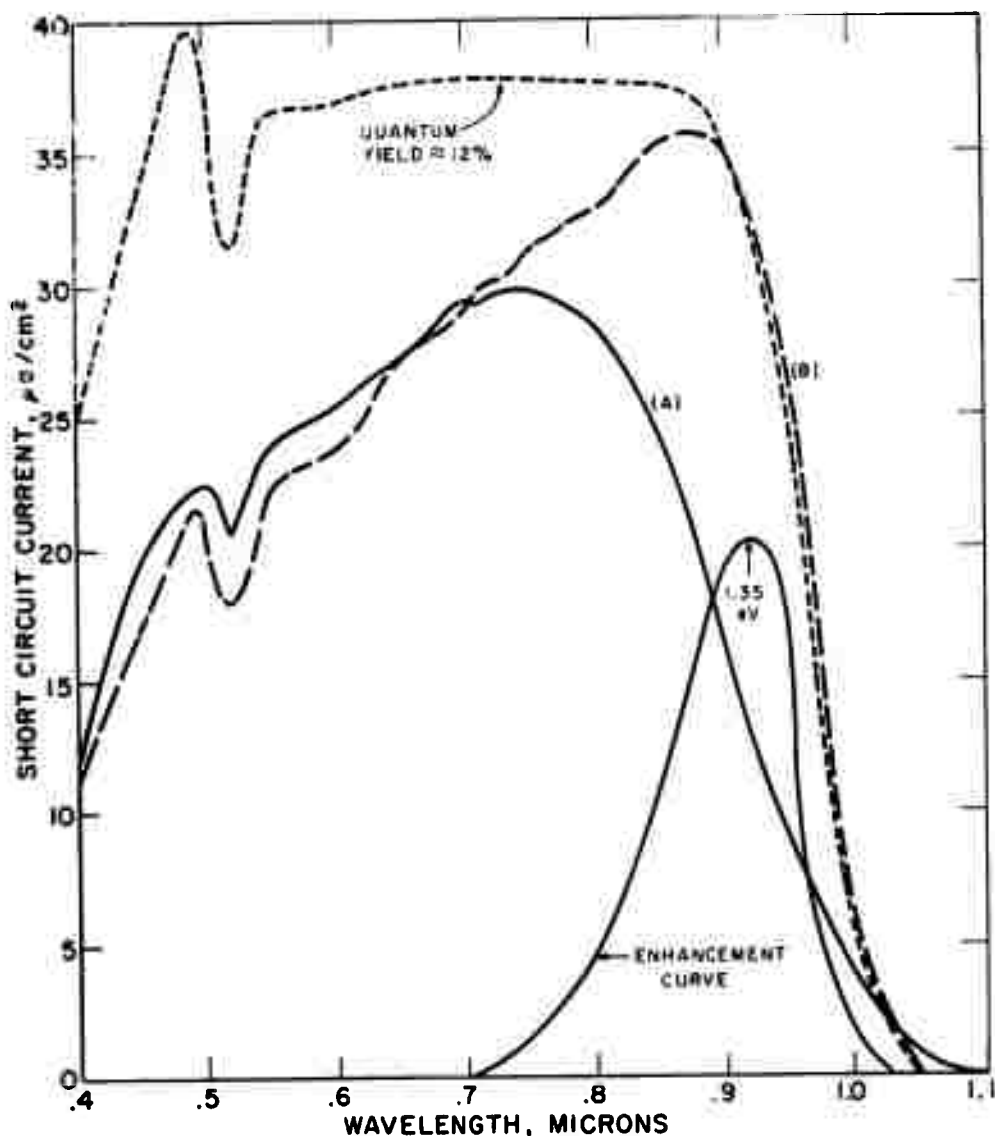
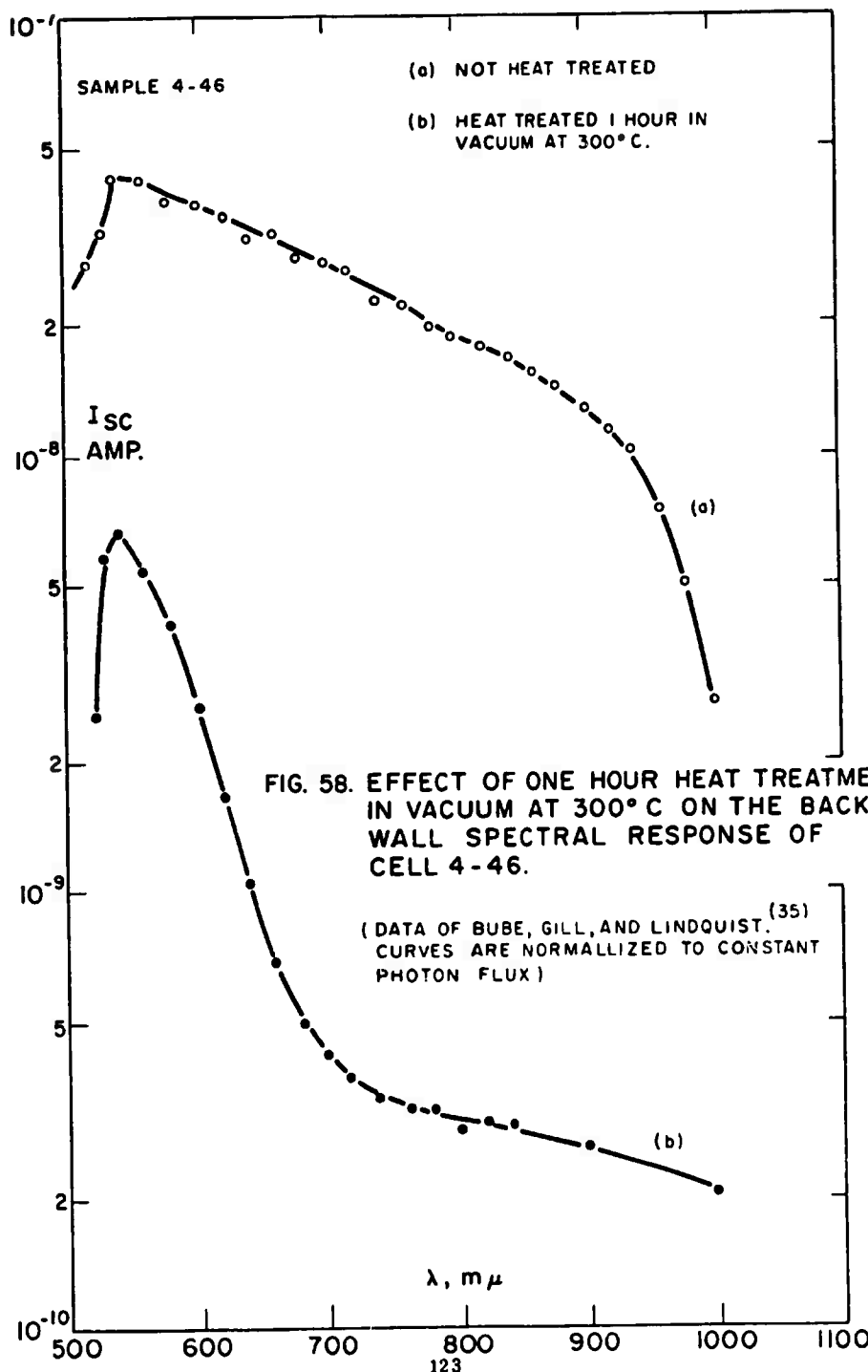


FIG. 57. SPECTRAL RESPONSE OF In-DOPED CdS SINGLE CRYSTAL SOLAR CELL. (A) MONOCHROMATIC RESPONSE. (B) RESPONSE WITH WHITE LIGHT ADDED. ADJUSTED TO CONSTANT ENERGY INPUT. CuCl IN DIP SOLUTION = 17 g/l. CELL AREA = 1 cm²



formation of a thick i-layer of CdS. The i-layer before heat-treatment is so thin that it presents no serious impedance to the flow of electrons generated in the Cu_2S layer. After heat treatment the photovoltaic response is controlled by the photoconductive response of the i-layer. The photovoltaic response after heat treatment is very similar to the photoconductive spectral response of Cu-compensated undoped CdS (see Fig. 47). The single-crystal cell under discussion here was prepared from an undoped CdS crystal. The small magnitude of the band-edge peak probably resulted from the use of the back-wall mode of operation. The n-CdS layer absorbs a large fraction of the incident light as the band edge of CdS is approached from longer wavelengths; thus the wavelengths most effective in exciting photoconductivity are attenuated before they reach the i-layer. Thus even at the peak, the photovoltaic current is limited by series resistance. The response before heat treatment is clearly not seriously limited by the resistance of the i-layer since there is only a smooth, well-behaved variation of output with wavelength between the band edges of CdS and Cu_2S . The sudden drop in output at wavelengths shorter than that at the band edge of CdS is due to very strong absorption in the n-CdS layer. The smooth decrease of output on the long wavelength side of this edge is very informative. The current arises from absorption of light in the Cu_2S layer. In the backwall mode, the more strongly absorbed short-wavelength photons are absorbed closer to the junction than the less strongly absorbed long-wavelength photons; hence the collection efficiency decreases as wavelength increases. (A similar decrease is shown in Fig. 16 of Ref. 35). In contrast, the behavior in frontwall mode is reversed, "blue" light being absorbed at the front surface of the Cu_2S which is furthest from the junction. This can be easily seen for example, in Fig. 45 wherein the response of all of the curves is not seriously limited by the resistance of the i-layer, even for the cell dipped for 40 seconds. If the "2-second" cell is normalized to an equal-photon-flux basis, the response between ~ 0.55 and $\sim 0.85 \mu$ becomes very nearly constant (like the quantum-yield curves of Fig. 57 and 59). This indicates that for this thickness of Cu_2S , the response is not limited by the diffusion length of the electrons in the Cu_2S . If the 5-second cell is normalized in this way, the response at 0.55μ remains slightly below the response at

0.85 μ . This trend continues for the 10-second cell and the 20-second cell, and for the 40-second cell, the response at 0.55 μ is only half the response at 0.85 μ . Recombination of electrons and holes is obviously increasing as the Cu_2S layer is thickened and the rate of recombination at short wavelengths over that at long wavelengths is also increasing with increasing Cu_2S thickness. All of these trends are in excellent qualitative agreement with our model for the CdS solar cell. The behavior at shorter wavelength is also in good agreement if we ignore the unexplained structure near 0.51 μ for the thin- Cu_2S cells. The blue response decreases even faster than the response at 0.55 μ in agreement with the idea that recombination becomes more pronounced as the absorption becomes stronger, provided that the Cu_2S layer is thicker than the diffusion length of the electrons. The last point can be appreciated in the behavior of the 1-second cell. The Cu_2S layer on this cell is so thin that the response at $\lambda > 0.55\mu$ is dominated almost entirely by absorption efficiency, the collection efficiency being uniformly high at all wavelengths in this range. The diminishing absorption at long wavelengths causes the peak of the spectral response to shift to shorter wavelengths as the Cu_2S thickness is decreased. This shift can be seen for all six cells in Fig. 45: the dashed line represents the locus of the response peaks as a function of Cu_2S thickness (dip time).

3.6.4 Thin Film Cells

In order to show that the above effects are also seen in thin film solar cells, the results on a Mylar-covered 2 cm^2 cell are shown in Fig. 59. The measurements on this cell were made under somewhat different conditions. The light intensity at 0.8 μ was slightly higher ($500 \mu \text{W/cm}^2$ vs. $430 \mu \text{W/cm}^2$) and the biasing light consisted of band-edge 0.522 μ light at $500 \mu \text{W/cm}^2$ instead of white light at $430 \mu \text{W/cm}^2$. The spectral response is seen to be very similar to those of the ceramic and single-crystal cells. This particular cell was chosen because it had an unusually high shunt resistance which allows good low light-level response. The quantum yield for this cell was nearly constant at 30% between 0.45 and 0.9 μ . The higher yield over that of the single-crystal cell (Fig. 57) is probably due to (1) the stronger and much more effective green-light bias, (2) a more nearly optimized Cu_2S thickness, and (3) greater convolutions of the Cu_2S layer that cause the "effective" Cu_2S thickness to be larger than the actual thickness.

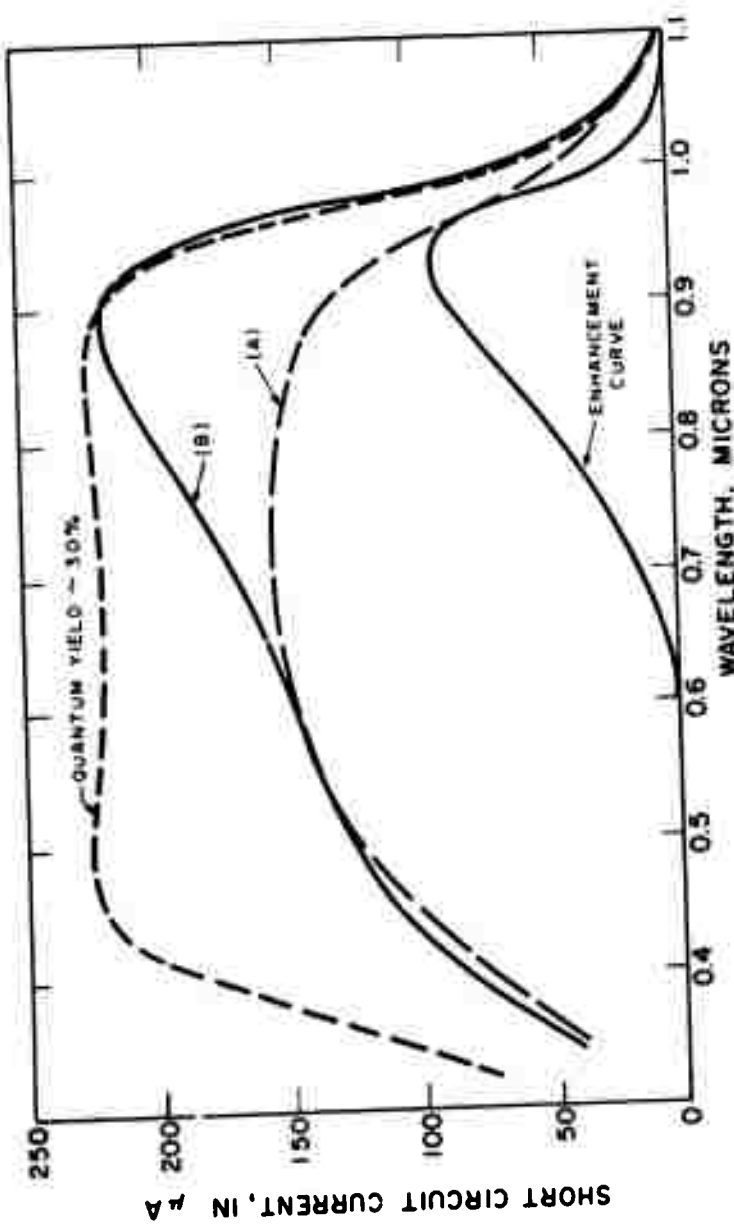


FIG. 59. SPECTRAL RESPONSE OF THIN FILM CdS SOLAR CELL No. B696E6.
 (A) MONOCHROMATIC RESPONSE ADJUSTED TO CONSTANT ENERGY INPUT
 OF $500 \mu\text{W}/\text{cm}^2$. (B) RESPONSE WITH GREEN LIGHT ADDED, $500 \mu\text{W}/\text{cm}^2$,
 522 Å . AREA = 2 cm^2 .

The short-wavelength threshold of the enhancement curve at 0.6μ is about midway between the thresholds of the undoped and In-doped ceramic cells. The thin film cell was prepared from undoped CdS, the same source material used for the undoped ceramic cells. It appears that vapor deposited CdS has a photoconductive response (after Cu-compensation) that is between the photoconductive response of Cu-compensated undoped and In-doped CdS. This could result from donor contamination during evaporation or excess Cd that exists in a state that makes it behave like a foreign donor (see Section 3.4.2).

3.6.5 Transient Effects

Another property which can be attributed to the photoconductivity of the i-layer is the slow transient effects observed in spectral response measurements. When the wavelength of the exciting light is swept past the photoconductive peak of the i-layer (centered at the band edge CdS and extending to slightly longer wavelength for thin film cells), the output of the cell remains high beyond the photoconductive peak for fast sweep rates (e.g., 8000 \AA/min), but drops off sharply when λ is varied slowly (e.g., 80 \AA/min). This indicates that charge carriers generated in the i-CdS layer live long enough (10-20 sec) so as to maintain the photoconductive "gate" open while neighboring wavelengths are being swept. This effect is shown by the spectral response curves of Fig. 60. The effect of sweep-direction alone is shown in Fig. 61 for a relatively fast sweep rate (2200 \AA/min).

Many new measurements dealing with similar effects, but in much greater detail, have been recently reported by the Stanford group.⁽²⁴⁾

3.6.6 Antimonochromatic Spectral Response

An antimonochromator for evaluating the spectral response of the CdS photovoltaic cells at a total radiant energy density of 10 to 100 mW/cm^2 has been constructed. This approach was chosen because a monochromator with this intensity level is both impractical and would not give a realistic analysis of the cell's spectral response. Since the photoconductivity and the photo-current generation arise from independent mechanisms with different spectral response, any analysis of the cell's spectral

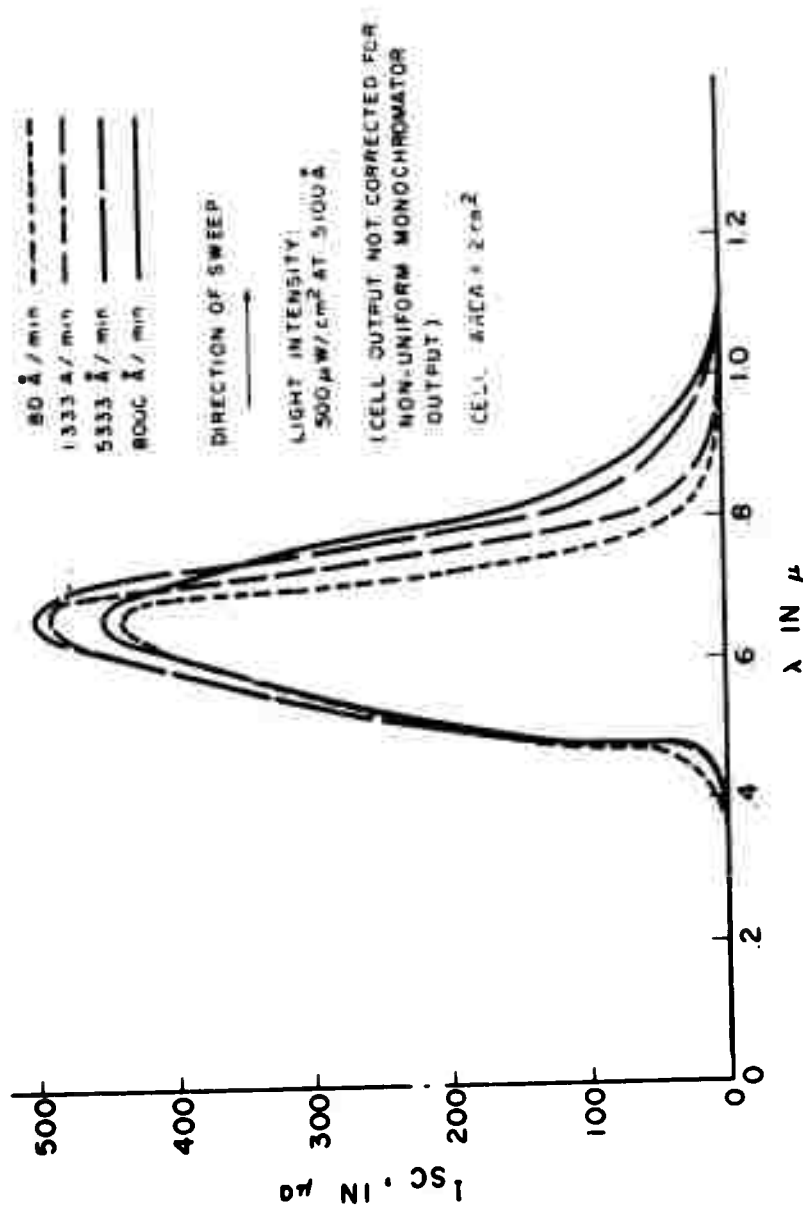


FIG. 60. THE EFFECT OF RATE OF SWEEP (INCREASE OF WAVELENGTH) ON THE SPECTRAL RESPONSE, CELL No. B-810D-5.

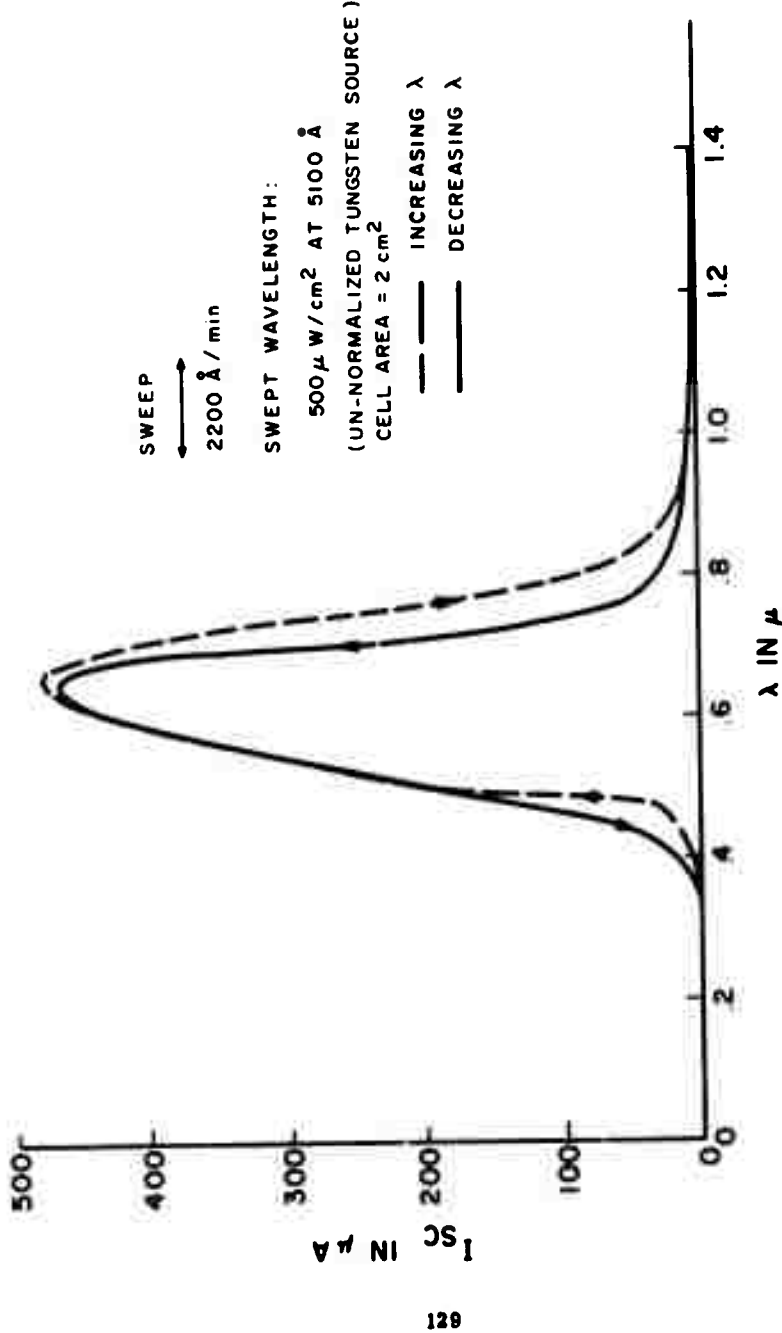


FIG. 61. SHORT CIRCUIT CURRENT AS A FUNCTION OF WAVELENGTH,
 ILLUSTRATING THE EFFECT OF THE DIRECTION OF SWEEP.
 CELL No. B-811E-6.

response must expose the cell to illumination in the wavelength bands which are responsible for the stimulation of each mechanism. Consequently, the antimonochromator first exposes a cell to a solar spectral distribution, and then removes a bandwidth of the radiation, the center wavelength of which may be continuously swept across the spectrum while some output parameter of the cell is being recorded.

The principle of operation of the antimonochromator is a modification of the van Cittent zero dispersion monochromator,⁽³⁶⁾ with the essential change being the replacement of the traversing slit for band selection with a traversing stop for band removal. A photograph of the antimonochromator is shown in Fig. 62. A schematic of the optical components is shown in Fig. 63. Using 145 mm focal length objective lenses, the image of the visible spectrum in the plane of the traveling stop is approximately 4 mm in width. A 0.5 mm wire stop, suitably curved to follow the curvature of the spectrum, and a straight, parallel input slit of 0.4 mm width produced an approximately 600 Å wide gap in the blackbody spectrum. The spectrum re-synthesized by the second half of the optical system presented about 15 to 50 mW/cm² (depending on the degree of alignment of the optics) over a 1 cm x 2 cm area with less than 1% of the intensity of the center of the stopped wavelength present (intensities over 100 mW/cm² are obtained over smaller areas). When the output of the antimonochromator was viewed with a hand-held visual spectroscope, the appearance was that of a very broad Fraunhofer line being swept across the blackbody spectrum. An improvement under consideration is the use of actual sunlight, directed to the input slit by a coelostat to obtain higher light intensities and a more accurate solar energy spectral distribution, particularly in the blue and blue-green regions which are predictably weak in the 3000°K incandescent source now in use.

The antimonochromator was calibrated by the following procedure:

- a) The center of the stopped band vs. drum reading was calibrated visually against Baird-Atomic narrow-band interference filters at about 500 Å intervals across the visual spectrum.

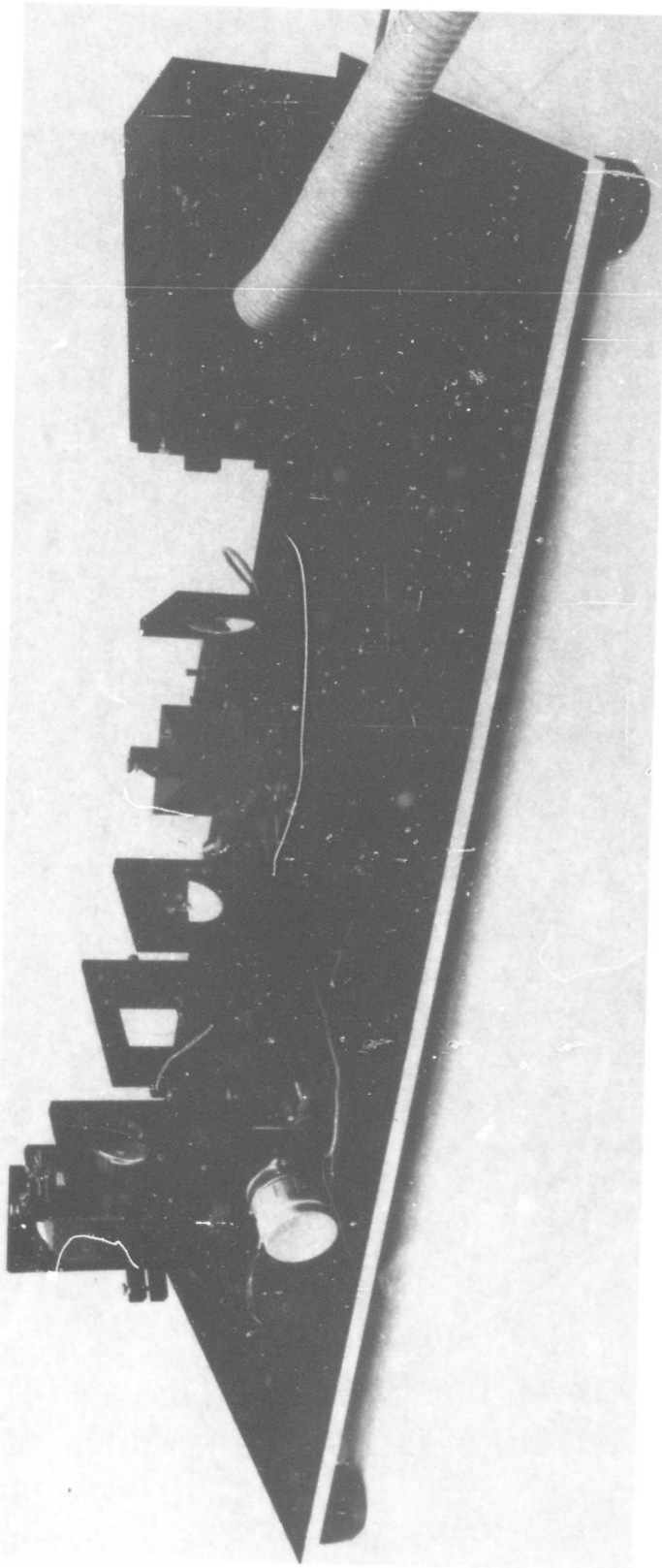


FIG. 62. PHOTOGRAPH OF THE 1-SUN ANTIMONOCROMATOR

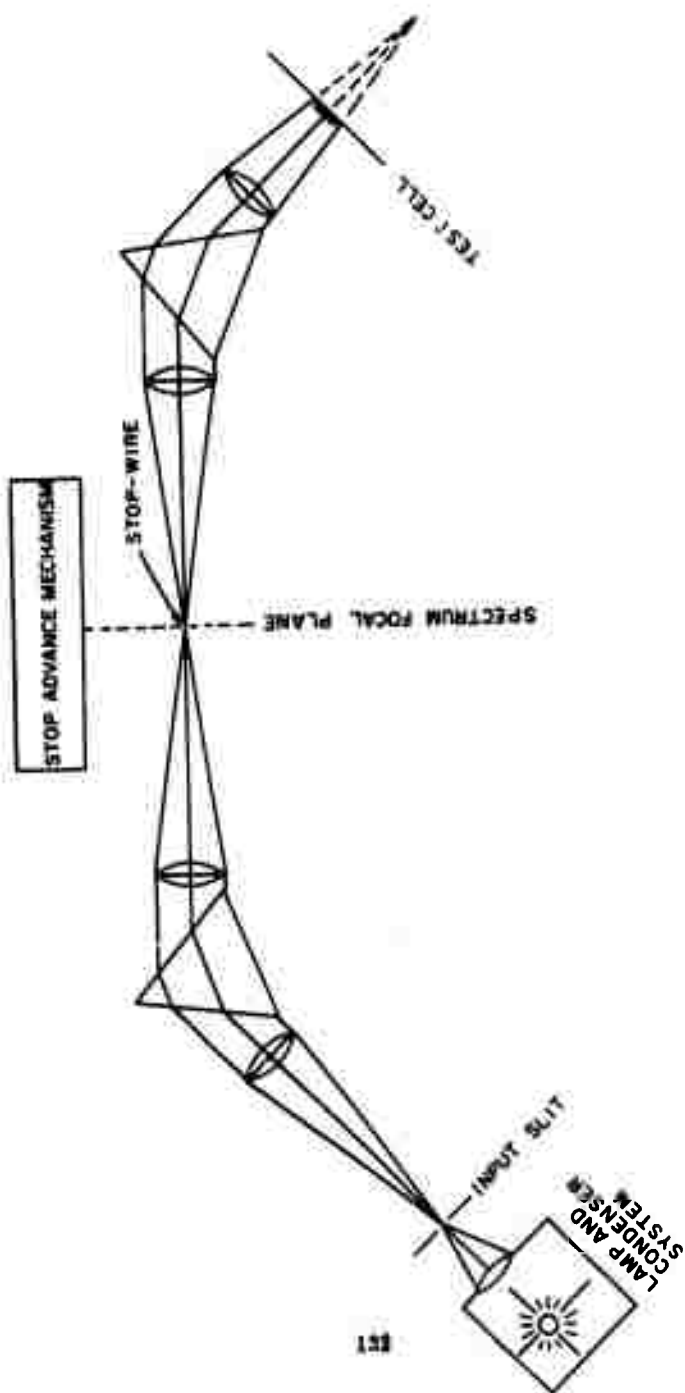


FIG. 63. SCHEMATIC OF THE ONE SUN ANTIMONOCROMATOR.

b) With the Bausch & Lomb Grating Monochromator, the calibration was extended into the IR to 1.5μ .

c) The calibration determined above was spot-checked against the prominent lines of the Hg spectrum.

d) The shape, intensity vs. λ , of the stopped-band was measured at six points across the 0.4μ to 1.5μ range by locating the stop at the desired "notch" wavelength with the antimonochromator output spectrum being scanned by the B&L monochromator and the B&L output being measured by a PbS photometer. Similarly, the antimonochromator output spectrum with the stop removed was measured to determine the total output spectral distribution.

e) The energy content of the stopped band was measured with a total radiation thermopile across the output spectrum from 0.4μ to 1.8μ .

The output color temperature, on the basis of the output spectral distribution measurement, was found to be a little lower than expected, about 2500°K . This appears to be due to the yellowish cast of the antimonochromator prisms. The dispersion of the antimonochromator prisms was also found to be more non-linear than anticipated, yielding a sharper resolution in the $.4 \mu$ to $.65 \mu$ band and a broader resolution in the $.65 \mu$ to 1.8μ band than expected. The half-height bandwidth varies from about 50 \AA at 0.4μ to about 1500 \AA at 1.5μ while the maximum extinction ratio varies from about 100:1 over the blue to green-yellow band to about 20:1 at 1.5μ .

Twenty seven cells of various types were examined with the antimonochromator: 4 thin-film cells, 11 In-doped-CdS ceramic cells, 10 undoped-CdS ceramic cells, and 2 In-doped CdS single-crystal cells. Typical examples of each of the four types of cells are shown, respectively, in Figs. 64, 65, 66 and 67. The curves are not normalized to equal energy because the structure, especially that at the band edge of CdS is dependent on light intensity in a highly non-linear way so that a linear normalization would introduce considerable unreal distortion. But since the energy in the stopped band varies considerably with wavelength, the curves must be interpreted in terms of the non-uniform spectral distribution of the light source, and the different bandwidths that apply at each wavelength. The spectral

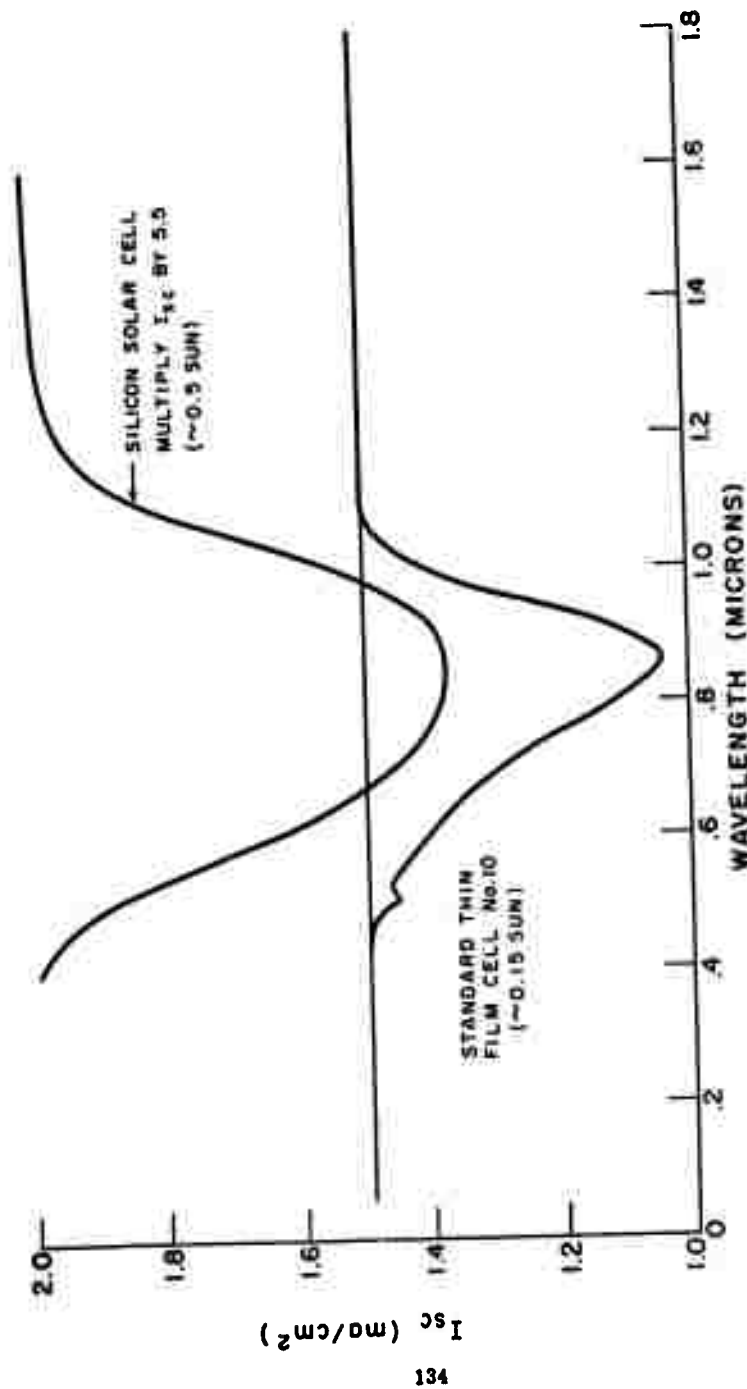


FIG. 64. ANTIMONOCHROMATIC SPECTRAL RESPONSE, Cds THIN FILM CELL.

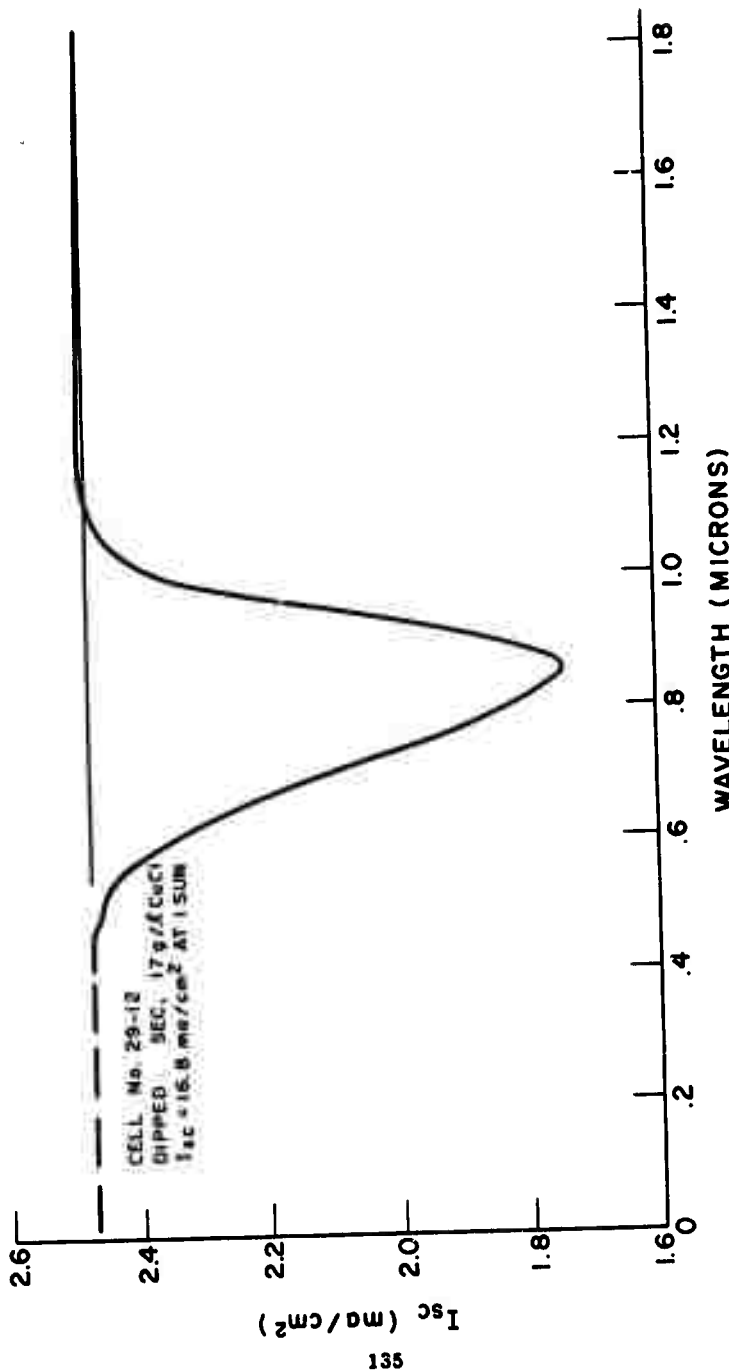


FIG. 65. ANTIMONOCHROMATIC SPECTRAL RESPONSE, In-DOPED CdS CERAMIC CELL

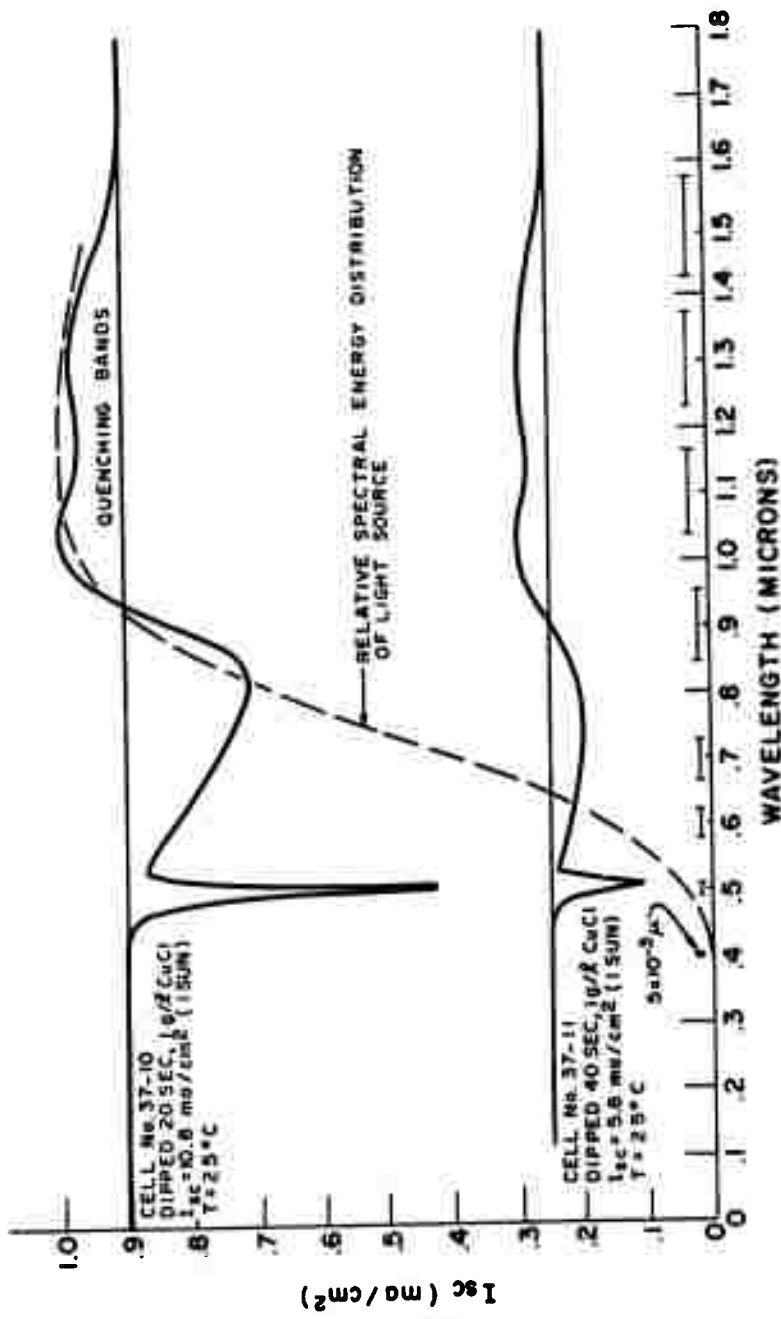


FIG. 66. ANTIMONOCHROMATIC SPECTRAL RESPONSE. UNDOPED CdS CERAMIC CELL.

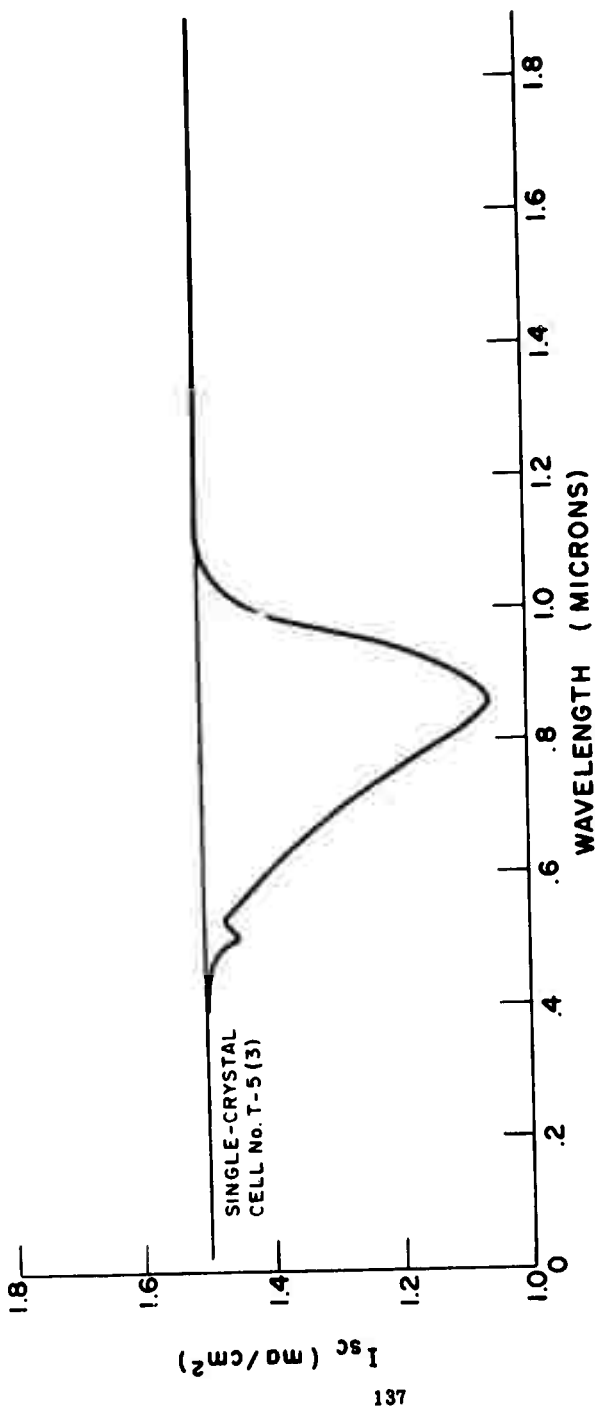


FIG. 67. ANTIMONOCHROMATIC SPECTRAL RESPONSE, Cds SINGLE CRYSTAL CELL.

distribution of the source is shown by the dashed curve in Fig. 66. The bandwidths are shown at selected regions by the range marks near the wavelength axis of Fig. 66. The current output of the cells was measured by the voltage developed across a $1\ \Omega$ resistor which yields a close approximation of the short-circuit current. For comparison, the response of a Si solar cell is shown in Fig. 64 (the total light intensity for this measurement was at ~ 0.5 suns, due to better alignment of the source optics).

In Figs. 64, 65, and 67 very little structure is seen. The behavior of the cells is similar to that of the Si cell shown in Fig. 64. The only differences are the larger long-wavelength threshold of the Si cell, its slightly broader response, and for the CdS cells, the presence of a small dip in output at the band edge of CdS. The broad bandwidth at the larger wavelengths artificially extends the threshold to somewhat longer wavelengths.

The behavior of the undoped CdS ceramic cell, shown in Fig. 66, is very different and much more informative. Two striking effects are clearly visible:

a) Over half of the short-circuit current is lost when a narrow 200 \AA band at 5100 \AA is removed. This happened in spite of the fact that only a very small percent of the total light energy was removed (notice the very small amount of green light in the light source spectral distribution). This demonstrates the strong "gating" action of the i-CdS layer. The effect is strong only in the undoped cells because the photoconductive response for these cells is wholly restricted to the narrow band-edge region (see Fig. 47). For this type of cell an artificial gain exceeding unity can be obtained by the use of green light in the presence of a strong constant light that does not contain green light.

b) Two broad quenching bands are seen at ~ 1.04 and $\sim 1.30\ \mu$. These are resolved in spite of the very large bandwidths used in this region. For cell 37-10, a 11% increase in current is obtained when the $\sim 1.04\ \mu$ band is excluded, and for cell 37-11, which had a thicker Cu_2S layer, a 20% increase in current was obtained. The corresponding energies at the maxima of the quenching bands are ~ 1.19 and $\sim 0.95\text{ eV}$. The threshold values for the onset of quenching are undoubtedly lower in energy and might well be as low as 1.1 eV and 0.8 eV , the two values found by the Stanford group⁽²⁴⁾

through detailed analysis of the enhancement effects of light-bias. They associate these energies with Cu centers. We have no evidence to refute this. It would, however, be desirable to study the photoconductive quenching spectrum of CdS crystals that do not contain Cu (e. g., S-compensated crystals) in order to see if these centers are absent in these crystals.

The quenching bands are not present or are feeble in the In-doped cells and in the thin film cells (which behave like lightly donor-doped cells) because the photoconductive excitation spectrum extends into this wavelength region, even though it is rather weak beyond 0.9μ (see Fig. 47). As pointed out by the Stanford group, when enhancement and quenching processes compete, enhancement of necessity dominates.

3.7 Miscellaneous Studies

3.7.1 Reaction of Zn and Ag at Metallized Substrate

Composite X-ray diffraction patterns of standard solar cells contain diffraction peaks due to CdS, the gold plated copper grid, and the cover plastic (Mylar in particular showing a very strong and broad peak at $\sim 3.36 \text{ \AA}$). In addition, a weak peak at 2.20 \AA has been consistently found. This peak was the only one that could not be correlated with one of the known components of the cell. X-ray examination of several standard cells in various stages of completion quickly established the identity of this peak as the strongest (300) line of a Zn-Ag compound having an approximate composition of ZnAg.

Even as the Zn is being plated onto the Ag-Pyre ML substrate, the bath temperature of $\sim 50^\circ\text{C}$ is high enough to cause the formation of an easily detectable amount of the cubic epsilon phase of the Zn-Ag phase diagram. (37) This phase has a solid solution range which includes the composition Zn_3Ag . The principal pattern after plating is that of Zn and Ag. Oven drying for a few minutes at $\sim 100^\circ\text{C}$ causes a major conversion of the Zn to Zn_3Ag and the formation of a small amount of the hexagonal close-packed zeta phase ($\sim \text{ZnAg}$). There is very little Zn left at this point. Heating the film at 200°C for 1 hour under N_2 caused further solid-state reaction. All of the Zn had been converted to ZnAg. No Zn or Zn_3Ag could be detected. The intensity of the Ag lines was progressively attenuated by the reaction and the growth of the overlying Zn-Ag compounds. The Ag lines after the 200°C

treatment were about 1/8 of their original intensity. The strongest line of the ZnAg phase was ~ 10 times stronger than the neighboring Ag lines. Therefore this line and only this line was strong enough to be detected through a standard thickness of CdS. In a separate experiment the reaction of Zn and Ag to form Zn_3Ag was found to be substantial at room temperature over a period of several days.

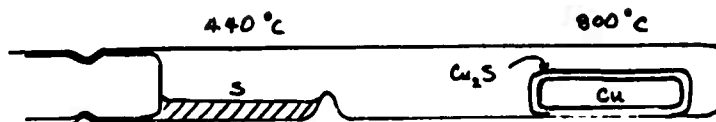
The Ag Pyre ML layer of standard cells has a thickness of 8μ and is 33% Ag by weight. Since Ag is much denser than Pyre ML, the equivalent thickness of the Ag alone is $\sim 0.5 \mu$. The thickness of the original Zn plating is 1.5μ . The corresponding masses per unit area are $5 \times 10^{-4} \text{ g/cm}^2$ for Ag and $10.7 \times 10^{-4} \text{ g/cm}^2$ for Zn. The composite Ag-Zn layer is thus 68% Zn by weight. If no Zn were lost by oxidation or by sublimation during subsequent processing, the final composition should be approximately Zn_3Ag (68% Zn is the center of the composition range of the epsilon phase). Since the compound ZnAg is observed in completed cells, it would appear that approximately half of the original Zn plating was lost in these cells--probably in the evaporator when the substrate was exposed to vacuum at $\sim 200^\circ\text{C}$. The fact that the Ag particles are dispersed in the Pyre ML probably causes many of the particles to be isolated and hence incapable of reacting with the Zn.

The ohmicity of the CdS:ZnAg junction is apparently adequate since most cells do not suffer from excessive series resistance. The resistivity of ZnAg, however, is probably much higher than that of Ag and long term changes due to continuing inter-diffusion of Zn and Ag are possible. The adhesion at the CdS:ZnAg interface could also be influenced by these changes. Ag diffusing into the CdS and compensating the n-type conductivity is another long-term possibility. These are some of the reasons why an alternate substrate system would be desirable.

3.7.2 Synthesis of Cuprous Sulfide

The unusually high diffusivity of copper vacancies in cuprous sulfide provides a simple means of synthesizing the compound from its constituent elements. High purity copper and sulfur (both 99.999+% from American Smelting and Refining Co.) were reacted in an evacuated fused-quartz tube

as shown below:



The copper was in the form of a 3/8" rod about 1" in length. A stoichiometric amount of sulfur was contained in the reservoir and was maintained near the normal boiling point of 444°C. The copper, maintained at 800°C, quickly formed a skin of Cu_2S which rapidly thickened with time. The reaction was completed in ~ 6 minutes. Several syntheses of this kind have been completed and similar results were obtained in each case.

The final product is in the form of a dense polycrystalline boule having a hollow center. The hollow center demonstrates that the reaction occurs by diffusion of Cu (via vacancies) through the Cu_2S and reaction with sulfur vapor at the outer surface. Assuming the diffusing species is singly charged ($\text{V}^- \text{Cu}^+$), the average ionic flux density during this reaction is equivalent to a current density of ~ 80 amp/cm². Cuprous sulfide clearly has an unusually high ionic diffusivity and conductivity (see Section 3.2.8).

The polycrystalline boule was composed of single-crystal grains as large as 75 mm³ in volume and the grain boundary structure indicated that lateral grain growth had occurred. Copper diffusing through the Cu_2S apparently reacts with sulfur from the vapor to extend the cuprous sulfide layer by epitaxial growth. A novel method of growing large single crystals of cuprous sulfide is suggested by these observations. We predict that diffusion of copper through a Cu_2S seed crystal will produce epitaxial growth at the opposite surface and that the high diffusivity of Cu will allow extended growth. The proposed scheme is shown in Fig. 68.

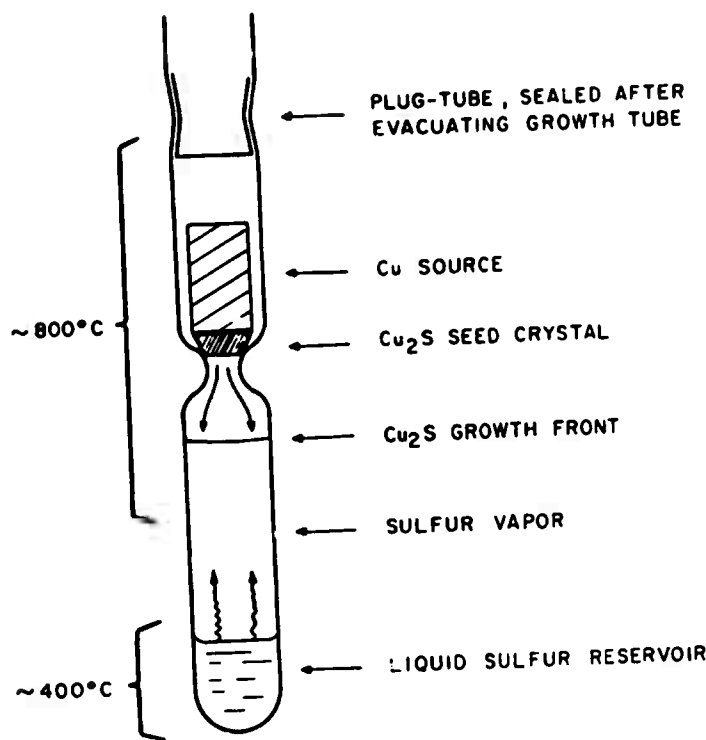


FIG. 68. PROPOSED METHOD OF PREPARING LARGE SINGLE CRYSTALS OF CUPROUS SULFIDE.

3.7.3 Cell Output vs. Angle of Illumination

In an attempt to see if the sinusoidal dependence of cell output on the angle of the parallel incident radiation is properly obeyed, measurements have been made on I_{sc} as a function of the angle of incidence, with ~ 1 sun white light. This dependence was verified, as shown in Fig. 69.

3.8 Calculation of Maximum Efficiency of CdS Solar Cells

3.8.1 Maximum Theoretical Efficiency

In this section the highest power efficiency that a CdS cell could attain under the most favorable possible conditions is calculated. Since many of the assumptions used in these calculations are necessarily unrealistic a subsequent estimate of a "maximum achievable efficiency" will follow the first calculation.

In the absence of degrading series and shunt resistance, the IV characteristics of most photovoltaic cells under illumination can be described by an equation of the form

$$I = I_L - I_o \left[e^{qV/AkT} - 1 \right] \quad (1)$$

where I_o , the reverse saturation current and A , the diode factor, are constants; and I_L is the light-generated current density in the junction. For the particular cases of Ge and Si photovoltaic cells, the observed IV characteristics can be fitted to the equation with high accuracy when the diode factor A has the values 1 and ~ 2 respectively. Furthermore, these values of A and the observed values of I_o agree well with the theoretical values computed from the basic material properties of Ge and Si. In the case of the CdS cell, I_o and A cannot (as yet) be independently calculated because of the absence of required material constants such as the difference in work function between CdS and Cu_2S . Nevertheless, for theoretical purposes, a value of unity for A can be assumed as the most favorable possible condition. This value applies to the case where the junction current is limited by the diffusion of photogenerated minority carriers to the junction.

Since I_o cannot be calculated, we are forced at this point to make an estimate. It appears that the safest way of estimating I_o is to estimate instead the maximum value of V_{oc} and then to compute I_o from the

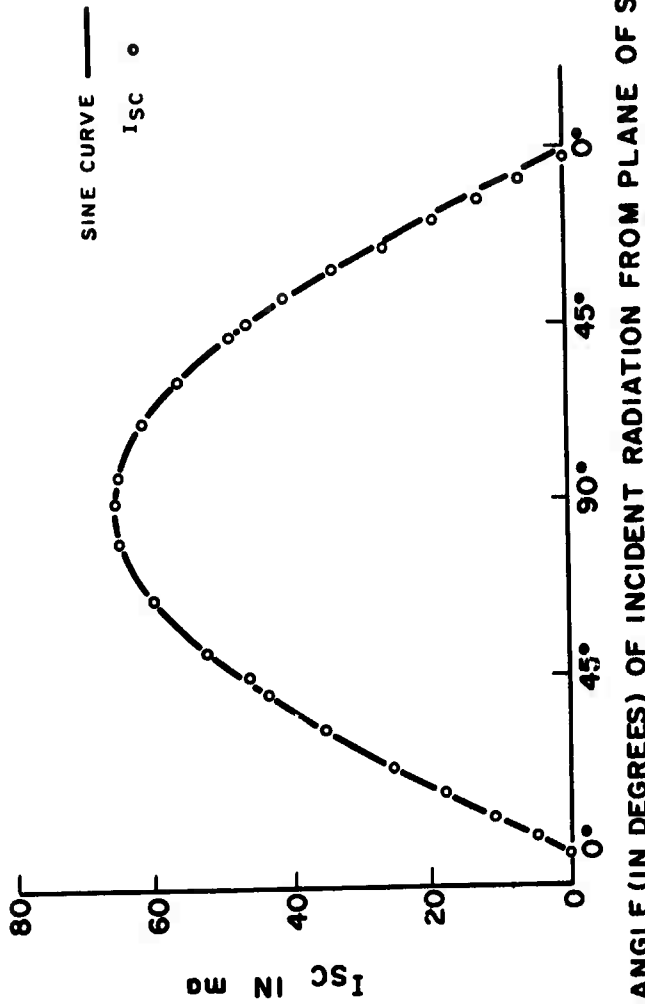


FIG. 69: COMPARISON OF SHORT CIRCUIT CURRENT vs. ANGLE OF INCIDENCE (~1 SUN WHITE RADIATION) AND SINE CURVE, NORMALIZED SO THAT THE MAXIMA COINCIDE. CELL No. B-696E-6.

diode equation. In order to do this, I_L must first be evaluated. From Table V, the total photon flux density in sunlight ($m = 0$) is found to be 6.5×10^{17} photons/cm²/sec. Of this total flux, very close to half, or 3.2×10^{17} photons/cm²/sec have energies greater than the band gap of Cu₂S ($E_G = 1.2$ eV, $\lambda = 1.02 \mu$) and are hence capable of being absorbed. Assuming unity absorption and collection efficiencies for these photons, $I_L = 3.2 \times 10^{17}$ electrons/cm²/sec, which, when multiplied by the electronic charge yields $I_L = 51$ ma/cm². This compares with 56 ma/cm² for the Si cell, which has a slightly smaller band gap.

We now compute I_o by estimating V_{oc} (intrinsic) as 0.500 volts, the maximum reliably observed room-temperature value for high efficiency CdS cells. (We are in effect now introducing V_{oc} as an adjustable parameter--a definite weakness in the analysis, but one which has the virtue of underestimating rather than overestimating the final results.) Among thousands of CdS cells produced with many intentional and unintentional variations, $V_{oc} = 0.50$ volts appears to be an upper limiting value. Hence, taking $V = V_{oc} = 0.50$ volts, $I = 0$, $I_L = 0.051$ amp/cm², $A = 1.0$, $T = 298^\circ K$, and noting that $I_o \ll I_L$, equation (1) yields $I_o = 10^{-10}$ amp/cm². Thus at room temperature, the "ideal" IV relation reduces to:

$$I = 0.051 - 10^{-10} e^{38.9 \times V} \text{ (amp/cm}^2\text{)} . \quad (2)$$

Multiplying equation (1) by V and setting $d(IV)/dV = 0$, the maximum-power voltage, V_m , is obtained:

$$V_m = \frac{AkT}{q} \ln \left[\frac{I_L}{I_o \left(\frac{qV_m}{AkT} + 1 \right)} \right] \quad (3)$$

which reduces in the present case to:

$$V_m = 0.0592 \log_{10} \left[\frac{5.1 \times 10^8}{38.9 V_m + 1} \right] \quad \text{for } A = 1.0 .$$

V_m is obtained by trial and error and is found to be $V_m = 0.441$ volts. Using this value for V , equation (2) gives $I_m = 0.048$ amp/cm². The short circuit current density, I_{sc} , assuming no reflection, cover absorption, or grid losses

TABLE V. QUANTUM INTENSITY OF SOLAR RADIATION (m=0)
(Computed from Table 16-8, Geophysics Handbook⁽³⁸⁾)

$\Delta \lambda (\mu)$	$Q, \text{Watts/m}^2$	% (of E_T)	$\lambda \text{ ave. } (\mu)$	$\frac{\Phi \text{ photons}}{\text{sec/cm}^2}$	$\Phi \text{ (Cumulative)}$
0.000-0.225	0.41	0.03	.1125	0.023×10^{15}	2.3×10^{13}
0.225-0.250	1.40	0.10	.2375	0.168×10^{15}	1.91×10^{14}
0.250-0.275	4.20	0.30	.2625	0.555×10^{15}	$.746 \times 10^{15}$
0.275-0.300	11.17	0.80	.2875	1.615×10^{15}	2.36×10^{15}
0.300-0.325	19.10	1.37	.3125	3.01×10^{15}	5.37×10^{15}
0.325-0.350	28.32	2.03	.3375	4.80×10^{15}	1.02×10^{16}
0.350-0.375	30.87	2.20	.3625	5.63×10^{15}	1.58×10^{16}
0.375-0.400	30.54	2.19	.3875	5.97×10^{15}	2.18×10^{16}
0.400-0.425	46.93	3.36	.4125	9.75×10^{15}	3.15×10^{16}
0.425-0.450	48.00	3.44	.4375	10.60×10^{15}	4.21×10^{16}
0.450-0.475	54.12	3.88	.4625	12.63×10^{15}	5.48×10^{16}
0.475-0.500	51.77	3.71	.4875	12.73×10^{15}	6.75×10^{16}
0.500-0.525	48.50	3.47	.5125	12.54×10^{15}	8.00×10^{16}
0.525-0.550	49.15	3.52	.5375	13.33×10^{15}	9.34×10^{16}
0.550-0.575	47.91	3.43	.5625	13.60×10^{15}	1.070×10^{17}
0.575-0.600	47.44	3.40	.5875	14.08×10^{15}	1.210×10^{17}
0.600-0.650	86.49	6.19	.625	27.3×10^{15}	1.483×10^{17}
0.650-0.700	78.78	5.64	.675	26.85×10^{15}	1.751×10^{17}
0.700-0.750	71.02	5.09	.725	26.0×10^{15}	2.012×10^{17}
0.750-0.800	63.56	4.55	.775	24.85×10^{15}	2.260×10^{17}
0.800-0.850	56.65	4.06	.825	23.55×10^{15}	2.50×10^{17}
0.850-0.900	50.36	3.61	.875	22.22×10^{15}	2.72×10^{17}
0.900-0.950	44.72	3.20	.925	20.85×10^{15}	2.93×10^{17}
0.950-1.000	39.71	2.84	.975	19.52×10^{15}	3.12×10^{17}
1.000-1.050	35.07	2.51	1.025	18.13×10^{15}	3.30×10^{17}
1.050-1.100	31.63	2.27	1.075	17.15×10^{15}	3.475×10^{17}
1.100-1.150	156.95	11.24	1.300	102.9×10^{15}	4.50×10^{17}
1.150-2.000	80.90	5.80	1.750	71.35×10^{15}	5.22×10^{17}
2.000-2.500	35.07	2.51	2.225	39.35×10^{15}	5.61×10^{17}
2.500-3.000	17.45	1.25	2.750	24.2×10^{15}	5.85×10^{17}
3.000-3.500	9.62	0.69	3.250	15.8×10^{15}	6.01×10^{17}
3.500-4.000	5.68	0.41	3.750	10.74×10^{15}	6.12×10^{17}
4.000-4.500	3.72	0.27	4.250	7.97×10^{15}	6.20×10^{17}
4.500-5.000	2.28	0.16	4.750	5.46×10^{15}	6.25×10^{17}
5.000-6.000	2.79	0.20	5.500	7.74×10^{15}	6.33×10^{17}
6.000-7.000	1.47	0.11	6.500	4.81×10^{15}	6.38×10^{17}
7.000- ∞	2.65	0.19	~ 10.0	13.37×10^{15}	6.51×10^{17}

is $I_{sc} = I_L = 0.051 \text{ amp/cm}^2$. The fill factor F is:

$$F = \frac{I_m V_m}{I_{sc} V_{oc}} = 83\% .$$

The power efficiency, using the solar constant $S = 140 \text{ W/cm}^2$, is:

$$\text{Eff (max)} = \frac{I_m V_m}{S(m=0)} = 15.1\%$$

This result applies to air-mass-zero solar radiation at a cell temperature of 25°C, and is restricted to the following assumptions:

- (1) Reflection, cover absorption, and grid losses are zero.
- (2) All photons with energy $> E_G$ (Cu_2S) are absorbed with formation of an equal number of e-h pairs.
- (3) 100% collection of generated pairs occurs.
- (4) Equation (1) applies with $A = 1.00$.
- (5) Series and shunt resistance effects are negligible.
- (6) Open circuit voltage is fixed at 0.500 volts.

3.8.2 Maximum Achievable Efficiency

If more realistic assumptions are used, an estimate of a maximum achievable efficiency can be made. Restraining the calculations again to 25°C and to air-mass-zero solar radiation, we invoke the following assumptions:

- (1) Grid loss = reflection loss = cover absorption loss = 5%.
- (2) Photons with $E > E_G$ (Cu_2S) are absorbed with an efficiency of 95%.
- (3) Minority carrier collection efficiency = 95%.
- (4) Equation (1) applies with $A = 1.70$.
- (5) Series and shunt resistance effects are negligible.
- (6) Open circuit voltage is limited to 0.500 volts.

The relevant quantities are then derived as follows:

$$I_{sc} = I_L = 0.051 (.95)^5 = 0.0394 \text{ amp/cm}^2 .$$

Equation (1), with $V = 0.500$, $I = 0$, and $A = 1.70$, gives

$$I_o = 4.18 \times 10^{-7} \text{ amp/cm}^2 .$$

Equation (3) then gives

$$V_m = 0.379 \text{ volts}$$

Equation (1) then gives

$$I_m = 0.0369 \text{ amp/cm}^2$$

Then

$$F = \frac{I_m V_m}{I_{sc} V_{oc}} = 71\%$$

and

$$\text{Eff (achievable)} = \frac{I_m V_m}{S_{(m=0)}} = 10.0\% .$$

Since the best of the present thin film and ceramic cells have A factors of about 1.70 and $V_{oc} \sim 0.50$ volts, almost all of the future increase in efficiency will be derived through increases in current output, a possible doubling being indicated by the above calculations. The improvements could be brought about by changes in the mechanical structure of the cell and through improvements in the electron lifetime in the Cu_2S layer. The empirical 0.500 voltage constraint was necessitated by a lack of appropriate information and was based on the highest reliably observed V_{oc} of high output cells. An increase in V_{oc} such as might result from an increase in electron lifetime in the Cu_2S would of course increase the computed efficiencies.

4. CRITICAL DISCUSSION OF THE RESULTS OF OTHERS IN RELATION TO THE CLEVITE MODEL

4.1 The Active Role of the Cu_2S Layer

At the Seventh Photovoltaic Specialists Conference,

Dr. J. J. Loferski presented the results of an ESRO research effort on "Photovoltaic Effects in the Cu-Cd-S System."⁽¹⁶⁾ Their results confirm in considerable detail the assignment of an "active" role to the Cu_2S layer that is the central theme of the Clevite model. Electron microprobe and low-energy proton damage experiments indicate an average thickness of Cu_2S between 0.10 and 0.15 μ . These thicknesses are somewhat less than our average value of 0.35 μ measured on high efficiency cells (see Section 3.2.1). The limited electron lifetime in presently formed Cu_2S limits the actual thickness to about 0.10 to 0.15 μ for maximum current collection. The observed current is, however, substantially larger than can be accounted for by a planar layer of this thickness using the highest measured values of the absorption coefficient. It is thus evident that the highly non-planar structure is an essential requirement for present high efficiency cells (>5%). A very recent paper⁽³⁹⁾ on the Matsushita ceramic cell likewise emphasizes the intergranular disposition of the Cu_2S , the maximum depth of penetration (not the actual thickness) amounting to about 60 μ . It is explicitly stated that this geometry greatly improves the absorption efficiency. The beneficial role of intergranular Cu_2S was recognized early in our research program, and it now appears nearly certain that this is indeed the case.

The use of a planar geometry in the ESRO study probably accounts for the somewhat low calculated collection efficiencies. The X-ray fluorescence and low-energy proton experiments would tend to yield low values for the amount of Cu_2S present in grain boundaries, as recognized by the authors. In addition, the 0.10 to 0.15 μ average thickness obtained in their fluorescence measurements was for an ESTEC cell with an efficiency of only 2.8% so that the Cu_2S layer might well have had an average thickness about half the value we have found on 5% cells. The essential parts of the ESRO results in regard to the role of the Cu_2S layer are therefore in reasonable agreement with the Clevite model.

4.2 The Existence and Nature of the i-CdS Layer

In regard to the existence and nature of the Cu-compensated i-layer and its relation to the well-known IV cross-over phenomenon, there is considerable disagreement and misunderstanding. The ESRO workers have computed a depletion layer thickness of $\sim 20 \mu$ for the i-n homojunction of the Clevite model and thereby argue that the i-layer between the Cu_2S and n-CdS should be viewed as being similar to the normal space-charge region found in an ordinary Si solar cell. They conclude that there is no necessity of considering this region as a distinct photo-conductive layer. It is apparent that the 20μ depletion thickness was arrived at by treating the i-layer as weakly n-type CdS with $n \approx 10^{13} \text{ cm}^{-3}$. We argue that the i-layer is not weakly n-type but p-type, and strongly so in the sense that the concentration of acceptors in this region substantially exceeds that of the donors. The dark resistivity remains high because the great depth of the acceptors precludes significant thermal ionization at room temperature. This point is readily appreciated when we consider the state of the compensation in this region. The i-n interface is defined as the points where the copper concentration equals the total donor concentration in the n-CdS base layer. The copper concentration between the interface and the Cu_2S layer must of necessity be larger than that at the interface since the latter was established by diffusion of Cu from the Cu_2S . The concentration of copper in the i-layer immediately adjacent to the Cu_2S has been established as $\sim 10^{18} \text{ cm}^{-3}$ for a diffusion temperature of 250°C (see Section 3.3.2). Even if some of the copper precipitated locally as Cu_2S upon cooling to room temperature, the precipitates would still act as sinks (acceptors) for electrons diffusing into this region from the n-CdS region during establishment of the equilibrium diffusion potential. Taking the average unprecipitated excess copper concentration as only 10^{17} cm^{-3} (which is about the same as the donor concentration in the n-CdS) a depletion layer thickness of $\sim 0.08 \mu$ is obtained. Since $[\text{Cu}] - [\text{D}]$ in the i-layer adjacent to the interface is less than the average concentration, a value of 10^{16} cm^{-3} or even 10^{15} cm^{-3} might be more appropriate for $[\text{Cu}] - [\text{D}]$ in this region. These concentrations still yield a depletion layer thickness of only 0.3 to 0.8 μ .

The weakly n-type character of the i-CdS layer that was assumed by the ESRO group finds apparent confirmation in the results of Brandhorst⁽²³⁾ who made dark capacitance measurements as a function of voltage on 2 cm² Clevite cells. Using a Schottky barrier treatment and allowing for a variable impurity profile in the junction region, the voltage-dependent capacitance measurements are used to derive the impurity profile (Figs. 2, 3 and 5 of Ref. 23). The principal objection we find in the interpretation of the results is that the net impurity in the i-layer seems to have been arbitrarily assumed to be a donor, i. e., that $N_D - N_A$ is positive. The computed results would have been the same if $N_D - N_A$ had been taken negative. The results would then be much more acceptable. The derived impurity concentration of 10^{15} cm^{-3} in the i-layer immediately adjacent to the i-n junction would then be identified as the excess concentration of diffused Cu acceptors over the total donor concentration in the CdS. The $2 \times 10^{17} \text{ cm}^{-3}$ concentration on the n-side of the junction is reasonably identified as the net donor concentration in the n-CdS layer. (These concentrations were corrected for the ratio of actual junction area to nominal cell area using a value of 3, as suggested by the author -- a number with which we agree.) If the 10^{15} cm^{-3} concentration was the residual concentration of uncompensated shallow donors, the resistivity of the i-layer would be only $10\text{-}100 \Omega\text{cm}$. The free-electron relaxation time $\rho e < 10^{-10} \text{ sec}$ would then preclude the measurement of capacitance at the frequency of 10^6 Hz used by the author. On the other hand, n-type CdS crystals that have been diffused with Cu at 250°C are known to develop dark resistivities $> 10^{10} \Omega\text{cm}$ in the diffused layer. The depletion-layer thickness computed for the as-received cell was $\sim 0.8 \mu$ and this was increased to $\sim 0.9 \mu$ by a 10 minute heat treatment at 200°C . Again, it would be difficult to understand why the diffusion front corresponding to the i-n junction would advance if the layer behind the front was not yet over-compensated with copper. The reassignment of the net impurity in the i-layer as Cu acceptors rather than donors makes the observed results much more reasonable..

The above discussion refers to the situation in the dark. Under illumination, the i-CdS does indeed behave like weakly n-type CdS and the depletion layer, with its associated electric field, includes the whole of the i-layer, much like the normal space-charge region of a wide p-n junction, as suggested by the ESRO group. Thus, under illuminated conditions the ESRO analysis is in good agreement with our model, as shown in Fig. 1 near the beginning of this report.

4. 3 Change in Barrier Height and the IV Cross-Over Phenomenon

Clevite's original model (late 1966)⁽⁴⁰⁾ differs from our present model in two respects: (1) The i-n homojunction in the dark in the original model was only slightly effected by illumination. In mid-1967⁽⁴¹⁾ this was changed so that the quasi-Fermi level in the i-layer moved substantially upwards during illumination so as to be much closer (~ 0.35 eV) to the bottom of the conduction band. A p-n heterojunction was thus invoked, although the i-n homojunction of the original model was retained for the situation in the dark. (2) In early 1968⁽⁴²⁾ the energy level where the conduction band of CdS joined the energy-band scheme of Cu_2S was displaced from the original position slightly above the bottom of the Cu_2S conduction band to a position 0.35 eV below this edge. This change was based on the experimentally observed open-circuit voltage at very high light levels and at low temperatures which indicated a barrier height of 0.85 eV, which is 0.35 eV less than ΔE_G (1.20 eV) of Cu_2S . The work function of Cu_2S implied from the similar properties of p-Si:n-CdS solar cells⁽³³⁾ to p- Cu_2S : n-CdS solar cells together with the reported values of the work functions of Si and CdS was also consistent with this change (Section 3.5.8.3). An electrostatic potential barrier of 1.2 eV changing to a value of 0.85 eV under illumination was thus invoked. Photoconductivity in the i-layer was retained in all three versions of the model as was the active light absorbing role of the Cu_2S layer.

The ESRO group, evidently unaware of the above modifications, have attributed to the Clevite model a change in series resistance of the i-layer as the explanation of the crossing of the dark and light IV curves. They find through analysis that a light-dependent series resistance is

insufficient to explain the cross-over effect and that a simultaneous voltage dependence must also be invoked in order to explain the effect. They suggest that a change in barrier height (involving changes in I_o and the diode A-factor) is a more reasonable explanation. Although the series resistance "explanation" of the cross-over effect might have been implicit in our original model, our subsequent modifications clearly show a change of barrier height accompanying the excitation of photoconductivity in the i-CdS layer. We state explicitly that the dark barrier of 1.2 eV changes under illumination to a barrier of 0.85 eV. Corresponding changes in I_o and the A-factor were experimentally determined (see Section 3.5.6). Thus the ESRO suggestion of changes in barrier height as a possible cause of the cross-over effect is in good agreement with the Clevite model. Other details, however, need clarification: They state that a slow shift of the IV curve is already observed in the dark when forward bias (~ 10 ma/cm²) is applied to a typical Clevite cell. This property, first investigated by Brandhorst,⁽⁴³⁾ has been studied in some detail in our laboratory and the effect is now attributed with reasonable certainty to a polarization resulting from electrolytic migration of Cu in the Cu₂S layer. Their observation that monochromatic light of low intensity ($\sim 10^{14}$ photons/cm²/sec) causes substantial shifts in voltage (measured at constant current) is fully consistent with the known photosensitivity of Cu-compensated CdS. Their finding that the effect is maximum for CdS-band-edge radiation and that a pronounced enhancement of red response is effected by this same radiation is very strong evidence for invoking photoconductivity in an i-CdS layer. While the authors admit that such results could be attributed to photoconductivity, they suggest that the low light-level response could also be explained as a change in occupancy of interface states. We see no need to invoke such an alternate possibility when a simpler explanation is at hand. We also fail to see why the occupancy of interface states should follow so closely the excitation spectrum of photoconductivity that is characteristic of CdS. This is not to imply that we do not think that interface states exist or that they play only a passive role -- on the contrary, as will be evident shortly.

The change in barrier height invoked by the Clevite model has been questioned by Gill, et al. (24) (the Stanford group); and they have advanced an interesting tunnelling mechanism (see Section 4.5) to replace the change-in-barrier-height explanation of the observed dark and light IV characteristics and other properties of the cell. Their principal objection to the Clevite model is that the total energy difference between the conduction bands of p- Cu_2S and n-CdS remains the same in the dark and in the light even though the band curvatures are strongly affected. The "barrier height" thus seems to be the same independent of illumination and the model therefore does not explain the cross-over effect (see Section 3.5.1).

In order to answer this apparently serious objection, we begin with some elementary considerations of electron flow in junctions: During forward biasing of a cell in the dark (n-CdS negative), the electron flow across the junction is from the n-CdS to the p- Cu_2S . The electrons must surmount an electrostatic potential barrier at the i-n junction which has an initial value of ~ 1.2 eV. As forward bias is applied externally, this barrier is reduced and the current rises exponentially according to the usual diode IV relationship. Because the excess Cu centers in the i-layer can trap face electrons, the forward dark current is probably space-charge limited. In the light, the "forward" flow of electrons between I_{sc} and V_{oc} is from the p- Cu_2S to the n-CdS, i.e., opposite to the forward flow of electrons in the dark (as for silicon solar cells). The diode in this case is not being "driven" as in the dark; the applied voltage is merely "bucking" the internally generated photovoltage. Under all conditions where useful power can be delivered from the cell, the electron current is always from the p- Cu_2S to the n-CdS. The "pumping" action of the junction field which gives rise to the potential of the electrons delivered by the cell is clearly the diffusion potential (modified by the loading conditions of the cell). The 0.35 eV energy difference that arises from the difference in the electron affinity of Cu_2S and CdS is not associated with an electric field since it exists before any charge flows across the junction. Electrons crossing the junction from the Cu_2S side (during cell

illumination) enter the many available states in the conduction band of CdS and are rapidly thermalized to the bottom of the conduction band. It is for this reason, according to the Clevite model, that the "CdS" solar cell produces less voltage than the Si solar cell in spite of the fact that Cu₂S has a band gap about 0.1 eV larger than that of Si. The "barrier" of a solar cell during normal operation is not a barrier at all to the flow of photogenerated minority carriers, but is a positive force aiding the flow of these carriers across the junction. Under short circuit conditions, the full force of the aiding barrier is in operation and a maximum collection of minority carriers is achieved. When the external flow of electrons is impeded by a load resistance, or the equivalent in an IV measuring circuit, the electrons begin to accumulate at the negative terminal (substrate electrode) and the cell becomes "forward" biased. While the strength of the aiding barrier is diminished, the flow of electrons from the Cu₂S is not materially affected, although the net electron flow across the junction is reduced. The situation can be viewed as a constant (voltage-independent) flow of electrons from the Cu₂S to the CdS diminished by a reverse flow of electrons corresponding to the "forward" flow of the biased diode, the latter electrons all ending their lives by recombination with holes in the p-Cu₂S layer.

When the cell is biased to the open-circuit-voltage point on the IV curve (~0.49 V), the diode recombination current equals the light generated current and the external current disappears. When the cell is driven by an external source to a voltage slightly greater than the V_{oc} of the cell the recombination current exceeds the generated current and the external current reverses sign. The IV curve passes monotonically through the V_{oc} point. There are no changes in the physical processes going on in the cell when the V_{oc} point is crossed, only the magnitude of the recombination current has (continuously) increased beyond the constant generated current. All of this, of course, is no more than a word description of the usual photovoltaic diode equation:

$$I = I_o (e^{qV/AkT} - 1) - I_L$$

I_L , the light generated current, remains constant even in the first quadrant ($V > V_{oc}$) because forward voltages exceeding the internal barrier voltage cannot be reached due to overheating of the cell. The sense of the collecting field is therefore the same under all achievable conditions of forward (or reverse) bias, and the electron affinity step is always present, down which the electrons from the Cu_2S always fall. Maximum forward voltages are ~ 0.65 V in the light (barrier height 0.85 eV) and ~ 1.0 V in the dark (barrier height 1.2 eV).

Returning now to the Stanford objection, we see that the difficulty lies in whether the electrons comprising the recombination current "see" or "feel" the 0.35 eV electron affinity step and whether they have to climb this step before recombining with holes in the Cu_2S layer. Clearly, these electrons want to get to the valence band of Cu_2S not the conduction band. The question is whether there is a mechanism by which these electrons can enter the valence band of Cu_2S without first entering the conduction band. In the discussion above it was pointed out that between I_{sc} and V_{oc} the net electron flow was from the Cu_2S to the CdS ; therefore, there is at first thought no need for any electrons to climb the 0.35 eV affinity step. The recombination current could then be viewed as normal recombination in the Cu_2S layer. However, we have also seen, according to the Clevite model, that the photogenerated electrons in the Cu_2S layer are unaware of the loading conditions of the cell since the voltage-dependent changes all occur beyond the affinity step. No field exists in the Cu_2S layer so the electrons, under the pressure of constant generation, diffuse to and drop off of the affinity "cliff" at a constant rate, independent of load condition. Thus the recombination rate in the Cu_2S layer of a given cell must also be constant, including conditions which yields I_{sc} . Since the observed quantum efficiency (measured at short-circuit current) of high output cells is very large ($\sim 70\%$ for visible light), the constant recombination rate in and on the outer surface of the Cu_2S layer cannot be very large, and this recombination rate remains constant independent of cell voltage. Since far greater overall recombination occurs under forward bias, this additional recombination must

involve electrons in the conduction band of the CdS next to the interface, either those arriving there from the Cu_2S ($V < V_{oc}$) or those driven to the interface from the n-CdS region by external voltage ($V > V_{oc}$), the transition between the two cases being smooth with no physical change of mechanisms. It would thus appear that recombination occurs principally at the Cu_2S -CdS interface, the electrons, in effect, travelling down 0.85 eV from the conduction band of CdS to the valence band of Cu_2S . The most obvious mechanism of recombination that comes to mind under these circumstances is recombination via interface states which are expected to be present in profusion at such a heterojunction. The concentration of holes on the Cu_2S side of the interface is, of course, always very large, and hence the holes are readily available for recombination. The holes, in fact, should tend to "fall up" the interface states just as the electrons tend to "fall down" through these states. Since the number of interface states and their properties (for a given cell) are constant, the recombination rate would seem to depend solely on the concentration of electrons in the conduction band of the CdS immediately adjacent to the interface. Under short-circuit conditions, the average electric field is a maximum and the field is concentrated close to the Cu_2S -CdS interface. The steady-state concentration of electrons in this region would therefore be very low. Regardless of the recombination properties of the interface states, the recombination rate for a particular cell would be a minimum under these conditions, and the collected current would be a maximum.

As the forward bias is increased (under constant illumination), the field in the CdS is progressively diminished and the electrons entering this region are not swept away as rapidly as before and their concentration in this region increases, leading thereby to an increased probability of capture by and recombination at the interface states. At $V \geq V_{oc}$, the junction field is evidently so reduced that the rate of electron collection cannot keep up with the influx of electrons into this region from the Cu_2S layer and from the reverse thermal diffusion of free electrons from the n-CdS layer. The increased population of electrons thus causes the recombination rate to equal or exceed the collection rate, depending on whether $V = V_{oc}$ or $V > V_{oc}$.

The above hypothesis overcomes the Stanford objection by not requiring the electrons to climb the affinity barrier. The effective barrier height in the light is thereby preserved at 0.85 eV. In the dark, the i-n barrier height is 1.20 eV, and electrons passing over this barrier fall into the p-Cu₂S: i-CdS accumulation zone and recombine via the interface states as suggested above. The idea that strong recombination might occur at interface states is not entirely hypothetical: In Section 3.6.1, the sharp dip in photovoltaic current at the band edge of CdS observed only for cells having thin Cu₂S layers was tentatively attributed to recombination at interface states. We have not been able to find any other reasonable explanation for the observed effect, and hence view this as an independent argument favoring the assignment of interface states as the principal recombination centers in the CdS solar cell. In closing, it should be noted that interface states are closely analogous to surface states which in many cases are known to function as fast recombination centers.

4.4 Cd and Cl in the Cu₂S Layer

Several laboratories have examined the Cu₂S: CdS heterojunction by electron microprobe analysis of cross-sections of thick layers of Cu₂S formed on single crystals of CdS. A residual gradient of Cd in the Cu₂S layer has been found, for example, by the ESRO group. They also found a residual Cu gradient on the CdS-side of the Cu₂S-CdS interface, and a small but finite and uniform concentration of Cl in the Cu₂S layer. Similarly, Palz et al. ⁽³⁾ have also detected Cd and Cl (~0.2%) in the Cu₂S layer by atomic absorption measurements. However, they found that both of these elements disappeared after heating the Cu₂S to 600°C in vacuum, indicating that the Cd was not present as CdS. We now add that since both Cd and Cl were removed by the heating, they probably left as CdCl₂, which is known to have an appreciable vapor pressure at 600°C. This would indicate that CdCl₂ was originally present as a residue due to insufficient rinsing of the Cu₂S following the formation process. Thick layers of dip-formed Cu₂S are riddled with a labyrinth of fine cracks which are difficult to rinse out. Some Cd, however, probably does exist in the Cu₂S lattice. Our indirect measurements (see Section 3.2.6),

which also suffer from uncertainties of sufficient rinsing, indicate a possible Cd content of $\approx 0.1\%$. In any case, the Cd distribution in the thin Cu_2S layer of real cells would not be concentrated near the Cu_2S -CdS interface as indicated by Brandhorst⁽²³⁾ (his Fig. 4). The entire Cu_2S layer is formed in 5 seconds at 90°C . Cd as well as Cu obviously diffuses through solid Cu_2S with relative ease at 90°C even though the probable cracks in this layer reduce the distance over which they have to diffuse. Since the cells are given subsequent heat treatments during normal processing at much higher temperatures and for much longer times (2 min. at 250°C plus ~ 1 hr. at 200°C plus a total of ~ 30 hrs. at 130°C) the Cd in the Cu_2S layer would surely be leveled by these treatments.

The gradient of Cu-concentration in the CdS shown by the ESRO group⁽¹⁶⁾ (their Fig. 17) does not appear reasonable and hence also throws suspicion on the observed Cd gradient on the Cu_2S -side. The depth of penetration of Cu $\approx 15\ \mu$ and the apparent concentration $\approx 10^{20}\text{ cm}^{-3}$ (based on the fluorescence intensity over Cu_2S $\approx 10^{22}\text{ cm}^{-3}$) are far too large for them to have resulted from the diffusion of Cu in CdS at 90°C in several hours. The solubility of Cu in CdS is only 10^{18} cm^{-3} at 250°C , and the extrapolated value at 100°C is only $\sim 10^{16}\text{ cm}^{-3}$ (see Fig. 21). The depth of penetration of Cu by diffusion where the concentration is $1/e$ of the surface concentration is given by $x = \sqrt{Dt}$. Taking D at 100°C (from Fig. 17) as $\sim 10^{-15}\text{ cm}^2/\text{sec}$ and $t = 4$ days $\approx 3 \times 10^5$ sec, x becomes $0.2\ \mu$. It has been our experience that the Cu_2S :CdS interface becomes very nonplanar on a microscopic scale as the thickness of the Cu_2S layer increases. If the Cu_2S layer is removed with a KCN solution after a $0.5\ \mu$ layer had been formed on a highly polished surface of a CdS crystal, the resulting surface is very mat, with almost no trace of specular reflection. For layers 20-50 μ thick, used by the ESRO group, the interface is expected to be even more irregular. We suggest that the reported concentration gradient of Cu may not be due to diffusion but may instead be a manifestation of an irregular interface. The Cd gradient likewise may be due to the same effect, although incomplete rinsing of the Cu_2S

might also be involved. On the other hand, for thick Cu_2S layers the high local concentration of dislocations that is expected near the interface due to the large lattice mismatch between Cu_2S and CdS , may give rise to more rapid local diffusion and perhaps to higher local solubilities than those observed in crystals in a less highly strained condition (very thin Cu_2S layers).

4.5 The Stanford Tunnelling Model

Extensive new measurements on the properties of $\text{Cu}_2\text{S}-\text{CdS}$ solar cells have been obtained at Stanford University. (24) Almost all of the experimental results, we believe, are compatible with the Clevite model. Nevertheless, there does appear to be a degree of ambiguity in the interpretation of the results. The model put forth by the Stanford group is identical to the Clevite model except for a difference in the conduction-band discontinuity at the $\text{Cu}_2\text{S}:\text{CdS}$ interface which results in a major difference in the interpretation of the controlling mechanism of the cell. They connect the bottom of the conduction band of CdS at a point ~ 0.1 eV above the bottom of the conduction band of Cu_2S , whereas we place it ~ 0.35 eV below the band edge. The small energy "spike" that thus results in their model is postulated to limit the flow of current across the junction. The efficiency of tunnelling through the spike is controlled by the width of the depletion layer which, in turn, is dependent (for heat treated cells) upon the photoelectronic properties of a Cu-compensated i- CdS layer. Before entering into points of difference we would like to emphasize the major points of agreement: (1) Intrinsic absorption of light occurs in the thin surface layer of Cu_2S and is the principal source of the observed photovoltaic current. (2) Heat-treatment of cells causes diffusion of Cu into the n- CdS layer and produces a compensated layer of CdS adjacent to the Cu_2S layer, the thickness of which depends upon the extent of the heat treatment. (3) The compensated layer of CdS has photoelectronic properties which are identical to the photoconductive properties of Cu-compensated CdS , but are manifest in a somewhat different form because the properties are observed in photovoltaic mode.

Our two principal objections to the Stanford tunnelling model are: (1) The effective electrostatic barrier in their model is the band gap of Cu_2S , 1.2 eV, which is not consistent with the maximum observed V_{oc} (~ 0.8 V) for cells measured at low temperatures and at high light intensities. Even if the tunnelling probability was unity, the large forward currents observed at voltages slightly greater than V_{oc} but much less than the barrier voltage are not compatible with such a large barrier. (2) The tunnelling probability seems to us to have been greatly overestimated. Their energy-band diagram (their Fig. 6.1) is for a heat-treated cell containing a Cu compensated layer at least a few tenths of a micron in thickness; yet they assume a value of 10^{17} cm^{-3} for the net donor concentration adjacent to the Cu_2S layer. Taking the conduction band spike as 0.1 eV, the width of the spike is then computed to be 20 \AA , from which they derive a tunnelling probability of 0.22. Even if the assumptions used were true, the 0.22 tunnelling probability is still not consistent with the quantum efficiencies of high output cells which are observed to be much greater than 0.22. The use of 10^{17} cm^{-3} as the net donor concentration in the i-CdS layer is clearly unreasonable for reasons discussed in Section 4.2. This concentration is however reasonable for unheat-treated cells, and this may be the source of the difficulty. We believe that tunnelling is a very likely process in unheat-treated cells. We have in fact suggested such processes (without invoking details) as a possible source of the poor squareness of the IV curves, the low open circuit voltages, and the instabilities of the IV curves observed for such cells. Tunnelling across the narrow $p^+ - n^+$ junction apparently occurs at highly localized regions of the junction and these regions act as shunting paths which gives rise to the observed effects. The IV characteristics are usually dominated by one or two local spots on the junction, and we have found that the dominant spots (and the IV trace) can be substantially altered by momentary passage of large currents. For unheat-treated cells, we are in substantial qualitative agreement with the Stanford group. But since all high efficiency cells that we are aware of have received some kind of heat treatment, the behavior of unheat-treated cells is not of particular interest.

For heat-treated cells, we find it difficult to justify the Stanford model. If indeed the Cu levels in the i-layer lie only 1.1 eV and 0.3 eV above the top of the valence band of CdS as suggested by the authors, the Fermi level in the dark should lie below the middle of the forbidden band. If the Fermi level is at the 1.1 eV level and the CdS conduction band joins the Cu_2S diagram 0.1 eV above the bottom of the conduction band of Cu_2S , the Fermi levels in the Cu_2S and CdS are approximately at the same position with respect to the vacuum level and no conduction-band spike should then result. Only a 0.1 eV affinity step (up for electrons moving from the Cu_2S to the i-CdS) would be present in the dark. If the Fermi level was below the 1.1 eV Cu level by an amount ΔE , the conduction band of the i-layer would curve upward from the top of the affinity step by ΔE before curving downward at the i-n junction. In neither case would tunnelling be expected in the dark since the width of the i-layer is now far too large. Under illumination, the band curvature shown is qualitatively the expected one because of the strong rise of the quasi-Fermi level in the i-layer. However, if we now treat this layer as weakly n-type, taking $n \approx 10^{13} \text{ cm}^{-3}$ (rather than 10^{17} cm^{-3}), the width of the spike is $\sim 2000 \text{ \AA}$ and the tunnelling probability is then exceedingly small. This however may not be a proper way of treating the illuminated case. The difficulty is in establishing the role of the excess Cu acceptors in this region. In the dark, many of the free electrons forced into this region by forward bias would be trapped by these acceptors and a negative bound space charge would result, impeding the further flow of electrons from the n-CdS to the Cu_2S . It is for this reason that we believe that the forward dark current is space-charge limited. During illumination, the optical liberation of electrons trapped at the Cu centers (directly from the centers or through intrinsic absorption with subsequent trapping of holes at the Cu centers) greatly increases the conductivity of the i-layer even for small light intensities and substantially overcomes the effects of the space charge. The gradient of Cu acceptors makes the region closest to the Cu_2S layer most resistant to change during illumination since the Cu concentration is highest there. The strong intrinsic absorption of light in the i-layer however tends to counteract the Cu-gradient effect.

Nevertheless we feel that the high copper concentration would prevent the conduction-band spike of the Stanford model from narrowing to a sufficiently small value to allow efficient tunnelling of electrons. In any case, the 10^{17} cm^{-3} donor concentration used in the Stanford calculations to partially justify the tunnelling mechanism is unrealistic for heat-treated cells.

The temperature independence of the dark IV characteristics has been emphasized by the Stanford group as an additional argument for the tunnelling model: A simple thermal activation over a barrier as implied in the Clevite model would be expected to show a moderately strong temperature dependence. Their argument however is based on the behavior of the forward dark characteristics (their Fig. 4.4). Under illumination, the forward IV characteristics do in fact have a moderately strong temperature dependence, the behavior being similar to that for Si solar cells (see Fig. 26). Since a cell model must apply for the illuminated case as well as the dark case, we could conclude that the observed temperature dependence in the light is an argument against the tunnelling model. Unfortunately, we do not yet have confirmation of the temperature independence of the dark characteristics. Even if this should turn out to be the case, the results may not be inconsistent with the Clevite model since the dark current is probably space-charge limited and such currents would not be expected to show a strong temperature dependence.

In concluding the discussion of the Stanford results, we re-emphasize that almost all of the experimental results are consistent with the Clevite model. The experiments on enhancement and quenching effects are particularly favorable, provided we keep in mind their use (in most cases) of undoped crystals of CdS which yield after cell fabrication and heat treatment, an i-layer having a narrow band-edge photoconductive excitation spectrum. The large infrared quenching effects observed at the higher energies are not seen in donor-doped CdS cells or in thin film cells which behave like lightly donor-doped CdS (see Section 3.6.6). The photoconductive excitation spectrum for these cells overlaps and hence tends to mask the quenching spectrum. We wish to mention

one other result obtained by the Stanford group. This is shown in their Fig. 4.9, where the dark capacitance of a particular cell is plotted as $1/C^2$ against reverse voltage bias. These are the only data that we have seen which behave in the expected manner and which might therefore be trusted to yield an accurate barrier height by extrapolation into the forward region. They obtain 1.1 eV for the barrier height which is close to the 1.2 eV value for our model when the cell is in the dark. In fact, if the last two points in the large reverse bias region are slightly ignored, the remaining 10 points yield an extrapolated barrier height that is very close to 1.2 eV.

5. FAILURE MECHANISMS

5.1 High-Temperature Degradation in Vacuum

Standard thin-film solar cells are known to degrade seriously over a period of several weeks at 150°C in vacuum or in inert-gas atmospheres (20-30% loss of efficiency). The IV characteristics show a progressive loss of fill factor followed by a progressive loss of short-circuit current. The open-circuit voltage remains essentially constant. The behavior is identical to that observed when an externally connected series resistance is gradually increased, as shown in Fig. 32 of Section 3.5.5. The mechanism of this degradation is understood. Copper diffusion, which is appreciable at 150°C, causes growth of the insulating CdS layer which results in a progressive and irreversible increase in series resistance. A much slower but measurable degradation occurs at 100°C. Extrapolation of the data to 65°C (the expected operating temperature in earth orbit), the time for a 10% degradation in efficiency is estimated to be 3 to 5 years. More recent tests at 100 and 150°C indicate that present cells are substantially more resistant to these changes than the earlier cells. However, based on the knowledge of the mechanism, only minor changes in the donor doping level in the CdS layer are expected to cause substantial changes in the magnitude of this mode of degradation. Clearly, a higher concentration of donors would require a correspondingly higher concentration of copper to affect compensation. Furthermore, the photoconductive spectral response is

known to extend to longer wavelengths for the donor-doped compensated layer so that even for the same thickness of the i-layer, a much lower series resistance is present in the donor-doped cell. Figure 70 shows the results for two ceramic cells containing $\sim 5 \times 10^{17} \text{ cm}^{-3}$ of In donors. The predicted improvement in stability is confirmed. In fact, a slight increase in efficiency is observed for one of the cells, resulting from an increase in short-circuit current.

The ability of present thin-film cells to withstand this mode of degradation appears to be adequate for operating temperatures up to $\sim 65^\circ\text{C}$. For operation at higher temperatures or for very long term operation, donor doping of the CdS layer would appear to be essential. This mode of failure is intrinsic to the cell but, fortunately, it is controllable.

5.2 Open-Circuit Degradation; Cu-Nodule Formation

It has been known for some time, principally through the work of Brandhorst⁽⁴³⁾ at NASA, Lewis, that thin-film CdS solar cells degrade seriously in a few days when they are illuminated under open-circuit conditions. Various vague mechanisms, usually involving ionic transport in the Cu_2S layer or in the i-CdS layer, had been hypothesized here and elsewhere but no direct evidence was available. Very recently, H. Nastelin and W. Dunn at Clevite observed the presence of tiny metallic nodules on the surface of the Cu_2S layer of cells that had been degraded by open-circuit illumination. A partial correlation between the presence of these nodules and cell degradation was also obtained.

That the metallic nodules, which have the appearance of copper, were indeed copper was verified in the following way: The Kapton cover located over one of the larger nodules was cut open and the nodule was carefully transferred to a micro-test tube. While observing the nodule with a microscope, a tiny drop of nitric acid was introduced. The nodule dissolved vigorously in the acid with the formation of a pale blue solution. The blue color was accentuated when a drop of NH_4OH was introduced, a well-known test for copper. These results together with the copper color of the nodules and the results of very recent microprobe

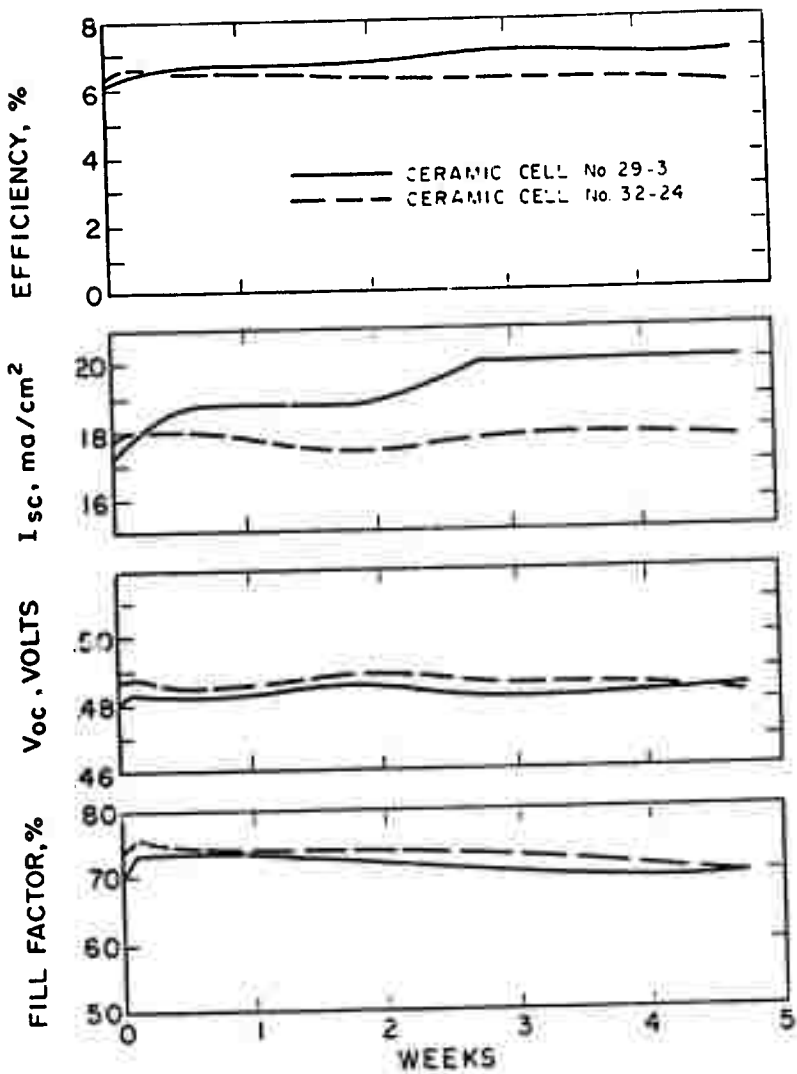


FIG. 70. ROOM TEMP PROPERTIES OF In-DOPED CERAMIC SOLAR CELLS vs. EXPOSURE TIME AT 150°C IN ARGON ATMOSPHERE AND AMBIENT LIGHT. AREA OF CELLS $\sim 1\text{cm}^2$. TESTED UNDER AIR-MASS ONE EQUIVALENT SUNLIGHT.

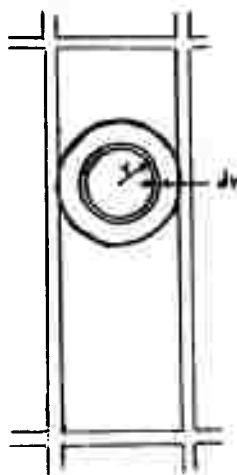
analyses leave no doubt that these nodules are indeed copper. With this verification, the probable mechanism of the open-circuit degradation becomes clear: Metallic copper is being deposited electrolytically with Cu_2S acting as the electrolyte, the grid acting as the anode, and localized metallic shorts to the substrate acting as cathodes. The cell is driven by the open-circuit photo-voltage. The total current passing through the shorts could be as large as the short-circuit current, although only a small fraction of this is ionic current.

The large ionic conductivity in Cu_2S at higher temperatures ($>110^\circ\text{C}$) has been known for a long time.^(6, 18) That substantial ionic conductivity exists at room temperature was surprising. The discovery of the nodules initiated a study of the solid-state electrolysis of Cu in Cu_2S . This is reviewed in Section 3.2.8. In addition to these results, many experiments on thin film cells have also been completed (some in cooperation with similar studies carried out in the Solar Battery Section of Clevite under other contracts).⁽⁴⁴⁾ First, the formation of Cu nodules in the dark by externally applied voltage was established. When the voltage was near V_{oc} , the nodules developed in a conical or barnacle-like shape, as in normal V_{oc} degradation. When the voltage was much larger than V_{oc} , the Cu developed in a flatter shape with tentacles extending in all directions.

While the nodules form on the surface of the Cu_2S layer, each of them has a "tap root" of Cu which extends through the CdS layer to the substrate. This was demonstrated by carefully cutting and lifting off the cover locally over the Cu-nodules and etching the surface with dilute HCl. The nodules were always lifted off with the cover since they were imbedded in the epoxy that was attached to the underside of the cover. A tiny dot of Cu was usually seen on the Cu_2S surface where the nodule was originally attached. Its size ($\sim 6\text{ }\mu$) was much smaller than the base diameter of the nodule ($\sim 100\text{ }\mu$). As the CdS was slowly etched away, the tiny dot was seen (under the microscope) to be the top of a tiny pillar of Cu about $6\text{ }\mu$ in diameter and $20\text{ }\mu$ high. Similar results were obtained on over 10 nodules. More than one tap root was seen in some cases.

(Etching of cross-sections where a nodule was intersected or nearly intersected also revealed Cu tap roots that extended to the substrate.) The tap roots could not be conveniently photographed because of the limited depth of field at the magnifications required.

It is of interest to calculate the magnitude of the currents that would be expected to pass through such tap roots: The end-to-end resistance of the tap root described above is only $1.3 \times 10^{-2} \Omega$, computed from the dimensions and the bulk resistivity of Cu. If $V_{oc} = 0.5$ V was applied across the root, a current of ~ 40 amps would flow. The sheet resistance of the Cu_2S layer between the nodule and the nearest grid lines is clearly much greater than the root resistance. In order to calculate this resistance, we approximate the grid rectangle with an equipotential circular grid having a diameter equal to the narrow width of the grid space. Then symmetry requires the current from a centrally located nodule to flow radially to the circular grid. We consider a symmetrically disposed ring of width dr at a general distance r from the center of the nodule. The current flowing to or from the nodule must traverse in series all of these differential rings. Hence the resistance between the nodule and the ring electrode is the sum of the resistances dR_i of all of the differential rings:



$$R = \int_{r_n}^{r_g} dR_i$$

r_n = radius of nodule
 r_g = radius of grid, but

$$dR_i = \rho \frac{dr}{2\pi rt}$$

t = thickness of Cu_2S

ρ = resistivity of Cu_2S

$$\therefore R = \frac{\rho}{2\pi t} \int_{r_n}^{r_g} \frac{dr}{r}$$

$$\text{or } R = \frac{2.3\rho}{2\pi t} \log_{10} \left(\frac{r_g}{r_n} \right)$$

Since R varies only as the log of (r_g / r_n) , its value is rather insensitive to our choice of the grid radius or the shape of the grid; i.e., most of the resistance occurs very close to the nodule. Taking $\rho \sim 5 \times 10^{-3} \Omega \text{ cm}$, $t = 2 \times 10^{-3} \text{ cm}$, $r_g = 200 \mu$, $r_n = 2 \mu$ (root size), $R = 120 \Omega$ which would pass 40 mA at 0.5 volts. At the other extreme, using $r_n = 40 \mu$ (nodule size), $R = 42 \Omega$ which would pass 120 mA at 0.5 volts. These calculated limiting values of nodule current are consistent with the observation of the growth of typical nodules in 1-2 days at point contacts passing ~ 100 mA from an external source. Since $3'' \times 3''$ cells in sunlight generates ~ 800 mA of current, ~ 10 to 20 nodules (and pre-nodule roots) of typical size could be grown in a few days -- as observed.

The nature of the cathodic shorting paths has not been identified, but it is certainly related to the flaws in the CdS layer. It is very likely that they are either direct contacts of Cu_2S to the metallized substrate at cracks, pinholes, or other openings in the CdS layer or metallic copper formed at the substrate, by displacement of Zn at the surface of the metallized layer. This failure mechanism is not an intrinsic limitation of the CdS cell. Some cells, albeit a small percentage, do not degrade at all, or very little. The fact that this effect is so variable is itself a strong indication of non-intrinsic behavior.

The failure mechanism described here calls for substantial current flow between the grid and the substrate at highly localized regions. This is consistent with the observations of "hot spots" detected on degraded cells when current from an external source is passed through the cell or when the cells are illuminated under open-circuit conditions. In the latter case, short-circuiting the cell causes the hot spots to disappear. The hot spots have been detected with thermographs at NASA, Lewis, on cells degraded under open-circuit conditions at Clevite. However, a one-for-one correlation between hot spots and nodules has not as yet been demonstrated. The fact that cells degraded under simulated earth orbit conditions also show the presence of hot spots, suggests that a similar type of failure may be occurring under these conditions. It is now known that the rapid degradation of cells observed in some of the

earlier thermocycling tests was due in part to the fact that the cells were left in an open-circuited condition during most of the test. However, the degradation observed in recent thermal cycling tests appears to be due to other effects since the observed degradation of short-circuit current with a minor loss of fill factor is not consistent with the development of shunts.

Some 3" x 3" cells have shunt resistances as low as 10Ω while the optimum load resistance is about 0.5Ω . Therefore, under optimum load, the photogenerated current in these cells is divided between the external load and the internal shunts in the ratio of ~20 to 1. For a load current of 800 mA at the maximum power point, ~40 mA should be flowing through the shunts. Past experience has indicated the shunt resistance obtained from the slope of the IV curve at the short-circuit current point usually represents the shunting resistance of one or two "weakest spots" of the cell. Since these spots are highly localized the 40 mA leakage current could correspond to a very high current density. Since 100 mA passing through a point contact on Cu_2S has been shown to result in the formation of typical nodules in a few days at room temperature, it would appear that cells with 10Ω shunt resistances should degrade rather rapidly even under optimum load conditions. However, a threshold voltage of ~ 0.4 V exists below which Cu does not plate out, as shown in Fig. 14. Since the cell is expected to operate at $V_{mp} \approx 0.37$ volts, little or no Cu plating is expected. However, since the threshold voltage is so very close to V_{mp} , precautions should be taken to prevent operation of the cells at voltages above V_{mp} .

The solution to this problem seems to be the elimination of the shunting paths that results from the flaws in the CdS film before the films are dipped in the Cu^+ solution. Flaws such as cracks formed after the dip should not be harmful. Cells having large shunt resistances may not be entirely free of open-circuit degradation; it may merely take longer for the electrolysis of Cu to proceed to a damaging extent. The electrolysis of Cu can be reversed by reversing the flow of current (grid electrode made negative). In this way, many degraded cells can be returned to full output. However, some cannot, and this may be due to the formation of

Cu nodules that make direct contact between the metallized substrate and the grid with no intermediate Cu_2S electrolyte. Only electronic current could pass through such a shunting path.

5.3 High-Temperature Degradation in Air

In Section 3.2.7 evidence was presented which showed that chalcocite (nominally Cu_2S) converts to djurleite (nominally $\text{Cu}_{1.96}\text{S}$) upon long standing at room temperature, and that similar changes to the high-temperature form of djurleite were affected by short treatments at 250°C. In Section 3.2.8, it was shown that Cu_2S heated in vacuum or inert atmospheres developed whiskers of Cu, showing that the composition of the solid becomes poorer in Cu with increasing temperature. It was also shown that the process in vacuum was reversible. Should rejection of Cu occur in the presence of oxygen (air), the metallic Cu would be oxidized to Cu_2O or CuO (depending on temperature and oxygen pressure) and the process would then be irreversible. Even at constant temperature, the presence of oxygen would tend to extract Cu at the surface until the thermodynamic activity of Cu in the Cu_{2-x}S layer was reduced to that in the surface oxide.

We believe that the above effects are responsible for the observed degradation of CdS solar cells when they are exposed to air at moderate temperatures, such as 150°C. The rate of degradation at this temperature is very much faster in air than in vacuum or in inert gas, one hour in air being equivalent to several weeks in vacuum. The form of the degradation is also entirely different: Vacuum degradation causes an increase in series resistance while air degradation introduces no changes in series resistance but only a decrease in short-circuit current, the fill factor remaining approximately constant. The effect is shown in Fig. 71. The loss of current is permanent as far as we have been able to determine. All of the IV curves in Fig. 71 are very nearly the same except for displacements along the current axis. This behavior is identical to that obtained when the light intensity is progressively diminished, or when the cell area is progressively diminished. Since the grid or substrate contact does not appear to be affected in any way (many dozens of

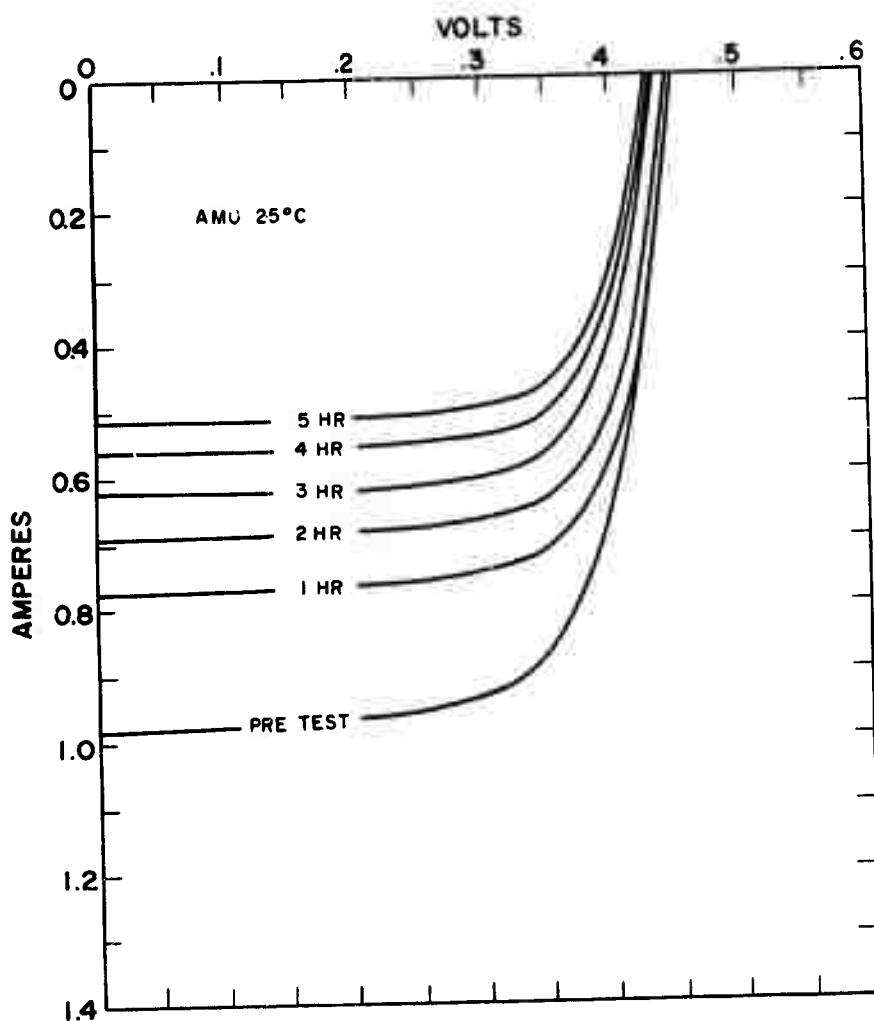


FIG. 71. HIGH-TEMPERATURE DEGRADATION OF CdS
SOLAR CELLS HEATED IN AIR, EXPOSURE
TEMPERATURE = 143°C

cells have been degraded in this manner -- with identical results), an effective loss of cell area does not seem to be responsible for the observed effects. The Kapton cover does not darken to any noticeable degree by such exposure; and the epoxy cover-plastic likewise suffers no appreciable darkening. Hence a change in the Cu_2S layer is most likely responsible. This could be either a decrease in absorption coefficient or an increase in recombination rate -- or both. A reaction with oxygen, for example, might form Cu_2O which is much more transparent than Cu_2S throughout most of the solar spectrum and the Cu_2S layer would be reduced in thickness. A decrease in short-circuit current would then be expected. On the other hand, if CuO or CuS were formed, the surface of the film would become darker and might thereby also lead to the observed effects. However, a thin layer of Cu_2S vacuum-deposited on a Pyrex substrate was found to become substantially lighter in color (by transmission) when it was heated for 10 minutes in air at 250°C . This would indicate that Cu_2O is a more likely possibility. There is also the possibility that the absorption coefficient of Cu_2S is reduced by changes in stoichiometry brought about by oxidation. Further tests will be needed to establish the nature of such reactions (a thermodynamic analysis of various possible reactions is now being carried out).

Since the degradation in air occurs for finished cells with Kapton or Mylar covers, these plastics and the epoxy layer must be permeable to oxygen. Permeability data supplied by DuPont indicate that a 1 mil Kapton film having a differential oxygen pressure of 1 atm will permeate 25 cm^3 of O_2 (standard P&T) per day for a 100 in^2 film at 25°C (presumably faster at higher temperature). The corresponding value for Mylar is $3 \text{ cm}^3/\text{day}$. For a $3'' \times 3''$ Kapton-covered cell in air ($P_{\text{O}_2} = 0.2 \text{ atm}$), the influx of oxygen could be as large as $0.49 \text{ cm}^3/\text{day}$ at room temperature. This rate of oxygen permeation would supply sufficient O_2 to react with all of the Cu_2S to form Cu_2O in about one day. Since such a reaction is not observed at 25°C , the reaction is evidently not limited by the availability of oxygen but by the kinetics or thermodynamics of the reaction.

Another effect which may be closely related to the above reactions is the apparent need to expose the Cu_2S layer to oxygen before any photovoltaic response is observable in newly formed cells. If the formation of the Cu_2S layer is carried out in an oxygen-free environment, the photovoltaic effect is absent or very feeble, as determined by probe tests. This test is used after the 250°C. heat treatment (in air for normal cells, in argon for these particular cells); and the voltage developed between the substrate and a gold probe electrode during illumination normally yields a strong photovoltaic response. Even momentary exposure to oxygen (air) before a 2 minute heat treatment in argon produces a normal response. The shortness of the exposure which produces favorable results indicates that only a surface reaction may be involved. The generation of Cu vacancies near the surface could greatly increase the electrical conductivity and thereby strongly influence the ohmicity of the grid (probe) contact.

The amount of surface reaction needed to affect large changes in the thin Cu_2S layer is surprisingly small. For example, a monolayer of CuO formed on the surface of the Cu_2S layer in effect produces $\sim (10^{22})^{2/3} \sim 4 \times 10^{14}$ Cu vacancies/cm². If these vacancies were uniformly distributed in the Cu_2S layer (10^{-5} cm actual thickness) then the concentration of vacancies (and free holes) would be increased by $4 \times 10^{14}/10^{-5} = 4 \times 10^{19}$ cm⁻³. This would account for the entire observed hole concentration in Cu_2S . In order to test for such effects the conductivity of Cu_2S formed in the absence of oxygen should be measured. This has not yet been done; but we have already noted increases in electrical conductivity by additional exposure to air at 250°C (see Section 3.2.3).

The mode of degradation described in this section is not directly relevant to space applications since no oxygen is present in the environment; however, this type of degradation is very important during cell fabrication and precautions must be taken to avoid exposure of the cells to high temperature in the presence of air (other than the initial 250°C exposure -- which appears to have a beneficial effect).

5.4 Thermal Cycling Degradation

Several laboratories have tested Clevite thin-film solar cells in simulated earth-orbit environments. These tests have been very limited in number, often including special cells of modified construction; and many of the "standard" cells were of early vintage. In addition, the load-dependent effects were not fully recognized during the early tests and there is still some question about the validity of some of the earlier measuring techniques. The more recent tests, (45) which did not suffer from these uncertainties and which involved cells that are more representative of presently produced cells, have shown that the cells suffer a definite but relatively mild degradation. The principal effect is a gradual loss of short-circuit current, with a somewhat smaller loss of fill factor. The open-circuit voltage remained essentially constant. In fact, the open-circuit voltage showed a small improvement in all cases during the early cycling period. About 10% of the current was lost after 2031 cycles.

No definite explanation for this mode of degradation exists.

The form of the degradation, however, provides evidence for two possibilities:

(1) The observed results can be interpreted as a loss of effective cell area, due for example to loosening of the grid. (The apparent loss of effective area by development of lateral cracks in the CdS layer as inferred from cross-section studies is now known to be an artifact--the cracks having been formed by improper sectioning technique.)

(2) The observed results can be interpreted as changes in the Cu₂S layer which reduce the collected current: a transformation to a different crystal structure, a decrease in optical absorption, or an increase in recombination rate. There is a possibility that the effect is a mild form of the air degradation discussed in the last section. Although the tests were performed in a vacuum at a pressure $< 10^{-7}$ Torr, and the maximum cell temperatures were only about 65°C, the tests lasted for long periods and we have already seen that very small amounts of oxygen can cause significant changes in the Cu₂S layer.

Additional tests are obviously needed to clarify the nature of this type of degradation. Accelerated tests, which would expose cells to conditions more extreme than those anticipated in actual application, would help to reduce the time of evaluation of intended improvements in cell design.

6. SUMMARY OF NEEDS FOR FUTURE WORK

In examining the results of this and other programs, the need for additional work in certain experimental areas has become evident. In this section, we summarize some specific types of experiments which should lead to improved understanding of the operating and failure mechanisms in the CdS solar cell.

(1) In order to clarify the role of the i-layer, IV measurements of the $\text{Cu}_2\text{S:}\text{i-CdS}$ junction should be made (such as those described in Section 3.5.8.1). Thin single crystals of CdS with and without In doping should be completely compensated with Cu and then formed into solar cells with provisions for varying the thickness of the CdS and for operating the cells in both front and backwall modes.

(2) In order to help identify the centers responsible for the infrared quenching bands observed for undoped-CdS solar cells, a comparison of the quenching characteristics of Cu-compensated and S-compensated CdS crystals or ceramics should be carried out.

(3) Further study should be made of the sharp loss of current at the band edge of CdS in the spectral response of cells having thin Cu_2S layers. Whether the loss can be attributed to a sharp rise of interface-recombination rate at this wavelength should be established, and alternative explanations should be sought.

(4) The temperature dependence of the dark IV characteristics should be determined on a representative number of cells having different construction, e. g., different i-layer thickness, or different doping in the p-CdS layer. Such data would improve our understanding of the nature of the barrier in the dark.

(5) The temperature dependence of the threshold voltage for electrolytic deposition of Cu should be established. The resistance of cells to this mode of failure above room temperature would then be known.

(6) The nature of the reaction of oxygen with Cu_2S should be established by experimental means. Electron diffraction analysis seems to be the most direct approach. Such data should be supported with chemical-thermodynamic (free-energy) analysis.

(7) The complex crystallography of the various cuprous sulfide phases should be clarified, including the effect of oxygen as well as those of temperature and composition. The form of the cuprous sulfide that exists on completed thin film solar cells should be established.

(8) The optimum doping level in the CdS layer should be re-examined in the light of the known degrading effects of heat treatments in air. The poor results obtained with high donor doping levels might be overcome if the i-layer was developed by prolonged heat treatment in vacuum. There are indications that standard process cells would yield improved short-circuit currents by such treatment.

These and other studies are expected to be carried out under Contract F 33(615)-69-C-1732, sponsored by Aerospace Research Laboratories.

7. ACKNOWLEDGMENTS

The authors wish to thank Mr. Ernest Benko and Mrs. Irene Cisan for colorimetric analysis; Miss Rose Kozak for spectrographic analyses; Mr. Dennis Stepka, Mr. Michael Panfil and Miss Dolores Wright for sample preparation; Dr. Henry Brandhorst of NASA, Lewis, for the use of their cryogenic facilities; and Dr. Richard Bube of Stanford University for constructive criticism.

8. REFERENCES CITED

1. F. A. Shirland, Advanced Energy Conversion 6, 201 (1966).
2. H. Diehl and G. F. Smith, "The Copper Reagents: Cuproine, Neocuproine, Bathocuproine," (The G. Frederick Smith Chemical Co., Columbus, Ohio, 1958).
3. W. Palz, G. Cohan Solal, J. Vedel, J. Fremy, D. T. Ngyen, and J. Valerio, Conf. Record, Seventh Photovoltaic Specialist Conference, Nov. 1968, IEEE Cat. No. 68C63ED.
4. L. R. Shiozawa, G. A. Sullivan, and F. Augustine, "Research on the Mechanism of the Photovoltaic Effect in High Efficiency Thin-Film Solar Cells," Contract AF 33(615)-5224, ARL 67-0190, Sept. (1967).
5. G. B. Abdullaev, Z. A. Zliyorova, E. H. Zamanova, and G. A. Asadov, Phys. Status Sol. 26, 65 (1968).
6. E. Hirahara, J. Phys. Soc. Japan 6, 428 (1951).
7. G. P. Sorokin, Yu. M. Papshev, and P. T. Oush, Soviet. Phys. Solid State 7, 810 (1966).
8. R. Marshall and S. S. Mitra, J. Appl. Phys. 36, 3882 (1965).
9. L. Eisenmann, Ann. Phys. 10, 129 (1952).
10. T. S. Moss, Solid State Electronics 2, 222 (1961).
11. H. Takeda, J. D. H. Donnay, E. H. Roseboom, and D. E. Appleman, Zeit. Krist. 125, 404 (1967).
12. E. N. Eliseev, L. E. Rudenko, L. A. Sinev, B. K. Koshurhikov, and N. I. Solovov, Mineralog. Sb., L'vovsk. Gos. Univ. 18, 385-400 (1964).
13. International Tables for X-Ray Crystallography, Vol. 2, Int'l Univ. of Crystallography (1959), p. 228.
14. J. Singer and P. A. Faeth, Appl. Phys. Letters 11, 130 (1967).
15. C. S. Barrett, Structure of Metals, 2nd Ed., McGraw-Hill Book Co., New York (1962), p. 54.
16. A. E. vanAerschot, J. J. Capart, K. H. David, M. Fabbricotti, K. H. Heffels, J. J. Loferski, and K. K. Reinhartz, Conf. Record, Seventh Photovoltaic Specialist Conference, Nov. 1968, IEEE Cat. No. 68C63ED.

17. S. Djurle, *Acta Chem. Scand.* 12, 1415-25 (1958).
18. E. Hirahara, *J. Phys. Soc. Japan* 6, 422 (1951).
19. R. L. Clarke, *J. Appl. Phys.* 30, 957 (1959).
20. W. Szeto and G. A. Somorjai, *J. Chem. Phys.* 44, 3490 (1966).
21. H. H. Woodbury, *J. Appl. Phys.* 36, 2287 (1965).
22. L. R. Shiozawa, F. A. Sullivan, and F. Augustine, "Research on the Mechanism of the Photovoltaic Effect in High-Efficiency CdS Thin-Film Solar Cells," Contract AF 33(615)-5224, Oct. (1968).
23. H. W. Brandhorst, Jr., *Conf. Record, Seventh Photovoltaic Specialist Conference*, Nov. 1968, IEEE Cat. No. 68C63ED.
24. W. D. Gill, "Mechanism of the Photovoltaic Effect in II-VI Compounds," *Prog. Rept. No. 4* (Oct. 1, 1968-March 31, 1969). Stanford Univ. Report No. SV-DMS-69-Grant NGR-05-020-214. Part of this reported in: W. D. Gill, P. F. Lindquist, and R. H. Bube, *Conf. Record, Seventh Photovoltaic Specialist Conference*, Nov. 1968, IEEE Cat. No. 68C63ED.
25. D. C. Reynolds, S. J. Czyzak, *Phys. Rev.* 96, 1705 (1954).
26. J. Woods and J. A. Champion, *J. Electron. & Control* 7, 243 (1959).
27. H. G. Grimmeiss and R. Memming, *J. Appl. Phys.* 33, 2217 (1962).
28. L. R. Shiozawa, J. M. Jost, and G. A. Sullivan, "Research on Improved II-VI Crystals," Contract F 33(615)-68-C-1601, 2nd Quarterly Progress Report, Dec. (1968).
29. R. H. Bube, Photoconductivity in Solids, John Wiley and Sons, New York (1960), p. 55 (and p. 349).
30. J. vanLaar and J. J. Scheer, *Philips Research Reports* 15, 1, (1960).
31. Iu. A. Shuba, *Soviet Phys., Tech. Phys.* 1, 1103 (1957).
32. R. W. Swank, *Phys. Rev.* 153, 844 (1967).
33. H. Okimura, M. Kawakami, and Y. Sakai, *Japan. J. Appl. Phys.* 6, 908 (1967).
34. J. vanLaar, J. J. Schur, *Philips Res. Rpts.* 17, 101 (1962); J. vanLaar and J. J. Scheer, *Philips Tech. Rev.* 29, 54 (1968); G. W. Gobeli and F. G. Allers, *Phys. Rev.* 127, 141 (1962); T. A. Calcott, *Phys. Rev.* 161, 746 (1967).

35. R. H. Bube, W. D. Gill, and P. F. Lindquist, "Mechanism of the Photovoltaic Effect in II-VI Compounds," Prog. Rept. No. 3, Stanford Univ. Report No. SU-DMS-69-R-2, Grant NGR-05-020-214, Sept. 30, 1968.

36. P. H. vanCittent, Revue D'Optique 5, 393 (1926); Ibid, 2, 57 (1923).

37. Metals Handbook, 1948 Ed., American Society for Metals, Cleveland, Ohio, p. 1155.

38. Geophysics Handbook, Revised Ed. USAF, MacMillan Co., New York (1961).

39. N. Nakayama, Japan, J. Appl. Phys. 8, 450 (1969).

40. L. R. Shiozawa, G. A. Sullivan, F. Augustine, and J. M. Jost, "Research on the Mechanism of the Photovoltaic Effect in High-Efficiency CdS Thin-Film Solar Cells," Contract AF 33(615)-5224, 2nd Quarterly Prog. Rpt., December, 1966.

41. L. R. Shiozawa, G. A. Sullivan, F. Augustine, J. M. Smith, III, and W. R. Cook, Jr., "Research on the Mechanism of the Photovoltaic Effect in High-Efficiency CdS Thin-Film Solar Cells," Contract AF 33(615)-5224, 5th Quarterly Prog. Rpt., October, 1967.

42. L. R. Shiozawa, G. A. Sullivan, F. Augustine, and J. M. Smith, III, "Research on the Mechanism of the Photovoltaic Effect in High-Efficiency CdS Thin-Film Solar Cells," Contract AF 33(615)-5224, 8th Quarterly Prog. Rpt., June, 1968.

43. H. B. Brandhorst, Jr., NASA, Lewis, private communication.

44. "Development of Improved Cadmium Sulfide Solar Cells," Contract NAS3-11845, NASA-Lewis Research Center (1969).

45. Thermal cycling tests have been conducted at Boeing MIT, and NASA (Lewis). The results of these and other tests are summarized in a report by F. A. Shirland, W. K. Bower, W. F. Dunn, and J. B. Green, "CdS Solar Cell Development," Final Report, Contract NAS3-9434, March 14, 1969; NASA Report No. CR 72534.

9. APPENDIX: Literature Review of the Cu-S Phase Diagrams, by
William R. Cook, Jr.

A great deal of work has been done on the reactions of copper with sulfur, going back as far as 1820. The principal impetus is the importance of copper sulfides as ore minerals. No attempt will be made to cover the material exhaustively but only to survey the more important results and to give a picture of the present status. In the copper-sulfur systems as in many others, continually refined X-ray diffraction techniques have disclosed the existence of phases and phase transitions that had been missed in earlier work. A review follows of the Cu-S diagram, using only literature data. In a few cases where our own data contradict the literature information, it has been noted, but the data have not been incorporated into the phase diagrams.

Five compounds have been confirmed and the existence of one other is possible. Several of these exist in more than one modification. Those known for a long time are the minerals covellite (CuS), chalcocite (Cu_2S), and digenite ($\text{Cu}_2\text{S}_5 = \text{Cu}_{1.8}\text{S}$). (In this review the decimal form of the formula, relating the number of coppers per sulfur, will be used, although formulas using whole numbers are also correct. This usage is common in the literature.) In addition $\text{Cu}_{1.96}\text{S}$ has been discovered, and $\text{Cu}_{1.9}\text{S}$ may also exist. Crystals of a Cu_xS with $1.96 > x > 1.8$ have been obtained in our laboratory, but have not been characterized completely as yet.

Covellite, CuS is a metallic blue color, platy, hexagonal, space group $\text{P}6_3/\text{mmc}$ ^(2, 3) with $a = 3.794 \pm .003 \text{ \AA}$ and $c = 16.332 \pm .010 \text{ \AA}$.⁽¹⁾ Its structure is known.^(2, 3) It has been reported that there are ordered and disordered varieties.⁽⁴⁾

Digenite, $\text{Cu}_{1.8}\text{S}$ is more bluish than chalcocite, which tends to be dull gray. The material is pseudocubic at room temperature, and cubic at higher temperatures, with a lattice constant around 5.56 \AA . The lattice constant varies with composition, particularly at high temperatures, where the composition can apparently vary all the way from Cu_2S to $\text{Cu}_{1.7}\text{S}$.⁽¹⁾ A number of workers have examined the crystal structure.⁽⁵⁻¹⁰⁾

There is general agreement that the sulfur atoms are in face-centered positions in the 5.6 \AA unit cell. Buerger⁽⁶⁾ believed the copper to be statistically distributed among the remaining positions of the antifluorite structure in the high temperature form, but most others have rejected this idea. The low temperature form has been found to have a structure that is evidently exactly cubic in dimension with the unit cell five times the high temperature cell.⁽¹⁰⁾ However, the symmetry is such as to indicate the true cell to be rhombohedral with $a = 16.16\text{\AA}$ and $\sigma = 13^\circ 56'$. The atom positions were determined for this cell.⁽¹⁰⁾

Chalcocite, Cu_2S is the common copper sulfide ore. It is dull gray and usually massive, with needle crystals rare. It was formerly believed that there was substantial solid solution with CuS ,⁽⁶⁾ but this is now considered incorrect.⁽¹⁾ The compound at room temperature is orthorhombic with $a = 11.881 \pm .004$, $b = 27.323 \pm .008$, and $c = 13.491 \pm .004\text{\AA}$,⁽¹¹⁾ space group $\text{Ab}2\text{m}$,⁽¹¹⁾ and is strongly pseudohexagonal. Near 105°C it transforms to a truly hexagonal cell, with $a = 3.961 \pm .004$, $c = 6.722 \pm .007\text{\AA}$ (at 152°C).⁽¹⁾ Near 450° it transforms again to a cubic phase which is presumed to be a continuous with digenite at those temperatures. The structure of low-temperature chalcocite has not been determined, and Djurle concluded that attempts to solve the structure of the hexagonal phase^(8, 9) were unsuccessful.

The synthetic compound djurleite ($\text{Cu}_{1.96}\text{S}$) was first reported by Djurle.⁽¹⁾ It was later identified in nature and named for the discoverer.^(12, 13) It exists in two forms. The symmetry of the room temperature form is orthorhombic or pseudo-orthorhombic, $a = 15.71$, $b = 13.56$, $c = 26.95\text{\AA}$.⁽¹⁴⁾ The X-ray diffraction pattern is similar to that of low-temperature chalcocite. Recently it has been reported to transform to tetragonal⁽¹⁾ at 86 \pm 2°, and to decompose at 154°C.⁽¹⁵⁾ It has also been reported as transforming at 100° to cubic, a phase presumably continuous with the cubic form of digenite.⁽¹⁾ The high temperature tetragonal form slowly transforms to the low temperature form with time.⁽¹⁶⁾ The space group of the tetragonal form is $\text{P}4_{3}2_{1}2$ with $a = 3.9962$, $c = 11.287\text{\AA}$; the structure has been determined.⁽¹⁶⁾

However, we have transformed crystals of orthorhombic djurleite to the tetragonal form in both air and argon at 250°C!

$\text{Cu}_{1.9}\text{S}$ has also been reported recently.⁽¹⁷⁾ Since none of the other careful investigations have disclosed its presence, it should still be regarded as unconfirmed. The structure is reported as hexagonal $a = 11.355$, $c = 13.506\text{\AA}$.

We have obtained a transformation on aging at room temperature from djurleite to a crystal of presumed composition Cu_xS with $1.96 > x > 1.8$ and with $c = 13.36\text{\AA}$. Nothing else is known about it at present.

One additional material has been reported in the literature, "Carmenite", $\text{Cu}_3\text{S}_2 = \text{Cu}_{1.5}\text{S}$. The material had some covellite in it,⁽¹⁸⁾ and so was probably a mixture of covellite and digenite.

Digenite as a distinct mineral compound has had a checkered history. Originally reported in 1844,⁽¹⁹⁾ it was later rejected as a mineral species on the assumption that it was a physical mixture of chalcocite and covellite.⁽¹⁸⁾ The transition in chalcocite at $\sim 105^\circ\text{C}$ was first discovered in 1851⁽²⁰⁾ by conductivity measurements. It was assumed by almost everyone that the cubic form (digenite) was simply that form of chalcocite occurring above 105° , particularly since after heating chalcocite to high temperature the material was cubic. In this regard Groth,⁽²¹⁾ however, vigorously maintained on the basis of the lack of any appreciable volume change that the symmetry above 105° could not be the known cubic phase, but that the transformation must be to a different symmetry. It took almost forty years to prove him correct. As a result of this confusion the older literature is full of references to "cubic chalcocite", which in many cases is digenite. The reason for this is twofold: if chalcocite is heated in air (as was done in many of the experiments even as late as 1941), the composition may drift, probably due to oxygen pickup, and the material can irreversibly enter the area of stability of digenite, from which it frequently does not revert.⁽⁶⁾ In addition, heating chalcocite to 500° or higher causes it to become cubic, isostructural with digenite. This material then would revert to orthorhombic when cooled, and it was not realized that there were, in fact, two high temperature transitions rather than one.

A current version of the Cu-S phase diagram is shown in Figs. 1 and 2. It is a composite of the various references, particularly nos. 1, 6, 7, 17, 22, and 23. Figure 2 shows the detail near Cu_2S . The complete Cu-S diagram of Rau⁽²³⁾ appears to be a composite of the literature itself, and is not a major part of his paper. The main emphasis was on the region of homogeneity of digenite. Rau has promised a paper that will explain the details of his diagram, however.

Over most of the Cu-S diagram the facts appear to be in good agreement. There are three areas that need further discussion, however: the area near pure sulfur, the high temperature boundary of the digenite solid solution, and the low temperature region between 33 and 36 atom% Cu (the low temperature digenite to chalcocite area).

The complete Cu-S diagram is not discussed by Rau, but is presumably the diagram at its own vapor pressure at the various temperatures. This distinction becomes important where volatile compounds are involved, and influences the interpretation of the extreme sulfur-rich end of the diagram. It should be recalled that sulfur boils at 444.6°C ⁽²⁴⁾ and is used as a temperature standard. Thus the high temperature region (which is dotted in) is at quite high pressure. (The pressure of Cu_2S , however, is only 0.014 mm at 1200° .)⁽²⁵⁾

Two recent versions exist of the solidus curve of digenite. That of Rau is shown as the lower curve in Fig. 2, and was determined to about 34.9%S from the high sulfur side. The upper curve comes from Johannsen and Vollmer⁽²²⁾ and was determined from the low sulfur side to about 35.2%S. The two curves do not agree very well. Incidentally, it should be noted that the compound melting at 1129° is not stoichiometric Cu_2S , but is about $\text{Cu}_{1.99}$.^(23, 26)

In the low temperature area there is rather poor agreement. Transition temperatures from hexagonal to cubic Cu_2S have been reported from 350° .⁽²⁷⁾ to 470° ,⁽²⁸⁾ and the transition in digenite from 60 to 65° .⁽⁹⁾ to 78° .⁽⁵⁾ The agreement is somewhat better on the orthorhombic-hexagonal transition in Cu_2S ^(15, 28) (100.3° to 110°).

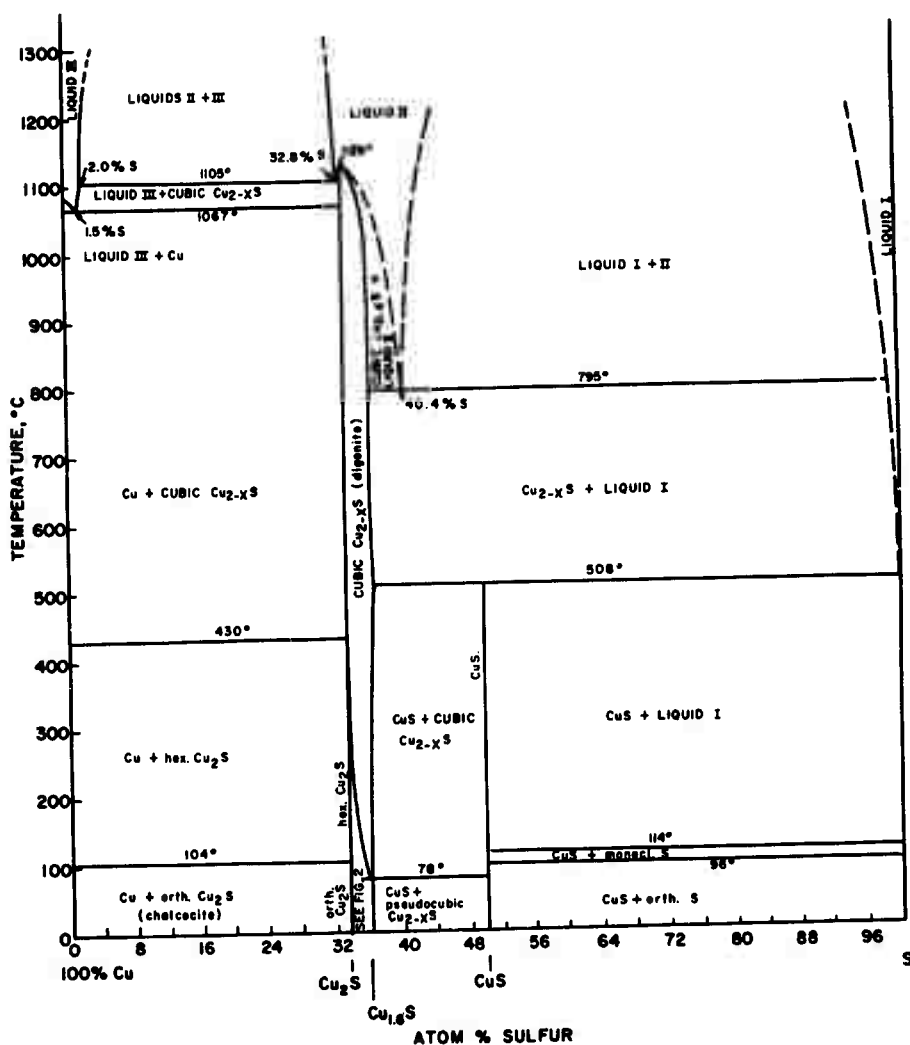


FIG. 1. Cu-S PHASE DIAGRAM

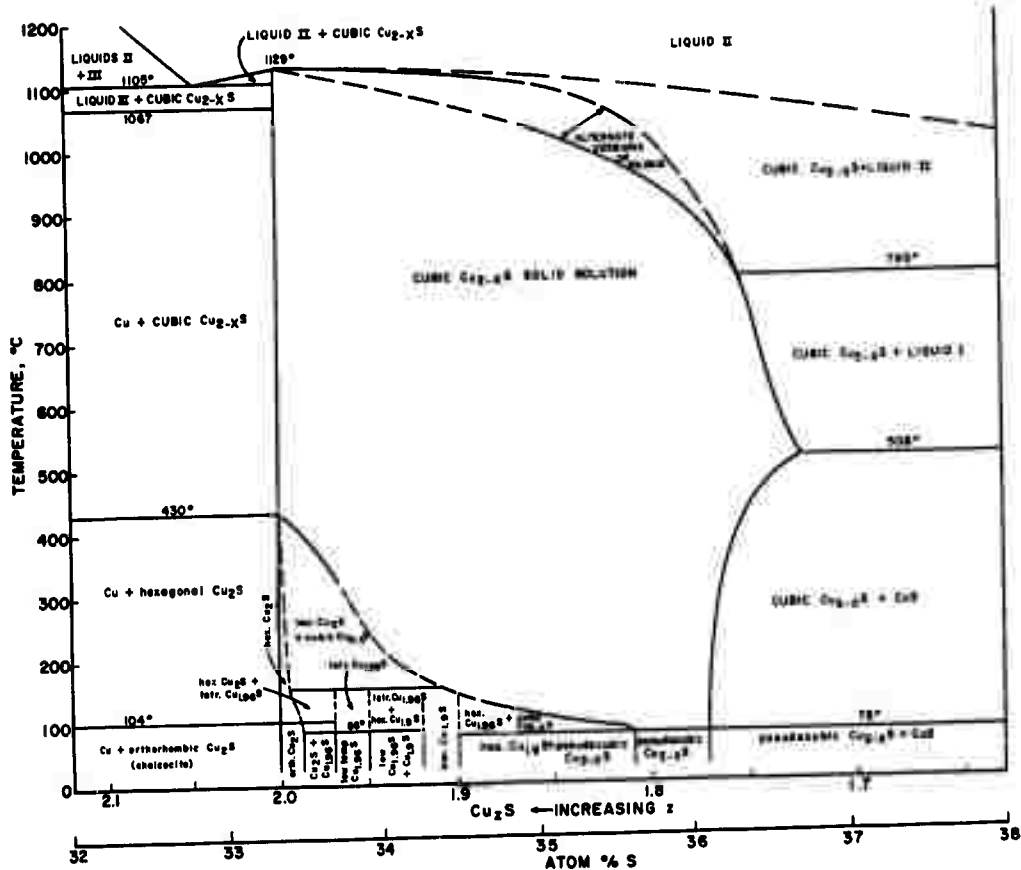


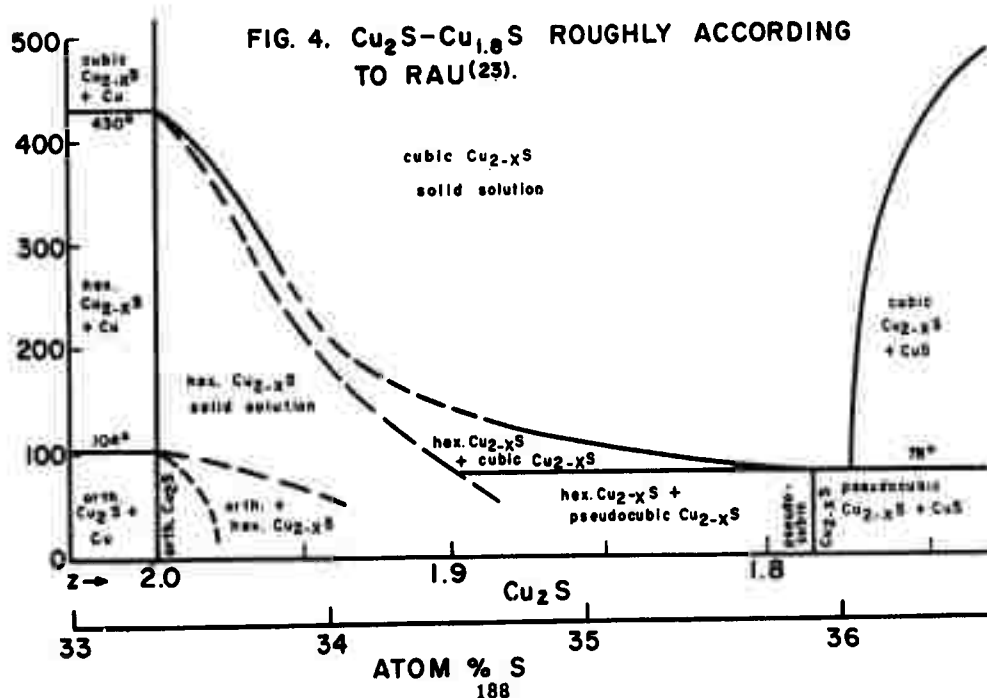
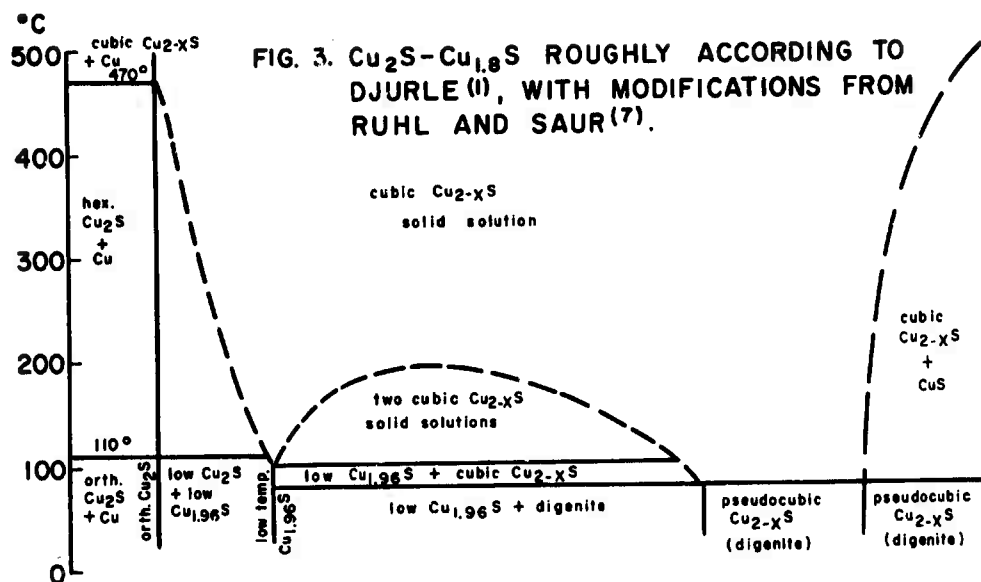
FIG. 2. Cu-S PHASE DIAGRAM IN THE VICINITY OF CHALCOCITE AND DIGENITE. BECAUSE OF CONFLICTING DATA, AREAS AROUND Cu_2S TO $Cu_{1.8}S$ ARE NOT CONSISTENT WITH THE PHASE RULE.

What is even more bothersome is the variety of phases reported. From pure chalcocite, Cu_2S it is suggested^(7, 17) that there is solid solution to about $\text{Cu}_{1.98}\text{S}$, although the results of Djurle⁽¹⁾ indicate that the minimum Cu content in Cu_{2-x}S is > 1.99 Cu. Likewise, the area of homogeneity of djurleite appears to be from roughly 1.97 to 1.95 Cu,⁽¹⁷⁾ or possibly a slightly narrower range.⁽¹⁾ The new hexagonal phase $\text{Cu}_{1.9}\text{S}$ is stated to be stable between 1.92 and 1.90 Cu.⁽¹⁷⁾ This has double the c lattice constant of hexagonal chalcocite, and no obvious relation between their a lattice constants. Rau⁽²¹⁾ extends the hexagonal chalcocite field towards lower compositions (see Fig. 3), but the basis for this was not stated. There seems no basis in the rest of the literature for relating the two hexagonal phases, particularly if $\text{Cu}_{1.96}\text{S}$ is truly tetragonal between 86° and 150°C.^(3, 6) (Mole⁽²⁹⁾ mentioned obtaining a hexagonal phase, but the lattice constants fitted hexagonal chalcocite, and the phase was probably ordinary chalcocite in which the orthorhombic superstructure was weak.)

Next is the digenite solid solution. Early work has shown a much wider compositional range than later work, probably because the phase was quenched from higher temperatures and did not represent equilibrium. A transition temperature depending on composition may also explain the variations in transition temperatures reported. The true width of the digenite solid solution field below the transition is probably no greater than $\text{Cu}_{1.82}$ to $\text{Cu}_{1.73}$.^(1, 30)

In Figs. 3 to 5 are attempted three alternate reconstructions of the phase diagram near Cu_2S to $\text{Cu}_{1.8}\text{S}$. All involve some interpretation of the data in the literature. It may be, for instance, that the boundary of cubic digenite between $\text{Cu}_{1.82}\text{S}$ and $\text{Cu}_{1.96}\text{S}$ in Fig. 3 should be drawn as a hump (as dotted line) rather than as a straight line. None of these figures incorporate recent data from our own experiments.

One other complication should be mentioned. For digenite, besides the stable "cubic" (probably rhombohedral) cell of 5 times the high temperature cell, there are two other metastable cells, one with 5 times the simple cell edge, the other with 6 times.⁽²⁹⁾ It is entirely possible that other stable cells may be found for low temperature digenite, representing



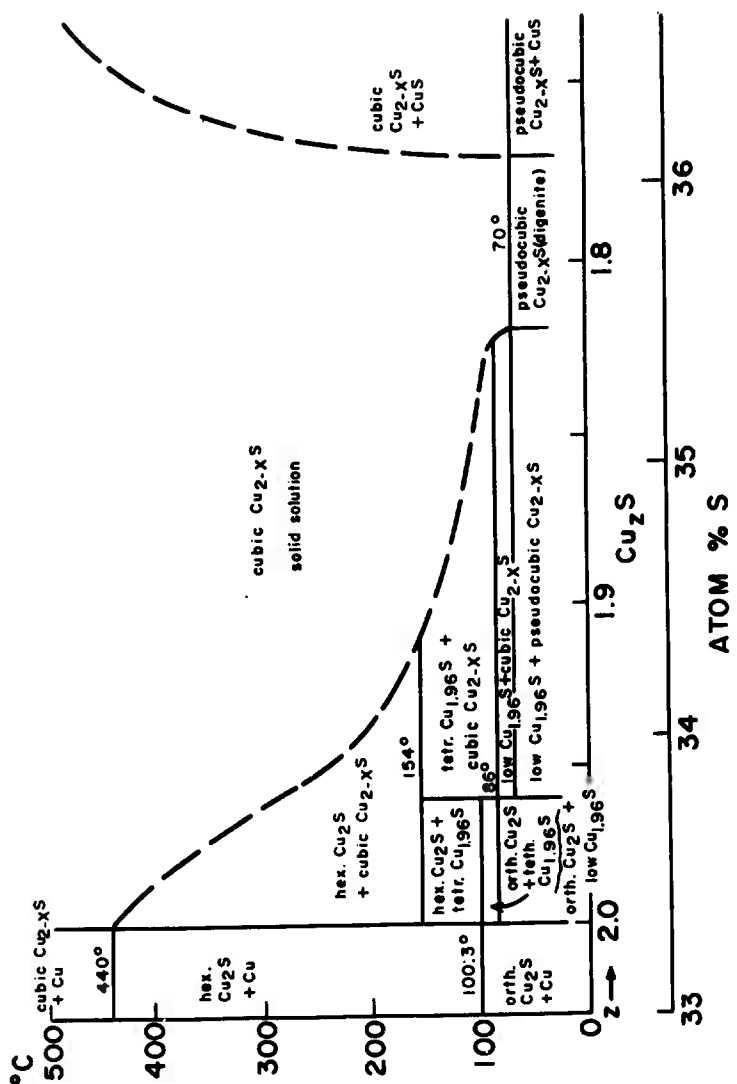


FIG. 5. $\text{Cu}_2\text{S}-\text{Cu}_{1.8}\text{S}$ ROUGHLY ACCORDING TO KULLERUD (25)
 $(\text{Cu}_{2-x}\text{S}$ SOLID SOLUTIONS DJURLE⁽¹⁾ AND RAU⁽¹⁹⁾)

a different ordering based upon small compositional differences. Such variations of superstructure have been found frequently in recent years. One such example familiar to the author is found in the $\text{Pb}(\text{Zr}, \text{Sn}, \text{Ti})\text{O}_3$ system.⁽³¹⁾

References

1. S. Djurle, *Acta Chem. Scand.* 12, 1415-26 (1958).
2. I. Oftedal, *Z. Krist.* 83, 9-25 (1932).
3. L. G. Berry, *Am. Min.* 39, 504-9 (1954).
4. *Structure Reports* 23, 142 (1959).
5. P. Rahlfs, *Z. Physik. Chem.* B31, 157-94 (1936).
6. N. W. Buerger, *Econ. Geol.* 36, 19-44 (1941).
7. W. Rühl and E. Saur, *Ber. Oberhess. Ges. Natur-u. Heilk. Giessen, Naturw. Abt.* 28, 35-47 (1957).
8. R. Ueda, *J. Phys. Soc. Japan* 4, 287-92 (1949).
9. N. V. Belov and V. P. Butuzov, *Compt. Rend. Acad. Sci. U.R.S.S.* 54, 717-20 (1946).
10. G. Donnay, J. D. H. Donnay, and G. Kullerud, *Am. Min.* 43, 228-42, (1958).
11. M. J. Buerger and N. W. Buerger, *Am. Mon.* 29, 55-65 (1944).
12. E. H. Roseboom, Jr., *Am. Min.* 47, 1181-4 (1962).
13. N. Morimoto, *Minearl. J.* 3, 338-44 (1962).
14. H. Takeda, J. D. H. Donnay, E. H. Roseboom, and D. E. Appleman, *Zeit. Krist.* 125, 404-13 (1967).
15. G. Kullerud, Handbook of Physical Constants, GSA Mem. 97, 323-44 (1966).
16. A. Janosi, *Acta Cryst.* 17, 311-13 (1964).
17. E. N. Eliseev, L. E. Rudenko, L. A. Sinev, B. K. Koshurhikov, and N. I. Solovov, *Mineralog. Sb., L'vovsk. Gos. Univ.* 18, 385-400 (1964).
18. Dana's System of Mineralogy 6th Ed., John Wiley and Sons, Inc. (1892), p. 56.
19. A. Breithaupt, *Ann. Phys.* 61, 671-5 (1844).
20. W. Hittorff, *Ann. Phys.* 84, 1-28 (1951).
21. P. Groth, Chemische Kristallographie I, 135-46 (1906).

22. F. Johannsen and H. Vollmer, *Z. Erzbergau u. Metallhuttenw.* 13, 313-22 (1960).
23. H. Rau, *J. Phys. Chem. Solids* 28, 903-16 (1967).
24. Handbook of Chemistry and Physics, Chemical Rubber Co., Cleveland, Ohio.
25. R. A. Isakova, N. V. Nesterov, and A. S. Shendyapin, *Tr. Inst. Met. i Obogashch., Akad. Nauk Kaz. SSR* 6, 156-9 (1963) (Chem. Abstr. 59, 13632, 1963).
26. E. Jensen, *Avhandl. Norske Videnskaps-Akad. Oslo. I. Mat. - Naturw. Klasse* 1947, No. 6, 14 pp.
27. K. K. Kelley, *U. S. Bur. Mines. Bull.* No. 476 (1949).
28. E. Hirahara, *J. Phys. Soc. Japan* 2, 211-13 (1947); 6, 422-7 (1951).
29. R. Mole, *Ann. Chem. (Paris)* 9, 145-80 (1954).
30. N. Morimoto and G. Kullerud, *Am. Min.* 48, 110-23 (1963).
31. D. Berlincourt, "Research on Piezoelectric Materials and Phenomena," Jan. 1, 1964 to June 30, 1965, Sandia Corp., P.O. No. 51-6529 and 53-0193, Sept. 30, 1965.

Unclassified

Security Classification

DOCUMENT CONTROL DATA - R&D

(Security classification of title, body of abstract and indexing annotation must be entered when the overall report is classified)

1. ORIGINATING ACTIVITY (Corporate author) Clevite Corporation Electronic Research Division Cleveland, Ohio 44108		2a. REPORT SECURITY CLASSIFICATION Unclassified
2b. GROUP		
3. REPORT TITLE Research on the Mechanism of the Photovoltaic Effect in High-Efficiency CdS Thin-Film Solar Cells		
4. DESCRIPTIVE NOTES (Type of report and inclusive dates) Scientific Final,		
5. AUTHOR(S) (Last name, first name, initial) L. R. Shiozawa J. M. Smith, III F. Augustine W. R. Cook, Jr. G. A. Sullivan		
6. REPORT DATE October 1969	7a. TOTAL NO. OF PAGES 210	7b. NO. OF REFS 31
8a. CONTRACT OR GRANT NO. AF33(615)-5224	9a. ORIGINATOR'S REPORT NUMBER(S) Project 303330	
9b. PROJECT NO. 7885	9b. OTHER REPORT NO(S) (Any other numbers that may be assigned this report) ARL 69-0155	
c. DoD Element 61102F	d. DoD Subelement 681301	
10. AVAILABILITY/LIMITATION NOTICES 1. This document has been approved for public release and sale; its distribution is unlimited.		
11. SUPPLEMENTARY NOTES TECH OTHER	12. SPONSORING MILITARY ACTIVITY Aerospace Research Laboratories (ARX) Office of Aerospace Research WPAFB, Ohio 45433	
13. ABSTRACT A tentative Cu ₂ S:CdS heterojunction model which involves intrinsic absorption in a thin Cu ₂ S surface layer and photoconductivity in an adjacent layer of CdS was studied by electrical, optical, and chemical measurements. The proposed barrier height in the dark of ~ 1.2 eV changing to ~ 0.85 eV in sunlight is consistent with the observed differences in the IV characteristics, the measured photoconductive properties of Cu-compensated CdS, the observed maximum low-temperature open-circuit voltage (0.8 V), and published work function data. The photoconductivity of the i-CdS layer which controls the current generated in the Cu ₂ S layer adequately explains the enhancement and quenching effects of biasing light as well as the transient properties of the cell. The lattice mismatch between the epitaxially formed Cu ₂ S and the CdS introduces strains and interface states, the latter acting as recombination centers during forward bias. The Cu ₂ S layer initially formed as chalcocite undergoes transformation to djurleite and other phases during room-temperature exposure to air, and these changes are accelerated at elevated temperatures, giving rise to rapid degradation of current output at 150°C. The measured diffusivity (~ 10 ⁻⁷ cm ² /sec) and mobility (~ 3 x 10 ⁻⁶ cm ² /V-sec) of Cu ions in Cu ₂ S is sufficiently large to account for the observed formation of Cu nodules during open-circuit illumination, the threshold voltage for this process being ~ 0.4 V. The diffusivity of Cu in CdS [D = 2.1 x 10 ⁻³ exp(0.96/kT) cm ² /sec] derived from capacitance and low-temperature solubility [([Cu] = 6.6 x 10 ²² exp(-0.505 eV/kT) cm ⁻³)] measurements indicates that the Abstract Cont'd.		

Continuation Sheet

Abstract

i-CdS layer grows to a thickness of $\sim 1 \mu$ during cell processing and that the subsequent thickening at 65°C is slow enough to allow 3 to 5 years of continuous operation. The more rapid degradation in vacuum at higher temperatures is shown to be controllable by donor doping of the CdS. Although the maximum theoretical efficiency is shown to be $\sim 15\%$, realistic constraints limit the achievable efficiency to $\sim 10\%$.

Security Classification				LINK A		LINK B		LINK C	
14.	KEY WORDS	ROLE	WT	ROLE	WT	ROLE	WT	ROLE	WT
		Solar cell. Photovoltaic mechanism. cadmium sulfide Cuprous sulfide Microstructure Spectral response Barrier height Diffusion Photoconductivity Degradation							
INSTRUCTIONS									
<p>1. ORIGINATING ACTIVITY: Enter the name and address of the contractor, subcontractor, grantee, Department of Defense activity or other organization (corporate author) issuing the report.</p> <p>2a. REPORT SECURITY CLASSIFICATION: Enter the overall security classification of the report. Indicate whether "Restricted Data" is included. Marking is to be in accordance with appropriate security regulations.</p> <p>2b. GROUP: Automatic downgrading is specified in DoD Directive 5200.10 and Armed Forces Industrial Manual. Enter the group number. Also, when applicable, show that optional markings have been used for Group 3 and Group 4 as authorized.</p> <p>3. REPORT TITLE: Enter the complete report title in all capital letters. Titles in all cases should be unclassified. If a meaningful title cannot be selected without classification, show title classification in all capitals in parenthesis immediately following the title.</p> <p>4. DESCRIPTIVE NOTES: If appropriate, enter the type of report, e.g., interim, progress, summary, annual, or final. Give the inclusive dates when a specific reporting period is covered.</p> <p>5. AUTHOR(S): Enter the name(s) of author(s) as shown on or in the report. Enter last name, first name, middle initial. If military, show rank and branch of service. The name of the principal author is an absolute minimum requirement.</p> <p>6. REPORT DATE: Enter the date of the report as day, month, year, or month, year. If more than one date appears on the report, use date of publication.</p> <p>7a. TOTAL NUMBER OF PAGES: The total page count should follow normal pagination procedures, i.e., enter the number of pages containing information.</p> <p>7b. NUMBER OF REFERENCES: Enter the total number of references cited in the report.</p> <p>8a. CONTRACT OR GRANT NUMBER: If appropriate, enter the applicable number of the contract or grant under which the report was written.</p> <p>8b, 8c, & 8d. PROJECT NUMBER: Enter the appropriate military department identification, such as project number, subproject number, system numbers, task number, etc.</p> <p>9a. ORIGINATOR'S REPORT NUMBER(S): Enter the official report number by which the document will be identified and controlled by the originating activity. This number must be unique to this report.</p> <p>9b. OTHER REPORT NUMBER(S): If the report has been assigned any other report numbers (either by the originator or by the sponsor), also enter this number(s).</p> <p>10. AVAILABILITY/LIMITATION NOTICE: Enter any limitations on further dissemination of the report, other than those imposed by security classification, using standard statements such as:</p> <p>(1) "Qualified requesters may obtain copies of this report from DDC."</p> <p>(2) "Foreign encumbrance and dissemination of this report by DDC is not authorized."</p> <p>(3) "U. S. Government agencies may obtain copies of this report directly from DDC. Other qualified DDC users shall request through _____."</p> <p>(4) "U. S. military agencies may obtain copies of this report directly from DDC. Other qualified users shall request through _____."</p> <p>(5) "All distribution of this report is controlled. Qualified DDC users shall request through _____."</p> <p>If the report has been furnished to the Office of Technical Services, Department of Commerce, for sale to the public, indicate this fact and enter the price, if known.</p> <p>11. SUPPLEMENTARY NOTES: Use for additional explanatory notes.</p> <p>12. SPONSORING MILITARY ACTIVITY: Enter the name of the departmental project office or laboratory sponsoring (paying for) the research and development. Include address.</p> <p>13. ABSTRACT: Enter an abstract giving a brief and factual summary of the document indicative of the report, even though it may also appear elsewhere in the body of the technical report. If additional space is required, a continuation sheet shall be attached.</p> <p>It is highly desirable that the abstract of classified reports be unclassified. Each paragraph of the abstract shall end with an indication of the military security classification of the information in the paragraph, represented as (TS), (S), (C), or (U).</p> <p>There is no limitation on the length of the abstract. However, the suggested length is from 150 to 225 words.</p> <p>14. KEY WORDS: Key words are technically meaningful terms or short phrases that characterize a report and may be used as index entries for cataloging the report. Key words must be selected so that no security classification is required. Identifiers, such as equipment model designation, trade name, military project code name, geographic location, may be used as key words but will be followed by an indication of technical context. The assignment of links, rules, and weights is optional.</p>									

Unclassified
Security Classification